Imperial College of Science,
Technology and Medicine

University of São Paulo,
Escola Politécnica

# The analytical and phenomenological sensitivity study of the flow-induced instabilities about a hinged circular cylinder with a splitter plate.

Robin Lucas Guillaume Basso

Supervised by
G. R. S. Assi, S. J. Sherwin, and Y. Hwang

Submitted in part fulfillment of the requirements for the joint degree
of Doctor of Philosophy in Aeronautics at Imperial College and in
Naval Engineering at the University of São Paulo.
October 5, 2021.

# Abstract

This thesis investigates the origin of flow-induced instabilities and their sensitivities in a flow over a rotationally flexible circular cylinder with a rigid splitter plate. A linear stability and sensitivity problem are formulated in the two-dimensional Eulerian frame by considering the geometric nonlinearity arising from the translations and rotational motion of an arbitrary geometry (cross-sectional structure's shape), which is not present in the stationary or purely translating stability methodology. This nonlinearity needs careful and consistent treatment in the linearised problem, particularly when considering the Eulerian frame of reference adopted in this study and not so widely considered.

Considering the one degree of freedom problem of the rotationally flexible circular cylinder with a rigid splitter plate, two types of instabilities arising from the fluid-structure interaction are found. The first type of instability is the stationary symmetry-breaking mode, which was well reported in previous studies. This instability exhibits a strong correlation with the length of the recirculation zone. A detailed analysis of the instability mode and its sensitivity reveals the importance of the flow near the tip region of the plate for the generation and control of this instability mode. The second type is an oscillatory torsional flapping mode, which has not been well reported. This instability typically emerges when the length of the splitter plate is sufficiently long. Unlike the symmetry breaking mode, it is not so closely correlated with the length of the recirculation zone. However, the sensitivity analysis also reveals the crucial role played by the flow near the tip region in this instability. Finally, it is found that many physical features of this instability are reminiscent of those of the flapping (or flutter instability) observed in a flow over a flexible plate or a flag, suggesting that these instabilities share the same physical origin.

The sensitivity analysis of both the symmetry breaking and flapping instability is also compared to the results obtained from a stationary circular cylinder fitted to a splitter plate of the same lengths. Physically meaningful analogies are noted between the sensitivity regions of the three instabilities.



**Keywords:** *Linear stability, adjoint-based sensitivity, fluid structure interaction, flow-induced instabilities, elastically-mounted non-symmetric bluff body.*

# Resumo

**Título:** Estudo de sensibilidade analítico e fenomenológico das instabilidades induzidas pelo escoamento ao redor de um cilindro pivotante com placa plana.

Esta tese investiga a origem das instabilidades induzidas pelo escoamento e suas sensibilidades ao redor de um cilindro rotacionalmente flexível com uma placa divisora rígida. Um problema de estabilidade e sensibilidade linear é formulado no sistema de coordenadas Euleriano bidimensional, considerando a não linearidade geométrica decorrente das translações e do movimento rotacional de uma geometria arbitrária que não está presente na metodologia de estabilidade estacionária ou puramente translacional. Essa não linearidade precisa de um tratamento cuidadoso e consistente no problema linearizado, particularmente quando se considera o sistema de coordenadas Euleriano adotado neste estudo e não tão amplamente usado.

Considerando o problema de um grau de liberdade do cilindro rotativamente flexível com uma placa divisora rígida, dois tipos de instabilidades decorrentes da interação fluido-estrutura são encontrados. O primeiro tipo de instabilidade é o modo de quebra de simetria estacionário, que já foi bem relatado em estudos anteriores. Esta instabilidade exibe uma forte correlação com o comprimento da zona de recirculação. Uma análise detalhada do modo de instabilidade e sua sensibilidade revela a importância do escoamento próximo à região da ponta da placa para a geração e controle deste modo de instabilidade. O segundo tipo é um modo de flapping oscilatório, que não foi bem estudado. Esta instabilidade surge normalmente quando a placa divisora é suficientemente longa. Ao contrário do modo de quebra de simetria, ela não está tão estreitamente correlacionada com o comprimento da zona de recirculação. A análise de sensibilidade, entretanto, também revela o papel crucial desempenhado pelo escoamento próximo à região da ponta da placa dessa instabilidade. Finalmente, verifica-se que muitas características físicas dessa instabilidade são reminiscentes daquelas do flapping (ou instabilidade de vibração) observada em um escoamento ao redor de uma placa flexível ou de uma bandeira, sugerindo que essas instabilidades compartilham a mesma origem física.

A análise de sensibilidade tanto da quebra de simetria quanto da instabilidade de flapping também são comparadas aos resultados obtidos de um cilindro estacionário montado junto com uma placa divisora de mesmo comprimento, e analogias fisicamente significativas são observadas entre as regiões de sensibilidade das três instabilidades.

**Palavras chaves:** *Estabilidade linear, sensibilidade baseada no método adjunto, interação*

*fluido-estrutura, instabilidades induzidas pelo escoamento, corpo rombudo não simétrico montado elasticamente.*

# Acknowledgements

First and foremost, I am incredibly grateful to my supervisors, Professor Gustavo R. S. Assi, Professor Spencer J. Sherwin and Professor Yongyun Hwang, for their invaluable advice, continuous support, and patience during my PhD study and without whom this work would not have been possible. Their immense knowledge and plentiful experience have encouraged me in all the time of my academic research and daily life.

I would also like to thank all the members of the Núcleo de dinâmicas e Fluidos (NDF) research centre, the Instabilities, Turbulence and Pattern Formation Group, and Sherwin Lab. Their kind help and support have made my study and life both in Brazil and in the United Kingdom a wonderful time.

Lastly, I would like to thank the Brazilian Ministry of Education, Coordenação de Aperfeiçoamento de Pessoal de Nível Superior (CAPES) for the funding that allowed me to conduct this thesis.

# Contents

**Abstract** **i**

**Resumo** **iii**

**Acknowledgements** **v**

**1 Introduction** **1**

1.1 Motivation and objectives . . . . . 1

1.2 Statement of originality . . . . . 6

1.3 Copyright Declaration . . . . . 6

1.4 Publications and conference proceedings . . . . . 6

**2 Physical mechanisms and empirical models** **8**

2.1 Flow around a stationary circular cylinder . . . . . 8

2.1.1 Steady laminar regime . . . . . 10

2.1.2 Unsteady laminar regime . . . . . 13

2.2 Flow around a stationary circular cylinder fitted to a splitter plate . . . . . 15

2.3 Flow induced motions . . . . . 17

2.3.1 Vortex-induced vibration . . . . . 19

2.3.2 Galloping . . . . . 21

2.3.3 Symmetry breaking . . . . . 28

**3 Problem formulation** **31**

3.1 Non-linear operator . . . . . 33

3.1.1 Fluid only . . . . . 33

3.1.2 Solid only . . . . . 34

3.1.3 Coupling . . . . . 35

3.1.4 Global operator . . . . . 36

3.2 Direct operator . . . . . 37

3.2.1 Fluid only . . . . . 37

3.2.2 Solid only . . . 38
3.2.3 Coupling . . . 39
3.2.4 Global operator . . . 43
3.3 Adjoint operator . . . 44
3.3.1 Inner product . . . 44
3.3.2 Global operator . . . 45
3.3.3 Receptivity to spatially localised feedbacks . . . 49

**4 Numerical methods 53**
4.1 The Spectral/hp Element Method . . . 53
4.1.1 The weighted residuals method . . . 54
4.1.2 Discretisation . . . 56
4.1.3 The Velocity Correction scheme . . . 61
4.2 Fluid-Structure Interaction treatment . . . 64
4.2.1 Fluid equations . . . 65
4.2.2 Structural equations . . . 67
4.3 Linear Stability Analysis . . . 71
4.3.1 The Selective Frequency Damping . . . 72
4.3.2 Solutions to the associated eigenvalue problem . . . 74
4.3.3 Implementation details . . . 75

**5 Numerical scheme convergence and formulation validation 77**
5.1 $h$-refinement . . . 78
5.2 $p$-refinement . . . 80
5.3 Domain size refinement . . . 81
5.3.1 Domain size for non-linear analysis . . . 82
5.3.2 Domain size for linear analysis . . . 85
5.4 Analytic formulation numerical validation . . . 87
5.4.1 Cross-flow VIV of a circular cylinder . . . 87
5.4.2 Symmetry breaking . . . 88
5.4.3 Torsional flapping . . . 89
5.4.4 Fictitious parameters . . . 90

**6 Freely rotating cylinder fitted to a splitter plate 92**
6.1 Problem description . . . 92
6.2 Stationary body . . . 97
6.2.1 Linear stability . . . 97

6.2.2 Adjoint-based sensitivity . . . 101
6.3 Symmetry breaking . . . 105
6.3.1 Linear stability . . . 105
6.3.2 Physical mechanism of instability . . . 108
6.3.3 Adjoint-based sensitivity . . . 113
6.4 Torsional flapping . . . 118
6.4.1 Linear stability . . . 119
6.4.2 Quasi-steady analysis . . . 122
6.4.3 Physical mechanism of instability . . . 124
6.4.4 Adjoint-based sensitivity . . . 127

**7 Conclusion** **131**
7.1 Achievements . . . 131
7.2 Future work . . . 132

**Bibliography** **133**

**A Adjoint equations** **141**
A.1 Structural adjoint operator . . . 141
A.2 Fluid adjoint operator . . . 142

**B Eigenvalue decomposition** **145**

# List of Tables


4.1 Splitting scheme coefficients. Extracted from Karniadakis et al. (1991). . . . . 62

5.1 $h$-refinement summary. . . . . 79
5.2 $p$-refinement summary. . . . . 80
5.3 $St \cdot 10^{-1}$ variations. Mesh 3, $P = 7$. . . . . 82
5.4 $\bar{C_d}$ variations. Mesh 3, $P = 7$. . . . . 83
5.5 $C_l{}' \cdot 10^{-1}$ variations. Mesh 3, $P = 7$. . . . . 83
5.6 Summary of dimensionless domain sizes ($/D$) used in literature for a circular cylinder, with or without splitter plate. . . . . 84
5.7 Values of $\lambda_r^{SB}$ at $Re = 60$, and $\lambda_r^{\dagger SB}$ at $Re = 50$, in function of the fictitious inertia $I_\theta^{Fict}$ for $I_\theta = 50$, $c_\theta = 0$ and $k_\theta = 1 \times 10^{-4}$. . . . . 91

6.1 Values of the vortex shedding mode frequency $\lambda_i^{VS,F}$ along the neutral stability curve in function of the splitter plate length. . . . . 99
6.2 Values of $\|\Theta_F\|_\infty (\equiv \max_{\mathbf{x}} \Theta_F)$ along the threshold of stability in function of the splitter plate length for the fixed cylinder case (matching figure 6.10). . . . . 105
6.3 Values of $\|\Theta_F\|_\infty (\equiv \max_{\mathbf{x}} \Theta_F)$ and $\Theta_S$ along the threshold of stability as a function of the splitter plate length. The cases here correspond to those in figure 6.19. . . . . 115
6.4 Values of $\|\Theta_F\|_\infty$ and $\Theta_S$ in function of the Reynolds number for $L/D = 1$ (matching figure 6.20). . . . . 116
6.5 Values of $\|\Theta_F\|_\infty$ and $\Theta_S$ in function of the plate length at $Re = 40$ (matching figure 6.21). . . . . 118
6.6 Values of $\Theta_{F,\max} (\equiv \max_{\mathbf{x}} |\Theta_F|)$ and $\Theta_S$ along the threshold of stability as a function of the splitter plate length. Here, $\lambda_r^{TF} \simeq 0$. . . . . 130

# List of Figures


1.1 Occurrences of the symmetry breaking instability in nature. Sub-figure ($a$) extracted from Knacke et al. (2004), other sources are unknown. . . . . 2

1.2 Diverse forms and examples of risers, cables and mooring lines of offshore structures. From left to right: floating wind turbines; sub-sea system (SS); fixed platform (FP); floating production, storage and offloading vessel (FPSO); floating production system platform (FPS); spar platform (SP); vertically moored tension leg platform (TLP); jack-up rig platform. Reproduced from *oilstates.com*. 3

1.3 Examples of experimental FIV suppressors, (a) helical strake, (b) axial slats, (c) streamlined fairing, (d) present splitter plate, (e) ribboned cable, (f) pivoted guiding vane, (g) spoiler plates. Adapted from Blevins (2001). . . . . 4

1.4 A schematic diagram of flow and structure configuration. Here, $\mathbf{u}_\infty(= (U_\infty, 0))$ is the freestream velocity, $\theta$ the counter-clockwise rotation angle of the cylinder of diameter $D$, along with the splitter plate of length $L$ and thickness $l$. $k_\theta$ correspond to the structural rotational stiffness, and $c_\theta$ to the rotational damping coefficient. . . . . 5

2.1 Global picture of the order of magnitude of the aerodynamic coefficients for an infinite smooth circular cylinder, and of the different regimes, as a function of the Reynolds number. Adapted from Zdravkovich (1997). . . . . 9

2.2 Experimental flow visualisations of the steady laminar regime around a circular cylinder. Extracted from van Dyke (1982) . . . . . 11

2.3 Near wake pattern in the steady, separated laminar regime (not to scale). . . . . 12

2.4 Normalised length of the recirculation wake bubble $L_f/D$ (measured from the rear stagnation point) for different Reynolds number. Adapted from Giannetti and Luchini (2007) and Zdravkovich (1997). . . . . 12

2.5 Experimental visualisation of the laminar Von Kármán vortex street at Reynolds number $Re = 140$. Extracted from van Dyke (1982). . . . . 13

2.6 Relationship between the Reynolds and Strouhal numbers for smooth and rough surfaces circular cylinders. Extracted from Blevins (2001) . . . . . 14

2.7 Evolution of the growth rate ($a$) and Strouhal number ($b$) of the vortex street in function of the Reynolds number. Extracted from Giannetti and Luchini (2007). 15

2.8 Fixed, rigid splitter plate aligned with the inflow configuration. . . . . 16

2.9 Effects of the splitter plate length variation on the flow behaviour. Extracted from (a) Kwon and Choi (1996*a*) and (b) Vu et al. (2016). . . . . 16

2.10 One degree of freedom mechanism schematic description for a circular cylinder oscillating in the cross flow direction. . . . . 17
2.11 Schematic of the principal possible amplitudes response curves of an non-circular body in function of different ranges of reduced velocity $U_R$. Adapted from Nakamura (1990). . . . . 18
2.12 Dynamic response of a circular cylinder oscillating in the cross flow direction at $Re = 150$ in function of the reduced velocity. Adapted from Carmo et al. (2011) 20
2.13 Forces projections and cross flow Galloping mechanism description. . . . . 22
2.14 Comparison of the experimental data for the aerodynamic force coefficient on a vertically oscillating rectangular section, to the quasi steady theory, as a function of the reduced velocity. Extracted from Blevins (2001), based on the work of Washizu et al. (1978). . . . . 24
2.15 Schematic of a rectangular prism section in torsional oscillation and diagram for determining $\alpha$ in terms of $R_r$. Adapted from Païdoussis et al. (2010) . . . . . 25
2.16 Quantities and mechanism description of the rotating cylinder fitter to a splitter plate. . . . . 26
2.17 Small tilting angle. . . . . 27
2.18 Equivalent configuration. . . . . 27
2.19 Extraction of the second coefficient $\partial_{\dot{\theta}}\mathfrak{m}_z$. . . . . 28
2.20 Mean and instantaneous positions of the filaments for different length and rigidity. Extracted from Bagheri et al. (2012*a*) . . . . . 29
2.21 Model comparison of the turn and drift angles as functions of the splitter-plate length, respectively, in (a) and (b) at $Re = 45$. Extracted from Lacis et al. (2014*a*) 29

3.1 Affine transformations, or structural degrees of freedom description. . . . . 32

4.1 Standard regions for (left) quadrilateral, and (right) triangular elements in terms of the Cartesian coordinates $(\xi_1, \xi_2)$. Adapted from Karniadakis and Sherwin (2005). . . . . 57
4.2 Two-dimensional expansion basis of order $P = 4$ for a quadrilateral element, constructed from a tensorial product of two one-dimensional expansions. Adapted from Karniadakis and Sherwin (2005). . . . . 58
4.3 Triangle-to-rectangle transformation. Adapted from Karniadakis and Sherwin (2005). . . . . 59
4.4 Construction of a fourth-order ($P = 4$) triangular expansion using the product of two modified principal functions $\psi_p^a(\eta_1)$ and $\psi_{pq}^b(\eta_2)$. Adapted from Karniadakis and Sherwin (2005). . . . . 59
4.5 Example of transformation from the physical Cartesian coordinate system to a different coordinate system. Extracted from Serson et al. (2016). . . . . 65
4.6 Description of possible structural degree of freedom and parameters considered. 68
4.7 Vorticity visualisation of the flow around a circular cylinder at $Re = 100$, with and without the use of the stabilisation technique. Extracted from Jordi et al. (2014). . . . . 73

5.1 Example of size distribution of elements (a) used for the discretisations 0 and 3. The close-up in (b) shows the quadrature points for $P = 7$ in both cases (0 and 3). 78

5.2 $h$-convergency diagrams. . . . . 80

5.3 $p$-convergency diagrams. . . . . 81

5.4 Example of size distribution of elements (a) used in the mesh for the splitter plate of length $L/D = 1$. The close-up in (b) shows the quadrature points for $P = 7$ . . . . . 85

5.5 Comparison of real part of the computed (a) direct and (b) adjoint eigenvalues for every splitter plate length close to the onset of the instability. Here, $L/D = 0.1$ for $Re = 47$, $L/D = 0.5$ for $Re = 55$, $L/D = 1.0$ for $Re = 72$, $L/D = 2.0$ for $Re = 95$, $L = 3.0$ for $Re = 114$, and $L = 4.0$ for $Re = 151$. . . . . 86

5.6 Real and imaginary part eigenvalues comparison for linear and adjoint simulations for every splitter plate length close to the critical threshold. From lower to higher $Re$, it is presented [$L/D = 0.1$, at $x^+ = 200$], [$L/D = 0.5$, at $x^+ = 200$], [$L/D = 1.0$, at $x^+ = 200$], [$L/D = 2.0$, at $x^+ = 200$], [$L/D = 3.0$, at $x^+ = 300$], and [$L/D = 4.0$, at $x^+ = 500$]. . . . . 87

5.7 Mesh3, $P = 7$, domain size matching Zhang et al. (2015). Real and imaginary part of the leading eigenvalue $\lambda$ in function of the reduced frequency $F_n$. Comparison of linear and adjoints present simulations $\lambda^L$ and $\lambda^\dagger$ to the linear simulations from reference Zhang et al. (2015) $\lambda^R$. . . . . 88

5.8 Comparison of the real part of eigenvalue of the symmetry breaking mode from the direct/adjoint mode computations and from full non-linear simulation: (a) $L/D = 1.0$ for $30 \leq Re \leq 50$; (b) $L/D = 0.1, 0.5, 1.0, 2.0, 3.0, 4.0$ at the Reynolds number near the onset of instability (note that growth rate is order of $10^{-3}$). Here, $\lambda^N$ indicates the eigenvalue obtained from full non-linear simulations, and the domain size is given by $|y| \leq 20$ and $|x| \leq 40$. . . . . 89

5.9 Comparison of (a) real and (b) imaginary parts of the eigenvalue of the torsional flapping mode from direct/adjoint mode calculations and full non-linear simulations. Here, $\lambda^N$ indicates the eigenvalue obtained from full non-linear simulations, and the domain size is given by $|y| \leq 30$ and $|x| \leq 40$. . . . . 90

6.1 A schematic diagram of flow and structure configuration. Here, $\mathbf{u}_\infty (= (U_\infty, 0))$ is the freestream velocity, $\theta$ the counter-clockwise rotation angle of the cylinder, $k_\theta$ rotational stiffness, and $c_\theta$ rotational damping coefficient. . . . . 93

6.2 Neutral stability diagram (a), and recirculation length comparison for different splitter plate lengths as a function of the Reynolds number (b). The two figures in inset of (a) are the $u$ velocity fields of the symmetry breaking mode ($L/D = 3$, $Re = 83$) and the torsional flapping modes ($L/D = 3$, $Re = 112$), respectively. . 95

6.3 Comparison of the eigenvalues spectrum (first two eigenvalues of highest magnitude, corresponding in that case to the symmetry breaking ($\lambda^{SB}$) and torsional flapping ($\lambda^{TF}$) modes) for two different splitter plate lengths; $L/D = 3$ and 4, at $Re = 100$. . . . . 97

6.4 The linear growth rate and frequency of the vortex shedding mode ($\lambda^{VS,F}$) in the case of a stationary cylinder as a function of the Reynolds number ($L/D = 1$). 98

6.5 Real part $u$-component of the vortex shedding direct mode shape evolution along the threshold of stability for different plate length. The red and blue colours denote positive and negative values respectively, and their brightness indicates the magnitude. The continuous lines are associated 0-isocontours of the perturbed fields. . . . . 99

6.6 Magnitude $\|\hat{\mathbf{u}}\|$ of the velocity components of the vortex shedding instability ($\lambda^{VS,F}$). The continuous lines are associated to the base flow streamlines for the corresponding Reynolds numbers. . . . . 100

6.7 Real part $u$-component of the vortex shedding adjoint mode shape evolution along the threshold of stability for different plate length. The red and blue colours denote positive and negative values respectively, and their brightness indicates the magnitude. The continuous lines are associated 0-isocontours of the perturbed fields. The far field visualisations (lower figures) represents the data up to 10% of maximum range. . . . . 101

6.8 Magnitude $\left\|\hat{\mathbf{u}}^{\dagger}\right\|$ of the velocity components of the vortex shedding instability ($\lambda^{VS,F}$). The continuous lines are associated to the base flow streamlines for the corresponding Reynolds numbers. . . . . 102

6.9 Normalised magnitude of the base flow vorticity. The continuous lines are associated to the base flow streamlines for the corresponding Reynolds numbers. . . 103

6.10 The sensitivity to spatially localised feedback $\Theta_F$ of the vortex shedding $\lambda^{VS,F}$ mode near the onset of the instability. The continuous lines are associated to the base flow streamlines for the corresponding Reynolds numbers. . . . . 104

6.11 The linear growth rate and frequency of symmetry breaking mode ($\lambda^{SB}$) and vortex shedding mode ($\lambda^{VS}$) as a function of the Reynolds number ($L/D = 1$, $I_\theta = 50$, $U_R = 3937$). Note that the frequency of the symmetry breaking mode is not drawn in (b), since $\lambda_i^{SB} = 0$. . . . . 106

6.12 The linear growth rate of symmetry breaking mode ($\lambda^{SB}$) and vortex shedding mode ($\lambda^{VS}$) as a function of the plate length $L/D$ ($I_\theta = 50$). . . . . 107

6.13 The linear growth rate of symmetry breaking mode ($\lambda^{SB}$) at $Re = 30$ and $L/D = 1$, as a function of (a) inertia and (b) reduced velocity. . . . . 108

6.14 Componentwise contributions to the instability growth rate (see ((6.4))): $\lambda_{p,r}$, pressure; $\lambda_{\nu,r}$ viscous stress; $\lambda_r$ the growth rate as a function of the Reynolds number. . . . . 109

6.15 Pressure and spanwise vorticity of the eigenmode of symmetry breaking instability for $L/D = 1$ for different Reynolds numbers. Here, the red and blue colours denote positive and negative values respectively, and their brightness indicates the magnitude. The continuous lines are associated to the base flow streamlines for the corresponding Reynolds numbers and the dotted contours represents the 0-isocontour of the perturbed fields. . . . . 110

6.16 Normalised pressure distribution: $p/\max(p)$ at the solid interface of the cylinder with a splitter plate length $L/D = 1$ for three different Reynolds numbers: $Re = 30$, 32, and 34. . . . . 111

6.17 Visualisation of the normalised perturbed velocity field modulus $\|\hat{\mathbf{u}}\|$ of the symmetry breaking mode $\lambda^{SB}$. The white lines indicate the base flow streamlines. . 113

6.18 Isocontours of the amplitude of the adjoint eigenmode of the symmetry breaking mode near the point of instability. Here, the contour levels are noramlised by the peak adjoint mode amplitude. . . . . 114

6.19 The sensitivity to spatially localised feedback $\Theta_F$ of the symmetry breaking mode near the onset of the instability. . . . . 115

6.20 Visualisation of the receptivity to spatially localised feedbacks, $\Theta_F$ of the symmetry breaking mode, for $L/D = 1.0$, varying the Reynolds number. . . . . 116

6.21 Comparison of the magnitude of (a-c) the direct mode $\|\hat{\mathbf{u}}\|$, (e-f) the magnitude of the adjoint mode $\left\|\hat{\mathbf{u}}^\dagger\right\|$ and (g-i) the sensitivity to localised forcing $\Theta_F$ for different plate length at $Re = 40$. . . . . 117

6.22 The linear frequency of torsional flapping mode and vortex shedding mode as a function of the Reynolds number ($I_\theta = 50$, $L/D = 0.1$ to 4, $U_R = 3937$). Here, $\lambda_r \simeq 0$. . . . . 119

6.23 Linear growth rate and frequency of the torsional flapping ($\lambda^{TF}$) and symmetry breaking ($\lambda^{SB}$) mode as a function of the Reynolds number ($I_\theta = 50$, $L/D = 4$, $U_R = 3937$). . . . . 120

6.24 Variation of linear growth rate and frequency of the torsional flapping ($\lambda^{TF}$) and the symmetry breaking mode ($\lambda^{SB}$) with the dimensionless inertia $I_\theta$ ($L/D = 4$, $U_R = 3937$, $Re = 100$). . . . . 120

6.25 Variation of linear growth rate and frequency of the torsional flapping ($\lambda^{TF}$) and the symmetry breaking mode ($\lambda^{SB}$) with the reduced velocity $U_R$ ($L/D = 4$, $I_\theta = 50$, $Re = 94$). . . . . 121

6.26 Coefficients of the quasi steady homogeneous differential equation of motion, resulting solution regime, and growth rate in the range of Reynolds number $70 \leq Re \leq 100$. . . . . 122

6.27 Componentwise contributions to the instability growth rate and frequency as a function of the Reynolds number for $L/D = 4$ (see (6.4)): $\lambda_{p,r}$, $\lambda_{p,i}$ pressure; $\lambda_{\nu,r}$, $\lambda_{\nu,i}$ viscous stress; $\lambda_r$, $\lambda_i$ the growth rate and frequency. Here, the critical Reynolds number for the onset of the instability is $Re_c \simeq 93.5$. . . . . 124

6.28 Pressure and spanwise vorticity of the eigenmode of symmetry breaking instability for $L/D = 4$ at $Re = 92$, 94 and 95. Here, the red and blue colours denote positive and negative values respectively, and their brightness indicates the magnitude. The white contour lines indicate $\hat{p} = 0$ and $\hat{\omega}_z = 0$. . . . . 125

6.29 Far field visualisation of the $u$-component of the real part of the vortex shedding (bottom) and torsional flapping (top) mode ($\lambda^{TF}$) for $L/D = 3$ at $Re = 112$. . . 127

6.30 Direct mode $\|\hat{\mathbf{u}}\|$, adjoint mode $\left\|\hat{\mathbf{u}}^\dagger\right\|$, and sensitivity to localised forcing $\Theta_F$ for $L/D = 3$: (a-c) the torsional flapping instability at $Re = 112$ (d-f) the vortex shedding instability at $Re = 114$. Here, white solid lines indicate streamlines of the corresponding base flow. . . . . 128

6.31 Direct mode $\|\hat{\mathbf{u}}\|$, adjoint mode $\left\|\hat{\mathbf{u}}^\dagger\right\|$, and sensitivity to localised forcing $\Theta_F$ for $L/D = 4$: (a-c) the torsional flapping instability at $Re = 94$ (d-f) the vortex shedding instability at $Re = 151$. Here, white solid lines indicate streamlines of the corresponding base flow. . . . . 129

# Nomenclature

### Abreviations

| | |
|---|---|
| $ALE$ | Arbitrary Lagrangian-Eulerian |
| $CFL$ | Courant-Friedrichs-Lewy |
| $d\text{-}o\text{-}f$ | Degree of freedom |
| $f\text{-}t\text{-}r$ | Free-to-rotate |
| $FIM$ | Flow-induced motion |
| $FIV$ | Flow-induced vibration |
| $FSI$ | Fluid-structure interaction |
| $SFD$ | Selective frequency damping |
| $VIV$ | Vortex-Induced vibration |

### Variables

| | |
|---|---|
| $\alpha$ | Angle of attack |
| $\bar{\Omega}$ | Cartesian domain |
| $\boldsymbol{\xi}$ | Structural state variable |
| $\boldsymbol{\xi}'$ | Perturbed structural state variable |
| $\boldsymbol{\xi}^\dagger$ | Adjoint structural state variable |
| $\boldsymbol{\eta}$ | Structural position vector |
| $\boldsymbol{\eta}'$ | Perturbed structural position vector |
| $\boldsymbol{\eta}^\dagger$ | Adjoint structural position vector |
| $\boldsymbol{\eta}_0$ | Base state structural position vector |
| $\boldsymbol{\zeta}$ | Structural velocity vector |
| $\boldsymbol{\zeta}'$ | Perturbed structural velocity vector |
| $\boldsymbol{\zeta}^\dagger$ | Adjoint structural velocity vector |

$\boldsymbol{\zeta}_0$ Base state structural velocity vector

$\chi$ In line degree of freedom structural motion

$\Delta_Q$ Discriminant of a quadratic polynomial

$\Gamma$ Boundary interface at rest

$\gamma$ Boundary interface

$\hat{\mathbf{u}}$ Direct flow velocity vector mode shape

$\hat{\mathbf{u}}^\dagger$ Adjoint flow velocity mode shape

$\hat{p}$ Direct flow pressure mode shape

$\hat{\boldsymbol{\xi}}$ Direct structural mode

$\hat{\mathbf{q}}^\dagger$ Adjoint fluid mode

$\hat{\mathbf{s}}$ Direct global mode

$\lambda$ Eigenvalue

$\lambda_i$ Imaginary part of the eigenvalue

$\lambda_r$ Real part of the eigenvalue

$\lambda_{\nu,i}$ Imaginary part of viscous component of the eigenvalue

$\lambda_{\nu,r}$ Real part of viscous component of the eigenvalue

$\lambda_{p,i}$ Imaginary part of pressure component of the eigenvalue

$\lambda_{p,r}$ Real part of pressure component of the eigenvalue

$\mathbf{F}$ Aerodynamic forces and moment vector in the $(x, y)$ Cartesian plane per unit length

$\mathbf{k}$ Unit vector along the $z$ direction orthogonal to the $x$-$y$ plane

$\mathbf{n}$ Unit outward-pointing normal vector at the interface

$\mathbf{n}'$ Perturbed unit outward-pointing normal vector at the interface

$\mathbf{n}_0$ Unit outward-pointing normal vector at the interface at rest

$\mathbf{q}$ Fluid state variable

$\mathbf{q}'$ Perturbed fluid state variable

$\mathbf{q}^\dagger$ Adjoint fluid state variable

$\mathbf{q}_0$ Base state fluid state variable

$\mathbf{r}$ Position vector from the hinge point to the boundary

$\mathbf{r}'$ Perturbed position vector from the hinge point to the boundary

| | |
|---|---|
| $\mathbf{r}_0$ | Position vector from the hinge point to the boundary at rest |
| $\mathbf{s}$ | Global state variable |
| $\mathbf{s}'$ | Perturbed global state variable |
| $\mathbf{s}^\dagger$ | Adjoint global state variable |
| $\mathbf{s}_0$ | Base state global state variable |
| $\mathbf{u}$ | Flow velocity vector |
| $\mathbf{u}'$ | Perturbed flow velocity vector |
| $\mathbf{u}^\dagger$ | Adjoint flow velocity |
| $\mathbf{u}_0$ | Base state flow velocity vector |
| $\mathbf{u}_\infty$ | Free stream flow velocity vector |
| $\mathbf{x}$ | Cartesian spatial location |
| $\mathfrak{F}$ | Aerodynamic forces vector in the $(x, y)$ Cartesian plane per unit length |
| $\mathfrak{F}^s$ | Structural force vector in the $(x, y)$ Cartesian plane per unit length |
| $\mathfrak{f}_x$ | Aerodynamic force in the $x$ Cartesian direction per unit length |
| $\mathfrak{f}_y$ | Aerodynamic force in the $y$ Cartesian direction per unit length |
| $\mathfrak{M}^s$ | Structural moment force vector in the $(x, y)$ Cartesian plane per unit length |
| $\mathfrak{m}_z$ | Aerodynamic moment around the $z$ Cartesian direction per unit length |
| $\nu$ | Fluid kinematic viscosity |
| $\Omega$ | Fluid domain |
| $\omega$ | Vorticity |
| $\omega_n$ | Natural angular frequency in the context direction |
| $\omega_v$ | Vortex shedding pulsation |
| $\omega_\theta$ | Natural rotational angular frequency around the $z$ Cartesian direction |
| $\omega_x$ | Natural angular frequency in the $x$ Cartesian direction |
| $\omega_y$ | Natural angular frequency in the $y$ Cartesian direction |
| $\partial\Omega$ | External boundary of the computational domain |
| $\psi$ | Cross flow degree of freedom structural motion |
| $\rho$ | Fluid density |
| $\sigma$ | Stress tensor |

| | |
|---|---|
| $\tau$ | Integration time horizon |
| $\Theta$ | Sensitivity map |
| $\theta$ | Rotation around the $z$ Cartesian direction |
| $\theta$ | Rotation degree of freedom structural motion |
| $\Theta_F$ | Fluid sensitivity map |
| $\Theta_S$ | Structural sensitivity |
| $\varepsilon$ | Viscous stress tensor |
| $\zeta_\theta$ | Torsional damping ratio |
| $\zeta_x$ | Damping ratio in the free stream flow direction |
| $\zeta_y$ | Damping ratio in the cross flow direction |
| $A$ | Structural response amplitude |
| $c_\theta$ | Rotational structural damping coefficient |
| $c_x$ | Structural damping coefficient in the free stream flow direction |
| $c_y$ | Structural damping coefficient in the cross flow direction |
| $D$ | Cylinder diameter |
| $E$ | Strain rate tensor |
| $F_D$ | Aerodynamic drag force |
| $F_L$ | Aerodynamic lift force |
| $f_v$ | Vortex emission frequency |
| $f_\theta$ | Structural natural frequency around the $z$ Cartesian direction |
| $f_n$ | Structural natural frequency in the context direction |
| $f_x$ | Structural natural frequency in the $x$ Cartesian direction |
| $f_y$ | Structural natural frequency in the $y$ Cartesian direction |
| $I_\theta$ | Moment of inertia |
| $k_\theta$ | Rotational structural stiffness |
| $k_x$ | Structural stiffness in the free stream flow direction |
| $k_y$ | Structural stiffness in the cross flow direction |
| $L$ | Splitter plate length |
| $L_f$ | Recirculation bubble length |

$m$ Structural mass

$p$ Flow pressure

$p'$ Perturbed flow pressure

$p^\dagger$ Adjoint flow pressure

$p_0$ Base state flow pressure

$R_r$ Reference radius

$t$ Time

$U_\infty$ Free-stream velocity in the streamwise direction

$x, y, z$ Cartesian coordinate system

**Non-dimensional numbers**

$C_D$ Aerodynamic coefficient of drag

$C_L$ Aerodynamic coefficient of lift

$C_M$ Aerodynamic moment coefficient

$C_x$ Aerodynamic coefficient in the $x$ Cartesian direction

$C_y$ Aerodynamic coefficient in the $y$ Cartesian direction

$I_{\theta,r}$ Dimensionless reduced moment of inertia

$Re$ Reynolds number

$St$ Strouhal number

$U_R$ Reduced velocity

**Operators**

$\bar{\mathcal{F}}$ Steady fluid operator

$\mathbf{\Delta}$ Marix containing the linearised canonical affine transformations

$\mathbf{\Lambda}$ Matrix form of the linearised fluid velocity operator

$\delta_\chi$ Linearised canonical in line affine transformation

$\delta_\psi$ Linearised canonical cross flow affine transformation

$\delta_\theta$ Linearised canonical rotation affine transformation

$\hat{\mathcal{F}}$ Steady linearised fluid operator

$\hat{\mathcal{H}}$ Steady linearised global operator

$\hat{\mathcal{S}}$ Steady structural operator

| | |
|---|---|
| $\mathbf{A}$ | Advection operator |
| $\mathbf{A}'$ | Linearised advection operator |
| $\mathbf{A}^\dagger$ | Adjoint advection operator |
| $\mathbf{B}$ | Blowing suction matrix |
| $\mathbf{D}$ | Damping matrix |
| $\mathbf{f}$ | Fluid stress operator |
| $\mathbf{I}$ | Identity matrix in two dimension |
| $\mathbf{K}$ | Stiffness matrix |
| $\mathbf{M}$ | Mass matrix |
| $\mathbf{M}^f$ | Fictitious mass matrix |
| $\mathbf{W}_F$ | Fluid weight matrix |
| $\mathbf{W}_S$ | Structural weight matrix |
| $\mathcal{A}$ | Aerodynamic force operator |
| $\mathcal{A}'$ | Linearised aerodynamic force operator |
| $\mathcal{A}^\dagger$ | Adjoint aerodynamic force operator |
| $\mathcal{B}$ | Global bilinear concomitant |
| $\mathcal{B}_F$ | Fluid bilinear concomitant |
| $\mathcal{B}_S$ | Structural bilinear concomitant |
| $\mathcal{F}$ | Fluid operator |
| $\mathcal{F}'$ | Linearised fluid operator |
| $\mathcal{F}'_u$ | Linearised fluid velocity operator |
| $\mathcal{F}^\dagger$ | Adjoint fluid operator |
| $\mathcal{H}$ | Global operator |
| $\mathcal{H}'$ | Perturbed global operator |
| $\mathcal{H}^\dagger$ | Adjoint global operator |
| $\mathcal{R}$ | Canonical rotation affine transformation |
| $\mathcal{S}$ | Structural operator |
| $\mathcal{S}'$ | Linearised structural operator |
| $\mathcal{S}^\dagger$ | Adjoint structural operator |

| | |
|---|---|
| $\mathcal{T}$ | Canonical total transformation |
| $\mathcal{T}_\chi$ | Canonical in line affine transformation |
| $\mathcal{T}_\psi$ | Canonical cross flow affine transformation |
| $\nabla_{\boldsymbol{\eta}}$ | Nabla operator with regard to the degree of freedoms structural motions directions |

# Chapter 1

# Introduction

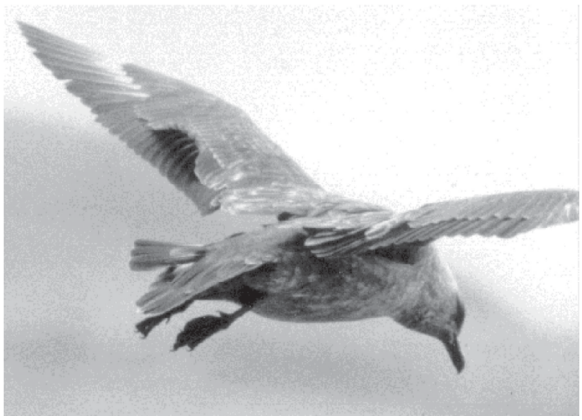
## 1.1 Motivation and objectives

Fluid-structure interaction (FSI) problems are of paramount importance in many engineering applications, particularly when designing lighter and more robust structures. In particular, the FSI problem in bluff body wakes has been one of the widely studied topics, as it is crucial for the design of many engineering structures, such as bridges, buildings, oil platforms, only to cite a few. The flow, which often involves vortex shedding in its wake, causes significant vibration, noise and drag of the given structure through instabilities in fluid and solid motions. Therefore, understanding the onset of such instabilities and the resulting self-sustaining drifts/oscillations arising in the FSI problems provides important physical insight into the development of simplified models and control strategies to mitigate undesirable motions or amplify and sustain locomotive or energy harvesting motions.

Several FSI problems of interest have previously been studied by employing the approaches developed in the context of hydrodynamic stability. Perhaps, one of the earliest work is by Cossu and Morino (2000), who performed a global linear stability analysis for a spring-mounted circular cylinder allowing for cross-flow oscillations. A similar FSI problem, including an in-line oscillation case, was studied by Meliga and Chomaz (2014) by coupling the fluid and solid motions via a weakly non-linear analysis. A linear stability analysis and a non-linear simulation were also recently performed in Dolci and Carmo (2018, 2019) for a spring-mounted circular cylinder with transverse oscillation. More recently, Negi et al. (2020) investigated a more general global stability analysis framework for FSI problems by employing the Arbitrary Lagrangian-Eulerian (ALE) framework (Fernandez and Tallec, 2002*a*), while a more detailed and generalised application of the ALE framework can be found in Pfister (2019) and Pfister and Marquet (2020) where non-linear numerical simulation and linear stability analysis were also performed for a flow over a circular cylinder with a flexible appendage.

Of particular interest to the present study are flow-induced instabilities, which have previously

been observed in a circular cylinder with a rigid or flexible splitter plate attached at the base (Assi et al., 2009; Assi, Franco and Vestri, 2014). The cylinder wake is one of the simplest model problems widely employed to study the onset of vortex shedding, the related FSI problem and their control. It is also directly relevant to industrial applications for the tall building design and the offshore energy harvesting, to which the addition of a passive appendage may be useful to suppress the vortex shedding. In the case of a rigid bluff body, many previous studies have demonstrated that placing such a device suppresses vortex shedding in the wake of the bluff body (Anderson and Szewczyk, 1997; Choi et al., 2008; Kwon and Choi, 1996*b*; Ozono, 1999; Roshko, 1954). When the appendage is allowed to rotate or deform by imposing relevant structural dynamics (*e.g.* coupling through the spring-mass-damper system, the elastic motion of the appendage, etc.), the cylinder exhibits a flow-induced 'static' instability which breaks the symmetry of the flow posed by the cylinder geometry (Assi et al., 2010; Assi, Bearman and Tognarelli, 2014; Bagheri et al., 2012*b*; Cimbala and Garg, 1991; Lacis et al., 2014*b*; Pfister and Marquet, 2020). It has been proposed that this instability provides an aiding mechanism for flight motion of insects and locomotion of swimming animals (Bagheri et al., 2012*b*; Bechert et al., 2006; Knacke et al., 2004; Lacis et al., 2014*b*; Park et al., 2010).



**(a)** Seagull at landing.



**(b)** Pteropod clione limacina.



**(c)** Ash seeds.



**(d)** Sycamore seed.

**Figure 1.1:** Occurrences of the symmetry breaking instability in nature. Sub-figure (*a*) extracted from Knacke et al. (2004), other sources are unknown.

Examples of such mechanism are visually presented for different flow regimes in figure 1.1 in which (a), birds feathers are acting as passive self-activated movable flaps enhancing the maximum lift of the wing of a seagull at landing (extracted from Knacke et al. (2004)); (b), the flexible rear-body shape of a pteropod clione limacina is suspected to dynamically adjusts accordingly to the front-body part flapping swimming motion to generate hydrodynamic lift and aid sustaining the weight of the pteropod (Bagheri et al., 2012*b*); (c) and (d) some plants, for example, use these interactions to help spread their seeds through the wind.

Further to this, in general, it is also possible to have a flow-induced 'dynamic' or 'oscillatory' instability of the body, and it has also been reported for the flow considered in this study. In relation to this, Pfister and Marquet (2020) recently reported that such an instability appears in a flow over a cylinder attached with a 'flexible' plate. In the present study, we will report that a similar dynamic instability also arises in the flow we consider here, especially when the splitter plate is long enough. This also indicates that the emergence of this type of instability may be more general for the structural systems allowing for a spanwise torsional deformation or rotation induced by the surrounding flow. Both 'static' and 'dynamic' instabilities are shown to have an overall sensitivity localised around the near-tip splitter plate region. This observation has also been analogously reported in experimental studies investigating the response of the torsional VIV of a thin plate under different tip-regions shapes (Toebes and Eagleson, 1961).



**Figure 1.2:** Diverse forms and examples of risers, cables and mooring lines of offshore structures. From left to right: floating wind turbines; sub-sea system (SS); fixed platform (FP); floating production, storage and offloading vessel (FPSO); floating production system platform (FPS); spar platform (SP); vertically moored tension leg platform (TLP); jack-up rig platform. Reproduced from *oilstates.com*.

The objective of the present study is to explore the flow-induced instabilities mentioned above for a detailed understanding of the role of the surrounding flow. For this purpose, it is considered

a circular cylinder with a rigid appendage, as is sketched in figure 1.4. The rigid body is allowed to rotate by coupling with a torsional spring-mass-damper system. This geometry is chosen first for its simplicity; the presence of the cylinder eliminates the assumption of a streamlined body in the range of flow regimes investigated in this study, and the splitter plate can break the wake symmetry by either rotating or if the whole structure oscillates vertically. Second, a cylinder fitted to a splitter plate has numerous industrial applications, and its choice was initially inspired by the offshore industry where all sorts of passive appendages might be fitted to a cylinder - which, in such case, may technically represent risers or cables immersed in diverse ocean currents, as depicted in figure 1.2 - to prevent premature structural fatigue of the cylinder due to different kinds of flow-induced motions (FIM), as presented in figure 1.3. Hence, the choice of the splitter plate thickness is also chosen in that sight. Finally, this choice is also found judicious due to the large amount of numerical and experimental data available.

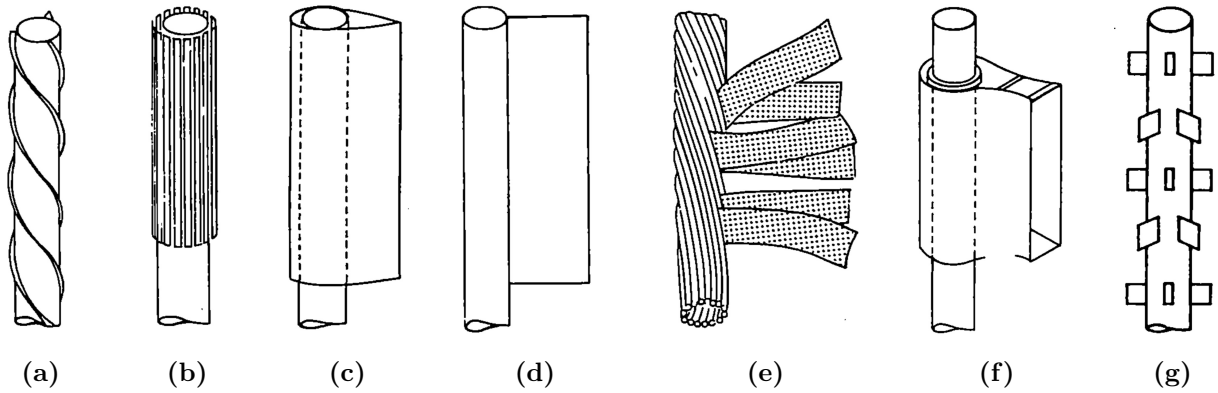



**Figure 1.3:** Examples of experimental FIV suppressors, (a) helical strake, (b) axial slats, (c) streamlined fairing, (d) present splitter plate, (e) ribboned cable, (f) pivoted guiding vane, (g) spoiler plates. Adapted from Blevins (2001).

A global linear instability analysis (Chomaz, 2005; Huerre and Monkewitz, 1990; Theofilis, 2011) is first formulated with the introduction of a small perturbation, which allows the utilisation of the stationary cylinder framework (i.e. the Eulerian framework) while being carefully validated with full non-linear simulation (Serson et al., 2016). Three different types of instabilities (i.e. vortex shedding mode, stationary symmetry breaking mode, oscillatory FSI mode) are found in the context of the global linear instability, and the physical mechanisms on their origin are analysed in detail. In particular, our analysis reveals that the oscillatory FSI instability shares the same origin with the 'flapping' mode previously observed in flags and/or flexible plates (Shelley and Zhang, 2011).

However, the linear framework is derived for an arbitrary geometry shape translating and/or rotating in the two-dimensional plane considered. The coupled fluid-structure system linearisation results in a spatially fixed domain configuration, where the structure displacement contribution is converted into modified kinematic and dynamic boundary conditions at the solid interface.

While the modified kinematic boundary condition no longer holds the "no-slip" assumption and a time-dependent blowing/suction type is derived, the modified dynamic boundary condition can be decomposed into the sum three contributions sources: the influence of the perturbed fluid variables on the structural base state, the influence of the structural changes on the fluid base state, and the influence of the fluid base state gradient on the structural base state.
These resulting modified boundary conditions of the linearised system are consistent with the work of Fernandez and Tallec (2002*a*) and Fernandez and Tallec (2002*b*) where the authors consider similar physical assumptions, yet a deformable solid of arbitrary shape. However, in the particular example of the cylinder plus splitter plate, the linearised dynamic boundary condition can be further simplified, and only the contribution of the fluid perturbed variables on the structural base state remains present at the first order.
The adjoint sensitivity analysis (Giannetti and Luchini, 2007; Luchini and Bottaro, 2014) is also performed for the first time for the FSI instabilities, with particular attention paid to understand the role of the flow around the appendage. Importantly, it is found that the flow around the tip of the appendage plays a crucial role in the generation of the stationary symmetry breaking and the dynamic flapping instabilities, opening a possibility of controlling them with simple redesign of the tip shape.

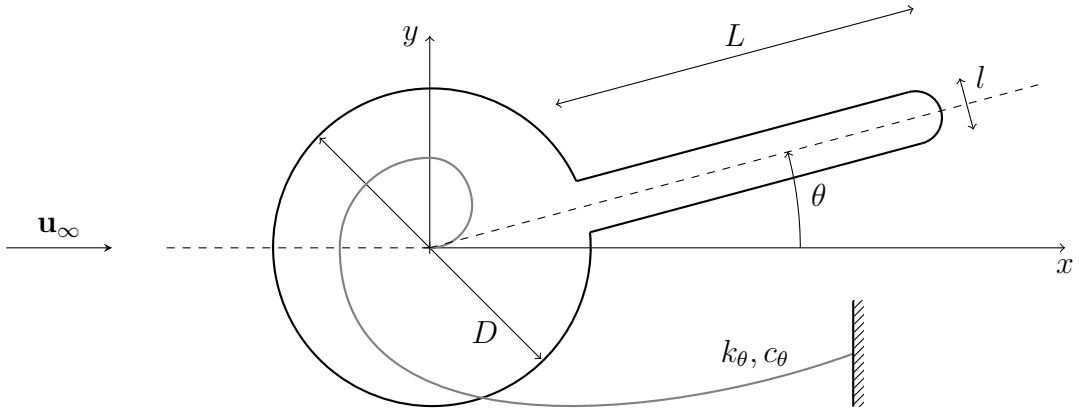



**Figure 1.4:** A schematic diagram of flow and structure configuration. Here, $\mathbf{u}_\infty(= (U_\infty, 0))$ is the freestream velocity, $\theta$ the counter-clockwise rotation angle of the cylinder of diameter $D$, along with the splitter plate of length $L$ and thickness $l$. $k_\theta$ correspond to the structural rotational stiffness, and $c_\theta$ to the rotational damping coefficient.

This thesis is organised as follows. In chapter §2, the possible flows regimes of interest taking place around a fixed circular cylinder with or without splitter plate are reviewed and described, as well as the principal flow-induced motions that the structure might undergo, that will help understand and describe the present results, and are classified in term of Reynolds number or reduced velocity, whether considering the structure mounted on an elastic basis or not. In chapter §3, the global stability and sensitivity analyses are formulated for an arbitrary three degree of freedom structural motion. In chapter §4, the numerical methods used in this study

to carry the simulations are introduced while in chapter §5, the global stability and sensitivity formulation from chapter §3 is validated using the numerical methods described in chapter §4. Finally, the formulated analyses are subsequently applied to the flow-induced instabilities, and the discussion on the role of the flow is given in chapter §6. This thesis concludes in chapter §7, with a summary of the achievements and suggested future works.

## 1.2 Statement of originality

The work presented hereafter is based on research carried out by the author at the Department of Aeronautics of Imperial College London and the Department of Naval and Ocean Engineering of the Escola Politécnica of the University of São Paulo, and it is all the author's own work and effort. No part of the present work has been submitted elsewhere for another degree or qualification. Where other sources of information have been used, they have been acknowledged.

## 1.3 Copyright Declaration

The copyright of this thesis rests with the author. Unless otherwise indicated, its contents are licensed under a Creative Commons Attribution-Non Commercial 4.0 International Licence (CC BY-NC).

Under this licence, you may copy and redistribute the material in any medium or format. You may also create and distribute modified versions of the work. This is on the condition that: you credit the author and do not use it, or any derivative works, for a commercial purpose.

When reusing or sharing this work, ensure you make the licence terms clear to others by naming the licence and linking to the licence text. Where a work has been adapted, you should indicate that the work has been changed and describe those changes.

Please seek permission from the copyright holder for uses of this work that are not included in this licence or permitted under UK Copyright Law.

## 1.4 Publications and conference proceedings

The following papers have been submitted to publication during the research:

1. Basso, R. L. G., Assi, G. R. S., Orselli, R. M., Saltara, F. (2017). Numerical investigation at low Reynolds number of the galloping instability of a circular cylinder with a splitter plate employing a Spectral/hp finite element method. *24th ABCM International Congress of Mechanical Engineering, Curitiba, PR, Brazil*

2. Basso, R. L. G., Serson, D., Assi, G. R. S. (2018). Flow-Induced vibrations investigation by coordinate transformation at low Reynolds number. *BBVIV 7 - Bluff Body Wakes and Vortex-Induced Vibrations*

3. Basso, R. L. G., Hwang, Y., Assi, G. R. S., Sherwin, S. J. (2021). Instabilities and sensitivities in a flow over a rotationally flexible cylinder. *Journal of Fluid Mechanics*

# Chapter 2

# Physical mechanisms and empirical models

This chapter reviews the principal flow regimes of interest of this study, in the case of a smooth circular cylinder immersed in a continuous, incompressible inflow of Newtonian fluid, namely the *steady* and *unsteady* laminar regimes. Once these two regimes of interest are reviewed, the influence of a splitter plate fitted to the cylinder for these same regimes is also stressed.
Lastly, three flow-induced motions (FIM) when considering the solid mounted on an elastic basis, namely the vortex-induced vibrations, the galloping phenomenon and the symmetry breaking, are reviewed.
All the sections follow the same approach: to determine the non-dimensional numbers that govern the different regimes or phenomena and to explore the impact of these non-dimensional numbers variations on the flow and structural mechanisms.

This chapter is organised as follows, the description of the flow regimes and mechanisms around a smooth circular cylinder is discussed in the first section §2.1 and is used as a benchmark when reviewing the influence of the splitter plate and some flow-induced motions of interest in the last two sections §2.2 and §2.3.

## 2.1 Flow around a stationary circular cylinder

In this first part of the study, the unique variable that governs the flow regime is chosen as the Reynolds number $Re$. It is defined as the ratio of inertial forces to viscous forces within a fluid and hence enables the characterisation of any flow regime by knowing some of the dimensional parameters for a given geometry.

Let $U_\infty$ be the free stream velocity of a given flow, $D$ the characteristic length of a given

geometry, (*i.e.* here the cylinder diameter), and $\nu$ the kinematic viscosity of the fluid in question, then the Reynolds number of this particular setting can be expressed as:

$$Re = \frac{U_\infty D}{\nu}. \tag{2.1}$$

In figure 2.1 the evolution of the aerodynamic coefficients over a broad range of two- and three-dimensional regimes are presented, where the over-bar ($\bar{.}$) and hat ($\hat{.}$) represents the mean and fluctuation magnitudes respectively, and the subscripts '$p$' and '$f$' represent the terms due to pressure and friction drag. In the case of a circular cylinder, the Reynolds number is based on the diameter of the cylinder as the characteristic length $D$.

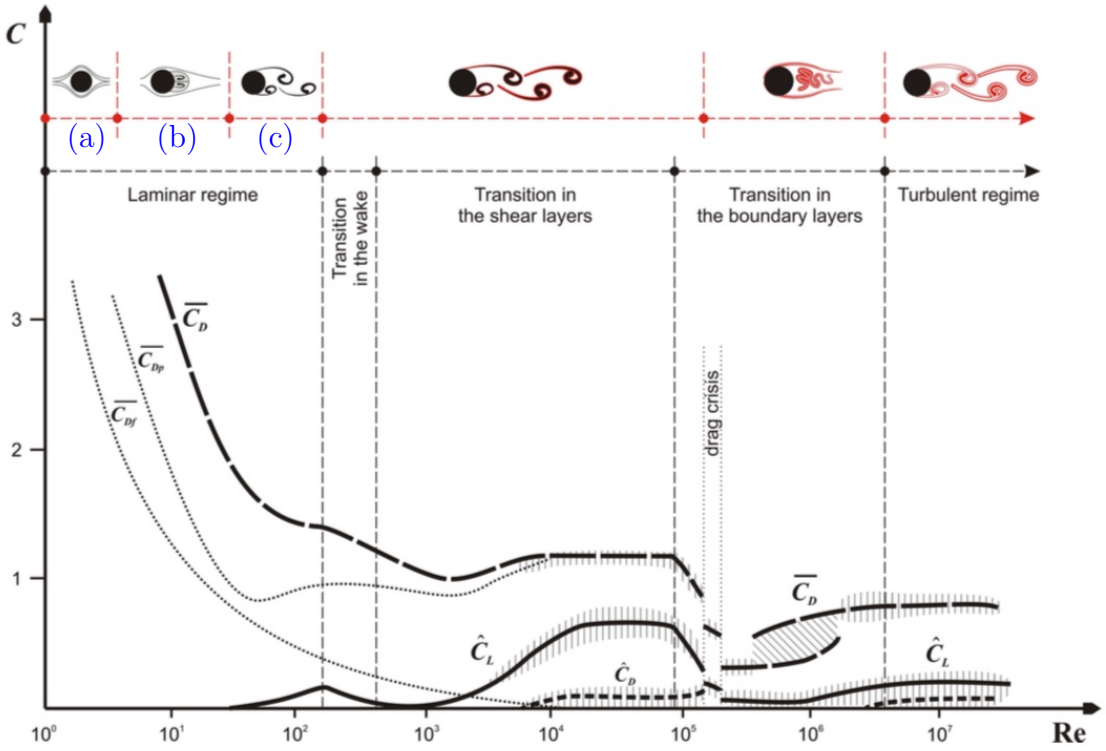



**Figure 2.1:** Global picture of the order of magnitude of the aerodynamic coefficients for an infinite smooth circular cylinder, and of the different regimes, as a function of the Reynolds number. Adapted from Zdravkovich (1997).

The aerodynamic drag $C_D$ and lift $C_L$ coefficients presented in figure 2.1 are linked to the aerodynamic forces through the relation:

$$\begin{aligned} F_L &= \frac{1}{2}\rho U_\infty^2 D C_L, \\ F_D &= \frac{1}{2}\rho U_\infty^2 D C_D, \end{aligned} \tag{2.2}$$

where $F_L$ and $F_D$ stands for lift and drag forces, corresponding to the aerodynamic forces acting in the cross-flow and streamwise directions, respectively, and $\rho$ is the fluid density.
Figure 2.1 clearly links the different flow regimes and hence the wake patterns to the Reynolds number, as well as the aerodynamic forces acting on the cylinder.
In this research, the focus is put on the first regimes depicted in figure 2.1, the two-dimensional laminar regime keeping $1 < Re < 160$. This small part of the spectrum represents, however, a good starting point to understand the principal mechanisms that take place at higher Reynolds numbers (more relevant to industrial applications), namely the separation and the unsteadiness of the flow.

The two-dimensional laminar regime is decomposed and reviewed into three sub categories: the steady laminar regime (separated and non-separated) §2.1.1 and the unsteady laminar regime §2.1.2. See $(a)$, $(b)$ and $(c)$ in figure 2.1. These three regimes ($(a)$, $(b)$ and $(c)$) are presented below from lower to higher Reynolds numbers.
Although figure 2.1 characterises different flow regimes for a more general Reynolds number range than the one studied in this work, this figure helps to understand where the relevance of the investigation may apply.

### 2.1.1 Steady laminar regime

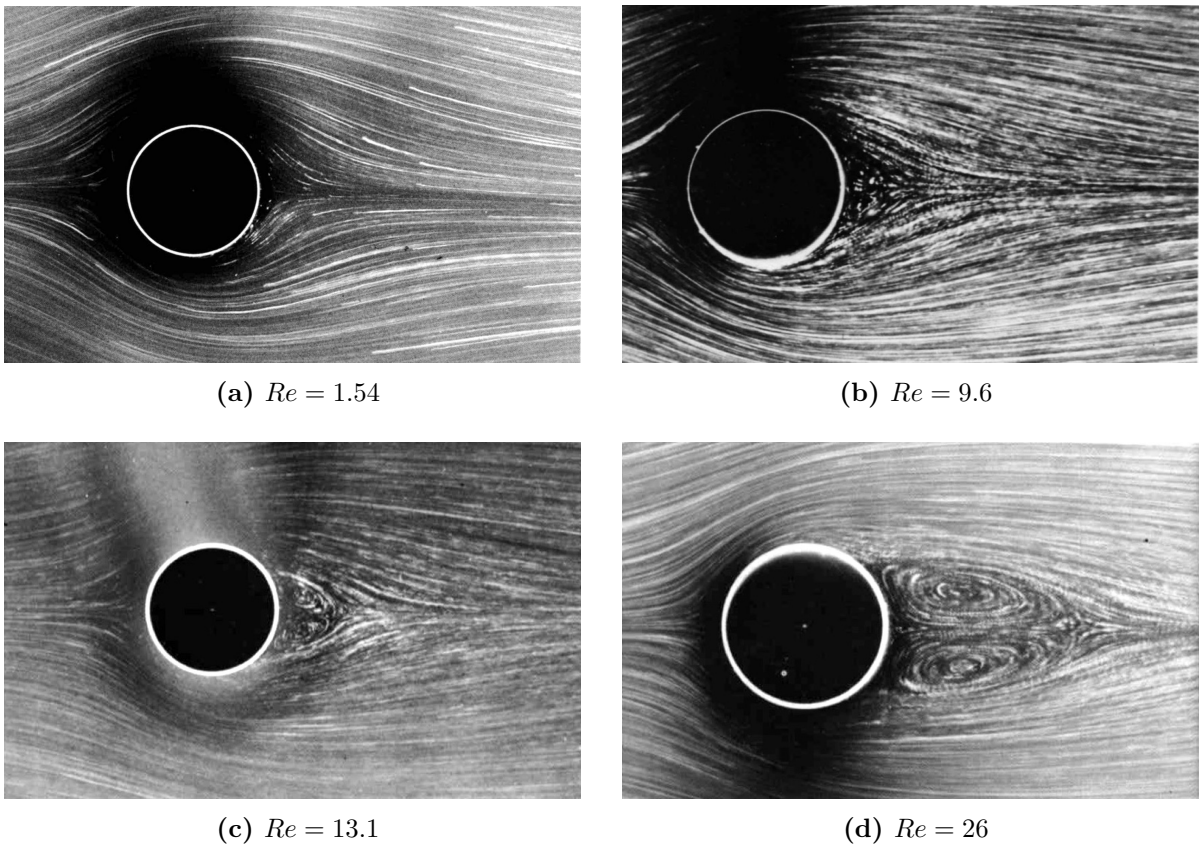
Around a smooth circular cylinder, the steady laminar regime is the first to appear in the Reynolds number scale and can be categorised by two fundamentals patterns presented below.

1. First, a non-separation regime, as presented in figure 2.2$(a)$. This regime can be characterised by a Reynolds number $0 < Re < 4$ to 5. In that case, it is said that the flow is highly viscous since the inertial forces are not of sufficient magnitude to overcome the viscous forces of the fluid so that the flow does not separate from the cylinder wall. This condition is commonly called "creeping flow" in the literature. In this specific instance, the flow remains symmetric in both in-flow and cross-flow directions and completely attached to the cylinder interface all over the boundary. Note that this regime is very different from an inviscid (i.e. potential) flow, even though the streamlines, at first sight, look similar.
   As depicted in figure 2.1, this regime corresponds to the maximum mean drag coefficient for the range presented, whereas the lift coefficient fluctuations remain at zero due to the steadiness of the regime (due to the symmetry of the geometry).

2. Beyond this point, a steady separation regime takes place up to roughly $Re < 48$, as presented in figure 2.2$(b)$, $(c)$, and $(d)$. In this regime, a back-flow region occurs in the near wake behind the cylinder, where the flow direction experiences a behaviour that might be considered counter-intuitive for a new audience. Indeed, the flow is following

the opposite direction to the free stream $U_\infty$ over a distance $L_f$ and as long as the flow maintains low speeds, these bubbles remain stable (*i.e.* steady), close to the cylinder wall, in a symmetrical configuration as schematised in figure 2.3.

For this regime, the aerodynamic drag coefficient decreases sharply as the Reynolds number increases (which might be seen as a drop of the kinematic viscosity), whereas the aerodynamic lift coefficient fluctuation still remains null also due to the complete steadiness of this regime (due to the symmetry of the geometry).



**(a)** $Re = 1.54$ **(b)** $Re = 9.6$

**(c)** $Re = 13.1$ **(d)** $Re = 26$

**Figure 2.2:** Experimental flow visualisations of the steady laminar regime around a circular cylinder. Extracted from van Dyke (1982)

Although the pictures from the figures 2.2($b$), ($c$), and ($d$) being visually different as the Reynolds number increases, the separated laminar regime presents similar characteristics along with its subsistence, as presented in figure 2.3.

In figure 2.3, grey lines represent the streamlines, and the upper and lower black lines the boundary layer thickness. The back-flow region and its characteristic length $L_f$ are highlighted, as well as the different positions of stagnation (*i.e.* point in the flow field where the local fluid velocity is zero) and separation points (*i.e* the position at which the boundary layer detach from the surface of the cylinder), labelled $S_i^t$ and $S_i$ respectively.

The positions of all the stagnation and separation points changes as a function of the Reynolds

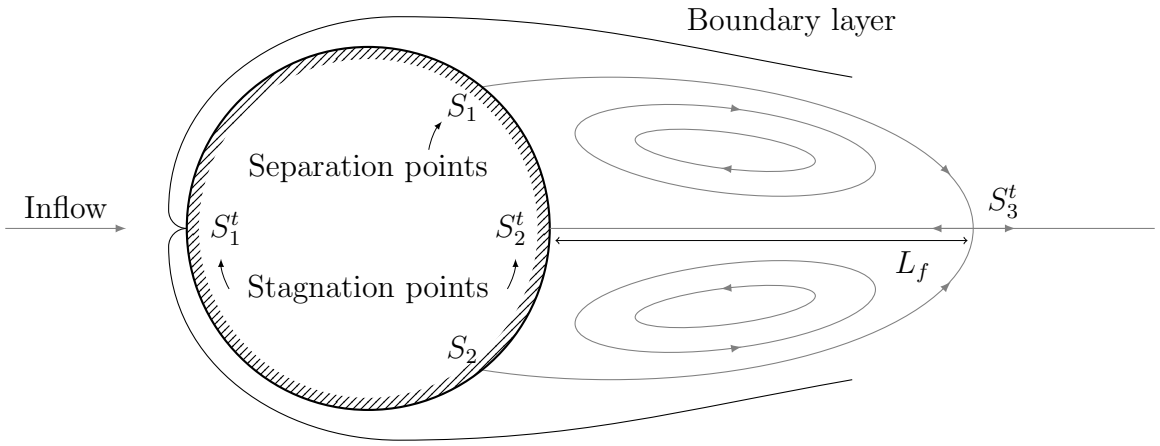



**Figure 2.3:** Near wake pattern in the steady, separated laminar regime (not to scale).

number, and hence the size of this closed wake evolves as the Reynolds number increases as presented in figure 2.4 where Zdravkovich (1997) and Giannetti and Luchini (2007) emphasised its length $L_f$ in an experimental and numerical study respectively.

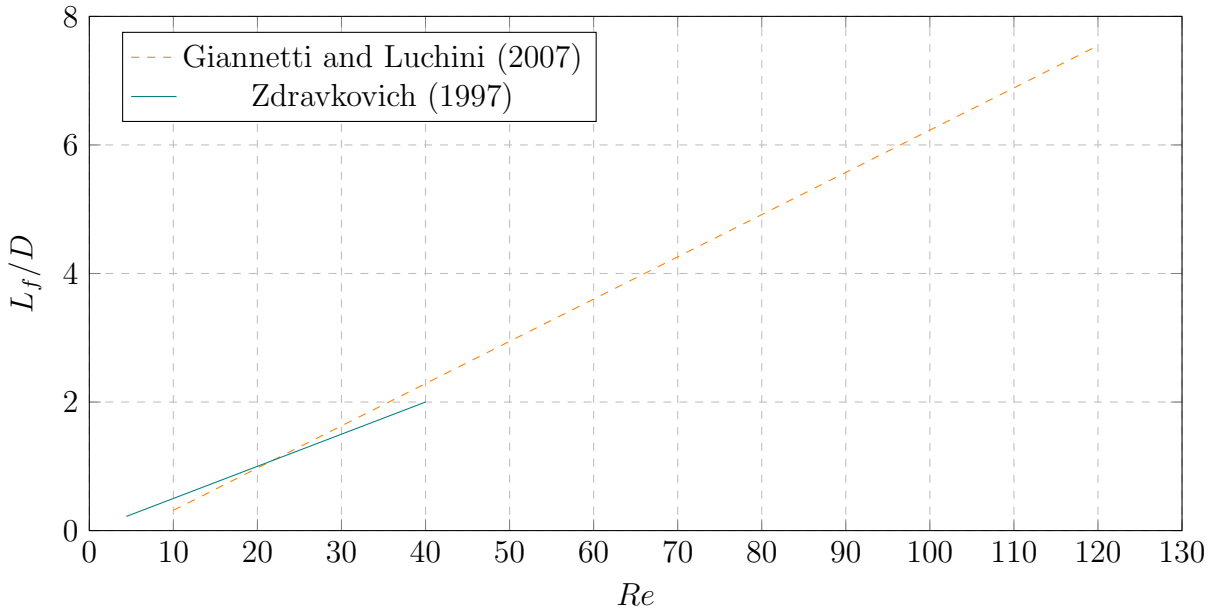



**Figure 2.4:** Normalised length of the recirculation wake bubble $L_f/D$ (measured from the rear stagnation point) for different Reynolds number. Adapted from Giannetti and Luchini (2007) and Zdravkovich (1997).

Interestingly, the re-circulation length $L_f$ of the numerical study matches the linear experimental results observed by Zdravkovich (1997) represented by a green line in figure 2.4

$$\frac{L_f}{D} = 0.05 \cdot Re \quad \text{for} \quad 4.4 \leq Re \leq 40, \tag{2.3}$$

over its domain of validity, however, the difference becomes more pronounced as the Reynolds number increases as a linear fit to the data presented in Giannetti and Luchini (2007) reads

$$\frac{L_f}{D} \simeq 0.0657 \cdot Re - 0.3410 \quad \text{for} \quad 10 \leq Re \leq 120. \tag{2.4}$$

It is also noted that the fit of the measured length $L_f$ from the numerical study does display the zero-length $L_f = 0$ from the non-separated regime.
This particular regime of steady, closed wake will be of paramount importance in this work, as it will allow an investigation of the principal flow-induced motions of the study (*i.e.* the symmetry breaking and torsional flapping) in a numerical setting of fluid-structure interaction, further explained in section §2.2.

### 2.1.2 Unsteady laminar regime

Further in the Reynolds number scale, a new pattern takes place. The viscous effects are no longer strong enough to hold in place the symmetric wake of the steady laminar regime, and the wake's symmetry begins to break: the two recirculating bubbles - upper and lower - start to be convected at the far-field. This is the first dynamic instability experienced by the fluid in the wake of the circular cylinder, and it is determined by its critical Reynolds number $Re \simeq 48$ (Blevins, 2001; Giannetti and Luchini, 2007; Williamson, 1996; Zdravkovich, 1997). This particular phenomenon appears for the whole range $48 \lesssim Re \lesssim 180$ and is known as the laminar Von Kármán vortex street or vortex shedding.

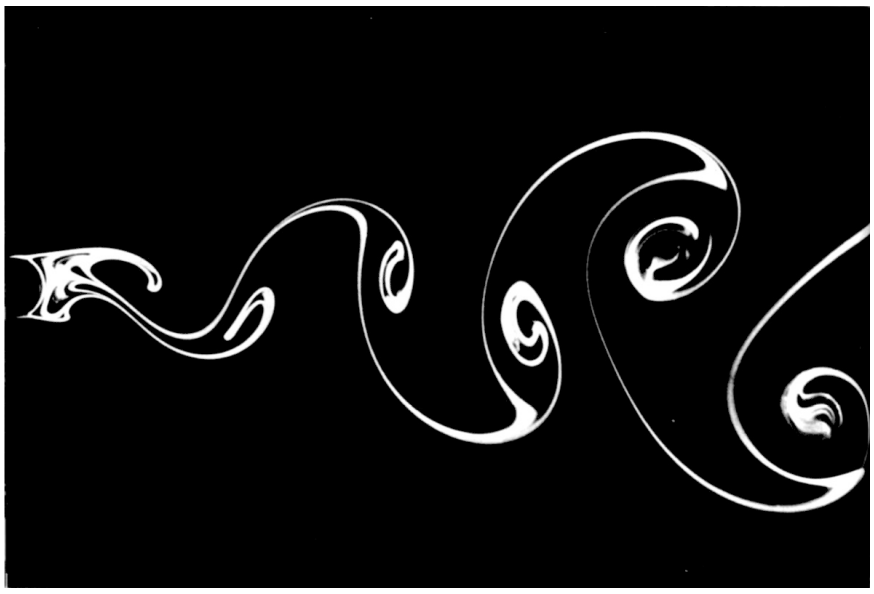


**Figure 2.5:** Experimental visualisation of the laminar Von Kármán vortex street at Reynolds number $Re = 140$. Extracted from van Dyke (1982).

From $Re \simeq 48$, as the Reynolds number keeps increasing, the roll-up of the wake at the far-field

grows in magnitude and gets closer to the near wake region. Figure 2.5 exhibits a snapshot of this phenomenon at $Re = 140$ where the regime is fully established.

From this point, a new non-dimensional number arises, the Strouhal number $St$. Physically, it represents the ratio of the convective time and the characteristic time of the non-stationarity and is expressed as follows

$$St = \frac{f_v D}{U_\infty}, \tag{2.5}$$

where $f_v$ stands for the frequency of emission of vortices, $D$ for the cylinder diameter, and $U_\infty$ for the free stream velocity. Note that when fully established, this regime is periodic of period $T_v = 1/f_v$ (*i.e.* $T_v$ represents the characteristic time of the non-stationarity, when the convective time is represented by the ratio $U_\infty/D$). On the same Reynolds number scale, as presented in figure 2.1, it should be noted that the Strouhal number evolves almost constantly for a smooth circular cylinder, as presented in figure 2.6. On this figure, experimental studies from Lienhard (1966) and Achenbach and Heinecke (1981) investigated the relationship between the Reynolds and Strouhal numbers for smooth and rough surfaces are presented.

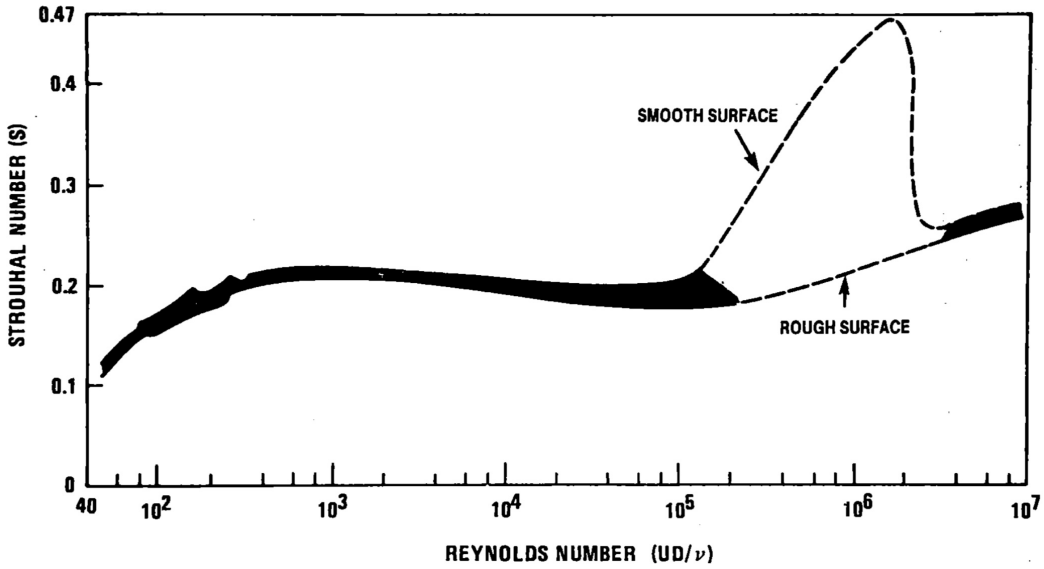



**Figure 2.6:** Relationship between the Reynolds and Strouhal numbers for smooth and rough surfaces circular cylinders. Extracted from Blevins (2001)

The transition from the steady separated state to the unsteady - periodic - state can be investigated through linear stability theory (see further the Section §4.3 in the present study) as presented in Giannetti and Luchini (2007) (see also the works of Barkley et al. (2008*a*); Carmo et al. (2008); Noack and Eckelmann (1994); Zebib (1987)) where the authors obtain, among others, a numerical value for the critical Reynolds number of the vortex shedding instability. Figure 2.7 presents the results of the numerical investigation of the first instability in the cylinder wake (*i.e.* the vortex shedding). Figure 2.7 (*a*) makes explicit the critical Reynolds number of this phenomenon by showing the growth rate of the instability at different Reynolds num-

bers and comparing the sign of this last one, whereas ($b$) shows the associated frequency of the instability for each Reynolds numbers. In fact, a negative growth rate corresponds to decay in the amplitude of the phenomenon, while a positive growth rate reports a growing amplitude (also see Barkley et al. (2008$a$) for a practical description).
Obtaining a figure equivalent to figure 2.7(a) is deterministic for the stability of any physical configuration, as the location of the critical parameter is made explicit (here the Reynolds number).

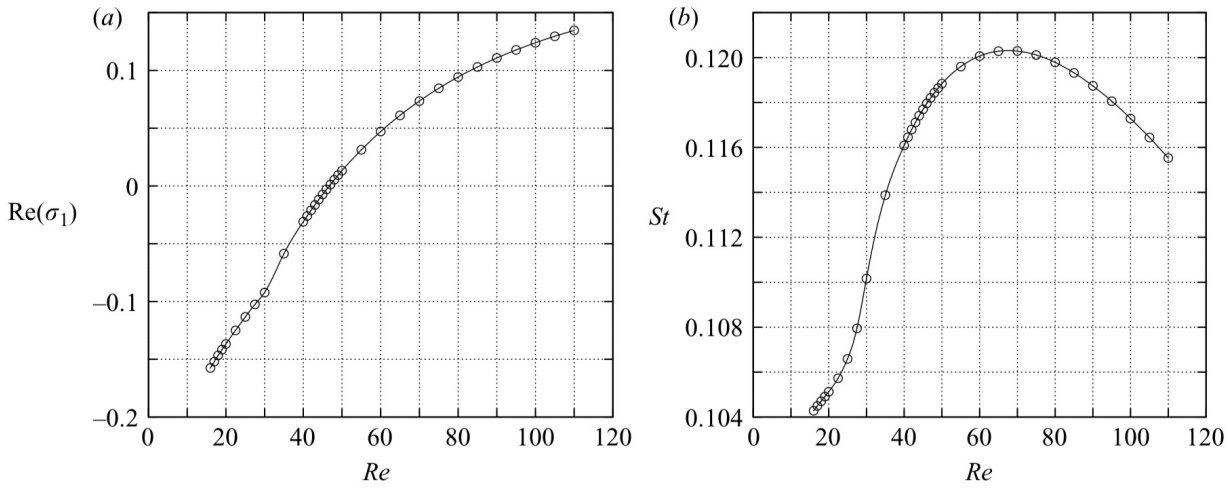



**Figure 2.7:** Evolution of the growth rate ($a$) and Strouhal number ($b$) of the vortex street in function of the Reynolds number. Extracted from Giannetti and Luchini (2007).

## 2.2 Flow around a stationary circular cylinder fitted to a splitter plate

As described in the previous section, the flow velocity profile inside a bluff body wake can show counter-intuitive behaviours such as either steady or unsteady back-flow regions. This section stresses the influence of a fixed splitter plate aligned with the inflow on the wake of a single circular cylinder, as presented in figure 2.8.

When a splitter plate is fixed to the cylinder, this has a direct influence on the critical Reynolds number for the Von Kármán vortex street formation, as well as the Strouhal number and on the back-flow region characteristic length $L_f$ at a given Reynolds number and studies have shown the placing of such a device can suppresses vortex shedding in the wake of the bluff body (Anderson and Szewczyk, 1997; Choi et al., 2008; Kwon and Choi, 1996$b$; Ozono, 1999; Roshko, 1954).

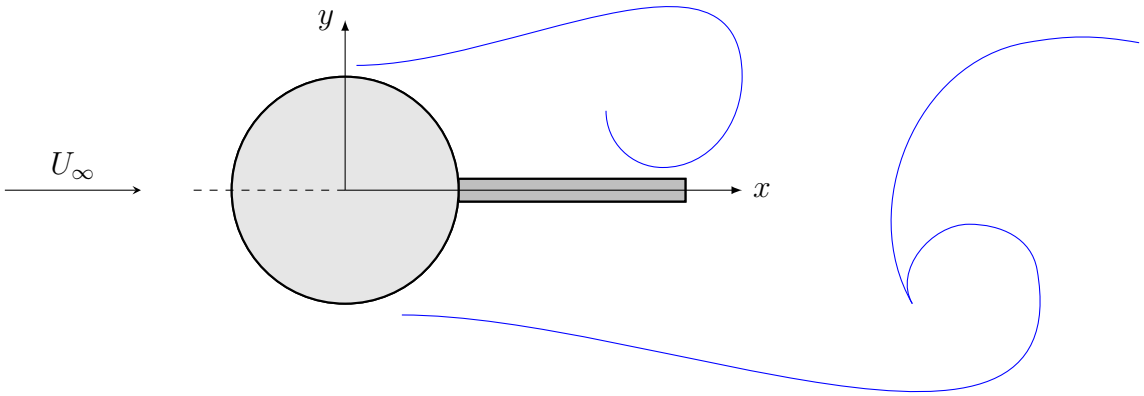
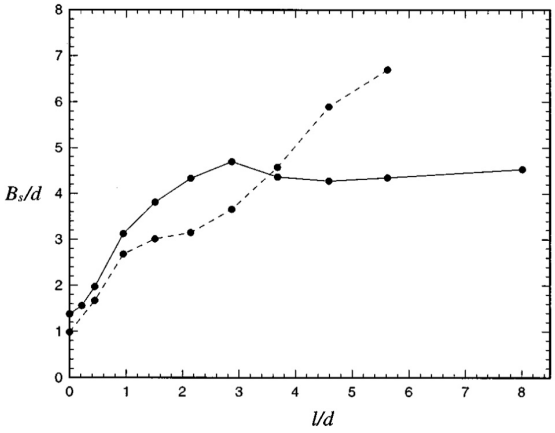


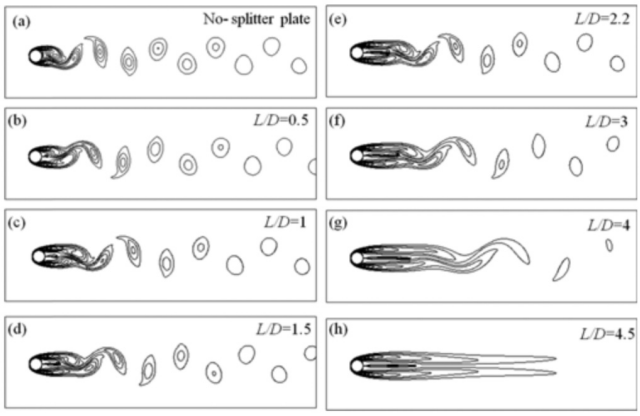

**Figure 2.8:** Fixed, rigid splitter plate aligned with the inflow configuration.

Figure 2.9 presents the impact of placing a fixed, rigid splitter plate on the flow characteristics presented in the sections above.

In their numerical studies, Kwon and Choi (1996*a*) and Vu et al. (2016) investigated the effect of a fixed splitter plate on the wake of a cylinder, respectively presented in figures 2.9 (a) and (b). The splitter plate tends to increase the back flow characteristic length here called $B_s$ in Kwon and Choi (1996*a*) (*v.s.* $L_f$ in the present study) as its own length $l$ (*v.s.* $L$ in the present study, note that in Kwon and Choi (1996*a*), the cylinder diameter is denoted $d$, *v.s.* $D$ in the present study) increase. Figure 2.9 (a) presents these observations for two different Reynolds numbers: $Re = 100$ and 160.




**(a)** Variation of the time-averaged separation-bubble size ($Bs \Leftrightarrow L_f$) with the length of the splitter plate: solid, $Re = 100$; dashed, $Re = 160$.




**(b)** Vorticity Contour Versus normalised splitter plate length $L/D$ at $Re = 160$.

**Figure 2.9:** Effects of the splitter plate length variation on the flow behaviour. Extracted from (a) Kwon and Choi (1996*a*) and (b) Vu et al. (2016).

The correlation between vortex shedding reduction and splitter plate length is also stressed in Figure 2.9 (b), where the influence of the splitter plate length on the Strouhal number is comprehensible implicitly, as the distance between two vortices tends to become more significant as the plate length increases ($L/D$ in figure 2.9 (b)) for a fixed flow configuration (*i.e.* fixing the Reynolds number).

## 2.3 Flow induced motions

Now, if the body in question is flexible enough for the hydrodynamics and the structural dynamics scales to be comparable, the variation of each domain will affect the other. Both are then coupled through the *kinematic* and *dynamic* conditions, further presented in sections §4.2.2.
The interaction between these two mediums gives rise to dynamic bifurcations and instabilities, such as various forms of flow-induced motions.

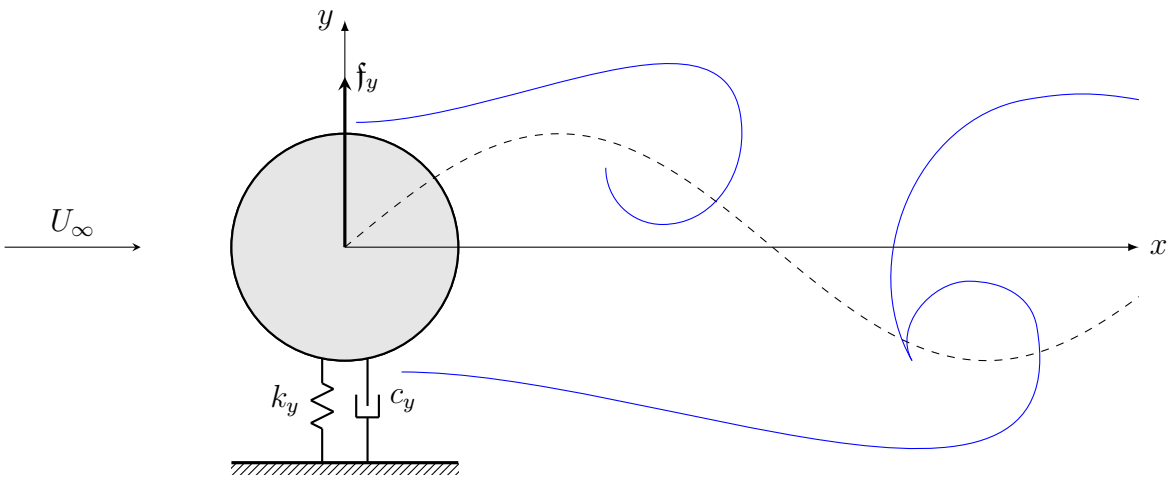



**Figure 2.10:** One degree of freedom mechanism schematic description for a circular cylinder oscillating in the cross flow direction.

This section reviews the principal interactions between the fluid and solid across the reduced velocity $U_R$ range. The reduced velocity is defined as the non-dimensional parameter that measures the ratio between the path length per cycle and the body width (or equivalently the ratio between the flow speed and characteristic speed of the structure undergoing free vibrations)

$$U_R = \frac{U_\infty}{f_n D}. \tag{2.6}$$

Assuming that the solid is steadily oscillating in time and where $f_n$ represents its natural

frequency in vacuum. In the following, another assumption is that the solid motion is governed by a linear oscillator in vacuum.

Taking the particular case of a translational cross-flow direction motion, relevant in the sections §2.3.1 and §2.3.2:

$$m\ddot{y} + c_y\dot{y} + k_y y = 0, \tag{2.7}$$

where $m$ correspond to the mass of the body per unit length, $c_y$ and $k_y$ to the structural damping and stiffness in the cross flow direction respectively and $y, \dot{y}, \ddot{y}$ the displacement, velocity and acceleration in the cross flow direction.

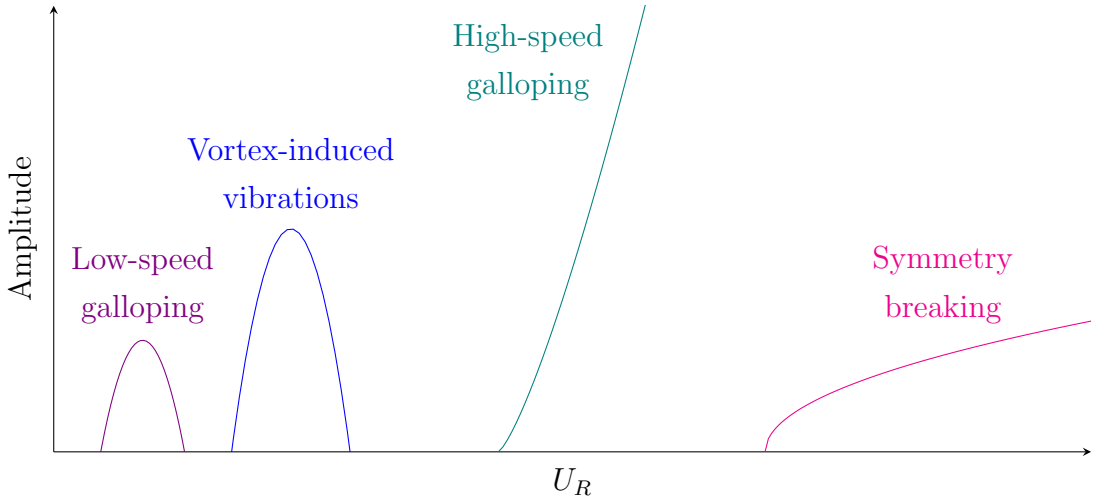



**Figure 2.11:** Schematic of the principal possible amplitudes response curves of an non-circular body in function of different ranges of reduced velocity $U_R$. Adapted from Nakamura (1990).

When the solid is immersed in a fluid - as schematically presented in figure 2.10 - the two mediums are coupled through the dynamic condition, which connects the structural and aerodynamic forces. This has the effect of feeding the right hand side of the expression (2.7) with the aerodynamic resultant force per unit length $\mathfrak{f}_y$ in the crossflow direction:

$$m\ddot{y} + c_y\dot{y} + k_y y = \mathfrak{f}_y. \tag{2.8}$$

For consistency with the rest of the study, this last expression can be rewritten in a canonical form such as it becomes function of the parameters of interest. In its canonical form, (2.8) reads:

$$\ddot{y} + 2\zeta_y\omega_n\dot{y} + \omega_n^2 y = \frac{\mathfrak{f}_y}{m}, \tag{2.9}$$

where the angular frequency $\omega_n$ and the damping ratio $\zeta_y$ are defined respectively as:

$$\omega_n = \sqrt{\frac{k_y}{m}} \quad \text{and} \quad \zeta_y = \frac{c_y}{2\sqrt{k_y m}}.$$

The amplitude response of the canonical form of the one degree of freedom oscillator (2.9) is reviewed in the following three sections under assumptions on the reduced velocity $U_R$ as summarised in figure 2.11.

It is noted that the low-speed galloping presented in figure 2.11 is considered out of the scope of the present study and is not reviewed below. However, its existence is considered relevant for the presentation of the above picture summarising the possible instabilities resulting from a fluid-structure coupling over the range of reduced velocity $U_R$.

### 2.3.1 Vortex-induced vibration

The first interaction of interest to appear on the reduced velocity scale $U_R$ is the vortex-induced vibration (VIV) of the circular cylinder oscillating in the cross-flow direction. Physically, when the time scales of both mediums are considered independently - when the solid is considered stationary for the fluid system, and when the solid is considered in vacuum for the structural system - are about the same order of magnitude, the coupled system may enter in resonance. When the time scales are comparable for the two mediums (*i.e* fluid and solid), the natural frequencies holds:

$$f_v \simeq f_n \quad \Rightarrow \quad U_R = \frac{U_\infty}{f_n D} \simeq \frac{U_\infty}{f_v D} = \frac{1}{St}, \tag{2.10}$$

where $St$ is the Strouhal number defined in equation (2.5), and $f_v$ denotes the vortex emission frequency and is associated to the fluid time scale.
As a consequence, a reduced velocity $U_R \simeq 5$ is expected for the resonance peak of the coupled system, for a large range of Reynolds numbers as presented in figure 2.6 where the values of the Strouhal number are expressed as a function of the Reynolds number.
A typical dynamic response curve of the cylinder displacement in function of the reduced velocity $U_R$ is presented in Figure 2.12, where in their work the authors have denoted the reduced velocity by $V_r$, *v.s.* $U_R$ in the present study.

This "bell-shaped" amplitude response ($A/D$ as a function of the reduced velocity) presented in the lower figure of 2.12 is typical for a wide range of Reynolds numbers and also extends for more complex three-dimensional flows. The width of the "bell-shaped" amplitude response is associated with the so called *lock-in* range (Blevins, 2001; Païdoussis et al., 2010; Zdravkovich, 1997). The *lock-in* region (here the fundamental band is presented) is the region of reduced velocity into which the cylinder vibration is able to synchronise (and control) to the shedding frequency.

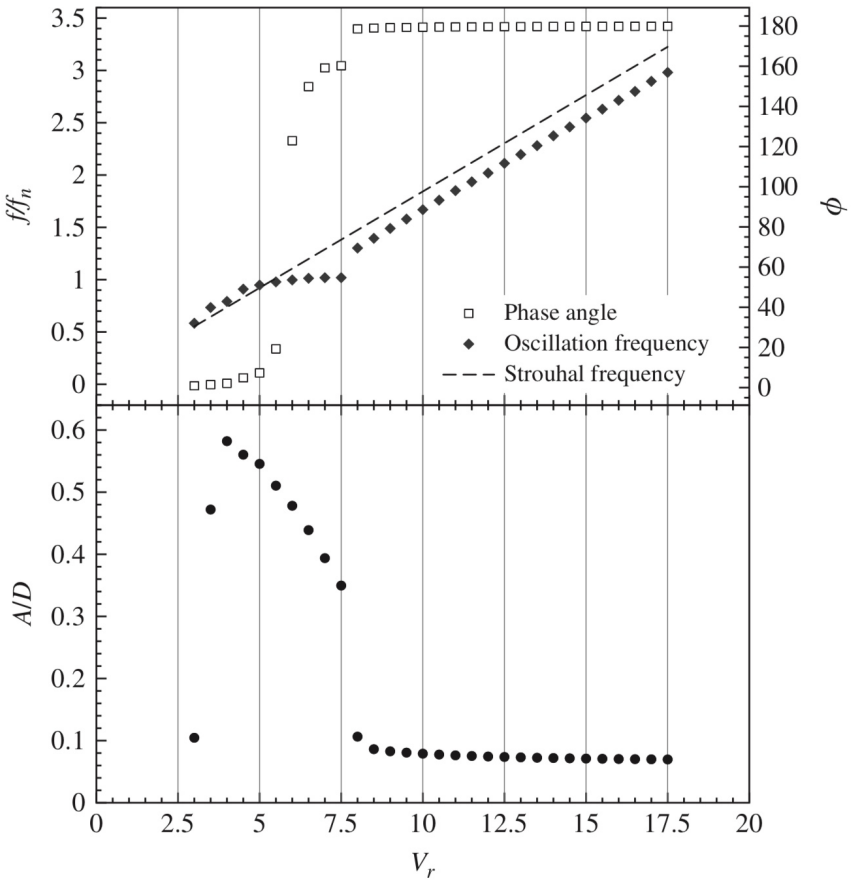



**Figure 2.12:** Dynamic response of a circular cylinder oscillating in the cross flow direction at $Re = 150$ in function of the reduced velocity. Adapted from Carmo et al. (2011)

Indeed, a pure theoretical resonance phenomenon would lead to a Dirac-type amplitude response, however, since the cylinder frequency locks and control the shedding frequency, the resonance occurs over a relatively wide reduced velocity range (*e.g.* in between 3 and 7.5 in Carmo et al. (2011)). Also, due to non-linearity in the complete mechanism of vortex-induced vibration, the maximum amplitude response is bounded by a maximum value (*e.g.* around $0.6D$ in Carmo et al. (2011)). Although their description is considered out of the scope of this study, it should be noted that the present work might be extensible to a higher Reynolds number or more complex geometries due to the similarities of the response curves observed for more complex flows.

### Aeroelastic approximation

Considering the case in which the scales of both $T_{fluid}$ and $T_{solid}$ are "close" (defined in practice by a range of frequency called lock-in, associated with the body's amplitudes and frequencies of oscillations *i.e.* corresponding to the range $3.5 \lesssim U_R \lesssim 7.5$ on figure 2.12), a simple analysis can be conducted assuming a nearly sinusoidal process of the vortex shedding of pulsation $\omega_v$. Indeed, considering a spring-mounted, damped, rigid cylinder of diameter $D$, as shown in figure

2.10, it is possible to express a single degree of freedom, harmonic model of vortex-induced vibration as proposed in Blevins (2001):

$$m\ddot{y} + 2m\zeta_y\omega_y\dot{y} + k_y y = \mathfrak{f}_y = F_L \tag{2.11}$$

$$m\ddot{y} + 2m\zeta_y\omega_y\dot{y} + k_y y = \frac{1}{2}\rho U^2 D C_L \sin(\omega_v t), \tag{2.12}$$

where $y$ is the displacement of the cylinder from its equilibrium position, $m$ is the mass per unit length of the cylinder (including added mass), $\zeta_y$ is the structural damping factor, $k_y$ is the structural stiffness. Since we describe the oscillations of the cylinder by a harmonic model, it is possible to deduce its circular natural frequency independently of the forcing function $F_L$ as

$$\omega_y = \sqrt{\frac{k_y}{m}} = 2\pi f_y. \tag{2.13}$$

Also, $\rho$ is the fluid density, $U_\infty$ is the free stream velocity, and $F_L$ is the lift force per unit length of the cylinder. We finally deduce the circular vortex shedding frequency $\omega_v = 2\pi f_v$ from the Strouhal number $St$.

### 2.3.2 Galloping

Any non-circular body is susceptible to gallop (Blevins, 2001; Païdoussis et al., 2010). This phenomenon is reviewed and described in this section separately for two structural degrees of freedom, the transverse cross-flow direction and the rotation in the Cartesian plane $(x, y)$. The cross-flow galloping is described conforming to the quasi-steady analysis extensively available in the literature, which can among others be found in Blevins (2001); Païdoussis et al. (2010), and a modified version of the classic quasi-steady analysis of the rotational galloping is presented, inspired from the analysis of the cross-flow direction.
Here are presented the assumptions on the body's response which are also possible in the case of "relatively" low reduced velocities, but assuming, however, $U_R \gg 5$ to contrast the potential VIV regime previously presented.

#### Quasi-steady aeroelasticity approximation

Let us consider the case that the flow's time scale $T_{fluid}$ is much smaller than the solid's time scale $T_{solid}$: $T_{fluid} \ll T_{solid}$. In that case, it can be assumed that the solid is moving linearly (in the sense that its displacement can be linearly fitted in time) over the time scale of reference $T_{Fluid}$, which constitutes the essence of the quasi-steady analysis.
Analogically, according to Blevins (2001), this assumption is only valid if the frequency of total periodic components of fluid force is well above the vibration frequency of the structure: $f_v \gg f_n$. Where $f_v$ is the shedding or vortex emission frequency and $f_n$ is the structural natural

frequency of vibration.

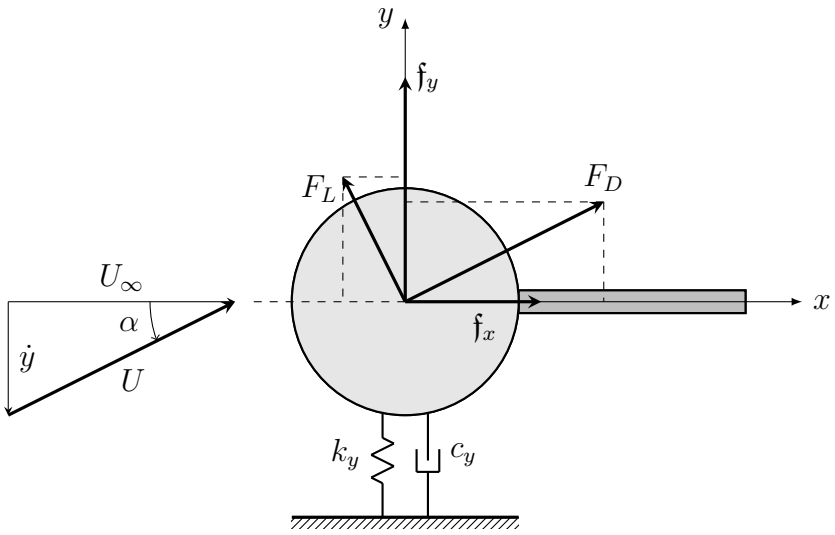



**Figure 2.13:** Forces projections and cross flow Galloping mechanism description.

The initial configuration used for this analysis is the spring-mounted circular cylinder fitted to a splitter plate as presented in figure 2.13. As the cylinder oscillates in the cross-flow direction, the orientation of the incoming flow perceived by the geometry evolves to becoming $U$, defined as the sum of the free stream velocity $U_\infty$ and the body's motion $\dot{y}$. Since the geometry in question is not rotationally symmetric about the $z$ axis, the resulting aerodynamic forces $F_L$ and $F_D$ becomes a function of the body velocity $\dot{y}$, hence implicitly of the further described "angle of attack" $\alpha$.
In the following, the lift force $F_L$ is described as the component which acts perpendicularly to the perceived flow $U$ and the drag force $F_D$ as the one which acts parallel to $U$, such as

$$F_D = \frac{1}{2}\rho U^2 D C_D, \tag{2.14}$$

$$F_L = \frac{1}{2}\rho U^2 D C_L, \tag{2.15}$$

where $C_L$ and $C_D$ are the aerodynamics coefficients of lift and drag, respectively, and $D$ is the diameter of the cylinder. One can express $\alpha$, the angle of attack and the magnitude of the perceived velocity $U$ as:

$$\alpha = \arctan\left(\frac{\dot{y}}{U_\infty}\right), \tag{2.16}$$

$$U = \sqrt{\dot{y}^2 + U_\infty^2}. \tag{2.17}$$

Assuming small perturbations of the solid, one can expand the quantities (2.16) and (2.17) in power series. Assuming a small angle of attack *i.e.* $\alpha \ll 1$ in (2.16) and (2.17), one obtains the

following linearised quantities

$$\alpha = \frac{\dot{y}}{U_\infty} + \mathcal{O}\left(\alpha^2\right), \tag{2.18a}$$

$$U = U_\infty + \mathcal{O}\left(\alpha^2\right), \tag{2.18b}$$

$$C_y(\alpha) = C_y|_{\alpha=0} + \left.\frac{\partial C_y}{\partial \alpha}\right|_{\alpha=0} \alpha + \mathcal{O}\left(\alpha^2\right). \tag{2.18c}$$

Here the terms proportional to $\alpha^2$ and higher powers of $\alpha$: $\mathcal{O}(\alpha^2)$ are neglected. To obtain the expression of the resulting forces $\mathfrak{f}_y$ and $\mathfrak{f}_x$, it is necessary to transform the lift and drag expressions in the $(x, y)$ basis, this is performed by rotating the system with an angle of $\alpha$

$$\begin{bmatrix} \mathfrak{f}_x \\ \mathfrak{f}_y \end{bmatrix} = \begin{bmatrix} \cos(\alpha) & -\sin(\alpha) \\ \sin(\alpha) & \cos(\alpha) \end{bmatrix} \begin{bmatrix} F_D \\ F_L \end{bmatrix}. \tag{2.19}$$

Finally, one obtains the resulting forces that are required to feed the structural equation of motion:

$$\mathfrak{f}_x = \frac{1}{2}\rho U_\infty^2 D C_x \quad ; \quad C_x = \frac{U^2}{U_\infty^2}\left(C_D\cos(\alpha) - C_L\sin(\alpha)\right), \tag{2.20a}$$

$$\mathfrak{f}_y = \frac{1}{2}\rho U_\infty^2 D C_y \quad ; \quad C_y = \frac{U^2}{U_\infty^2}\left(C_D\sin(\alpha) + C_L\cos(\alpha)\right). \tag{2.20b}$$

One can now express the motion of the structure as a function of the resulting forces and the linearised terms. Using the expressions (2.18) and (2.20) in the canonical form (2.9) leads to:

$$m\ddot{y} + 2m\zeta_y\omega_y\dot{y} + k_y y = \mathfrak{f}_y \tag{2.21}$$

$$m\ddot{y} + 2m\omega_y\left(\zeta_y - \frac{\rho U D}{4m\omega_y}\left.\frac{\partial C_y}{\partial \alpha}\right|_{\alpha=0}\right)\dot{y} + k_y y = \frac{1}{2}\rho U^2 D\, C_y|_{\alpha=0}. \tag{2.22}$$

A stability criterion of the equation (2.22) can be derived from the value of the total resulting damping, presented below.

### Den Hartog criterion

For commodity, equation (2.22) is expressed as a function of the net damping factor of vertical motion $\zeta_T$,

$$\zeta_T = \zeta_y - \frac{\rho U D}{4m\omega_y}\left.\frac{\partial C_y}{\partial \alpha}\right|_{\alpha=0}, \tag{2.23}$$

in which case a solution of the equation (2.22) can be obtained in the pseudo-periodic regime, of the form:

$$y = \frac{-\frac{1}{2}\rho U^2 D\, C_y|_{\alpha=0}}{k_y} + A_y e^{-\zeta_T\omega_y t}\sin\left[\omega_y\sqrt{1-\zeta_T^2}t + \phi\right]. \tag{2.24}$$

Thus one obtains that the vertical oscillations will increase or decrease in time depending on the sign of $\zeta_T$. Since the only variable in the expression of $\zeta_T$ (see expression (2.23)) is the slope of the curve of $C_y$ around zero, one can make explicit the divergence criterion of the pseudo-periodic solution (2.24) as:

$$\lim_{t\to\infty}|y| \to \begin{cases} \text{potentially} \quad \infty \quad \text{if} \quad \left.\frac{\partial C_y}{\partial \alpha}\right|_{\alpha=0} > 0, \\ 0 \quad \text{if} \quad \left.\frac{\partial C_y}{\partial \alpha}\right|_{\alpha=0} < 0. \end{cases} \tag{2.25}$$

This is the Den-Hartog (1956) criterion of stability. Regarding the validity of this criterion, Blevins (2001) claims that this theory is applicable safely at reduced velocity $U_R = U/f_y D$ above 20, for a rectangular section of ratio $L/D = 2$. When according to Bearman et al. (1987), this theory is applicable safely at a reduced velocity above 30, considering a square prism.

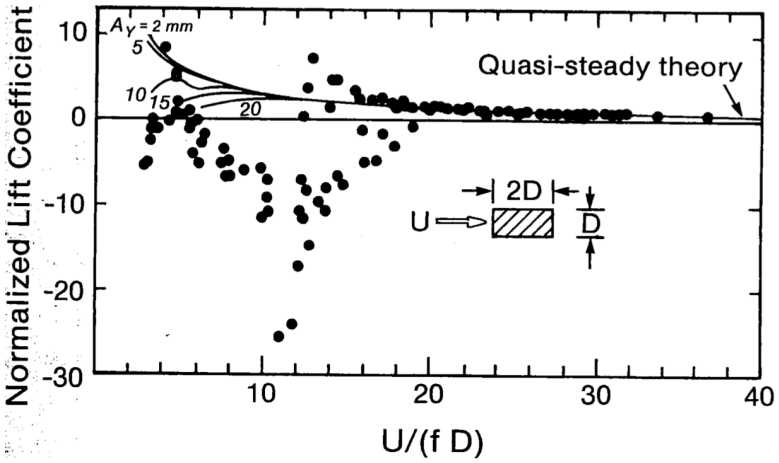



**Figure 2.14:** Comparison of the experimental data for the aerodynamic force coefficient on a vertically oscillating rectangular section, to the quasi steady theory, as a function of the reduced velocity. Extracted from Blevins (2001), based on the work of Washizu et al. (1978).

Indeed, as shown in figure 2.14, the experimental data for the aerodynamic force converge through the quasi steady theory as the reduced velocity increases, and the critical reduced velocity for this rectangular cross section ration is about 20. However, the agreement between experimental data and quasi steady theory is shape dependent, meaning that the minimum reduced velocity for which the quasi steady theory is applicable safely changes as the cross section changes.

### Torsional galloping

The Galloping phenomenon can also occur in torsion and be described in a similar manner as its translational counterpart. However, by following the same approach as the one described above (see Slater (1969) and Blevins (2001)), one encounters that the angle of attack $\alpha$ is expressed

evaluating the motion of the whole section by defining a reference radius $R_r$ on the rotating section (here the distance between the wheel cross and the hinge point), such that there is a unique value of transverse velocity $R_r\dot{\theta}$ at the angle $\beta$ (see figure 2.15).

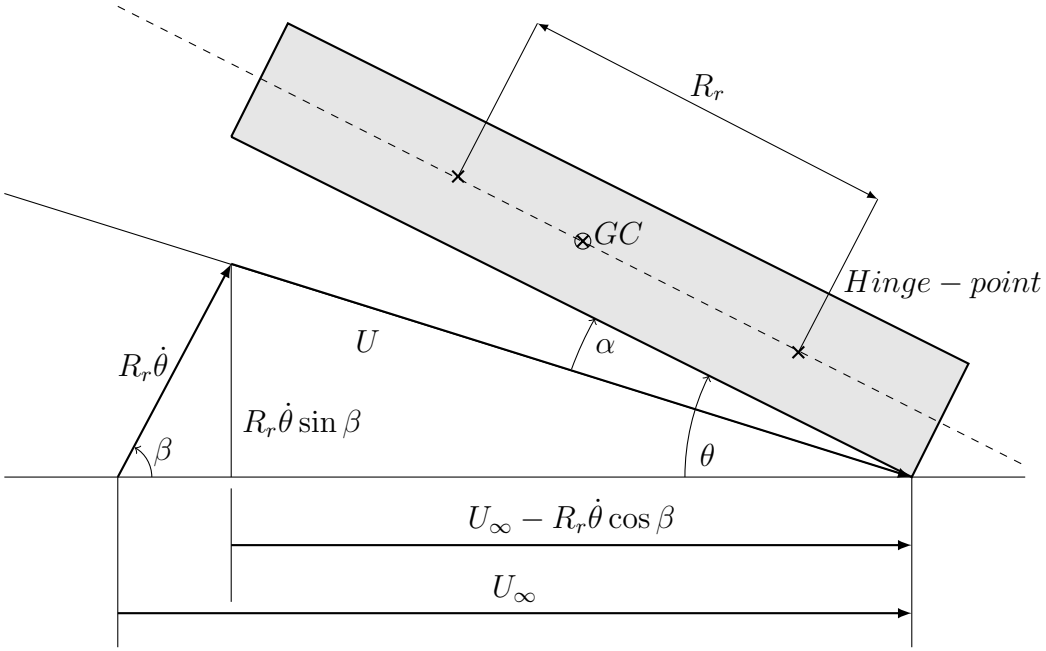



**Figure 2.15:** Schematic of a rectangular prism section in torsional oscillation and diagram for determining $\alpha$ in terms of $R_r$. Adapted from Païdoussis et al. (2010)

Following this approach, both the angle of attack $\alpha$ and perceived velocity $U$ are functions of the reference radius $R_r$. In practice, however, the choice of $R_r$ is not rigorous. Indeed, one obtains values of $R_r$ depending on the structure's profile. To cite a few examples, there is for instance:

- For rectangles with hinge point of torsion superposed to their centroid (geometric centre), $R_r$ is generally taken to be half the depth of the rectangle (corresponding to the instantaneous angle of attack at the leading edge) (Nakamura and Mizota, 1975).
- For right-angle sections facing the wind about the apex of the angle, we commonly choose $R_r$ as the sum of half of the force and aft length of the section (Slater, 1969).
- For airfoils, $R_r$ is also commonly defined as the one-quarter chord point from the leading edge (tenuous choice for separated flows) (Bisplinghoff et al., 1966).

This quasi-steady analysis has been further disqualified (see Nakamura (1990); Nakamura and Mizota (1975); Nakamura and Yoshimura (1982)) when comparing the obtained results to experimental data.

In order to avoid the multiple approximations of the reference radius $R_r$ for each geometry studied in this work, here is presented a modified linearised model built on the same classic

quasi-steady theory and geometry of study as shown in figure 2.16.

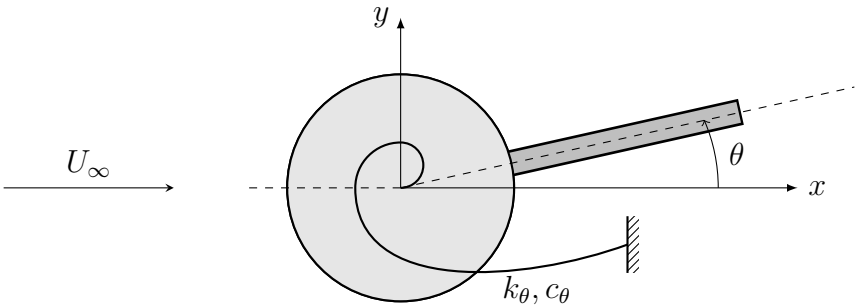



**Figure 2.16:** Quantities and mechanism description of the rotating cylinder fitter to a splitter plate.

To do so, a linear relationship is assumed between the aerodynamic forces and the structural variables: the angle $\theta$ and angular velocity $\dot{\theta}$.
Looking at the following non-linear problem

$$I_\theta \ddot{\theta} + 2I_\theta \zeta_\theta \omega_\theta \dot{\theta} + k_\theta \theta = \mathfrak{m}_z, \tag{2.26}$$

where $\mathfrak{m}_z$ is the aerodynamic moment around the $z$ axis, the moment $\mathfrak{m}_z$ is here assumed function of the angular position and velocity *i.e.* $\mathfrak{m}_z = \mathfrak{m}_z(\theta, \dot{\theta})$ and the problem (2.26) is then Taylor expanded around $(\theta_0, \dot{\theta}_0)$ as follows:

$$I_\theta \ddot{\theta} + \left( 2I_\theta \zeta_\theta \omega_\theta - \left. \frac{\partial \mathfrak{m}_z}{\partial \dot{\theta}} \right|_{(\theta,\dot{\theta})=(\theta_0,\dot{\theta}_0)} \right) \dot{\theta} + \left( k_\theta - \left. \frac{\partial \mathfrak{m}_z}{\partial \theta} \right|_{(\theta,\dot{\theta})=(\theta_0,\dot{\theta}_0)} \right) \theta = 0, \tag{2.27}$$

which have, for the initial conditions $(\theta_0, \dot{\theta}_0) = (0, \dot{\theta}_0)$, the following analytical aperiodic solution:

$$\theta_{sol} = \frac{\dot{\theta}_0}{(r_1 - r_2)} \left( e^{r_1 t} - e^{r_2 t} \right), \tag{2.28}$$

where:

$$r_{1,2} = \frac{-\left(2I_\theta \zeta_\theta \omega_\theta - \partial_{\dot{\theta}} \mathfrak{m}_z\right) \pm \sqrt{\Delta}}{2I_\theta}, \tag{2.29}$$

and

$$\Delta = \left(2I_\theta \zeta_\theta \omega_\theta - \partial_{\dot{\theta}} \mathfrak{m}_z\right)^2 - 4\left(I_\theta \left(k_\theta - \partial_\theta \mathfrak{m}_z\right)\right) \quad \text{assumed } > 0. \tag{2.30}$$

In practice, $\dfrac{\partial \mathfrak{m}_z}{\partial \dot{\theta}}$ and $\dfrac{\partial \mathfrak{m}_z}{\partial \theta}$ results from quasi-steady simulations described in the sub sections below.
It is also noted that as in the representation initially presented in Slater (1969) and Blevins (2001), this system is susceptible to both torsional galloping and static torsional divergence. First, the system can torsionally gallop if the coefficient of $\dot{\theta}$ in the equation (2.27) becomes

negative (negative damping).
The phenomenon of divergence (or buckling), for its part, occurs when the sum of the structural and the aerodynamic torsional stiffness terms falls to zero: the coefficient of $\theta$ in the equation (2.27).

### First quasi steady coefficient computation strategy: $\partial_\theta \mathfrak{m}_z$

The first quasi steady coefficient $\dfrac{\partial \mathfrak{m}_z}{\partial \theta}$ is straightforwardly extracted by imposing a small tilting angle $\theta$ and measuring the moment about this $\theta$, as presented in Figure 2.17.

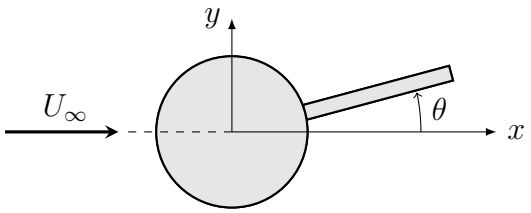



**Figure 2.17:** Small tilting angle.

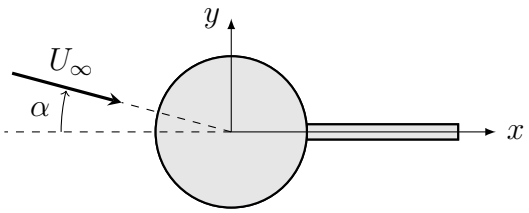



**Figure 2.18:** Equivalent configuration.

The moment is actually extracted after applying a small angle of attack $\alpha$ to the original geometry, corresponding to the tilted angle $\theta$, as drafted in figure 2.18.

### Second quasi steady coefficient computation strategy: $\partial_{\dot\theta} \mathfrak{m}_z$

The second coefficient $\partial_{\dot\theta} \mathfrak{m}_z$ is then numerically extracted imposing a small, constant angular velocity $\dot\theta$ at the interface boundary and measuring the moment about $\theta = \theta_0$. To do so, let us consider a rotating moving boundary, as sketched in figure 2.19. Considering the polar coordinates:

$$\begin{cases} r = \sqrt{x^2 + y^2} \\ \theta = \arctan\left(\dfrac{y}{x}\right) \end{cases} \quad \text{and,} \quad \begin{cases} x = r\cos(\theta) \\ y = r\sin(\theta) \end{cases} . \tag{2.31}$$

In Cartesian coordinates, the velocity at the boundary reads:

$$\begin{cases} \dot x = \dot r\cos(\theta) - r\dot\theta\sin(\theta) \\ \dot y = \dot r\sin(\theta) + r\dot\theta\cos(\theta) \end{cases} \Rightarrow \begin{cases} \dot x = -r\dot\theta\sin(\theta) \\ \dot y = r\dot\theta\cos(\theta) \end{cases} \Leftrightarrow \begin{cases} \dot x = -\dot\theta y \\ \dot y = \dot\theta x \end{cases} . \tag{2.32}$$

Considering a zero radial velocity $\dot r = 0$.

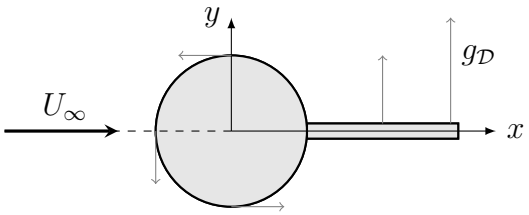



**Figure 2.19:** Extraction of the second coefficient $\partial_{\dot{\theta}}\mathfrak{m}_z$.

At the boundary interface, for a constant angular velocity of magnitude $\kappa \ll 1$, the Dirichlet boundary condition $g_{\mathcal{D}}$ reads then:

$$\begin{cases} u = -\kappa y \\ v = \kappa x \end{cases} . \tag{2.33}$$

This approach have shown to be accurate, comparing the resulting expression (2.28) to full non-linear simulations (further presented in section §4.2), for the range of parameters (*i.e.* $Re$, $U_R$, and shapes) studied in this work.

### 2.3.3 Symmetry breaking

When the splitter plate is allowed to freely rotate around a hinge point in an unconstrained manner (*i.e.* $k_\theta \longrightarrow 0$), which translates in terms of reduced velocity as $U_R \longrightarrow \infty$ (as we recall $U_R = U_\infty/(f_n D) = U_\infty/(\sqrt{k_\theta/I_\theta}D)$), the coupled physics (fluid and structural) might behave differently than the periodic motions presented above. Indeed, the cylinder might exhibits a flow-induced 'static' instability which breaks the symmetry of the flow posed by the cylinder geometry (Assi et al., 2010; Assi, Bearman and Tognarelli, 2014; Bagheri et al., 2012*b*; Cimbala and Garg, 1991; Lacis et al., 2014*b*; Pfister and Marquet, 2020) in the case of steady or unsteady flow configurations. It has also been proposed that this instability provides an aiding mechanism for flight motion of insects and locomotion of swimming animals (Bagheri et al., 2012*b*; Lacis et al., 2014*b*; Park et al., 2010).

Regardless of the steadiness of the flow, the outcome of this phenomenon has been shown to rely on the splitter plate length highly: if it is long enough, no considerable changes are noted compared to the fixed case; hence no structural rotation is observed, and the splitter plate might act as a vortex shedding suppressor. This case is depicted in Figure 2.21 for plate lengths longer than about two cylinder diameters.

On the other hand, if the splitter plate length is short enough to interact with the back-flow region, this will result in symmetry breaking in both mediums, depicted in figure 2.21 for plate lengths shorter than about two cylinder diameters.

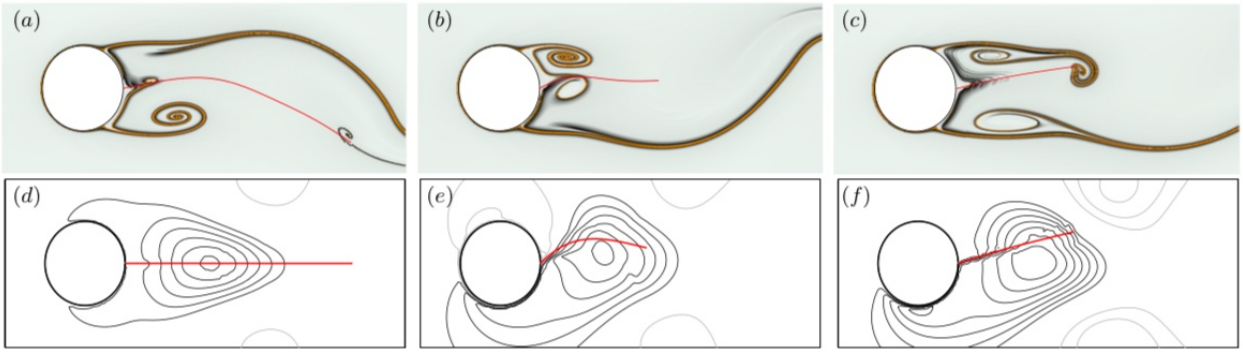
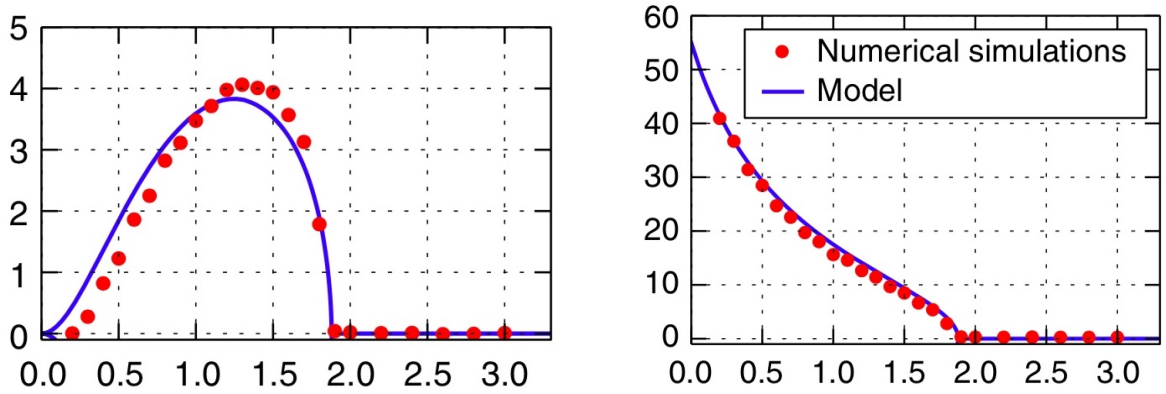



**Figure 2.20:** Mean and instantaneous positions of the filaments for different length and rigidity. Extracted from Bagheri et al. (2012*a*)

In a numerical study, Bagheri et al. (2012*a*) investigates the effect of the turn angle on the aerodynamic forces, depending on the length and flexibility of a splitter plate considered as a filament for unsteady flow configurations. This study shows that the presence of passive short filaments in unsteady wakes can generate lift without increasing drag and thus could be used to act in favour of the aerodynamics in separated flows if one is interested in locomotion. Figure 2.20 presents instantaneous (see figure 2.20(a-c)) and time-averaged (see figure 2.20(d-e)) position of the filament, this filament leaves its initial position to stick to one side or another (up or down on this figures) and tend to reattach the flow at its tip partially. This geometrical modification consequently changes the mean pressure and velocities distributions in the near wake, resulting in aerodynamic forces alterations.




**(a)** Drift angle in function of normalised splitter plate length.

**(b)** Turn angle in function of normalised splitter plate length.

**Figure 2.21:** Model comparison of the turn and drift angles as functions of the splitter-plate length, respectively, in (a) and (b) at $Re = 45$. Extracted from Lacis et al. (2014*a*)

In another study, Lacis et al. (2014*a*) validates experimentally and numerically a model of turn angle (describing the angle $\theta$ adopted by the geometry in its steady-state), based on the wake characteristics without any appendices.

Although not being based on the flow properties of the actual geometries of study, this model captured the general shapes of both drift accurately and turn-angle as a function of the splitter plate length and the critical length for which the phenomenon initiates, as shown in figure 2.21. In this study, the drift angle is characterised by the change of direction of the velocity vector of the freely falling body in a still fluid compared to the gravitational acceleration vector. This angle is a direct consequence of aerodynamic forces modifications due to symmetry breaking.

# Chapter 3

# Problem formulation

This chapter aims to interpret and describe the motion of a body as the combination of different geometric transformations of the initial boundary location, which will serve as a basis and starting point to obtaining the desired operators.
Here, the analysis is presented assuming a rigid body displacement in a two-dimensional Euclidian plane, making homogeneous coordinates (see equation (3.1)) the natural choice of investigation, along with affine transformations. Such hypothesis will lead to a three degree of freedom structural motion (two translations and one rotation) coupled to the surrounding fluid medium through the aerodynamic forces.
The chapter is organised as follows, in section §3.1 the *full-order* or *non-linear* coupled fluid-structure system is first described such that its model results from the coupling (in §3.1.3) of the fluid only (in §3.1.1) and solid only (in §3.1.2) systems, both obtained under the physical assumptions considered in this work. Second, in section §3.2 the *linear, or direct* operator is obtained, again by coupling the first order fluid only (in §3.2.1) and solid only (in §3.2.2) systems considered independently, at their interface through *kinematic* and *dynamic* conditions. Finally, the *adjoint* operator (in §3.3) is obtained by judicious manipulation of the *direct* operator under the choice of a physically meaningful inner product presented in section §3.3.1.

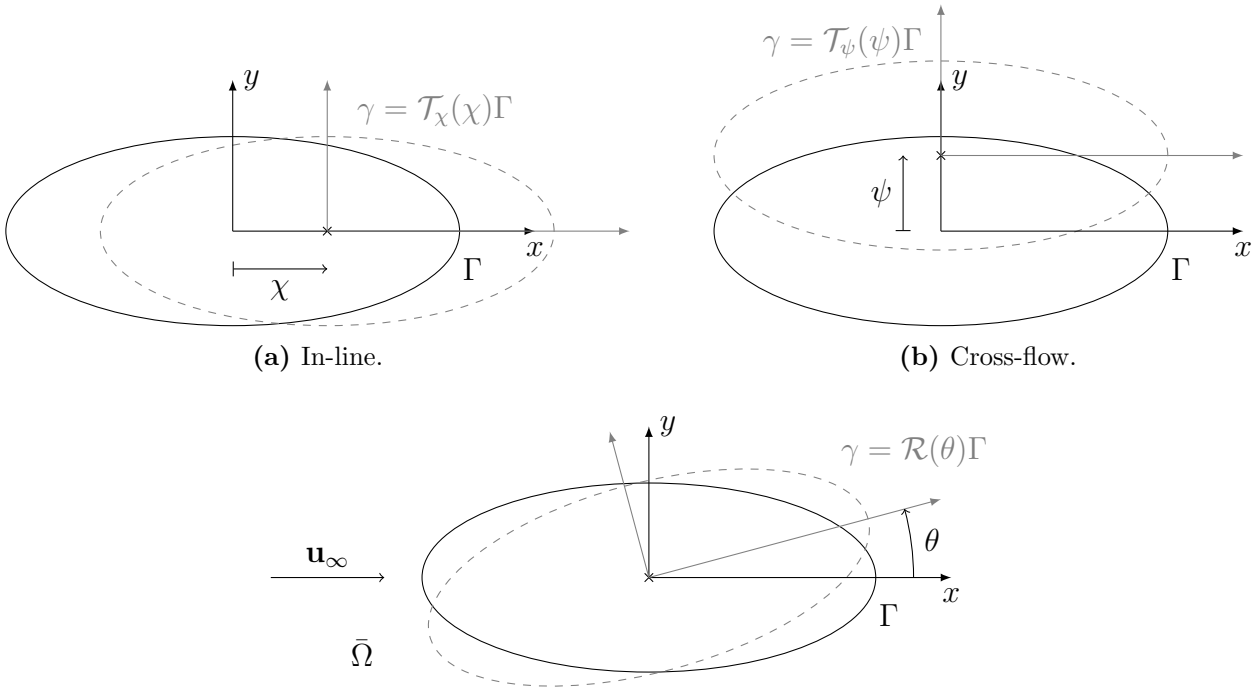
To develop the analysis presented in the following sections, let us consider $\bar{\Omega}$, a bounded subset of the two-dimensional euclidian plane, which will further correspond to our computational domain. In a homogeneous coordinate system, the domain $\bar{\Omega}$ reads:

$$\bar{\Omega} := \left\{(x, y, 1) \in \mathbb{R}^3 \quad | \quad x^- \leq x \leq x^+ \text{ and } y^- \leq y \leq y^+; \quad x^-, x^+, y^-, y^+ \in \mathbb{R}\right\}, \tag{3.1}$$

where $x^-, x^+, y^-, y^+$ represent the outer boundaries of the domain $\bar{\Omega}$.
Note that the representation of a point in the plane domain $\bar{\Omega}$ have three coordinates, under the homogeneous coordinate representation, where the last one set to unity is acting as coordinator of the system and have no physical interpretation in this work. This counter-intuitive choice of representation is made to maintain further consistency when considering geometric

transformations (*i.e.*, combining translations and rotations in the two-dimensional Euclidian plane by matrix multiplication).

Figure 3.1 describes the possible transformations of a subset $\Gamma \subset \bar{\Omega}$ corresponding to the boundary of an object considered in this work, respectively the in-line $\mathcal{T}_\chi$ and cross-flow $\mathcal{T}_\psi$ translations (*i.e* along the $x$ and $y$ Cartesian axis respectively. The free-stream in the stream-wise direction $\mathbf{u}_\infty = (U_\infty, 0)$ flow is arbitrarily assumed parallel to the $x$ axis all along this work), as well as the rotation $\mathcal{R}$ around the $z$ axis.




**(a)** In-line.

**(b)** Cross-flow.

**(c)** Torsion.

**Figure 3.1:** Affine transformations, or structural degrees of freedom description.

A continuous, closed interface boundary $\Gamma$ (*i.e* the boundary of the object) can be formally described as

$$\Gamma := \left\{(x, y, 1) \in \bar{\Omega} \quad | \quad (x, y, 1) = (r(s)\cos(s), r(s)\sin(s), 1); \quad s \in [0; 2\pi); \quad r \in \mathcal{C}^0\left([0; 2\pi), \mathbb{R}\right)\right\}, \tag{3.2}$$

where $s \in \mathbb{R}$ vary in the interval $[0; 2\pi)$, and $r$ is of class $\mathcal{C}^0$ (continuous) from $[0; 2\pi)$ into $\mathbb{R}$, such as $r(s) \in \mathbb{R}$, and correspond to the distance from the center to the boundary at the angle $s$. Independently represented in Figure 3.1, the three transformations analytically reads

$$\mathcal{T}_\chi(\chi) = \begin{bmatrix} 1 & 0 & \chi \\ 0 & 1 & 0 \\ 0 & 0 & 1 \end{bmatrix}; \quad \mathcal{T}_\psi(\psi) = \begin{bmatrix} 1 & 0 & 0 \\ 0 & 1 & \psi \\ 0 & 0 & 1 \end{bmatrix}; \quad \mathcal{R}(\theta) = \begin{bmatrix} \cos(\theta) & -\sin(\theta) & 0 \\ \sin(\theta) & \cos(\theta) & 0 \\ 0 & 0 & 1 \end{bmatrix}. \tag{3.3}$$

The canonical affine transformations presented in Figure 3.1 can be easily combined together to describe a more complex motion (*i.e.* two or three degrees of freedom), and $\Gamma$ can be relocated according to the total transformation matrix $\mathcal{T}(\chi, \psi, \theta)$ such as:

$$\gamma = \{(x, y, 1) \in \Omega \quad | \quad (x, y, 1) \in \mathcal{T}(\chi, \psi, \theta)\Gamma\}, \tag{3.4}$$

is the new location of $\Gamma$ after displacement.

Finally, the total transformation matrix $\mathcal{T}(\chi, \psi, \theta)$ is obtained multiplying the three canonical affine transformations presented in Figure 3.1 and equations (3.3) and reads

$$\begin{aligned} & \gamma = \mathcal{T}(\chi, \psi, \theta)\Gamma \\ \Leftrightarrow \quad & \gamma = \begin{bmatrix} \cos(\theta) & -\sin(\theta) & \chi \\ \sin(\theta) & \cos(\theta) & \psi \\ 0 & 0 & 1 \end{bmatrix} \begin{bmatrix} x \\ y \\ 1 \end{bmatrix} \\ \Leftrightarrow \quad & \gamma = \left(\mathcal{T}_\chi(\chi).\mathcal{T}_\psi(\psi).\mathcal{R}(\theta)\right)\Gamma. \end{aligned} \tag{3.5}$$

## 3.1 Non-linear operator

This section reviews the general behaviour of the quantities considered based on the physical limitations that are judged suitable: governing equations on both sides (*i.e.* fluid and solid) are obtained assuming the flow incompressible and the solid moving linearly around its equilibrium position. The fluid's nature is assumed Newtonian, and the solid material is considered rigid and non-porous.
This section can be seen as an extension of the section §4.2, in a static configuration, to obtain the operator-form of the problem.

### 3.1.1 Fluid only

The Navier-Stokes equations model the fluid motion in an incompressible regime. Throughout this work, the equations of motion and all the related variables are made dimensionless with $U_\infty$ and the characteristic length $D$ of the problem (*i.e.* further the cylinder diameter in Chapter §6). The dimensionless spatial location is denoted by $\mathbf{x} = (x, y)$, where $x$ and $y$ are the streamwise and transverse coordinates as presented in figure 3.1, and the velocity is given by $\mathbf{u} = (u, v)$ with its streamwise and transverse components $u$ and $v$. The fluid domain is denoted by $\Omega \subset \bar{\Omega}$, the inner boundary of which (*i.e.* $\partial\Omega_{in} = \gamma$) is given by the body surface. The geometric centre of the body is set to be located at $(x, y) = (0, 0)$.

Hence the following momentum and mass conservation laws reads

$$\begin{cases} \dfrac{\partial \mathbf{u}}{\partial t} + (\mathbf{u}\cdot\nabla)\mathbf{u} = -\nabla p + Re^{-1}\nabla^2\mathbf{u} & \text{in } \Omega \\ \nabla\cdot\mathbf{u} = 0 & \text{in } \Omega \end{cases}, \tag{3.6}$$

where $p$ is the dimensionless pressure and the Reynolds number $Re = U_\infty D/\nu$ where the density and the kinematic viscosity of the fluid are by $\rho$ and $\nu$, respectively.

The expression (3.6) can be compactly in operator form, rewritten as

$$\mathcal{F}\mathbf{q} = \mathbf{0}, \quad \text{where} \quad \mathcal{F} = \left[\begin{array}{c|c} -\partial_t - \mathbf{A} + Re^{-1}\nabla^2 & -\nabla \\ \hline \nabla\cdot & 0 \end{array}\right] \quad \text{and} \quad \mathbf{q} = \begin{bmatrix} \mathbf{u} \\ p \end{bmatrix}, \tag{3.7}$$

where $\partial_t$ stands for the partial time derivative $\partial/\partial_t$, and $\mathbf{A}$ stands for the advection term

$$\mathbf{A}\mathbf{u} = (\mathbf{u}\cdot\nabla)\mathbf{u}. \tag{3.8}$$

### 3.1.2 Solid only

In vacuum (*i.e* neglecting all fluid interactions), we consider a linear behaviour of the three-dimensional rigid body motion presented in Figure 3.1. The three degree of freedom motion $(\chi, \psi, \theta)$ is hence governed by the linear expression

$$\begin{bmatrix} m & 0 & 0 \\ 0 & m & 0 \\ 0 & 0 & I_\theta \end{bmatrix} \begin{bmatrix} \ddot{\chi} \\ \ddot{\psi} \\ \ddot{\theta} \end{bmatrix} + \begin{bmatrix} c_\chi & 0 & 0 \\ 0 & c_\psi & 0 \\ 0 & 0 & c_\theta \end{bmatrix} \begin{bmatrix} \dot{\chi} \\ \dot{\psi} \\ \dot{\theta} \end{bmatrix} + \begin{bmatrix} k_\chi & 0 & 0 \\ 0 & k_\psi & 0 \\ 0 & 0 & k_\theta \end{bmatrix} \begin{bmatrix} \chi \\ \psi \\ \theta \end{bmatrix} = \begin{bmatrix} 0 \\ 0 \\ 0 \end{bmatrix}, \tag{3.9}$$

where $\dot{(\cdot)}$ indicates $\mathrm{d}/\mathrm{d}t$, $m$ and $I_\theta$ stands for the dimensionless mass and moment of inertia respectively, and $c_i$, $k_i$ for the dimensionless damping coefficients and stiffness (or spring constants) respectively in all directions of motion (*i.e.* $\chi$, $\psi$, $\theta$).
All structural quantities are described in Figure 4.6, and can be compactly re-written as

$$\mathbf{M}\ddot{\boldsymbol{\eta}} + \mathbf{C}\dot{\boldsymbol{\eta}} + \mathbf{K}\boldsymbol{\eta} = \mathbf{0}. \tag{3.10}$$

Equivalently, the second-order differential equation (3.10) can be rewritten as a system of first-order differential equations

$$\begin{cases} \dot{\boldsymbol{\eta}} - \boldsymbol{\zeta} & = \mathbf{0} \\ \mathbf{M}\dot{\boldsymbol{\zeta}} + \mathbf{C}\boldsymbol{\zeta} + \mathbf{K}\boldsymbol{\eta} & = \mathbf{0} \end{cases}, \tag{3.11}$$

where $\boldsymbol{\eta}$ and $\boldsymbol{\zeta}$ representing the spatial positions and velocities of the object respectively

$$\boldsymbol{\eta} = \begin{bmatrix} \chi \\ \psi \\ \theta \end{bmatrix}, \quad \boldsymbol{\zeta} = \begin{bmatrix} \dot{\chi} \\ \dot{\psi} \\ \dot{\theta} \end{bmatrix}.$$

### 3.1.3 Coupling

As initially stated in section §4.2.2, the fluid and solid system are coupled at the interface $\gamma$ through *kinematic* and *dynamic* boundary conditions.

1. The kinematic condition, which connects directly the velocities. No mixing nor slipping at the interface are considered so:
$$\mathbf{u}(\gamma) = \dot{\gamma}, \tag{3.12}$$
the fluid velocity is equal to the solid velocity at the interface.

2. The dynamic condition, which connects the forces. It results from the pressure and viscous forces from the fluid side, and the modal force on the solid side,
$$\begin{cases} \dot{\boldsymbol{\eta}} - \boldsymbol{\zeta} & = \mathbf{0} \\ \mathbf{M}\dot{\boldsymbol{\zeta}} + \mathbf{C}\boldsymbol{\zeta} + \mathbf{K}\boldsymbol{\eta} & = \mathbf{Fq} \end{cases}, \tag{3.13}$$
considering here the pressure and viscous forces from the fluid side $\mathbf{Fq} = [\mathfrak{f}_x \ \mathfrak{f}_y \ \mathfrak{m}_z]^T$ and where the aerodynamic forces $\mathfrak{F} = [\mathfrak{f}_x \ \mathfrak{f}_y]^T$ per unit span:
$$\begin{aligned} \mathfrak{F}(\mathbf{u}, p) &= \oint_\gamma \left\{ \left[ -p\mathbf{I} + Re^{-1} \left( \nabla\mathbf{u} + (\nabla\mathbf{u})^T \right) \right] \cdot \mathbf{n} \right\} \mathrm{d}l \\ \mathfrak{F}(\mathbf{u}, p) &= \oint_\gamma \{ \mathbf{fq} \cdot \mathbf{n} \} \mathrm{d}l, \\ \mathfrak{F}(\mathbf{u}, p) &= \oint_\gamma \{ \sigma \cdot \mathbf{n} \} \mathrm{d}l, \end{aligned} \tag{3.14}$$
where $\mathbf{I}$ represents the identity matrix, $\mathbf{n}$ the unit outward-pointing normal vector at the interface, $\mathbf{f}$ the stress operator, equivalently $\sigma = \mathbf{fq}$ is the stress tensor, and $\mathrm{d}l$ the infinitesimal arc-length of $\gamma$. The aerodynamic moment $\mathfrak{m}_z$ per unit span:
$$\begin{aligned} \mathfrak{m}_z(\mathbf{u}, p)\mathbf{k} &= \oint_\gamma \left\{ \mathbf{r} \times \left( \left[ -p\mathbf{I} + Re^{-1} \left( \nabla\mathbf{u} + (\nabla\mathbf{u})^T \right) \right] \cdot \mathbf{n} \right) \right\} \mathrm{d}l \\ \mathfrak{m}_z(\mathbf{u}, p)\mathbf{k} &= \oint_\gamma \{ \mathbf{r} \times (\mathbf{fq} \cdot \mathbf{n}) \} \mathrm{d}l, \\ \mathfrak{m}_z(\mathbf{u}, p)\mathbf{k} &= \oint_\gamma \{ \mathbf{r} \times (\sigma \cdot \mathbf{n}) \} \mathrm{d}l, \end{aligned} \tag{3.15}$$

where $\mathbf{k}$ is the unit vector along the $z$ direction orthogonal to the $x$-$y$ plane and $\mathbf{r}$ is the position vector from the hinge point to the boundary $\gamma$.

The structural motion governed by (3.13) is compactly rewritten in operator form in function of the state variables $\boldsymbol{\xi} = [\boldsymbol{\eta}\ \boldsymbol{\zeta}]^T$ and $\mathbf{q} = [\mathbf{u}\ p]^T$ as

$$\mathcal{S}\boldsymbol{\xi} - \mathcal{A}\mathbf{q} = \mathbf{0}, \tag{3.16}$$

where the aerodynamic forces and structural operators are respectively given by

$$\mathcal{A} = \left[\begin{array}{c} \mathbf{0} \\ \hline \mathbf{M}^{-1}\mathbf{F} \end{array}\right] \quad \text{and} \quad \mathcal{S} = \left[\begin{array}{c|c} -\mathbf{I}\partial_t & \mathbf{I} \\ \hline -\mathbf{M}^{-1}\mathbf{K} & -\mathbf{M}^{-1}\mathbf{C} - \mathbf{I}\partial_t \end{array}\right]. \tag{3.17}$$

### 3.1.4 Global operator

Finally, the coupled FSI problem can then be entirely rewritten compactly in operator form in terms of the governing $\mathcal{H}$ global operator, constituted of the fluid, aerodynamic forces and structural operators, and $\mathbf{s} = [\boldsymbol{\xi}\ \mathbf{q}]^T$ the global state variable as

$$\begin{aligned} \mathcal{H}\mathbf{s} &= \mathbf{0} \\ \Leftrightarrow \quad \left[\begin{array}{c|c} \mathcal{F} & \mathbf{0} \\ \hline \mathcal{A} & \mathcal{S} \end{array}\right] \left[\begin{array}{c} \mathbf{q} \\ \hline \boldsymbol{\xi} \end{array}\right] &= \mathbf{0}, \end{aligned} \tag{3.18a}$$

associated with the boundary condition on the internal boundary $\gamma$

$$\begin{cases} \mathbf{u} = \dot{\gamma} & \text{on } \gamma \\ \dfrac{\partial p}{\partial \mathbf{n}} = 0 & \text{on } \gamma \end{cases}. \tag{3.18b}$$

Note that the pressure boundary condition on the wall is natural in the sense that the pressure on both sides of the interface (*i.e.* internal and external) is assumed to be locally balanced. In the present study, the interface does not locally deform under the action of the flow, and hence the approximation of the boundary condition is verified.
Finally, prescribing on the external boundaries the flow inlet and outlet respectively, $\partial\Omega^{ext}_{in}$ and $\partial\Omega^{ext}_{out}$:

$$\begin{cases} \mathbf{u} = \mathbf{u}_\infty & \text{on } \partial\Omega^{ext}_{in} \\ \dfrac{\partial p}{\partial \mathbf{n}} = 0 & \text{on } \partial\Omega^{ext}_{in} \end{cases} \quad \text{and,} \quad \begin{cases} \dfrac{\partial \mathbf{u}}{\partial \mathbf{n}} = \mathbf{0} & \text{on } \partial\Omega^{ext}_{out} \\ p = 0 & \text{on } \partial\Omega^{ext}_{out} \end{cases}. \tag{3.18c}$$

In the following sub-sections, the direct (*i.e* linearised) and adjoint operators of $\mathcal{H}$ are sought, and the governing systems are consistently expressed in operator form (*i.e.* respectively $\mathcal{H}'$ and

$\mathcal{H}^{\dagger}$).

## 3.2 Direct operator

In this section, the description of a linear operator $\mathcal{H}'$ of $\mathcal{H}$ referenced in this work as the *direct* operator is sought. Hence the interest is in studying the system's linear behaviour around a particular solution of the system (3.18), considered as the base state.
The general approach follows the idea that the global operator $\mathcal{H}$ in equation (3.18a) is expanded in the neighbourhood of a base state $\mathbf{s}_0$, considering the state variable $\mathbf{s}$, by introducing a small perturbation to both fluid and solid motions

$$\mathbf{s} = \mathbf{s}_0 + \varepsilon_1 \mathbf{s}' \quad \Leftrightarrow \quad \begin{cases} \mathbf{q} = \mathbf{q}_0 + \varepsilon_1 \mathbf{q}' \\ \boldsymbol{\xi} = \boldsymbol{\xi}_0 + \varepsilon_1 \boldsymbol{\xi}' \end{cases} \qquad \text{with} \quad \varepsilon_1 \ll 1, \tag{3.19}$$

and the direct (*i.e* differential) operator $\mathcal{H}' = \mathrm{d}\mathcal{H}_{\mathbf{s}_0}$ is made explicit following the Taylor-Young formula

$$\mathcal{H}\left(\mathbf{s}_0 + \varepsilon_1 \mathbf{s}'\right) = \mathcal{H}\left(\mathbf{s}_0\right) + \varepsilon_1 \mathrm{d}\mathcal{H}_{\mathbf{s}_0}\left(\mathbf{s}'\right) + o(\parallel \varepsilon_1 \mathbf{s}' \parallel^2), \tag{3.20}$$

where $\mathrm{d}\mathcal{H}_{\mathbf{s}_0}$ is the differential of $\mathcal{H}$ in the neighbourhood of the base state $\mathbf{s}_0$.
However, because the global system behaves like two independent systems (fluid and solid) coupled at the interface by a special condition, extra care is needed at this interface to express the total first-order contribution. Indeed, the neighbourhood of a fluid quantity at a particular location needs to be evaluated in the neighbourhood of this particular location.
In the following sections, the operators $\mathcal{F}$ and $\mathcal{S}$ are independently linearised and combined through the kinematic and dynamic boundary conditions.

### 3.2.1 Fluid only

The linearisation of the incompressible Navier-Stokes equations is part of the most straightforward and can directly be obtained applying the Taylor-Young formula to the equation (3.7) without any other considerations. Mathematically,

$$\mathbf{q} = \mathbf{q}_0 + \varepsilon_1 \mathbf{q}' \quad \Leftrightarrow \quad \begin{cases} \mathbf{u} = \mathbf{u}_0 + \varepsilon_1 \mathbf{u}' \\ p = p_0 + \varepsilon_1 p' \end{cases} . \tag{3.21}$$

In the neighbourhood of the base flow $\mathbf{q}_0$ it follows $\mathcal{F}'$ according to

$$\mathcal{F}\left(\mathbf{q}_0 + \varepsilon_1 \mathbf{q}'\right) = \mathcal{F}\left(\mathbf{q}_0\right) + \varepsilon_1 \mathrm{d}\mathcal{F}_{\mathbf{q}_0}\left(\mathbf{q}'\right) + o\left(\parallel \varepsilon_1 \mathbf{q}' \parallel^2\right), \tag{3.22}$$

and the Navier-Stokes equations can be written in terms proportionals to $\varepsilon_1$:

- At $o(1)$:

$$\begin{cases} \dfrac{\partial \mathbf{u}_0}{\partial t} + (\mathbf{u}_0 \cdot \nabla)\mathbf{u}_0 = -\nabla p_0 + Re^{-1}\nabla^2 \mathbf{u}_0 & \text{in } \Omega \\ \nabla \cdot \mathbf{u}_0 = 0 & \text{in } \Omega \end{cases}. \tag{3.23}$$

- At $o(\varepsilon_1)$:

$$\begin{cases} \dfrac{\partial \mathbf{u}'}{\partial t} + (\mathbf{u}' \cdot \nabla)\mathbf{u}_0 + (\mathbf{u}_0 \cdot \nabla)\mathbf{u}' = -\nabla p' + Re^{-1}\nabla^2 \mathbf{u}' & \text{in } \Omega \\ \nabla \cdot \mathbf{u}' = 0 & \text{in } \Omega \end{cases}. \tag{3.24}$$

Finally, in operator form, the fluid direct operator reads

$$\mathcal{F}'\mathbf{q}' = \mathbf{0} \quad \text{where} \quad \mathcal{F}' = \left[\begin{array}{c|c} -\partial_t - \mathbf{A}' + Re^{-1}\nabla^2 & -\nabla \\ \hline \nabla\cdot & 0 \end{array}\right], \tag{3.25}$$

where $\mathbf{A}'$ stands for the linearised advection term:

$$\mathbf{A}'\mathbf{u}' = (\mathbf{u}' \cdot \nabla)\mathbf{u}_0 + (\mathbf{u}_0 \cdot \nabla)\mathbf{u}'. \tag{3.26}$$

### 3.2.2 Solid only

In the context studied in this work, the structural equations are already considered linear, hence the linearisation process is particularly unambiguous in that case.
After introducing a small perturbation to the structural variables, the change in position reads

$$\begin{cases} \boldsymbol{\eta} = \boldsymbol{\eta}_0 + \varepsilon_1 \boldsymbol{\eta}' \\ \boldsymbol{\zeta} = \boldsymbol{\zeta}_0 + \varepsilon_1 \boldsymbol{\zeta}' \end{cases} \quad \Rightarrow \quad \begin{cases} \chi = \chi_0 + \varepsilon_1 \chi' \\ \psi = \psi_0 + \varepsilon_1 \psi' \\ \theta = \theta_0 + \varepsilon_1 \theta' \end{cases}. \tag{3.27}$$

In the neighbourhood of the structural position and velocity at rest (structural base state) $\boldsymbol{\xi}_0$ one obtain $\mathcal{S}'$ following

$$\mathcal{S}\left(\boldsymbol{\xi}_0 + \varepsilon_1 \boldsymbol{\xi}'\right) = \mathcal{S}\left(\boldsymbol{\xi}_0\right) + \varepsilon_1 \mathrm{d}\mathcal{S}_{\boldsymbol{\xi}_0}\left(\boldsymbol{\xi}'\right) + o\left(\| \varepsilon_1 \boldsymbol{\xi}' \|^2\right). \tag{3.28}$$

The linearisation of the linear structural operator (3.17) is straightforward, and leads to

$$\mathcal{S}' = \mathcal{S}. \tag{3.29}$$

### 3.2.3 Coupling

In the linearisation process, most of the attention needs to be put into the coupling of the operators $\mathcal{F}'$ and $\mathcal{S}'$. Indeed, applying the kinematic boundary condition will determine the actual boundary conditions at the interface $\gamma$ of the coupled linearised problem (see 1. below), whereas applying the dynamic boundary condition will determine the resulting linearised counterpart operator $\mathcal{A}'$ of $\mathcal{A}$ (see 2. below).

1. The kinematic boundary condition: this condition is applied to the moving boundary expression, initially given by equation (3.5), and is here evaluated at the expansion in the neighbourhood of the structural position $\boldsymbol{\eta}_0 = [\chi_0 \ \psi_0 \ \theta_0]^T$ as

$$\begin{aligned}
\gamma &= \mathcal{T}\left(\boldsymbol{\eta}_0 + \varepsilon_1 \boldsymbol{\eta}'\right)\Gamma \\
&= \left(\mathcal{T}\left(\boldsymbol{\eta}\right)|_{\boldsymbol{\eta}=\boldsymbol{\eta}_0} + \varepsilon_1 \mathrm{d}\mathcal{T}_{\boldsymbol{\eta}_0}\left(\boldsymbol{\eta}\right) + o\left(\| \ \varepsilon_1 \boldsymbol{\eta}' \ \|^2\right)\right)\Gamma \\
&= \mathcal{T}\left(\boldsymbol{\eta}_0\right)\Gamma + \varepsilon_1 \left(\boldsymbol{\eta}' \cdot \nabla_{\boldsymbol{\eta}} \, \mathcal{T}\left(\boldsymbol{\eta}\right)|_{\boldsymbol{\eta}=\boldsymbol{\eta}_0}\right)\Gamma + o\left(\| \ \varepsilon_1 \boldsymbol{\eta}' \ \|^2\right) \\
&= \mathcal{T}\left(\boldsymbol{\eta}_0\right)\Gamma + \varepsilon_1 \left(\chi' \left.\frac{\partial \mathcal{T}\left(\boldsymbol{\eta}\right)}{\partial \chi}\right|_{\boldsymbol{\eta}=\boldsymbol{\eta}_0} + \psi' \left.\frac{\partial \mathcal{T}\left(\boldsymbol{\eta}\right)}{\partial \psi}\right|_{\boldsymbol{\eta}=\boldsymbol{\eta}_0} + \theta' \left.\frac{\partial \mathcal{T}\left(\boldsymbol{\eta}\right)}{\partial \theta}\right|_{\boldsymbol{\eta}=\boldsymbol{\eta}_0}\right)\Gamma + o\left(\| \ \varepsilon_1 \boldsymbol{\eta}' \ \|^2\right) \\
\gamma &= \Gamma + \varepsilon_1 \left(\chi' \delta_\chi + \psi' \delta_\psi + \theta' \delta_\theta\right)\Gamma + o\left(\| \ \varepsilon_1 \boldsymbol{\eta}' \ \|^2\right), \qquad (3.30)
\end{aligned}$$

where for clarity, the following variables are introduced

$$\nabla_{\boldsymbol{\eta}} = \begin{bmatrix} \frac{\partial}{\partial \chi} \\ \frac{\partial}{\partial \psi} \\ \frac{\partial}{\partial \theta} \end{bmatrix}; \quad \delta_\chi = \begin{bmatrix} 0 & 0 & 1 \\ 0 & 0 & 0 \\ 0 & 0 & 1 \end{bmatrix}; \quad \delta_\psi = \begin{bmatrix} 0 & 0 & 0 \\ 0 & 0 & 1 \\ 0 & 0 & 1 \end{bmatrix}; \quad \delta_\theta = \begin{bmatrix} 0 & -1 & 0 \\ 1 & 0 & 0 \\ 0 & 0 & 1 \end{bmatrix}, \qquad (3.31)$$

and where the structural position at rest is considered as $\boldsymbol{\eta}_0 = [0 \ 0 \ 0]^T$. It is also noted that the coordinator of the system is kept set to 1 in a matter of mathematical consistency.
Equation (3.30) hence describes the linearised displacement of the body after a small perturbation.
Now, at the solid interface boundary $\gamma$, the fluid velocity reads (further injecting the expression (3.30) into the expression (3.32)):

$$\begin{aligned}
\mathbf{u}(\gamma) &= \mathbf{u}_0(\gamma) + \varepsilon_1 \mathbf{u}'(\gamma) \\
&= \mathbf{u}_0\left(\Gamma + \varepsilon_1 \mathrm{d}\mathcal{T}_{\boldsymbol{\eta}_0}\left(\boldsymbol{\eta}\right)\Gamma\right) + \varepsilon_1 \mathbf{u}'\left(\Gamma + \varepsilon_1 \mathrm{d}\mathcal{T}_{\boldsymbol{\eta}_0}\left(\boldsymbol{\eta}\right)\Gamma\right) \\
&= \mathbf{u}_0\left(\Gamma\right) + \varepsilon_1 \mathrm{d}\mathbf{u}_{0\Gamma}\left(\mathrm{d}\mathcal{T}_{\boldsymbol{\eta}_0}\left(\boldsymbol{\eta}\right)\Gamma\right) + \varepsilon_1 \mathbf{u}'\left(\Gamma\right) + \varepsilon_1^2 \mathrm{d}\mathbf{u}'_\Gamma\left(\mathrm{d}\mathcal{T}_{\boldsymbol{\eta}_0}\left(\boldsymbol{\eta}\right)\Gamma\right) \qquad (3.32) \\
\mathbf{u}(\gamma) &= \mathbf{u}_0(\Gamma) + \varepsilon_1 \left(\chi' \delta_\chi + \psi' \delta_\psi + \theta' \delta_\theta\right)\Gamma \cdot \nabla \mathbf{u}_0(\Gamma) + \varepsilon_1 \mathbf{u}'(\Gamma) + o\left(\| \ \varepsilon_1 \left(\mathrm{d}\mathcal{T}_{\boldsymbol{\eta}_0}\left(\boldsymbol{\eta}\right)\Gamma\right) \ \|^2\right). \qquad (3.33)
\end{aligned}$$

For ease of notation, the matrix $\boldsymbol{\Delta}$ that contains the quantities (vectors) $\delta_\chi\Gamma$, $\delta_\psi\Gamma$, and

$\delta_\theta\Gamma$ is defined as

$$\begin{aligned}\boldsymbol{\Delta} &= \begin{bmatrix}\delta_\chi\Gamma & \delta_\psi\Gamma & \delta_\theta\Gamma\end{bmatrix} \\ &= \begin{bmatrix}1 & 0 & -y \\ 0 & 1 & x \\ 1 & 1 & 1\end{bmatrix},\end{aligned} \tag{3.34}$$

such as (3.33) finally reads:

$$\mathbf{u}(\gamma) = \mathbf{u}_0(\Gamma) + \varepsilon_1\boldsymbol{\Delta}\boldsymbol{\eta}' \cdot \nabla\mathbf{u}_0(\Gamma) + \varepsilon_1\mathbf{u}'(\Gamma) + \mathcal{O}\left(\varepsilon_1^2\right), \tag{3.35}$$

in which for ease of notation, the terms of higher order are regrouped into the notation $\mathcal{O}\left(\varepsilon_1^2\right)$.
Note that we equivalently obtain the general expression of the total fluid field $\mathbf{q} = [\mathbf{u}\ p]^T$ at the interface as

$$\begin{aligned}\mathbf{q}(\gamma) &= \mathbf{q}_0(\Gamma) + \varepsilon_1\boldsymbol{\Delta}\boldsymbol{\eta}' \cdot \nabla\mathbf{q}_0(\Gamma) + \varepsilon_1\mathbf{q}'(\Gamma) + \mathcal{O}\left(\varepsilon_1^2\right) \\ \Leftrightarrow \quad \mathbf{q}(\gamma) &= \mathbf{q}_0(\Gamma) + \varepsilon_1\tilde{\mathbf{q}}(\Gamma) + \mathcal{O}\left(\varepsilon_1^2\right),\end{aligned} \tag{3.36}$$

in which the quantity $\tilde{\mathbf{q}} = \boldsymbol{\Delta}\boldsymbol{\eta}' \cdot \nabla\mathbf{q}_0 + \mathbf{q}'$ corresponds to the total first order (or perturbed) fluid variable defined as the sum of a base flow contribution and the initial perturbed quantity (*i.e.* $\mathbf{q}'$).
In order to apply the kinematic boundary condition to (3.35), such as the velocity at the boundary must match the velocity of the boundary, the velocity of the interface $\dot{\gamma}$ must be made explicit. This is achieved by deriving the linearised structural position expression (3.30) with regard to the time $t$ as

$$\begin{aligned}\frac{\partial\gamma}{\partial t} &= \frac{\partial\Gamma}{\partial t} + \varepsilon_1\frac{\partial}{\partial t}\left[\left(\chi'\delta_\chi + \psi'\delta_\psi + \theta'\delta_\theta\right)\Gamma\right] \\ \dot{\gamma} &= \dot{\Gamma} + \varepsilon_1\left(\dot{\chi}'\delta_\chi + \dot{\psi}'\delta_\psi + \dot{\theta}'\delta_\theta\right)\Gamma + \varepsilon_1\left(\chi'\delta_\chi + \psi'\delta_\psi + \theta'\delta_\theta\right)\dot{\Gamma} \\ \dot{\gamma} &= \dot{\Gamma} + \varepsilon_1\boldsymbol{\Delta}\boldsymbol{\zeta}' + \varepsilon_1\left(\chi'\delta_\chi + \psi'\delta_\psi + \theta'\delta_\theta\right)\dot{\Gamma}.\end{aligned} \tag{3.37}$$

As a consequence, the kinematic boundary condition initially presented in equation (3.12) finally reads (combining the expressions (3.35) and (3.37) and neglecting the non-linear terms)

$$\begin{aligned}\mathbf{u}(\gamma) &= \dot{\gamma} \\ \Leftrightarrow \quad \mathbf{u}_0(\Gamma) + \varepsilon_1\boldsymbol{\Delta}\boldsymbol{\eta}' \cdot \nabla\mathbf{u}_0(\Gamma) + \varepsilon_1\mathbf{u}'(\Gamma) &= \dot{\Gamma} + \varepsilon_1\boldsymbol{\Delta}\boldsymbol{\zeta}' + \varepsilon_1\left(\chi'\delta_\chi + \psi'\delta_\psi + \theta'\delta_\theta\right)\dot{\Gamma}.\end{aligned} \tag{3.38}$$

Thus, decomposing the expression of the fluid velocity at the solid interface (3.38) into terms proportional to $\varepsilon_1$ and neglecting a base state structural motion gives

- At $\mathcal{O}(1)$:

$$\mathbf{u}_0(\Gamma) = \dot{\Gamma} = 0, \tag{3.39}$$

- At $\mathcal{O}(\varepsilon_1)$:

$$\begin{aligned} \boldsymbol{\Delta\eta}' \cdot \nabla \mathbf{u}_0(\Gamma) + \mathbf{u}'(\Gamma) &= \boldsymbol{\Delta\zeta}' \\ \Rightarrow \quad \mathbf{u}'(\Gamma) &= \boldsymbol{\Delta\zeta}' - (\boldsymbol{\Delta} \cdot \nabla \mathbf{u}_0(\Gamma))\, \boldsymbol{\eta}'. \end{aligned} \tag{3.40}$$

The expression of the perturbed fluid variable $\mathbf{u}'$ is hence finally obtained at the solid boundary in the expression (3.40) as a function of the perturbed structural positions $\boldsymbol{\eta}'$ and velocities $\boldsymbol{\zeta}'$ as well as the base flow gradient evaluated at the non-perturbed interface.

2. The dynamic boundary condition: considering both the total first-order contribution of fluid and structural quantities involved in the evaluation of the aerodynamic forces and moments

$$\begin{cases} \mathbf{q} = \mathbf{q}_0 + \varepsilon_1 \tilde{\mathbf{q}} \\ \mathbf{r} = \mathbf{r}_0 + \varepsilon_1 \mathbf{r}' \\ \mathbf{n} = \mathbf{n}_0 + \varepsilon_1 \mathbf{n}' \end{cases}. \tag{3.41}$$

Injecting the quantities (3.41) into the expressions of the aerodynamic forces and moments given by the expressions (3.14) and (3.15) leads to

$$\begin{aligned} \mathfrak{F}\left(\mathbf{q}_0 + \varepsilon_1 \tilde{\mathbf{q}}\right) &= \oint_\gamma \left\{\mathbf{f}\left(\mathbf{q}_0 + \varepsilon_1 \tilde{\mathbf{q}}\right) \cdot \left(\mathbf{n}_0 + \varepsilon_1 \mathbf{n}'\right)\right\} \mathrm{d}l \\ \mathfrak{m}_z\left(\mathbf{q}_0 + \varepsilon_1 \tilde{\mathbf{q}}\right) \mathbf{k} &= \oint_\gamma \left\{\left(\mathbf{r}_0 + \varepsilon_1 \mathbf{r}'\right) \times \left(\mathbf{f}\left(\mathbf{q}_0 + \varepsilon_1 \tilde{\mathbf{q}}\right) \cdot \left(\mathbf{n}_0 + \varepsilon_1 \mathbf{n}'\right)\right)\right\} \mathrm{d}l, \end{aligned}$$

thus by linearity of the operator $\mathbf{f}$, the expressions involving the terms proportional to $\varepsilon_1$ are easily obtained as

- At $\mathcal{O}(1)$:

$$\begin{aligned} \mathfrak{F}\left(\mathbf{q}\right) &= \oint_\gamma \left\{\mathbf{f}\mathbf{q}_0 \cdot \mathbf{n}_0\right\} \mathrm{d}l \\ \mathfrak{m}_z(\mathbf{q})\mathbf{k} &= \oint_\gamma \left\{\mathbf{r}_0 \times \left(\mathbf{f}\mathbf{q}_0 \cdot \mathbf{n}_0\right)\right\} \mathrm{d}l. \end{aligned}$$

- At $\mathcal{O}(\varepsilon_1)$:

$$\mathfrak{F}(\mathbf{q}) = \oint_\gamma \{(\mathbf{f}\mathbf{q}_0 \cdot \mathbf{n}') + (\mathbf{f}\tilde{\mathbf{q}} \cdot \mathbf{n}_0)\}\mathrm{d}l \tag{3.42}$$

$$\mathfrak{m}_z(\mathbf{q})\mathbf{k} = \oint_\gamma \{\mathbf{r}' \times (\mathbf{f}\mathbf{q}_0 \cdot \mathbf{n}_0) + \mathbf{r}_0 \times (\mathbf{f}\mathbf{q}_0 \cdot \mathbf{n}') + \mathbf{r}_0 \times (\mathbf{f}\tilde{\mathbf{q}} \cdot \mathbf{n}_0)\}\mathrm{d}l, \tag{3.43}$$

or in full,

$$\mathfrak{F}(\mathbf{q}) = \oint_\gamma \{(\mathbf{f}\mathbf{q}_0 \cdot \mathbf{n}') + (\mathbf{f}\,(\boldsymbol{\Delta\eta}' \cdot \nabla\mathbf{q}_0) \cdot \mathbf{n}_0) + (\mathbf{f}\mathbf{q}' \cdot \mathbf{n}_0)\}\mathrm{d}l$$

$$\mathfrak{m}_z(\mathbf{q})\mathbf{k} = \oint_\gamma \left\{ \underbrace{\mathbf{r}' \times (\mathbf{f}\mathbf{q}_0 \cdot \mathbf{n}_0) + \mathbf{r}_0 \times [(\mathbf{f}\mathbf{q}_0 \cdot \mathbf{n}')}_{\textit{geometric contribution}} + \underbrace{(\mathbf{f}\,(\boldsymbol{\Delta\eta}' \cdot \nabla\mathbf{q}_0) \cdot \mathbf{n}_0)}_{\textit{base flow contribution}} + (\mathbf{f}\mathbf{q}' \cdot \mathbf{n}_0)] \right\}\mathrm{d}l.$$

Finally, expressions (3.42) and (3.43) represent the general first-order expressions for the force and moment in the perturbed space.

It is noted that in the above equation, the term $\boldsymbol{\Delta\eta}' \cdot \nabla\mathbf{q}_0 = \hat{\mathbf{q}}$ written in full reads

$$\boldsymbol{\Delta\eta}' \cdot \nabla\mathbf{q}_0 = \begin{bmatrix} \hat{u} \\ \hat{v} \\ \hat{p} \end{bmatrix} = \begin{bmatrix} \chi' - \theta' y \\ \psi + \theta' x \end{bmatrix} \cdot \begin{bmatrix} \dfrac{\partial u_0}{\partial x} & \dfrac{\partial v_0}{\partial x} & \dfrac{\partial p_0}{\partial x} \\ \dfrac{\partial u_0}{\partial y} & \dfrac{\partial v_0}{\partial y} & \dfrac{\partial p_0}{\partial y} \end{bmatrix}$$

$$\Leftrightarrow \quad \begin{bmatrix} \hat{u} \\ \hat{v} \\ \hat{p} \end{bmatrix} = \chi' \begin{bmatrix} \dfrac{\partial u_0}{\partial x} \\ \dfrac{\partial v_0}{\partial x} \\ \dfrac{\partial p_0}{\partial x} \end{bmatrix} + \psi' \begin{bmatrix} \dfrac{\partial u_0}{\partial y} \\ \dfrac{\partial v_0}{\partial y} \\ \dfrac{\partial p_0}{\partial y} \end{bmatrix} + \theta' \begin{bmatrix} -y\dfrac{\partial u_0}{\partial x} + x\dfrac{\partial u_0}{\partial y} \\ -y\dfrac{\partial v_0}{\partial x} + x\dfrac{\partial v_0}{\partial y} \\ -y\dfrac{\partial p_0}{\partial x} + x\dfrac{\partial p_0}{\partial y} \end{bmatrix}$$

$$\Leftrightarrow \quad \begin{bmatrix} \hat{u} \\ \hat{v} \\ \hat{p} \end{bmatrix} = \chi' \begin{bmatrix} \hat{u}^\chi \\ \hat{v}^\chi \\ \hat{p}^\chi \end{bmatrix} + \psi' \begin{bmatrix} \hat{u}^\psi \\ \hat{v}^\psi \\ \hat{p}^\psi \end{bmatrix} + \theta' \begin{bmatrix} \hat{u}^\theta \\ \hat{v}^\theta \\ \hat{p}^\theta \end{bmatrix},$$

hence can finally be expressed as

$$\hat{\mathbf{q}} = \chi'\hat{\mathbf{q}}^\chi + \psi'\hat{\mathbf{q}}^\psi + \theta'\hat{\mathbf{q}}^\theta, \tag{3.44}$$

and can equivalently be decomposed into the forces and moment expressions

$$\begin{bmatrix} \mathfrak{F}^0 \\ \mathfrak{m}_z^0 \end{bmatrix} = \chi' \begin{bmatrix} \oint_\gamma (\mathbf{f}\hat{\mathbf{q}}^\chi \cdot \mathbf{n}_0)\mathrm{d}l \\ \oint_\gamma (\mathbf{r}_0 \times \mathbf{f}\hat{\mathbf{q}}^\chi \cdot \mathbf{n}_0)\mathrm{d}l \end{bmatrix} + \psi' \begin{bmatrix} \oint_\gamma (\mathbf{f}\hat{\mathbf{q}}^\psi \cdot \mathbf{n}_0)\mathrm{d}l \\ \oint_\gamma (\mathbf{r}_0 \times \mathbf{f}\hat{\mathbf{q}}^\psi \cdot \mathbf{n}_0)\mathrm{d}l \end{bmatrix} + \theta' \begin{bmatrix} \oint_\gamma (\mathbf{f}\hat{\mathbf{q}}^\theta \cdot \mathbf{n}_0)\mathrm{d}l \\ \oint_\gamma \mathbf{r}_0 \times (\mathbf{f}\hat{\mathbf{q}}^\theta \cdot \mathbf{n}_0)\mathrm{d}l \end{bmatrix},$$

where $\mathfrak{F}^0$ and $\mathfrak{m}_z^0$ stands for the forces and moments induced by the base flow contributions respectively, the last expression can finally be compactly rewritten as

$$\begin{bmatrix} \mathfrak{f}_x^0 \\ \mathfrak{f}_y^0 \\ \mathfrak{m}_z^0 \end{bmatrix} = \begin{bmatrix} k_x^\chi & k_x^\psi & k_x^\theta \\ k_y^\chi & k_y^\psi & k_y^\theta \\ k_z^\chi & k_z^\psi & k_z^\theta \end{bmatrix} \begin{bmatrix} \chi' \\ \psi' \\ \theta' \end{bmatrix}. \tag{3.45}$$

Thus the base flow contribution on the aerodynamic forces and moment can be interpreted as an added stiffness term which should be added to the structural stiffness matrix $\mathbf{K}$ of the linearised operator $\mathcal{S}'$ in the expression (3.29). By doing so, the total first-order aerodynamic forces and moment can be evaluated, taking into account the perturbed field $\mathbf{q}'$ and the geometric contribution only.

The expression (3.45) is the general form of the added stiffness term in the case of a three-dimensional structural motion. In the simplified case of one-dimensional motion in either in-line, cross-flow or rotation direction, the matrix in expression (3.45) reduces to a unique scalar corresponding the diagonal terms of the matrix in the expression (3.45) and respectively reads $k_x^\psi$, $k_y^\psi$ or $k_z^\theta$.

It has recently been shown that the contribution of the added stiffness originating from the base flow stress and the geometrical change by the rotation of the cylinder is analytically zero (Negi et al., 2020), and it have been made the same observation numerically in the present study. Therefore, both the base flow and geometric contributions to the linearised forces and moment are not considered further in the following sections. Hence no approximations of the quantities $\mathbf{r}'$ and $\mathbf{n}'$ have been made in the presented results.

### 3.2.4 Global operator

The global direct operator $\mathcal{H}'$ governing the system is further written in operator form, combining the results from the sections above and reads

$$\begin{aligned} \mathcal{H}'\mathbf{s}' &= \mathbf{0} \\ \Leftrightarrow \quad \left[\begin{array}{c|c} \mathcal{F}' & \mathbf{0} \\ \hline \mathcal{A} & \mathcal{S} \end{array}\right] \begin{bmatrix} \mathbf{q}' \\ \boldsymbol{\xi}' \end{bmatrix} &= \mathbf{0}. \end{aligned} \tag{3.46a}$$

It is noted that the global direct operator $\mathcal{H}'$ only differs from $\mathcal{H}$ by the expression of $\mathcal{F}'$ (*i.e* the linearised advection term $\mathbf{A}$' replacing the non-linear advection term $\mathbf{A}$), and the complexity ultimately appears in the boundary conditions at the fluid-structure interface $\gamma$, where the coupling compactly reads

$$\begin{cases} \mathbf{u}' = \mathbf{B}\boldsymbol{\xi}' \\ \dfrac{\partial p'}{\partial \mathbf{n}_0} = 0 \end{cases}, \tag{3.46b}$$

and where $\mathbf{B}$ stands for the direct boundary terms at the interface, involving a general three degree of freedom structural motion

$$\begin{aligned}
\mathbf{B} &= \begin{bmatrix} -\delta_\chi \Gamma \cdot \nabla \mathbf{u}_0 & -\delta_\psi \Gamma \cdot \nabla \mathbf{u}_0 & -\delta_\theta \Gamma \cdot \nabla \mathbf{u}_0 & \delta_\chi \Gamma & \delta_\psi \Gamma & \delta_\theta \Gamma \end{bmatrix} \\
&= \begin{bmatrix} -\dfrac{\partial u_0}{\partial x} & -\dfrac{\partial u_0}{\partial y} & y\dfrac{\partial u_0}{\partial x} - x\dfrac{\partial u_0}{\partial y} & 1 & 0 & -y \\ -\dfrac{\partial v_0}{\partial x} & -\dfrac{\partial v_0}{\partial y} & y\dfrac{\partial v_0}{\partial x} - x\dfrac{\partial v_0}{\partial y} & 0 & 1 & x \\ 1 & 1 & 1 & 1 & 1 & 1 \end{bmatrix} \\
\mathbf{B} &= \begin{bmatrix} -\boldsymbol{\Delta} \cdot \nabla \mathbf{u}_0 & \boldsymbol{\Delta} \end{bmatrix}. \qquad (3.47)
\end{aligned}$$

Finally, prescribing on the external boundaries inlet and outlet, respectively: $\partial\Omega_{in}^{ext}$ and $\partial\Omega_{out}^{ext}$

$$\begin{cases} \mathbf{u}' = \mathbf{0} & \text{on } \partial\Omega_{in}^{ext} \\ \dfrac{\partial p'}{\partial \mathbf{n}} = 0 & \text{on } \partial\Omega_{in}^{ext} \end{cases} \quad \text{and,} \quad \begin{cases} \dfrac{\partial \mathbf{u}'}{\partial \mathbf{n}} = \mathbf{0} & \text{on } \partial\Omega_{out}^{ext} \\ p' = 0 & \text{on } \partial\Omega_{out}^{ext} \end{cases}.$$

The direct boundary term $\mathbf{B}$ in expression (3.47) can eventually be seen as the sum of the contributions of each transformation $\mathcal{T}_\chi, \mathcal{T}_\psi$, and $\mathcal{R}$ considered independently, which makes it easily split when investigating the response of a system of one or two structural degrees of freedom only.

## 3.3 Adjoint operator

### 3.3.1 Inner product

Formally, the inner product in the present study is defined for two arbitrary global state variables $\mathbf{s}_1 = [\mathbf{q}_1 \ \boldsymbol{\xi}_1]^T$ and $\mathbf{s}_2 = [\mathbf{q}_2 \ \boldsymbol{\xi}_2]^T$, such that

$$\begin{aligned}
\langle \mathbf{s}_1, \mathbf{s}_2 \rangle &= \langle \mathbf{q}_1, \mathbf{q}_2 \rangle_F + \langle \boldsymbol{\xi}_1, \boldsymbol{\xi}_2 \rangle_S \\
&= \int_0^\tau \left[ \int_\Omega \left( \mathbf{q}_1^H \mathbf{W}_F \mathbf{q}_2 \right) \mathrm{d}\mathbf{x} + \boldsymbol{\xi}_1^H \mathbf{W}_S \boldsymbol{\xi}_2 \right] \mathrm{d}t, \qquad (3.48a)
\end{aligned}$$

where the superscript $(\cdot)^H$ indicates the complex conjugate transpose, the subscripts $_F$ and $_S$ indicate the quantities related to fluid and structure, respectively, and $\tau$ represents the time horizon of the integration. The weight matrices are given by

$$\mathbf{W}_F = \begin{bmatrix} \mathbf{I} & 0 \\ 0 & 0 \end{bmatrix}, \quad \mathbf{W}_S = \begin{bmatrix} \mathbf{K} & 0 \\ 0 & \mathbf{M} \end{bmatrix}, \qquad (3.48b)$$

where $\mathbf{I}$ is the identity matrix in $\mathbb{R}^{2\times 2}$. For clarity, however, the time integration in the inner product definition (3.48a) is dropped without any consequence on the presented results in the rest of the study, and the appropriate boundary conditions induced by the time integration in the inner product (3.48a) are presented in Appendix §A.
The choice of this inner product is made so that the corresponding norm physically represents the total energy of the given fluid-structure system (omitting the time integration):

$$\begin{aligned} \|\mathbf{s}\|^2 = \langle \mathbf{s}, \mathbf{s} \rangle &= \int_\Omega \left( \mathbf{q}^H \mathbf{W}_F \mathbf{q} \right) \mathrm{d}\mathbf{x} + \boldsymbol{\xi}^H \mathbf{W}_S \boldsymbol{\xi} \\ &= \int_\Omega \left( \bar{\mathbf{u}} \cdot \mathbf{u} \right) \mathrm{d}\mathbf{x} + \boldsymbol{\zeta}^H \mathbf{M} \boldsymbol{\zeta} + \boldsymbol{\eta}^H \mathbf{K} \boldsymbol{\eta} \\ &= 2 \left( E_{k,F} + E_{k,S} + E_{p,S} \right), \end{aligned}$$

where $E_{k,F}$, $E_{k,S}$ and $E_{p,S}$ are the dimensionless fluid kinetic energy, structural kinetic energy and structural spring-potential energy, respectively.

### 3.3.2 Global operator

In contrast to the non-linear $\mathcal{H}$ and direct operators $\mathcal{H}'$ presented above, the adjoint operator $\mathcal{H}^\dagger$ do not directly result from a reasoning based on physical assumptions but rather by the following expression involving the inner product (3.48a):

$$\left\langle \mathcal{H}' \mathbf{s}', \mathbf{s}^\dagger \right\rangle = \left\langle \mathbf{s}', \mathcal{H}^\dagger \mathbf{s}^\dagger \right\rangle + \mathcal{B}\left( \mathbf{s}', \mathbf{s}^\dagger \right), \tag{3.49}$$

and the adjoint boundary conditions are obtained by enforcing the bilinear concomitant in expression (3.49) to be zero: *i.e.*

$$\mathcal{B}\left( \mathbf{s}', \mathbf{s}^\dagger \right) = \mathbf{0}. \tag{3.50}$$

To do so, it is first considered the adjoint variables $\mathbf{s}^\dagger$, *i.e.* respectively

$$\mathbf{s}^\dagger = \begin{bmatrix} \mathbf{q}^\dagger \\ \boldsymbol{\xi}^\dagger \end{bmatrix}, \quad \text{where:} \quad \mathbf{q}^\dagger = \begin{bmatrix} \mathbf{u}^\dagger \\ p^\dagger \end{bmatrix} \quad \text{and} \quad \boldsymbol{\xi}^\dagger = \begin{bmatrix} \boldsymbol{\eta}^\dagger \\ \boldsymbol{\zeta}^\dagger \end{bmatrix}.$$

Expanding the adjoint definition given by the expression (3.49) using the expression of the inner product (3.48a) results in the following development

$$\begin{aligned} & \left\langle \mathcal{H}' \mathbf{s}', \mathbf{s}^\dagger \right\rangle = \left\langle \mathcal{F}' \mathbf{q}', \mathbf{q}^\dagger \right\rangle_F + \left\langle \mathcal{A} \mathbf{q}', \boldsymbol{\xi}^\dagger \right\rangle_S + \left\langle \mathcal{S} \boldsymbol{\xi}', \boldsymbol{\xi}^\dagger \right\rangle_S \\ \Leftrightarrow \quad & \left\langle \mathcal{H}' \mathbf{s}', \mathbf{s}^\dagger \right\rangle = \left\langle \mathbf{q}', \mathcal{F}^\dagger \mathbf{q}^\dagger \right\rangle_F + \mathcal{B}_\mathcal{F}\left( \mathbf{q}', \mathbf{q}^\dagger \right) + \left\langle \mathcal{A} \mathbf{q}', \boldsymbol{\xi}^\dagger \right\rangle_S + \left\langle \boldsymbol{\xi}', \mathcal{S}^\dagger \boldsymbol{\xi}^\dagger \right\rangle_S. \end{aligned} \tag{3.51}$$

Hence the global direct operator $\mathcal{H}'$ is decomposed term by term, which allows one to subsequently solve three independent sub-problems associated with the obtention of the adjoint

operators $\mathcal{F}^\dagger$, $\mathcal{A}^\dagger$ and $\mathcal{S}^\dagger$ corresponding the adjoints fluid, aerodynamic forces and structural operators, respectively, along with the appropriate adjoint boundary conditions. At this point, it is noted that the fluid $\mathcal{F}'$ and structural $\mathcal{S}$ operators are decoupled from each other in the expression (3.51), since constituting the diagonal terms of the operator $\mathcal{H}'$. Hence the coupling between the adjoint structural and fluid variables will be obtained from a calculus involving the resulting fluid bilinear concomitant $\mathcal{B}_\mathcal{F}$ and the structural inner product on the aerodynamic forces operator.
For clarity, the expressions of the fluid and structural adjoint operators $\mathcal{F}^\dagger$ and $\mathcal{S}^\dagger$ are given in this section, and the calculus leading to their obtention is further detailed in Appendix A:

- The adjoint structural operator:

$$\mathcal{S}^\dagger = \left[\begin{array}{c|c} \mathbf{I}\partial_t & -\mathbf{I} \\ \hline \mathbf{M}^{-1}\mathbf{K} & -\mathbf{M}^{-1}\mathbf{C} + \mathbf{I}\partial_t \end{array}\right], \tag{3.52}$$

  without associated resulting boundary terms.

- The adjoint fluid operator:

$$\mathcal{F}^\dagger = \left[\begin{array}{c|c} \partial_t - \mathbf{A}^\dagger + Re^{-1}\nabla^2 & -\nabla \\ \hline \nabla\cdot & 0 \end{array}\right], \tag{3.53}$$

  where $\mathbf{A}^\dagger$ is the adjoint of the linearised advection term and is defined as $\mathbf{A}^\dagger\mathbf{u}^\dagger = -(\mathbf{u}_0 \cdot \nabla)\mathbf{u}^\dagger + (\mathbf{u}_0\nabla)^T \cdot \mathbf{u}^\dagger$.

- The resulting terms from the fluid adjoint operator (detailed in Appendix A.2):

$$\begin{aligned} \mathcal{B}_\mathcal{F}\left(\mathbf{q}', \mathbf{q}^\dagger\right) &= \oint_\gamma \left[\mathbf{u}^\dagger \cdot \left(\left(Re^{-1}\nabla\mathbf{u}' - p'\mathbf{I}\right)\cdot\mathbf{n}\right) - \mathbf{u}' \cdot \left(\left(Re^{-1}\nabla\mathbf{u}^\dagger - p^\dagger\mathbf{I}\right)\cdot\mathbf{n}\right)\right] \mathrm{d}l \\ \Leftrightarrow \quad \mathcal{B}_\mathcal{F}\left(\mathbf{q}', \mathbf{q}^\dagger\right) &= \oint_\gamma \left[\underbrace{\mathbf{u}^\dagger \cdot (\mathbf{f}\mathbf{q}'\cdot\mathbf{n})}_{\text{gives B.C.}} - \underbrace{\mathbf{u}' \cdot \left(\mathbf{f}\mathbf{q}^\dagger\cdot\mathbf{n}\right)}_{\text{gives } \mathcal{A}^\dagger}\right] \mathrm{d}l. \end{aligned} \tag{3.54}$$

The strategy is now to rewrite the resulting terms (3.54) such as one can obtain the adjoint aerodynamic forces and moment operator $\mathcal{A}^\dagger$ with the right-hand side of the integrand in (3.54), to further be used in the global adjoint operator $\mathcal{H}^\dagger$.
To do so, the fluid bilinear concomitant in (3.54) is injected into the following expression where $\mathcal{A}^\dagger$ is sought of the form

$$\begin{aligned} \mathcal{B}_\mathcal{F}\left(\mathbf{q}', \mathbf{q}^\dagger\right) + \left\langle \mathcal{A}\mathbf{q}', \boldsymbol{\xi}^\dagger \right\rangle_S &= \left\langle \boldsymbol{\xi}', \mathcal{A}^\dagger\mathbf{q}^\dagger \right\rangle_S \\ \oint_\gamma \left[\mathbf{u}^\dagger \cdot (\mathbf{f}\mathbf{q}'\cdot\mathbf{n}) - \mathbf{u}' \cdot \left(\mathbf{f}\mathbf{q}^\dagger\cdot\mathbf{n}\right)\right] \mathrm{d}l + \left\langle \mathcal{A}\mathbf{q}', \boldsymbol{\xi}^\dagger \right\rangle_S &= \left\langle \boldsymbol{\xi}', \mathcal{A}^\dagger\mathbf{q}^\dagger \right\rangle_S . \end{aligned} \tag{3.55}$$

Indeed, from the expression (3.51) we want

$$\left\langle \mathcal{H}'\mathbf{s}', \mathbf{s}^\dagger \right\rangle = \left\langle \mathbf{q}', \mathcal{F}^\dagger \mathbf{q}^\dagger \right\rangle_F + \underbrace{\mathcal{B}_\mathcal{F}\left(\mathbf{q}', \mathbf{q}^\dagger\right) + \left\langle \mathcal{A}\mathbf{q}', \boldsymbol{\xi}^\dagger \right\rangle_S}_{=\left\langle \boldsymbol{\xi}', \mathcal{A}^\dagger \mathbf{q}^\dagger \right\rangle_S} + \left\langle \boldsymbol{\xi}', \mathcal{S}^\dagger \boldsymbol{\xi}^\dagger \right\rangle_S .$$

Finally, enforcing the left-hand side of the integrand in (3.54) to be zero will deliver the adjoint boundary conditions at the solid interface.

Hence, the adjoint aerodynamic operator $\mathcal{A}^\dagger$ is first obtained by judiciously rewriting the term $\mathbf{u}' \cdot \left(\mathbf{f}\mathbf{q}^\dagger \cdot \mathbf{n}\right)$ in the expression (3.54) such as

$$\begin{aligned} \oint_\gamma \left[-\mathbf{u}' \cdot \left(\mathbf{f}\mathbf{q}^\dagger \cdot \mathbf{n}\right)\right] \mathrm{d}l &= \left\langle \boldsymbol{\xi}', \mathcal{A}^\dagger \mathbf{q}^\dagger \right\rangle_S \\ \Leftrightarrow \oint_\gamma \left[-\mathbf{B}\boldsymbol{\xi}' \cdot \left(\mathbf{f}\mathbf{q}^\dagger \cdot \mathbf{n}\right)\right] \mathrm{d}l &= \boldsymbol{\xi}' \cdot \mathbf{W}_S \mathcal{A}^\dagger \mathbf{q}^\dagger \\ \Leftrightarrow -\boldsymbol{\xi}' \cdot \mathbf{W}_S \oint_\gamma \mathbf{W}_S^{-1} \left[\mathbf{B} \cdot \left(\mathbf{f}\mathbf{q}^\dagger \cdot \mathbf{n}\right)\right] \mathrm{d}l &= \boldsymbol{\xi}' \cdot \mathbf{W}_S \mathcal{A}^\dagger \mathbf{q}^\dagger, \end{aligned} \tag{3.56}$$

where by identification, one obtains the expression of the adjoint aerodynamic operator $\mathcal{A}^\dagger$ as

$$\mathcal{A}^\dagger \mathbf{q}^\dagger = -\oint_\gamma \begin{bmatrix} \mathbf{K}^{-1} & 0 \\ 0 & \mathbf{M}^{-1} \end{bmatrix} \left[\mathbf{B} \cdot \left(\mathbf{f}\mathbf{q}^\dagger \cdot \mathbf{n}\right)\right] \mathrm{d}l. \tag{3.57}$$

Recalling that at the solid interface $\gamma$, the perturbed velocity fluid variable $\mathbf{u}'$ evolves as

$$\begin{cases} \mathbf{u}' = \mathbf{B}\boldsymbol{\xi}' \\ \dfrac{\partial p'}{\partial \mathbf{n}} = 0 \end{cases} \quad \text{at the solid interface.} \tag{3.58}$$

The adjoint boundary conditions are then obtained balancing the left hand side of the integrand of the expression (3.54) with the term $\left\langle \mathcal{A}\mathbf{q}', \boldsymbol{\xi}^\dagger \right\rangle_S$ in the expression (3.51), such as

$$\begin{aligned} \oint_\gamma \left[\mathbf{u}^\dagger \cdot (\mathbf{f}\mathbf{q}' \cdot \mathbf{n})\right] \mathrm{d}l &= -\left\langle \mathcal{A}\mathbf{q}', \boldsymbol{\xi}^\dagger \right\rangle_S \\ \Leftrightarrow \oint_\gamma \left[\mathbf{u}^\dagger \cdot (\mathbf{f}\mathbf{q}' \cdot \mathbf{n})\right] \mathrm{d}l &= -\begin{bmatrix} \mathbf{0} \\ \mathbf{M}^{-1}\mathbf{F}\mathbf{q}' \end{bmatrix} \cdot \begin{bmatrix} \mathbf{K} & 0 \\ 0 & \mathbf{M} \end{bmatrix} \begin{bmatrix} \boldsymbol{\eta}^\dagger \\ \boldsymbol{\zeta}^\dagger \end{bmatrix} \\ \Leftrightarrow \oint_\gamma \left[\mathbf{u}^\dagger \cdot (\mathbf{f}\mathbf{q}' \cdot \mathbf{n})\right] \mathrm{d}l &= -\mathbf{F}\mathbf{q}' \cdot \boldsymbol{\zeta}^\dagger \\ \Leftrightarrow \oint_\gamma \left[\mathbf{u}^\dagger \cdot (\mathbf{f}\mathbf{q}' \cdot \mathbf{n})\right] \mathrm{d}l &= -\left[\left(\oint_\gamma \begin{bmatrix} \dot{\chi}^\dagger \\ \dot{\psi}^\dagger \end{bmatrix} \cdot (\mathbf{f}\mathbf{q}' \cdot \mathbf{n})\, \mathrm{d}l\right) + \left(\oint_\gamma \begin{bmatrix} -y \\ x \end{bmatrix} \cdot (\mathbf{f}\mathbf{q}' \cdot \mathbf{n})\, \mathrm{d}l\right) .\dot{\theta}^\dagger\right], \end{aligned}$$

in which by identification, one finally obtains the following adjoint boundary condition at the

interface, compactly rewritten as

$$\begin{cases} \mathbf{u}^\dagger = -\left(\delta_\chi \dot{\chi}^\dagger + \delta_\psi \dot{\psi}^\dagger + \delta_\theta \dot{\theta}^\dagger\right)\Gamma \\ \dfrac{\partial p^\dagger}{\partial \mathbf{n}} = 0 \end{cases} \quad \text{at the solid interface.} \tag{3.59a}$$

Finally, the global adjoint operator $\mathcal{H}^\dagger$ governing the coupled fluid-structure adjoint system can be then compactly written in operator form as

$$\mathcal{H}^\dagger = \left[\begin{array}{c|c} \mathcal{F}^\dagger & \mathbf{0} \\ \hline \mathcal{A}^\dagger & \mathcal{S}^\dagger \end{array}\right], \quad \text{such as} \quad \mathcal{H}^\dagger \mathbf{s}^\dagger = \mathbf{0}. \tag{3.59b}$$

Summarising, one has in full in the domain, the adjoint fluid variables $\mathbf{q}^\dagger = [\mathbf{u}^\dagger \; p^\dagger]^T$ solutions of

$$\begin{cases} -\dfrac{\partial \mathbf{u}^\dagger}{\partial t} - (\mathbf{u}_0 \cdot \nabla)\mathbf{u}^\dagger + (\nabla \mathbf{u}_0)^T \cdot \mathbf{u}^\dagger = -\nabla p + Re^{-1}\nabla^2 \mathbf{u}^\dagger \\ \nabla \cdot \mathbf{u}^\dagger = 0 \end{cases} \quad \text{in } \Omega, \tag{3.60a}$$

and on the internal boundary $\gamma$

$$\begin{cases} \mathbf{u}^\dagger = -\boldsymbol{\Delta}\boldsymbol{\zeta}^\dagger \\ \dfrac{\partial p^\dagger}{\partial \mathbf{n}_0} = 0 \end{cases} \quad \text{at the solid interface.} \tag{3.60b}$$

Again, it is noted that similarly to the direct problem, the adjoint boundary condition at the interface can be seen as the sum of the contributions from each transformation $\mathcal{T}_\chi, \mathcal{T}_\psi$, and $\mathcal{R}$ taken independently. However, as opposed to the direct problem, the boundary condition of the adjoint problem is only a function of the adjoint structural velocities $\boldsymbol{\zeta}^\dagger$.
At last, the adjoint structural variables $\boldsymbol{\xi}^\dagger = [\boldsymbol{\eta}^\dagger \; \boldsymbol{\zeta}^\dagger]^T$ are solution of

$$\begin{cases} \dot{\boldsymbol{\eta}}^\dagger - \boldsymbol{\zeta}^\dagger = \mathbf{K}^{-1} \displaystyle\oint_\Gamma -(\boldsymbol{\Delta} \cdot \nabla \mathbf{u}_0) \cdot \left(\mathbf{f}\mathbf{q}^\dagger \cdot \mathbf{n}\right) \mathrm{d}l \\ \dot{\boldsymbol{\zeta}}^\dagger - \mathbf{C}\mathbf{M}^{-1}\boldsymbol{\zeta}^\dagger + \mathbf{K}\mathbf{M}^{-1}\boldsymbol{\eta}^\dagger = \mathbf{M}^{-1} \displaystyle\oint_\Gamma \boldsymbol{\Delta} \cdot \left(\mathbf{f}\mathbf{q}^\dagger \cdot \mathbf{n}\right) \mathrm{d}l \end{cases}. \tag{3.60c}$$

Equivalently, solving the system with regard to $\bar{t} = \tau - t$, restore the positive sign in front of the time derivative in the Navier-Stokes equations in the domain, and the adjoint fluid system reads

$$\begin{cases} \dfrac{\partial \mathbf{u}^\dagger}{\partial \bar{t}} - (\mathbf{u}_0 \cdot \nabla)\mathbf{u}^\dagger + (\nabla \mathbf{u}_0)^T \cdot \mathbf{u}^\dagger = -\nabla p^\dagger + Re^{-1}\nabla^2 \mathbf{u}^\dagger \\ \nabla \cdot \mathbf{u}^\dagger = 0 \end{cases}. \tag{3.61a}$$

Without any changes on the internal boundary $\gamma$ (*i.e.* $\equiv$ to expression (3.60b)) and the adjoint

structural variables $\boldsymbol{\xi}^\dagger = [\boldsymbol{\eta}^\dagger \ \boldsymbol{\zeta}^\dagger]^T$ are now solution of

$$\begin{cases} -\dot{\boldsymbol{\eta}}^\dagger - \boldsymbol{\zeta}^\dagger = \mathbf{K}^{-1} \oint_\Gamma -(\boldsymbol{\Delta}\cdot\nabla\mathbf{u}_0)\cdot\left(\mathbf{f}\mathbf{q}^\dagger\cdot\mathbf{n}\right)\mathrm{d}l \\ -\dot{\boldsymbol{\zeta}}^\dagger - \mathbf{C}\mathbf{M}^{-1}\boldsymbol{\zeta}^\dagger + \mathbf{K}\mathbf{M}^{-1}\boldsymbol{\eta}^\dagger = \mathbf{M}^{-1}\oint_\Gamma \boldsymbol{\Delta}\cdot\left(\mathbf{f}\mathbf{q}^\dagger\cdot\mathbf{n}\right)\mathrm{d}l \end{cases}. \tag{3.61b}$$

Finally, prescribing on the external boundaries inlet and outlet, respectively, $\partial\Omega_{in}^{ext}$ and $\partial\Omega_{out}^{ext}$ the boundary conditions:

$$\begin{cases} \mathbf{u}^\dagger = \mathbf{0} & \text{on } \partial\Omega_{in}^{ext} \\ \dfrac{\partial p^\dagger}{\partial\mathbf{n}} = 0 & \text{on } \partial\Omega_{in}^{ext} \end{cases} \quad \text{and,} \quad \begin{cases} \mathbf{u}^\dagger = \mathbf{0} & \text{on } \partial\Omega_{out}^{ext} \\ \dfrac{\partial p^\dagger}{\partial\mathbf{n}} = 0 & \text{on } \partial\Omega_{o}^{ext}ut \end{cases}.$$

This change in the time variable is only made for easier implementation to the existing numerical scheme solving the adjoint fluid system. Indeed, by doing so, one can re-use the direct solver with a modified advection operator to numerically solve an adjoint problem.

### 3.3.3 Receptivity to spatially localised feedbacks

In this section, the direct and adjoint operators, presented in expressions (3.46) and (3.59) respectively, are reformulated such as they involve normal-modes solutions in the form

$$\mathbf{s}'(x,y,t) = \hat{\mathbf{s}}(x,y)e^{\lambda t}, \tag{3.62}$$

in which the notation $\hat{(\cdot)}$ denotes the mode shape associated to the corresponding quantity and $\lambda$ is a complex eigenvalue linked to the time evolution and behaviour of the solution, to be obtained. Applying the notation (3.62) to all quantities individually leads to:

$$\mathbf{u}'(x,y,t) = \hat{\mathbf{u}}(x,y)e^{\lambda t}, \quad p'(x,y,t) = \hat{p}(x,y)e^{\lambda t}, \quad \boldsymbol{\eta}'(t) = \hat{\boldsymbol{\eta}}e^{\lambda t}, \quad \boldsymbol{\zeta}'(t) = \hat{\boldsymbol{\zeta}}e^{\lambda t}. \tag{3.63}$$

This particular form of the solutions allows one to consider the following eigenvalue problem for global linear stability

$$\hat{\mathcal{H}}\hat{\mathbf{s}} = \lambda\hat{\mathcal{I}}\hat{\mathbf{s}}, \tag{3.64a}$$

where

$$\hat{\mathcal{I}} = \begin{bmatrix} \mathbf{I}_2 & 0 & \mathbf{0} & \mathbf{0} \\ 0 & 0 & \mathbf{0} & \mathbf{0} \\ \mathbf{0} & \mathbf{0} & \mathbf{I}_3 & \mathbf{0} \\ \mathbf{0} & \mathbf{0} & \mathbf{0} & \mathbf{I}_3 \end{bmatrix}, \quad \hat{\mathcal{H}} = \left[\begin{array}{c|c} \hat{\mathcal{F}} & \mathbf{0} \\ \hline \mathcal{A}' & \hat{\mathcal{S}} \end{array}\right], \tag{3.64b}$$

where $\mathbf{I}_{2,3}$ are the identity operators in $\mathbb{R}^{2\times2}$ and $\mathbb{R}^{3\times3}$ respectively, and

$$\hat{\mathcal{F}} = \left[\begin{array}{c|c} -\mathbf{A}' + Re^{-1}\nabla^2 & -\nabla \\ \hline \nabla\cdot & 0 \end{array}\right], \quad \hat{\mathcal{S}} = \left[\begin{array}{c|c} \mathbf{0} & \mathbf{I}_3 \\ \hline -\mathbf{M}^{-1}\mathbf{K} & -\mathbf{M}^{-1}\mathbf{C} \end{array}\right], \tag{3.64c}$$

along with associated boundary conditions (3.46b) considering the state variable $\hat{\mathbf{s}}$.

Considering now a small perturbation given to the linear operator of the eigenvalue problem in (3.64): *i.e.* $\hat{\mathcal{H}} \to \hat{\mathcal{H}} + \varepsilon_2\delta\hat{\mathcal{H}}$ with $\varepsilon_2 \ll 1$. This then yields small changes in the eigenvalue and the eigenfunction, such that:

$$\lambda \to \lambda + \varepsilon_2\delta\lambda + o(\varepsilon_2^2), \quad \hat{\mathbf{s}} \to \hat{\mathbf{s}} + \varepsilon_2\delta\hat{\mathbf{s}} + o(\varepsilon_2^2). \tag{3.65}$$

Injecting these perturbed expressions in (3.64) leads to the expression

$$(\hat{\mathcal{H}} + \varepsilon_2\delta\hat{\mathcal{H}})\,(\hat{\mathbf{s}} + \varepsilon_2\delta\hat{\mathbf{s}}) = (\lambda + \varepsilon_2\delta\lambda)\,\hat{\mathcal{I}}\,(\hat{\mathbf{s}} + \varepsilon_2\delta\hat{\mathbf{s}})\,.$$

By decomposing the above expression in terms proportional to $\varepsilon_2$, one obtains

- At $\mathcal{O}(1)$:
$$\hat{\mathcal{H}}\hat{\mathbf{s}} = \lambda\hat{\mathcal{I}}\hat{\mathbf{s}}. \tag{3.66}$$

- At $\mathcal{O}(\varepsilon_2)$:
$$\hat{\mathcal{H}}\delta\hat{\mathbf{s}} + \delta\hat{\mathcal{H}}\hat{\mathbf{s}} = \lambda\delta\hat{\mathbf{s}} + \delta\lambda\hat{\mathbf{s}}. \tag{3.67}$$

Right dotting the expressions (3.66) and (3.67) by the $\lambda$ associated adjoint vector $\hat{\mathbf{s}}^\dagger = [\hat{\mathbf{q}}^\dagger\ \hat{\boldsymbol{\xi}}^\dagger]^T$, integrating over the domain $\Omega$ and multiplying by the appropriate weights leads to the reformulation of the expressions (3.66) and (3.67) involving the inner product $\langle\cdot,\cdot\rangle$,

- At $\mathcal{O}(1)$:
$$\langle\hat{\mathcal{H}}\hat{\mathbf{s}}, \hat{\mathbf{s}}^\dagger\rangle = \langle\lambda\hat{\mathbf{s}}, \hat{\mathbf{s}}^\dagger\rangle.$$

- At $\mathcal{O}(\varepsilon_2)$:
$$\langle\delta\hat{\mathbf{s}}, \hat{\mathcal{H}}^\dagger\hat{\mathbf{s}}^\dagger\rangle + \langle\delta\hat{\mathcal{H}}\hat{\mathbf{s}}, \hat{\mathbf{s}}^\dagger\rangle = \langle\delta\hat{\mathbf{s}}, \lambda\hat{\mathbf{s}}^\dagger\rangle + \delta\lambda\langle\hat{\mathbf{s}}, \hat{\mathbf{s}}^\dagger\rangle. \tag{3.68}$$

By noting that $\lambda$ is also the eigenvalue of the adjoint operator $\mathcal{H}^\dagger$ associated to the eigenvector $\mathbf{s}^\dagger$ (and one can write $\lambda^\dagger$ as the adjoint eigenvalue given by $\lambda^\dagger = \bar{\lambda}$ where the overbar $(\bar{\cdot})$ indicates the complex conjugate), the following expression holds,

$$\langle\delta\hat{\mathbf{s}}, \hat{\mathcal{H}}^\dagger\hat{\mathbf{s}}^\dagger\rangle = \langle\delta\hat{\mathbf{s}}, \lambda\hat{\mathbf{s}}^\dagger\rangle,$$

and the expression (3.68) finally reads:

$$\begin{aligned} \langle \delta\hat{\mathcal{H}}\hat{\mathbf{s}}, \hat{\mathbf{s}}^\dagger \rangle &= \delta\lambda \langle \hat{\mathbf{s}}, \hat{\mathbf{s}}^\dagger \rangle \\ \Leftrightarrow \quad \delta\lambda &= \frac{\langle \delta\hat{\mathcal{H}}\hat{\mathbf{s}}, \hat{\mathbf{s}}^\dagger \rangle}{\langle \hat{\mathbf{s}}, \hat{\mathbf{s}}^\dagger \rangle}. \end{aligned} \tag{3.69}$$

It is noted that the above analysis (*i.e.* expressions (3.65) to (3.69)) is the standard method (*e.g* Chomaz (2005); Giannetti and Luchini (2007)) to obtain the *sensitivity* or *drift* of the eigenvalue (3.69).

The sensitivity of the eigenvalue can now be studied with (3.69) by considering various types of the perturbation $\delta\hat{\mathcal{H}}$ depending on the control mechanism of interest: *e.g.* secondary cylinder (Marquet et al., 2008; Strykowski and Sreenivasan, 1990). Instead of focusing on a particular perturbation mechanism, a perturbation of a general form is considered in the present study, given by

$$\delta\hat{\mathcal{H}}\hat{\mathbf{s}} = \hat{\mathcal{I}}\hat{\mathbf{s}}. \tag{3.70}$$

Here, the perturbation for fluid variables is in the form of a spatially localised feedback identical to that in Giannetti and Luchini (2007), while that for structural variables lies in the stiffness $\mathbf{K}$ and mass or inertia $\mathbf{M}$ which directly affect the total energy of the fluid-structure system here.

In particular, application of the Cauchy-Schwarz inequality to the expression (3.69) for $\delta\hat{\mathcal{H}}$ in the expression (3.70) results in the following bound for $\delta\lambda$:

$$|\delta\lambda| \leq \frac{\|\hat{\mathbf{u}}\|_F \left\|\hat{\mathbf{u}}^\dagger\right\|_F + |\hat{\boldsymbol{\xi}}| \cdot |\hat{\boldsymbol{\xi}}^\dagger|}{|\langle \hat{\mathbf{s}}, \hat{\mathbf{s}}^\dagger \rangle|}, \tag{3.71}$$

where $\|\cdot\|_F^2 = \int_\Omega (\cdot)^2 \, \mathrm{d}\mathbf{x}$. Using the expression (3.71), one may define a sensitivity field given in the fluid domain $\Omega$, such that

$$\Theta_F(x, y) = \frac{\|\hat{\mathbf{u}}\|_F \left\|\hat{\mathbf{u}}^\dagger\right\|_F}{|\langle \hat{\mathbf{s}}, \hat{\mathbf{s}}^\dagger \rangle|}, \tag{3.72a}$$

which characterises the spatial location where the given eigenvalue responds sensitively to the fluid part of the perturbation in expression (3.70).

Similarly, a scalar quantity characterising the sensitivity to the solid part of the perturbation can be defined such that

$$\Theta_S = \frac{|\hat{\boldsymbol{\eta}}| \cdot |\hat{\boldsymbol{\eta}}^\dagger| + |\hat{\boldsymbol{\zeta}}| \cdot |\hat{\boldsymbol{\zeta}}^\dagger|}{|\langle \hat{\mathbf{s}}, \hat{\mathbf{s}}^\dagger \rangle|}. \tag{3.72b}$$

Finally, the comparison of the values of $\Theta_F$ with those of $\Theta_S$ allows one to characterise the relative importance of one to the other. Finally, it is noted that the sensitivity in (3.72) measures the effect of a perturbation in the form of (3.70) in terms of the total energy of the system.

Therefore, the coupling effect for the instabilities originating from FSI should be reflected in (3.72). Having pointed this out, the form of (3.70) does not directly add a perturbation to the coupling terms in (3.12) and (3.13). However, adding a perturbation to (3.12) is equivalent to considering a different boundary condition that is not the no-slip condition (*e.g.* a slip boundary condition), and, similarly, having a physically feasible perturbation to (3.13) is equivalent to changing $\mathbf{M}$, which will be examined through a parametric study in chapter §6 (through $I_{\theta,r}$).

# Chapter 4

# Numerical methods

The goal of this section is to introduce the numerical methods which are employed throughout this work. For a more concrete and mathematical description, the reader is mainly referred to Karniadakis and Sherwin (2005) for the Spectral/hp Element Method, to Karniadakis et al. (1991) and Guermond and Shen (2003) for the so-called velocity correction scheme, and to Luo and Bewley (2004) and Serson et al. (2016) for the coordinate transformation strategy, as the material presented in this section is not original, and only a brief review of the general concepts used in the scope of the present study are presented in this section.

## 4.1 The Spectral/hp Element Method

The Spectral/hp Element Method (Karniadakis and Sherwin, 2005), a class of high-order finite element method, is employed to perform all the numerical simulations presented throughout this work. In order to obtain a numerical approximation of a solution to the physical model used in the present scope (*i.e.* the Navier-Stokes equations in incompressible regime), the governing set of partial differential equations (3.6) first needs to be discretized.
This first step is directly included in the Spectral/hp Element Method resolution procedure as it derives from both the Finite Element Method and the classical Spectral Method, and the discretization process originates from the ideas of the Finite Element Method.
Indeed, the computational domain $\Omega$ is subdivided into a set of non-overlapping sub-domains $\Omega^e$, and the global approximated solution of the equations (3.6) over the whole domain $\Omega$ is constructed from the combination of all the local approximations evaluated on every element $\Omega^e$ of $\Omega$. Over the elements $\Omega^e$, local approximations are obtained by linearly combining functions belonging to the set of basis functions, which are chosen beforehand.
To ensure continuity of the approximated solution over the domain $\Omega$ (*i.e.* between the elements $\Omega^e$), the set of basis functions is chosen such as it satisfies related constraints. In the case of the Finite Element Method, the set of basis functions is commonly chosen to be linear or quadratic

in nature, corresponding to a low order approximation of the solution over an element $\Omega^e$. Hence, to improve the accuracy of the global solution over $\Omega$, the actual size of every element must be reduced. As we commonly refer to the characteristic dimension of an element $\Omega^e$ by the letter $h$, refining the subdivision of the domain $\Omega$ is known as $h$-refinement.
As opposed to the Finite Element Method, the Spectral Method uses a set of basis functions of higher order, leading to a better approximation of the solution over the domain $\Omega$. The increase in accuracy of the global solution is made by raising the order of the basis functions. As we commonly refer to the order of a polynomial by the letter $p$, this action is naturally named after $p$-refinement.

Combining the flexibility to both refining the order of interpolation over one element $\Omega^e$ from the Spectral Method and spatially refining the discretization of the domain $\Omega$, the convergence of the Spectral/hp Element Method can be achieved by varying both $h$ (mesh) and $p$ (order), hence the name Spectral/hp and its suitability to problems that require high spatial fidelity and long time integration (as numerical errors usually propagate through time steps).

### 4.1.1 The weighted residuals method

This section presents the general concept of the weighted residual method along with the Galerkin formulation on the particular example of a linear differential equation. These concepts can then be extended to the resolution of a set of partial differential equations.
Over a spatial domain $\Omega$, an approximate solution to a set of partial differential equations needs to satisfy a finite number of conditions that are specific to the choice of the numerical scheme. As stated above, the Spectral/hp Element Method borrows the discretization procedure of the Finite Element Method and hence the same framework of weighted residuals to specify these conditions. To describe this procedure, let us consider a linear differential equation defined over the domain $\Omega$, denoted by

$$\mathbb{L}(u) = 0, \tag{4.1}$$

subject to appropriate initial and boundary conditions, and we admit that the sought approximate solution has the form

$$u^\delta(\mathbf{x}, t) = u_0(\mathbf{x}, t) + \sum_{j=1}^{N_{\text{dof}}} \hat{u}_j(t)\mathbf{\Phi}_j(\mathbf{x}), \tag{4.2}$$

where $u_0(\mathbf{x}, t)$ satisfies the initial and boundary conditions, $\hat{u}_j(t)$ are the $N_{\text{dof}}$ unknown coefficients and $\mathbf{\Phi}_j$ are analytic functions called the expansion (or trial) functions. These functions should satisfy homogeneous boundary conditions (*i.e.* 0 on Dirichlet boundaries), as the physical boundary conditions of the problem are already included in $u_0(\mathbf{x}, t)$. Substituting the

decomposition (4.2) into the expression (4.1) results in a residual, $R \neq 0$:

$$\mathbb{L}\left(u^{\delta}\right) = R\left(u^{\delta}\right). \tag{4.3}$$

The residual $R$ is put under conditions to obtain a unique description of the coefficients $\hat{u}_j(t)$, such as (4.3) is reduced to a system of ordinary differential equations with regard to $\hat{u}_j(t)$. The principle of weighted residuals lies in the choice of the condition under which the residual $R$ is put: the inner product of the residual with respect to an arbitrary test (or weight) function is equal to zero, that is,

$$(v(\mathbf{x}), R) = 0, \tag{4.4}$$

where it is introduced the test function $v(\mathbf{x})$ and the (Legendre) inner product $(f, g)$ over a domain $\Omega$ is defined as

$$(f, g) = \int_{\Omega} f(\mathbf{x}) g(\mathbf{x}) \, \mathrm{d}\mathbf{x}. \tag{4.5}$$

The direct consequence of this decomposition is that the approximation $u^{\delta}$ will be exact if (4.4) is true $\forall\ v(\mathbf{x})$. However, $v(\mathbf{x})$ can be chosen such as it is represented by an arbitrary linear combination of a finite set of known functions $v_i(\mathbf{x})$ (and $u^{\delta}$ will then be an approximation), that is,

$$v(\mathbf{x}) = \sum_{i=1}^{N_{\mathrm{dof}}} a_i v_i(\mathbf{x}), \tag{4.6}$$

and where $a_i$ are arbitrary coefficients. Finally, substituting (4.6) and (4.3) into (4.4) leads to

$$\int_{\Omega} \sum_{i=1}^{N_{\mathrm{dof}}} a_i v_i(\mathbf{x}) \mathbb{L}\left(u^{\delta}\right) \mathrm{d}\mathbf{x} = 0. \tag{4.7}$$

Under the assumption $\dfrac{\partial \mathbb{L}}{\partial t} = 0$, and injecting (4.2) into (4.7), one gets

$$\int_{\Omega} \sum_{i=1}^{N_{\mathrm{dof}}} a_i v_i(\mathbf{x}) \mathbb{L}\left[u_0(\mathbf{x}) + \sum_{j=1}^{N_{\mathrm{dof}}} \hat{u}_j \mathbf{\Phi}_j(\mathbf{x})\right] \mathrm{d}\mathbf{x} =$$

$$\sum_{i=1}^{N_{\mathrm{dof}}} a_i \left\{ \int_{\Omega} v_i(\mathbf{x}) \mathbb{L}\left[u_0(\mathbf{x})\right] \mathrm{d}\mathbf{x} + \int_{\Omega} v_i(\mathbf{x}) \mathbb{L}\left[\sum_{j=1}^{N_{\mathrm{dof}}} \hat{u}_j \mathbf{\Phi}_j(\mathbf{x})\right] \mathrm{d}\mathbf{x} \right\} = 0. \tag{4.8}$$

As the coefficients $a_i$ are arbitrary, the following set of algebraic equations is sufficient to determine $\hat{u}_j$:

$$\sum_{j=1}^{N_{\mathrm{dof}}} \left\{ \hat{u}_j \int_{\Omega} v_i(\mathbf{x}) \mathbb{L}\left[\mathbf{\Phi}_j(\mathbf{x})\right] \right\} \mathrm{d}\mathbf{x} = -\int_{\Omega} v_i(\mathbf{x}) \mathbb{L}\left[u_0(\mathbf{x})\right] \mathrm{d}\mathbf{x}, \quad i = 1, 2, \ldots, N_{\mathrm{dof}}. \tag{4.9}$$

Or equivalently in matrix form

$$\mathbf{A}\hat{\mathbf{u}} = \mathbf{b}, \tag{4.10}$$

where $\hat{\mathbf{u}}$ is the vector composed of the coefficients $\hat{u}_j$ and the components of the matrix $\mathbf{A}$ are given by

$$A_{ij} = \int_\Omega v_i(\mathbf{x}) \mathbb{L}\left[\mathbf{\Phi}_j(\mathbf{x})\right] \mathrm{d}\mathbf{x}, \tag{4.11}$$

and the vector $\mathbf{b}$ is given by

$$b_i = -\int_\Omega v_i(\mathbf{x}) \mathbb{L}\left[u_0(\mathbf{x})\right] \mathrm{d}\mathbf{x}. \tag{4.12}$$

Finally, the numerical scheme is determined by the choice of the expansion functions $\mathbf{\Phi}_j(\mathbf{x})$ and test functions $v_i(\mathbf{x})$ within the framework of weighted residuals. Here, set of test functions is the same as the set of expansion functions (*i.e.*, $v_j(\mathbf{x}) = \mathbf{\Phi}_j(\mathbf{x})$), situation which correspond to the Galerkin formulation. For information about the possible choices of the expansion and test functions, the reader is referred to Karniadakis and Sherwin (2005).

### 4.1.2 Discretisation

This section first presents the idea behind the formulation of expansion basis, taking the particular example of quadrilateral elements in practice used in this work in the boundary layer regions of the domain. Triangular elements were used elsewhere in an unstructured fashion, and as their expansion basis is formulated according to the same concept, an explicit formulation is not provided in this document. However, the key differences between quadrilateral and triangular elements are briefly reviewed.
The second part of this section reviews the key concepts of the method from the element-wise approximation of the solution to the global solution assembly, without going into a deep explicit formulation as these are beyond the purpose of this document.

#### 2D Expansions of quadrilateral elements

As stated above, quadrilateral and triangular elements were used to carry out the two-dimensional simulations of the Navier-Stokes equations. As a one-dimensional modal basis is at the root of the formulation of the two-dimensional basis, it is first presented, followed by the particular case of a quadrilateral element. The one-dimensional basis is expressed as

$$\phi_p(\xi) = \psi_p^a(\xi) = \begin{cases} \dfrac{1-\xi}{2}, & p = 0, \\ \left(\dfrac{1-\xi}{2}\right)\left(\dfrac{1+\xi}{2}\right)\mathcal{P}_{p-1}^{1,1}(\xi), & 0 < p < P, \\ \dfrac{1+\xi}{2}, & p = P, \end{cases} \tag{4.13}$$

where $\xi$ is the one-dimensional coordinate, which varies from $-1$ to 1, and $\mathcal{P}_{p-1}^{1,1}(\xi)$ is a type of Jacobi polynomial of order $p$. Details on the properties of the different sets of polynomials (Jacobi and others) can be found in Karniadakis and Sherwin (2005).
For the two-dimensional case, the standard region $\mathcal{Q}^2$ for quadrilateral elements is defined as

$$\Omega_{\text{st}} = \mathcal{Q}^2 = \{-1 \leq \xi_1, \xi_2 \leq 1\}\,. \tag{4.14}$$

Figure 4.1(left) presents the region defined by $\mathcal{Q}^2$ in a standard Cartesian coordinate system, along with a representation of a triangular region (figure 4.1(right)).

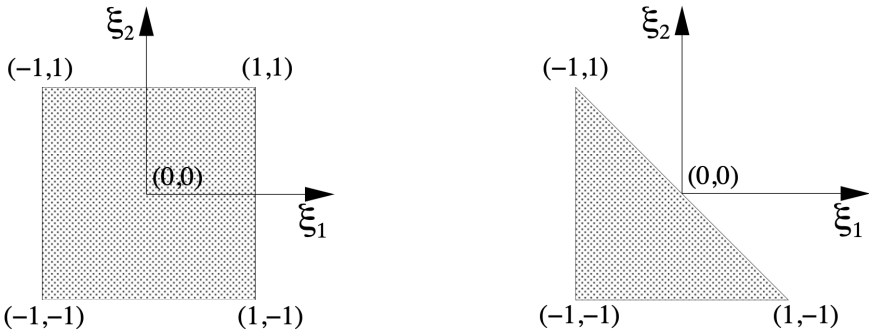



**Figure 4.1:** Standard regions for (left) quadrilateral, and (right) triangular elements in terms of the Cartesian coordinates $(\xi_1, \xi_2)$. Adapted from Karniadakis and Sherwin (2005).

From that standard region, constructing a two-dimensional basis can be done in a straightforward manner by taking a product of the one-dimensional basis (4.13) (which can be thought of as a one-dimensional tensor), in each of the Cartesian directions:

$$\phi_{pq}\left(\xi_1, \xi_2\right) = \psi_p^a\left(\xi_1\right)\psi_q^a\left(\xi_2\right), \quad 0 \leq p, q, \quad p \leq P, \quad q \leq Q. \tag{4.15}$$

It is noted that a priori, no conditions on the polynomials order $P$ and $Q$ in the different Cartesian directions are imposed, and these are not necessarily equal. However, in this work, due to the nature of the problem investigated, the condition $P = Q$ has always been used. Figure 4.2 shows an example of this two-dimensional expansion basis in the case of a polynomial order $P = 4$.
Boundary and interior modes can be further extracted from the decomposition of the modal expansion (4.15). Defined in the standard region, the boundary and interior modes are, by definition, the nonzero modes on the boundaries and zero on the boundaries. This distinction becomes helpful when a simple $C^0$ global expansion basis is required, as a global expansion can be generated from the local expansions simply by matching the shape of the boundary modes.

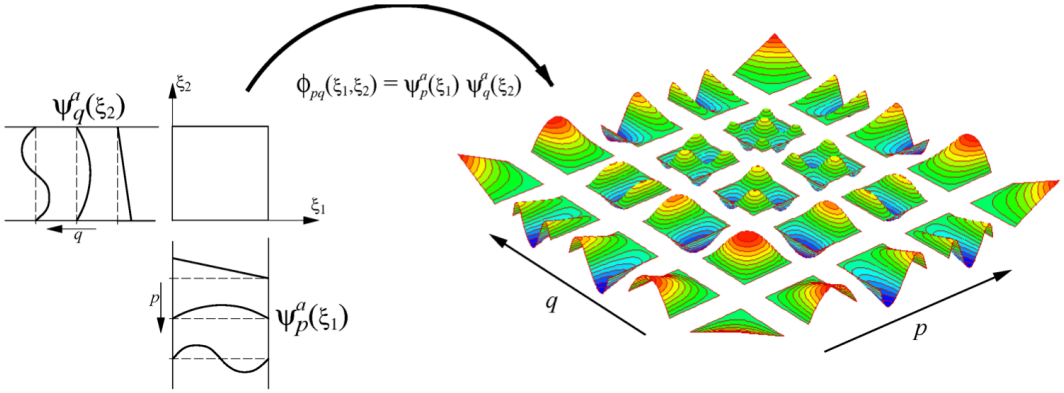



**Figure 4.2:** Two-dimensional expansion basis of order $P = 4$ for a quadrilateral element, constructed from a tensorial product of two one-dimensional expansions. Adapted from Karniadakis and Sherwin (2005).

In the case of a two-dimensional expansion, the boundary modes are further divided into two categories, the vertex and the edge modes. The vertex modes have support along one vertex and zero at all other vertices, and the edges modes have a unit magnitude along one edge and are zero at all other edges and vertices. For clarity on this particular point, in figure 4.2(right), the vertex modes are represented in the corners of the standard region, whereas the edge modes are the modes in between the vertexes along the edges of the standard region.

Although not directly made explicit in this document, as considered beyond its purpose, all the operations (such as integration or differentiation) must approximate the solution undertaken in the standard regions. In this study, the Gaussian quadrature is employed to perform the numerical integration with adequate precision due to the exact integration for polynomials. The Gaussian quadrature defines a series of integration points in the integration region on which the values of the function (or quantity of interest) that is being integrated are sought. These points are called quadrature points.
The operations in the standard regions are, however, fully detailed in Karniadakis and Sherwin (2005).

### 2D Expansions of triangular elements

The triangular region between constant independent limits, is defined by the transformation (Karniadakis and Sherwin, 2005):

$$\eta_1 = 2\frac{1+\xi_1}{1-\xi_2} - 1, \quad \eta_2 = \xi_2. \tag{4.16}$$

Using this coordinate system $(\eta_1, \eta_2)$, the triangular pattern element is defined by:

$$\Omega_{\text{st}} = \mathcal{T}^2 = \{(\eta_1, \eta_2) \mid -1 \leq \eta_1, \eta_2 \leq 1\} \tag{4.17}$$

The transformation defined in equation (4.16) collapses the standard quadrilateral region into a unit triangle and $(\eta_1, \eta_2)$ are hence described as the collapsed coordinates, as shown in figure 4.3. One consequence is that the coordinate $\eta_1$ has a multiple value at $(\eta_1, \eta_2) = (1, -1)$. This type of singularity also appears in cylindrical and spherical coordinate systems.

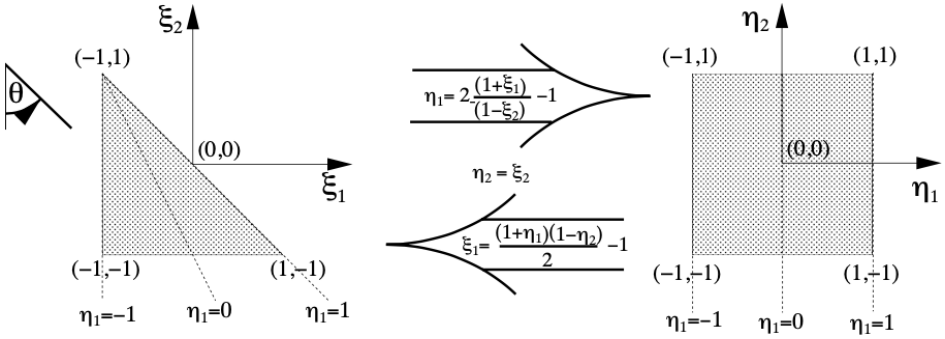



**Figure 4.3:** Triangle-to-rectangle transformation. Adapted from Karniadakis and Sherwin (2005).

In order to keep the boundary interior decomposition, the expansion basis cannot directly be obtained by a tensor product of principal functions. It must be the product of a one-dimensional tensor $\psi_p(\eta_1(\xi_1, \xi_2))$ with a two-dimensional tensor $\psi_{pq}(\eta_2(\xi_2))$. The bi-dimensional expansion $\phi_{pq}(\xi_1, \xi_2)$ on the standard region $\mathcal{T}^2$ is shown in Figure 4.4 and an illustrative example.

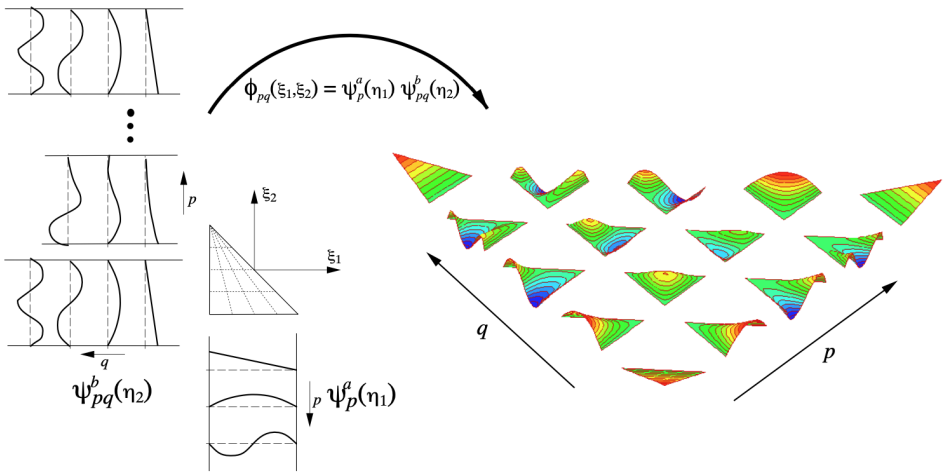



**Figure 4.4:** Construction of a fourth-order ($P = 4$) triangular expansion using the product of two modified principal functions $\psi^a_p(\eta_1)$ and $\psi^b_{pq}(\eta_2)$. Adapted from Karniadakis and Sherwin (2005).

### Standard - Local representation

Since all the operations are made in the standard regions, a mapping is necessary to transform an element $\Omega^e$ into its counterpart $\Omega^{std}$ corresponding to the standard region. This mapping can be understood as a diffeomorphism between $\Omega^e$ and $\Omega^{std}$, as a quadrilateral element will

be mapped to a standard quadrilateral region, a triangular element to a standard triangular region and so on.

As an example, the case of the mapping of a straight-sided two-dimensional quadrilateral element of vertex $A, B, C$ and $D$ of coordinates ($x_i^A$, $x_i^B$, $x_i^C$, $x_i^D$, $i = 1, 2$) mapped to its standard region $\mathcal{Q}^2$ is presented:

$$\begin{aligned}\chi(\xi_1, \xi_2) = &\frac{(1-\xi_1)(1-\xi_2)}{4}\mathrm{x}_i^A + \frac{(1+\xi_1)(1-\xi_2)}{4}\mathrm{x}_i^B \\ &+\frac{(1-\xi_1)(1+\xi_2)}{4}\mathrm{x}_i^C + \frac{(1+\xi_1)(1+\xi_2)}{4}\mathrm{x}_i^D.\end{aligned} \tag{4.18}$$

For curved edges elements, a function $f^{kn}(\xi_i)$ can be used to map the curved edges of the element, where $kn$, $n = A, B, C, D$ represents each curve edge. Gordon and Hall (1973) proposed the following blending function to define the elemental mapping for curved-edges elements:

$$\begin{aligned}\chi(\xi_1, \xi_2) = f^{kA}(\xi_1)\frac{(1-\xi_2)}{2} + f^{kC}(\xi_1)\frac{(1+\xi_2)}{2} + f^{kD}(\xi_2)\frac{(1-\xi_1)}{2} + f^{kB}(\xi_2)\frac{(1+\xi_1)}{2} \\ -f^{kA}(-1)\frac{(1-\xi_1)(1-\xi_2)}{4} - f^{kA}(1)\frac{(1+\xi_1)(1-\xi_2)}{4}. \\ -f^{kC}(-1)\frac{(1-\xi_1)(1+\xi_2)}{4} - f^{kC}(1)\frac{(1+\xi_1)(1-\xi_2)}{4}\end{aligned} \tag{4.19}$$

It is noted that the Jacobian of these transformations $J$ will appear in the operations (integration, differentiation...) - involving the quantities from the local regions - made in the standard regions.

### Global representation

Summarising the above sections, the global domain $\Omega$ is decomposed into elemental sub-domains $\Omega^e$ which are then mapped to standard regions (section §4.1.2), in which a basis expansion is defined (section §4.1.2). The Galerkin formulation (section §4.1.1) requires that the operation such as integration and differentiation are done at the elementary level, which implies the contribution of each element to be added in a final step during the assembly of the global matrix system.

The global solution in the domain $\Omega$ is obtained under the simple $C^0$ continuity condition between the elements when combining the contribution of all the local approximations. This step is a standard procedure used in the Finite Element Method (see Zienkiewicz and Taylor (2000)) and is undertaken during the final system assembly.

In practice, the process of global assembly consists of summing the equations generated for the local degrees of freedom (corresponding to a single global degree of freedom). After this step, a global system with dimensions equal to the number of global degrees of freedom is produced, and once the global system is solved, the value of each global degree of freedom corresponds to

the value of its local degree of freedom counterpart.

### 4.1.3 The Velocity Correction scheme

In the above sections, the spatial approximation of a partial differential equation solution using the Spectral/hp Element Method has been reviewed. However, in the context of this study, the system of partial differential equations considered (4.20) is time-dependent, non-linear and coupled between its state variables, in addition to being spatially varying. Hence a strategy is required in order to obtain an accurate final approximation of the transient solution. The velocity-correction scheme (Guermond and Shen, 2003; Karniadakis et al., 1991) has precisely been developed to uncouple the system by separating the pressure from the velocity and solve them separately in addition to provide an accurate multi-step time integration of the solution (stiffly stable time discretisation).
The general concepts of the velocity-correction scheme are presented in this section, on the example of the actual equation being solved in this study, the unsteady Navier-Stokes equations in the incompressible regime, expressed here in non-dimensional form ($\rho = 1$):

$$\begin{aligned} \frac{\partial \mathbf{u}}{\partial t} &= -(\mathbf{u}\cdot\nabla)\mathbf{u} - \nabla p + Re^{-1}\nabla^2\mathbf{u}, \\ \nabla\cdot\mathbf{u} &= 0, \end{aligned} \tag{4.20}$$

where $\mathbf{u}$ is the velocity, $p$ is the pressure, and $Re$ is the Reynolds number. The system of equations (4.20) is solved in a computational domain $\Omega$, along with the boundary conditions

$$\begin{aligned} \mathbf{u} &= \mathbf{u}_{\mathfrak{D}} \text{ on } \Gamma_{\mathfrak{D}}, \\ \frac{\partial \mathbf{u}}{\partial \mathbf{n}} &= \mathbf{u}_{\mathfrak{N}} \text{ on } \Gamma_{\mathfrak{N}}, \end{aligned} \tag{4.21}$$

along with appropriate initial conditions and both essential and natural boundary conditions for the pressure on $\Gamma_{\mathfrak{N}}$ and $\Gamma_{\mathfrak{D}}$, respectively. In equations (4.21), $\Gamma_{\mathfrak{D}}$ and $\Gamma_{\mathfrak{N}}$ denotes the boundary regions on which a Dirichlet and Neumann type boundary condition are applied, respectively. For clarity throughout this section (as well as in section §4.2), the convective and viscous terms of the expression (4.20) are re-written in term of operators $\mathbf{A}$ and $\mathbf{L}$, respectively

$$\mathbf{A}(\mathbf{u}) = -(\mathbf{u}\cdot\nabla)\mathbf{u} \quad \text{and} \quad Re^{-1}\mathbf{L}(\mathbf{u}) = Re^{-1}\nabla^2\mathbf{u}. \tag{4.22}$$

Finally, using the notations (4.22), the expressions (4.20) and (4.21) are considered together to define the problem as:

$$\begin{aligned} \frac{\partial \mathbf{u}}{\partial t} &= \mathbf{A}(\mathbf{u}) - \nabla p + Re^{-1}\mathbf{L}(\mathbf{u}) && \text{in } \Omega, \\ \nabla \cdot \mathbf{u} &= 0 && \text{in } \Omega, \\ \mathbf{u} &= \mathbf{u}_{\mathfrak{D}} && \text{on } \Gamma_{\mathfrak{D}}, \\ \frac{\partial \mathbf{u}}{\partial \mathbf{n}} &= \mathbf{u}_{\mathfrak{N}} && \text{on } \Gamma_{\mathfrak{N}}. \end{aligned} \tag{4.23}$$

The momentum equation in (4.23) is discretised in time using a backward differentiation formula to approximate the time derivative, and the convective term is written explicitly using a polynomial extrapolation from previous time-steps. Doing so, at time-step $n+1$, the momentum equation reads

$$\frac{\gamma_0 \mathbf{u}^{n+1} - \sum_{q=0}^{J_i-1} \alpha_q \mathbf{u}^{n-q}}{\Delta t} = \sum_{q=0}^{J_e-1} \beta_q \mathbf{A}\left(\mathbf{u}^{n-q}\right) - \nabla p^{n+1} + \nu \mathbf{L}\left(\mathbf{u}^{n+1}\right), \tag{4.24}$$

where $J_e$ and $J_i$ are the integration orders of the explicit and implicit terms, respectively, and the splitting scheme coefficients $\alpha$, $\beta$ and $\gamma$ for orders up to 3 are presented in table 4.1. In this work, a $2^{nd}$ order scheme has been used for all the simulations. It can be seen in expression (4.24) that the non-linear convective terms are now treated explicitly, whereas the viscous terms are treated implicitly, which numerically stabilise the simulation with regard to the time variable.

| Coefficient | $1^{st}$ order | $2^{nd}$ order | $3^{rd}$ order |
|---|---|---|---|
| $\gamma_0$ | 1 | 3/2 | 11/6 |
| $\alpha_0$ | 1 | 2 | 3 |
| $\alpha_1$ | 0 | -1/2 | -3/2 |
| $\alpha_2$ | 0 | 0 | 1/3 |
| $\beta_0$ | 1 | 2 | 3 |
| $\beta_1$ | 0 | -1 | -3 |
| $\beta_2$ | 0 | 0 | 1 |

**Table 4.1:** Splitting scheme coefficients. Extracted from Karniadakis et al. (1991).

For clarity, expression (4.24) can be rewritten as

$$\frac{\gamma_0 \mathbf{u}^{n+1} - \mathbf{u}^{+}}{\Delta t} = \mathbf{A}^{*} - \nabla p^{n+1} + \nu \mathbf{L}\left(\mathbf{u}^{n+1}\right), \tag{4.25}$$

with the notations

$$\sum_{q=0}^{J_i-1} \alpha_q \mathbf{u}^{n-q} = \mathbf{u}^+, \quad \text{and} \quad \sum_{q=0}^{J_e-1} \beta_q \mathbf{A}\left(\mathbf{u}^{n-q}\right) = \mathbf{A}^*. \tag{4.26}$$

A key step in Karniadakis et al. (1991) is to split the right-hand-side of (4.25) at this stage using the following three steps:

$$\begin{aligned} \frac{\hat{\mathbf{u}} - \mathbf{u}^+}{\Delta t} &= \mathbf{A}^*, \\ \frac{\tilde{\mathbf{u}} - \hat{\mathbf{u}}}{\Delta t} &= -\nabla p^{n+1}, \\ \frac{\gamma_0 \mathbf{u}^{n+1} - \tilde{\mathbf{u}}}{\Delta t} &= Re^{-1}\mathbf{L}\left(\mathbf{u}^{n+1}\right), \end{aligned} \tag{4.27}$$

where $\hat{\mathbf{u}}$ and $\tilde{\mathbf{u}}$ are hence intermediate fields. In order to avoid a costly inversion of the global mass matrix that would normally be required by the projection problem at the first time step after the spatial discretisation, the analytical expression of $\hat{\mathbf{u}}$ from the first step is in practice directly substituted in the second equation. By doing so, the first equation only involves the direct calculation of $\hat{\mathbf{u}}$ in the physical space, without performing the projection to the solution space. Secondly, the pressure is obtained by taking the divergence of the equation and imposing $\nabla \cdot \tilde{\mathbf{u}} = 0$, resulting in the following Poisson equation

$$\nabla^2 p^{n+1} = \nabla \cdot \left(\frac{\hat{\mathbf{u}}}{\Delta t}\right), \tag{4.28}$$

which requires appropriate pressure boundary conditions to be solved. In particular, this boundary condition is proposed by Karniadakis et al. (1991) and reads

$$\frac{\partial p^{n+1}}{\partial \mathbf{n}} = \mathbf{n} \cdot \left[\mathbf{A}^* - Re^{-1}(\nabla \times \nabla \times \mathbf{u})^*\right]. \tag{4.29}$$

Finally, the third equation is a Helmholtz equation for the velocity. The resulting Poisson and Helmholtz problems are solved in practice using the Spectral/hp Element Method described above (Cantwell et al., 2015) in the scope of steady problems . The reader is also referred to Vos et al. (2011) for additional practical information on the subject.

Note that a boundary layer analysis can be conducted to evaluate the error in the divergence condition of the velocity field $\mathbf{u}$ at the time level $n+1$, *i.e.*, $\mathbf{Q} \equiv \mathbf{Q}^{n+1} = \nabla \cdot \mathbf{u}^{n+1} = 0$ (Karniadakis et al., 1991).
Setting the right-hand side of the equation (4.25) to 0, after taking its divergence leads to the

divergence equation,

$$\begin{aligned} & \nabla \cdot \mathbf{u} - \gamma_0 \nu \Delta t \nabla^2 (\nabla \cdot \mathbf{u}) = 0, \\ \Leftrightarrow \quad & \mathbf{Q} - \gamma_0 \nu \Delta t \nabla^2 \mathbf{Q} = 0. \end{aligned}$$

Hence, there exist a numerical boundary layer of thickness $l = \sqrt{\gamma_0 \nu \Delta t}$ into which the boundary divergence is $\mathbf{Q}_w = -l(\partial \mathbf{Q}/\partial \mathbf{n})_w$, where $\mathbf{Q} = \mathbf{Q}_w e^{-s/l}$ ($s$ is a general coordinate normal to the boundary). It follows that $\mathbf{Q}_w$ is of order $\mathcal{O}(\partial \mathbf{u}/\partial \mathbf{n})$, according to a similar order of magnitude analysis (Karniadakis et al., 1991).

## 4.2 Fluid-Structure Interaction treatment

When the interest is brought to a fluid-structure interaction problem, a strategy needs to be put in place to carry on the coupling between the two domains, fluid and structure. As a matter of global numerical efficiency, it is chosen here to employ coordinate transformations to consider the temporal deformation of the fluid domain $\Omega$ further to the displacement of the structure. This section briefly describes the process behind this idea.
Figure 4.5 shows the idea of coordinate transformation, where the two domains are presented. The physical domain corresponds to the deformed mesh - *i.e.*, the domain in which the structure moves - when in practice, the computational domain remains non-deformed. The effect of the theoretical motion of the object is "added" to the fluid governing equations through a forcing term described in more detail in this section below.

Using the Spectral/hp Element Method, along with the velocity correction scheme, the approach was extended (see Serson et al. (2016)) to include a weak coupling between the fluid and the structures. After each time-step and calculating the explicit part of the time-integration scheme (*i.e.*, a solution to the fluid problem), the fluid forces are extracted and used to update the displacements of the bodies, which are then used to obtain a new coordinate transformation for the fluid solver, based on their corresponding displacement.

In the following, the fluid treatment is first described, followed by the considerations that need to be made to compute the time-dependent bodies displacements. The entire modifications to the original velocity correction scheme to include the coordinate transformations are not reviewed in this document as they are beyond its purpose. However, as for the Spectral/hp Element Method section, the principles are reviewed.

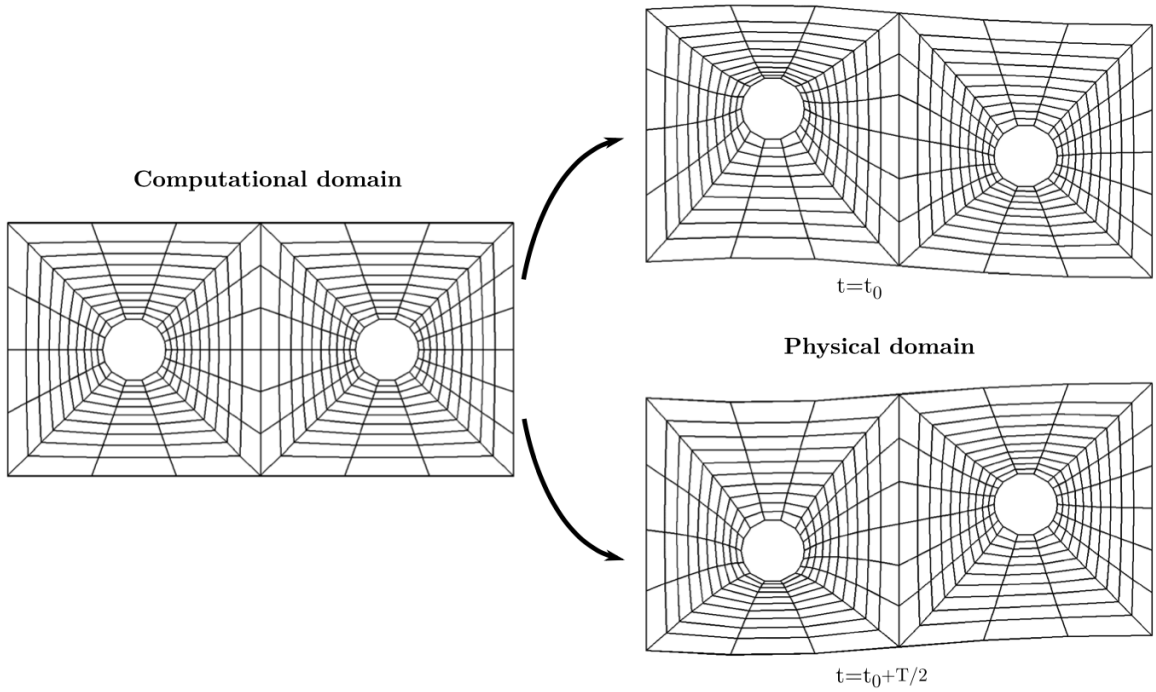



**Figure 4.5:** Example of transformation from the physical Cartesian coordinate system to a different coordinate system. Extracted from Serson et al. (2016).

### 4.2.1 Fluid equations

The contravariant form of the Navier-Stokes equations in time-dependent curvilinear coordinate systems is considered here as it is an invariant form of the equations under the choice of coordinate system (Luo and Bewley, 2004).
According to the concepts belonging to this approach, a general time-dependent coordinate transformation is first represented by:

$$\begin{aligned} \bar{x} &= \bar{x}(x, y, z, t), \\ \bar{y} &= \bar{y}(x, y, z, t), \\ \bar{z} &= \bar{z}(x, y, z, t), \end{aligned} \tag{4.30}$$

where the overbar $(\bar{.})$ represents the usual Cartesian system and the transformed (*i.e.* computational) coordinate system by $(x, y, z, t)$. In this coordinate system, the Navier-Stokes equations for an incompressible, Newtonian fluid, in the domain $\Omega$ reads (Serson et al., 2016):

$$\begin{aligned} \frac{\partial \mathbf{u}}{\partial t} &= \mathbf{A}(\mathbf{u}) - \frac{\nabla p}{J} + Re^{-1}\mathbf{L}(\mathbf{u}) + \mathbf{Q}(\mathbf{u}, p), \\ \nabla \cdot \mathbf{u} &= 0, \end{aligned} \tag{4.31}$$

where $J$ is the Jacobian of the transformation from the transformed to the Cartesian system, and the non-linear advection, diffusion, and forcing operator, respectively, reads

$$\begin{aligned} \mathbf{A}(\mathbf{u}) &= -(\mathbf{u}.\nabla)\mathbf{u}, \\ Re^{-1}\mathbf{L}(\mathbf{u}) &= Re^{-1}\nabla^2\mathbf{u}, \\ \mathbf{Q}(\mathbf{u},p) &= \left[\bar{\mathbf{A}}(\mathbf{u}) - \mathbf{A}(\mathbf{u})\right] + \left[\frac{\nabla p}{J} - \bar{\mathbf{G}}(p)\right] + Re^{-1}\left[\bar{\mathbf{L}}(\mathbf{u}) - \mathbf{L}(\mathbf{u})\right]. \end{aligned}$$

In the current choice of numerical implementation, it is noted that $\mathbf{Q}(\mathbf{u},p)$ is hence a forcing term that imposes the coordinate transformation and can be seen as the difference between the Cartesian and transformed expressions. The forcing term $\mathbf{Q}(\mathbf{u},p)$ also depends on the particular nature of the transformation employed, even though it is not explicit in the equations.
It is noted that at this step, the momentum equation of the Navier–Stokes equations has been restated in a form that is almost the same as its Cartesian counterpart, with an additional forcing term, and the Jacobian dividing the pressure gradient. The Jacobian is included here for analytical convenience, as it will allow the equations to be simplified using the incompressibility condition $\nabla \cdot (J\mathbf{u}) = 0$ (Serson et al., 2016).

Using the Einstein summation convention notation (summing over the index variables - here $i, j, k$ - appearing twice in a single term, where in the case of superscripts and subscripts, the upper indices represent components of contravariant vectors, whereas the lower indices represent components of covariant vectors), the operators in the Cartesian coordinate system read (Luo and Bewley, 2004):

$$\begin{aligned} \bar{\mathbf{A}}(\mathbf{u}) &= u^j u^i_{,j} + V^j u^i_{,j} - u^j V^i_{,j}, \\ \nu\bar{\mathbf{L}}(\mathbf{u}) &= \nu g^{jk} u^i_{,jk}, \\ \bar{\mathbf{G}}(p) &= g^{ij} p_{,j}, \end{aligned} \tag{4.32}$$

where $V^j = -\dfrac{\partial x^j}{\partial t}$ is the velocity of the coordinate system, $g^{ij} = \dfrac{\partial x^i}{\partial x^k}\dfrac{\partial x^j}{\partial x^k}$ denote the inverse of the metric tensor, and a comma with an index in the subscript denotes covariant differentiation:

$$u^i_{,j} = \frac{\partial u^i}{\partial x^j} + \Gamma^i_{jk} u^k, \tag{4.33}$$

where $\Gamma^i_{jk}$ are the Christoffel symbols of the second kind.

As a reminder, contravariant vectors have components that $contra - vary$ with a change of basis (*e.g.* position, velocity, acceleration... etc), whereas covariant vectors have components that $co - vary$ with a change of basis.

It is noted that in expression (4.32), the velocity of the coordinate system appears twice and

might be confusing. This is due to the expression of the intrinsic derivative of a time-varying contravariant vector $R^j$ (Luo and Bewley, 2004):

$$\frac{\mathrm{D}R^j}{\mathrm{D}t} = \frac{\partial R^j}{\partial \tau} + R^j_{,i}\left(u^i - V^i\right) + R^i V^j_{,i}. \tag{4.34}$$

It is now clear that applying the expression (4.34) to the fluid velocity $u^i$ (instead of $R^i$), and deriving the momentum conservation equation leads to the modified advection term presented in expression (4.32). The reader is referred to Luo and Bewley (2004) for the complete proof.

Finally, the momentum equation in tensorial notation and fully rewritten:

$$\frac{\partial u^i}{\partial t} = -u^j u^i_{,j} + V^j u^i_{,j} - u^j V^i_{,j} - g^{ij} p_{,j} + \frac{1}{Re}\left(g^{jk} u^i_{,j}\right)_{,k}. \tag{4.35}$$

Practically the momentum equation is restated in a similar form to the original Navier–Stokes equations with an additional forcing term and the additional presence of the Jacobian dividing the pressure gradient. This modified momentum equation is solved by a modified velocity correction scheme (Serson et al., 2016) which precisely follows the same concept shown in section §4.1.3 and hence is not presented in detail in this document.

We recall that the reader is referred to Luo and Bewley (2004) for a more complete and detailed description of this theory, and to Serson et al. (2016) for its application to the Spectral/hp elements method and the velocity correction scheme (Cantwell et al., 2015).

### 4.2.2 Structural equations

Throughout this research, the general motion of a rigid structure in the two-dimensional Cartesian plane $(x, y)$ is physically studied under the assumption of being a solution of the following linear equation

$$\begin{bmatrix} m & 0 & 0 \\ 0 & m & 0 \\ 0 & 0 & I_\theta \end{bmatrix} \begin{bmatrix} \ddot{x}(t) \\ \ddot{y}(t) \\ \ddot{\theta}(t) \end{bmatrix} + \begin{bmatrix} c_x & 0 & 0 \\ 0 & c_y & 0 \\ 0 & 0 & c_\theta \end{bmatrix} \begin{bmatrix} \dot{x}(t) \\ \dot{y}(t) \\ \dot{\theta}(t) \end{bmatrix} + \begin{bmatrix} k_x & 0 & 0 \\ 0 & k_y & 0 \\ 0 & 0 & k_\theta \end{bmatrix} \begin{bmatrix} x(t) \\ y(t) \\ \theta(t) \end{bmatrix} = \begin{bmatrix} \mathfrak{f}_x(\mathbf{u}, p) \\ \mathfrak{f}_y(\mathbf{u}, p) \\ \mathfrak{m}_z(\mathbf{u}, p) \end{bmatrix}, \tag{4.36}$$

where the over dot $(\dot{-})$ represents the time derivative, $m$ is the mass of the structure, $I_\theta$ its moment of inertia around $\theta$, $c_i$ and $k_i$ are the structural damping and stiffness in the Cartesian direction $i$ respectively, and $\mathfrak{f}_x$, $\mathfrak{f}_x$ and $\mathfrak{m}_z$ represents the aerodynamic forces and moment in the Cartesian $x$, $y$ and $z$ directions respectively, which are all functions of the fluid velocity field $\mathbf{u}$ and pressure $p$. The structural quantities are also described in figure 4.6 for clarity.

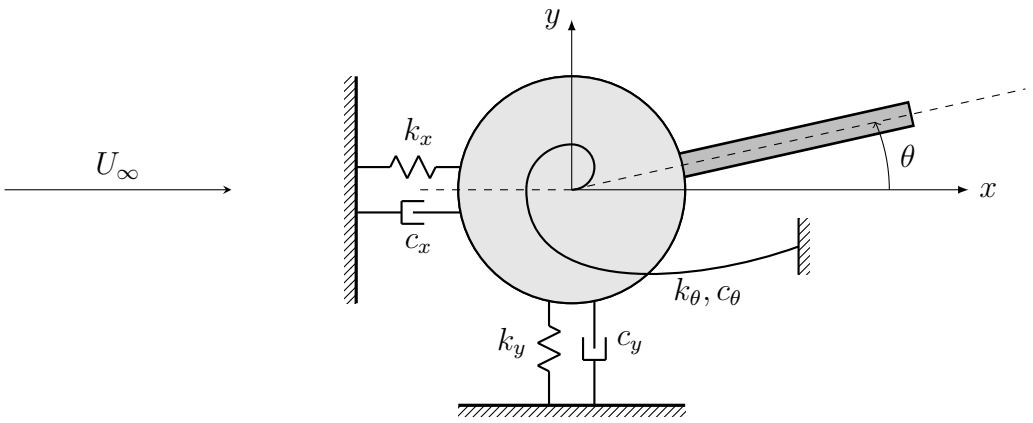



**Figure 4.6:** Description of possible structural degree of freedom and parameters considered.

The expression (4.36) is in practice compactly re-written as

$$\mathbf{M}\ddot{\boldsymbol{\xi}} + \mathbf{C}\dot{\boldsymbol{\xi}} + \mathbf{K}\boldsymbol{\xi} = \mathbf{F}(\mathbf{u}, p), \tag{4.37}$$

where $\boldsymbol{\xi} = [x\ y\ \theta]^T$, and such as it can be decomposed in a system of differential equations,

$$\begin{aligned} \dot{\boldsymbol{\beta}} - \boldsymbol{\alpha} &= \mathbf{0} \\ \mathbf{M}\dot{\boldsymbol{\beta}} + \mathbf{C}\boldsymbol{\beta} + \mathbf{K}\boldsymbol{\alpha} &= \mathbf{F}(\mathbf{u}, p), \end{aligned} \tag{4.38}$$

where $\boldsymbol{\alpha} = \boldsymbol{\xi}$, and $\boldsymbol{\beta} = \dot{\boldsymbol{\xi}}$. The system (4.38) is solved at each time step by the linear multi-steps Adams-Bashforth (for the velocities of the rigid, solid body) and Adams-Moulton (for the positions of the rigid, solid body) numerical schemes, such as velocities and positions are functions of values from previous time steps, respectively. Linear multi-step methods have been proven to be more reliable than single step methods and hence have been chosen in this work in the scope of the high fidelity numerical framework: the spectral/hp element method.
For a $p$-step scheme, the velocities at the step $n+p$ are first obtained by

$$\boldsymbol{\beta}_{n+p} = \boldsymbol{\beta}_{n+p-1} + \Delta t \sum_{i=0}^{p-1} C_{pi}^B \left( \frac{\mathbf{F}(\mathbf{u}, p) - \mathbf{C}\boldsymbol{\beta}_{n+i} - \mathbf{K}\boldsymbol{\alpha}_{n+i}}{\mathbf{M}} \right), \tag{4.39}$$

where $\Delta t$ is the time step size and $C_{pi}^B$ the Adams-Bashforth coefficients. The positions at step $n+p$ are then obtained by

$$\boldsymbol{\alpha}_{n+p} = \boldsymbol{\alpha}_{n+p-1} + \Delta t \sum_{i=0}^{p-1} C_{pi}^M \boldsymbol{\beta}_{n+i}, \tag{4.40}$$

where $C_{pi}^M$ are the Adams-Moulton coefficients, and using $\boldsymbol{\beta}$ resulting from the expression (4.39). The coefficient matrices $C_{pi}^B$ and $C_{pi}^M$ are presented in matrix form below for up to a $p = 3$-step

approach

$$\mathbf{C}^B = \begin{bmatrix} 1 & 0 & 0 \\ -1/2 & 3/2 & 0 \\ 5/12 & -4/3 & 23/12 \end{bmatrix} \quad \text{and} \quad \mathbf{C}^M = \begin{bmatrix} 1 & 0 & 0 \\ 1/2 & 1/2 & 0 \\ -1/12 & 2/3 & 5/12 \end{bmatrix}. \tag{4.41}$$

Across the study, a two-step scheme Adams-Bashforth and Adams-Moulton have been used for all the simulations.

This fluid-structure loosely coupled approach is known to have numerical instabilities at low added mass ratios (Gerbeau et al., 2005). To address this issue, a fictitious mass and inertia term has been added to the structural scheme in the same fashion as described in Baek and Karniadakis (2012). In that case, the following expression including the added fictitious mass or inertia $\mathbf{M}^f$ is considered:

$$\left(\mathbf{M} + \mathbf{M}^f\right) \ddot{\boldsymbol{\xi}} + \mathbf{C}\dot{\boldsymbol{\xi}} + \mathbf{K}\boldsymbol{\xi} = \mathbf{F}(\mathbf{u}, p) + \mathbf{M}^f \ddot{\boldsymbol{\xi}}, \tag{4.42}$$

in which the structural acceleration on the right-hand side of the equations is obtained by linear extrapolation of the previous time step, and the fictitious mass matrix $\mathbf{M}^f$ can be written as

$$\mathbf{M}^f = \begin{bmatrix} m^{Fict} & 0 & 0 \\ 0 & m^{Fict} & 0 \\ 0 & 0 & I_\theta^{Fict} \end{bmatrix}. \tag{4.43}$$

Conceptually, the coupling between fluid and solid can be seen as the contributions at the fluid-solid interface from both "kinematic" and "dynamic" boundary conditions. These two conditions are presented below in the case of the numerical treatment requirements to consider the coordinate transformations. However, the same approach will be used to formally derive the global operators in section §3.1.3 and §3.2.3.

**The kinematic condition**

This kind of boundary condition connects the velocities directly. No mixing nor slipping at the fluid-structure interface $\Gamma$ are considered, so the Dirichlet type boundary condition for the velocities in each direction $i$ is obtained trivially by

$$u^i = V^i = \dot{\xi}^i \quad \text{on } \Gamma, \tag{4.44}$$

where we recall $V^i$ the velocity of the coordinate system.

**The dynamic condition**

This kind of boundary condition connects the forces and moments. It results from the pressure and viscous forces $\sigma$ from the fluid side and the modal force $\mathfrak{f}^s$ on the solid side. Such as for an arbitrary deformation,

$$\begin{aligned} \mathfrak{F}^s(\boldsymbol{\xi}) &= \mathfrak{F}(\mathbf{u}, p), \\ \mathfrak{F}^s(\boldsymbol{\xi}) &= \oint_\Gamma \left\{ \left[ -p\mathbf{I} + Re^{-1} \left( \nabla \mathbf{u} + \nabla^T \mathbf{u} \right) \right] . \mathbf{n} \right\} . \boldsymbol{\phi}_F \, dS, \end{aligned} \tag{4.45}$$

where the modal shape $\boldsymbol{\phi}_F$ is known (in the case of a not deformable, oscillatory cylinder in the vertical direction, $\boldsymbol{\phi}_F$ will be the unit vector of the direction of motion), and $\mathbf{n}$ is the outward unit normal vector on $\Gamma$. Equivalently for the moments

$$\begin{aligned} \mathfrak{M}^s(\boldsymbol{\xi}) &= \mathfrak{M}(\mathbf{u}, p) \\ \mathfrak{M}^s(\boldsymbol{\xi}) &= \oint_\Gamma \left\{ \mathbf{r} \times \left[ -p\mathbf{I} + Re^{-1} \left( \nabla \mathbf{u} + \nabla^T \mathbf{u} \right) \right] . \mathbf{n} \right\} . \boldsymbol{\phi}_M \, dS, \end{aligned} \tag{4.46}$$

where the modal shape $\boldsymbol{\phi}_M$ is also known (corresponding in the study case as the vector containing the Cartesian axis corresponding to the direction of motion) and $\mathbf{r}$ is the vector containing the distances of $dS$ from the hinge point.

Since that in the chosen numerical representation, all the computations are executed in the transformed coordinate system, the transformation needs to be taken into account in the aerodynamic forces and moments computation in order to obtain their Cartesian counterparts. In the Cartesian coordinate system $(\bar{x}, \bar{y}, \bar{z})$, the aerodynamic forces are obtained in each $i$ direction by integrating over the surface $\Gamma$

$$\bar{\mathfrak{F}}^i = \oint_\Gamma \bar{\sigma}^{ij} d\bar{S}_i, \tag{4.47}$$

and the moments by

$$\bar{\mathfrak{M}}^i = \oint_\Gamma \left[ \bar{r}_i \times \left( \bar{\sigma}^{ij} \bar{n}_i \right) \right] d\bar{S}, \tag{4.48}$$

where $\bar{\sigma}^{ij}$ is the stress tensor defined by:

$$\bar{\sigma}^{ij} = -\delta^{ij} p + Re^{-1} \left[ \frac{\partial \bar{u}^i}{\partial \bar{x}^j} + \frac{\partial \bar{u}^j}{\partial \bar{x}^i} \right], \tag{4.49}$$

and $d\bar{S}_i = \bar{n}_i d\bar{S}$ is the surface element oriented by the normal vector when $\bar{r}_i$ is the *i-th* component of the distance of $d\bar{S}$ from the hinge point.

In the transformed coordinate system $(x, y, z)$, these quantities read:

$$\sigma^{ij} = -g^{ij}p + \nu \left[ g^{pj} u^i_{,p} + g^{pi} u^j_{,p} \right], \tag{4.50}$$

and $dS_i = Jn_i dS$, where $J$ stands for the Jacobian of the deformation to the cartesian system.

So finally, in the *i-th* direction:

$$\mathfrak{F}^i = \oint_\Gamma \sigma^{ij} J n_i dS, \tag{4.51}$$

and:

$$\mathfrak{M}^i = \oint_\Gamma \left[ r_i \times \left( \sigma^{ij} n_i \right) \right] J dS. \tag{4.52}$$

## 4.3 Linear Stability Analysis

In the scope of linear stability analysis considered in this research, the equations system is linearised around its base flow, and the evolution in time of a given perturbed quantity over this base state is questioned (see §3.2). This section aims to present the basics of the theory on which the section §3.2 is further built, taking the example of the linearisation process of the Navier-Stokes equations in an incompressible regime.

The general idea behind linear stability analysis is to rewrite the solution of the equation system of interest (*i.e* the Navier-Stokes equations in incompressible regime (4.20)) into the sum of a basic state $(\mathbf{U}, P)$, that we refer as the base flow field, and a perturbed state $(\mathbf{u}', p')$, that we refer as perturbation field. So the solution now reads

$$(\mathbf{u}, p) = (\mathbf{U}, P) + \varepsilon(\mathbf{u}', p') \quad \text{where} \quad \varepsilon \ll 1. \tag{4.53}$$

Injecting the quantity (4.53) into the expression (4.20) leads to

$$\begin{gathered} \frac{\partial \mathbf{U}}{\partial t} + \varepsilon \frac{\partial \mathbf{u}'}{\partial t} + (\mathbf{U} \cdot \nabla)\mathbf{U} + \varepsilon \left( \mathbf{U} \cdot \nabla \mathbf{u}' + \mathbf{u}' \cdot \nabla \mathbf{U} \right) = -\left( \nabla P + \varepsilon \nabla p' \right) + Re^{-1} \nabla^2 \mathbf{U} + \varepsilon Re^{-1} \nabla^2 \mathbf{u}' \\ \nabla \cdot \mathbf{U} + \varepsilon \nabla \cdot \mathbf{u}' = 0, \end{gathered} \tag{4.54}$$

neglecting the terms proportional to $\varepsilon^2$. The first order terms (*i.e.* proportional to $\varepsilon$) of the expression (4.54) finally reads

$$\begin{gathered} \frac{\partial \mathbf{u}'}{\partial t} + \mathbf{U} \cdot \nabla \mathbf{u}' + \mathbf{u}' \cdot \nabla \mathbf{U} = -\nabla p + Re^{-1} \nabla^2 \mathbf{u}' \\ \nabla \cdot \mathbf{u}' = 0, \end{gathered} \tag{4.55}$$

and the base state $(\mathbf{U}, P)$ is simply solution of the equation (4.20).

Since we recognise the linearised Navier-Stokes equations (4.55) of the same structure as their non-linear counterpart, they can numerically be solved using the same techniques after modification of the advection term.
From this point, the equation (4.55) is rewritten in terms of the operator that evolve the perturbation field forward in time, and hence implicitly depends on $t$ (Barkley et al., 2008*a*)

$$\mathbf{u}'(\mathbf{x},t) = \mathcal{F}'_u(\mathbf{U},t)\mathbf{u}'(\mathbf{x},0), \tag{4.56}$$

where $\mathcal{F}'_u$ is, therefore, the linear operator of the problem solving the velocity vector $\mathbf{u}'$, and the linear stability of the base state is investigated through the equation (4.56). In this work, we only consider steady base flows, so the perturbation equations (4.55) are autonomous and eigenmode solutions are assumed to be of the form

$$\mathbf{u}'(\mathbf{x},t) = \hat{\mathbf{u}}(\mathbf{x})e^{\lambda t} \quad \text{where} \quad \hat{\mathbf{u}}, \lambda \in \mathbb{C}, \tag{4.57}$$

and associated to the eigenproblem

$$\mathcal{F}'_u(\mathbf{U},T)\hat{\mathbf{u}} = \lambda\hat{\mathbf{u}}. \tag{4.58}$$

the time $T$ is in practice, an arbitrary positive value chosen sufficiently large to allow the perturbation to evolve and will later correspond to Arnoldi's period in section §4.3.3.
The stability of the base state $(\mathbf{U}, P)$ is at last determined from the real part of the dominant (largest modulus) eigenvalues $\lambda$ of $\mathcal{F}'_u$. If $\lambda_r > 0$ (the subscript $r$ denotes the real part), there exists exponentially growing solutions of the equation (4.55) and the flow is said linearly unstable, conversely if every single eigenvalue has negative real part ($\lambda_r < 0$) then the flow is said to be linearly stable (*i.e.* every solution of (4.55) eventually decays to zero). Finally $\lambda_r = 0$ represents a bifurcation point.
On the other hand, the imaginary part of the eigenvalues $\lambda_i$ (the subscript $i$ denotes the imaginary part) determines the frequencies associated with the modes $\hat{\mathbf{u}}$.

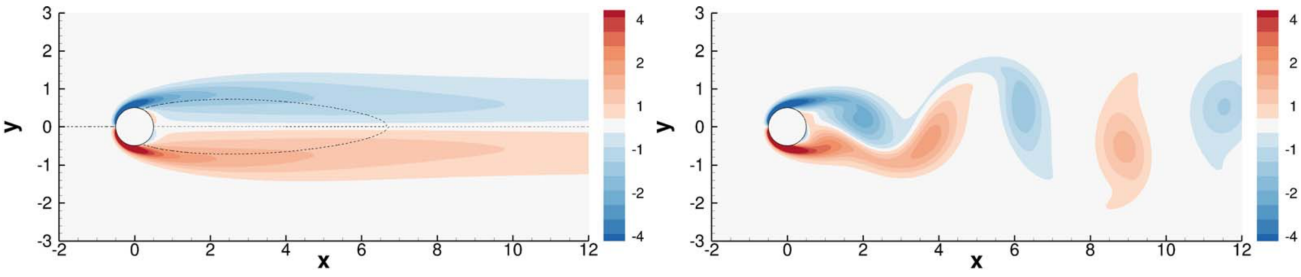
The linear stability analysis is further employed to investigate the problem considered (*i.e.*, fluid-structure interactions) in this research, and the operators involved are presented in section §3.2.

### 4.3.1 The Selective Frequency Damping

The first step in the process of linear stability analysis investigation is to generate a base state, and its quality is directly correlated to the accuracy of the results. Across this study, only steady base flows are considered.
The method used to generate the steady-state solution of the Navier-Stokes equations as the

base flow for unstable configurations is the encapsulated formulation of the Selective Frequency Damping (SFD) method (Akervik et al., 2006*a*; Jordi et al., 2014).

Figure 4.7 presents an example of visualisation of a stabilised flow around a circular cylinder at $Re = 100$ using the SFD method along with its re-circulation bubble region in dashed line (4.7a), opposed to its non-stabilised counterpart (4.7b). Figure 4.7b is obtained by solving the incompressible Navier-Stokes equations (4.20) as presented in section §4.1.3.




**(a)** Steady-state obtained by SFD. **(b)** Conventional simulation.

**Figure 4.7:** Vorticity visualisation of the flow around a circular cylinder at $Re = 100$, with and without the use of the stabilisation technique. Extracted from Jordi et al. (2014).

The concept of the SFD method is presented here in a continuous formulation, which can serve as a basis to derive the discrete formulation (Jordi et al., 2014). Given a system of differential equations

$$\dot{\mathbf{q}} = \bar{\mathcal{F}}\mathbf{q}, \tag{4.59}$$

with appropriate initial and boundary conditions, where $\mathbf{q}$ represents the problem state variables and $\bar{\mathcal{F}}$ is the operator of the system (4.59). Hence, practically applied to the present study, $\mathbf{q} = (\mathbf{u}, p)$ represents the fluid variables and $\bar{\mathcal{F}}$ is the steady Navier Stokes operator (without the time derivative term). By definition, the investigated steady-state $\mathbf{q}_s$ of this problem is reached when $\dot{\mathbf{q}}_s = \bar{\mathcal{F}}\mathbf{q}_s = \mathbf{0}$.
A linear forcing term is added on the right-hand side of the expression (4.59) containing a control coefficient $\chi \in \mathbb{R}^+$ and a steady-state target solution $\mathbf{q}_s$ such as

$$\dot{\mathbf{q}} = \bar{\mathcal{F}}\mathbf{q} - \chi\left(\mathbf{q} - \mathbf{q}_s\right). \tag{4.60}$$

This approach is widely used in the field of control theory problems (Kim and Bewley, 2007), under the name "proportional feedback control". Although a trivial solution to the equation (4.60) would be $\mathbf{q} = \mathbf{q}_s$ where $\bar{\mathcal{F}}\mathbf{q}_s = 0$, the steady-state is not known beforehand and hence $\mathbf{q}_s$ is replaced by a low-pass filtered version of $\mathbf{q}$, denoted $\bar{\mathbf{q}}$. Hence the solution is gradually "stabilised" by damping the most important frequencies (Akervik et al., 2006*b*). This concept originates from the work of Pruett et al. (2003, 2006) to derive a temporal filtered model for large-eddy simulations.

In practice, the differential form of the transfer function of the first-order low-pass time filter is used for the SFD method

$$\dot{\bar{\mathbf{q}}} = \frac{\mathbf{q} - \bar{\mathbf{q}}}{\Delta}, \tag{4.61}$$

where $\bar{\mathbf{q}}$ is the above described temporally filtered quantity, and $\Delta \in \mathbb{R}^{+*}$ is the so-called filter width. The expression (4.61) can be advanced in time using any appropriate integration scheme, so that the equation (4.60) is reformulated and the continuous-time formulation of the SFD method (as it was first introduced (Akervik et al., 2006*b*)) reads

$$\begin{cases} \dot{\mathbf{q}} = \bar{\mathcal{F}}\mathbf{q} - \chi(\mathbf{q} - \bar{\mathbf{q}}) \\ \dot{\bar{\mathbf{q}}} = \dfrac{\mathbf{q} - \bar{\mathbf{q}}}{\Delta} \end{cases} . \tag{4.62}$$

Finally, the steady-state solution is reached when $q = \bar{q}$, which we numerically approximate by $\|\mathbf{q} - \bar{\mathbf{q}}\|_\infty < tol$. The practical time discretisation of this approach is detailed in Jordi et al. (2014), and can also be connected to other works on of modified time stepping approaches to compute bifurcation analysis (Tuckerman and Barkley, 2000).
The rate of convergence of $\|\mathbf{q} - \bar{\mathbf{q}}\|_\infty \to 0$ is known to be correlated to the choice of the parameters $\chi$ and $\Delta$. Large values will increase the chance of convergence yet lower its rate, whereas small values will reduce the "damping factor", and hence the method may not converge. For all the SFD simulations undertaken in this research, the parameters $\chi = 1$, $\Delta = 2$ and $tol = 10^{-8}$ have shown an acceptable behaviour of the convergence and quality of the solution.

### 4.3.2 Solutions to the associated eigenvalue problem

Once the base state $(\mathbf{U}, P)$ is obtained, the associated eigenvalue problem (4.58) can be investigated. In this study, a numerically suitable approach to investigate the dominant eigenvalues of the linear operator $\mathcal{F}'_u$ is the Arnoldi's method, through which one can obtain a finite set of the approximated dominant eigenvalues.
The principles of this approach are presented in this section and are based on the practical formulation described in Barkley et al. (2008*b*). The reader is also referred to Saad (1992) for a more formal and detailed presentation of the topic.

The idea of Arnoldi's iteration is to project the matrix form $\mathbf{\Lambda}$ of the operator $\mathcal{F}'_u$ onto a finite-dimensional Krylov subspace $\mathbf{K}_{n+1}$ where direct diagonalization is possible. It is noted that because the columns of this matrix are not in general orthogonal, it is extracted an orthogonal basis via a Gram–Schmidt orthogonalization. The resulting set of vectors is then an orthogonal basis of the Krylov subspace $\mathbf{K}_{n+1}$. The vectors of this basis are finally considered to span good approximations of the eigenvectors corresponding to the $n+1$ largest eigenvalues.
In practice, the $n+1$ vectors of the Krylov sequence $\left[\mathbf{u}_0, \mathbf{\Lambda}\mathbf{u}_0, \mathbf{\Lambda}^2\mathbf{u}_0, \ldots, \mathbf{\Lambda}^n\mathbf{u}_0\right]$ are obtained by power iteration, ($n$ repeated actions of the operator $\mathbf{\Lambda}$) starting from an arbitrary random initial

vector $\mathbf{u}_0$ of unit norm (*i.e.* $\|\mathbf{u}_0\| = 1$), and normalized one by one by $\alpha_i = \|\mathbf{\Lambda u}_{i-1}\|\,,\ \forall i \in [\![1, n]\!]$

$$\mathbf{K}_{n+1} = [\mathbf{u}_0, \mathbf{u}_1, \mathbf{u}_2, \ldots, \mathbf{u}_n] = \left[\frac{\mathbf{u}_0}{\alpha_0}, \frac{\mathbf{\Lambda u}_0}{\alpha_1}, \frac{\mathbf{\Lambda u}_1}{\alpha_2}, \ldots, \frac{\mathbf{\Lambda u}_{n-1}}{\alpha_n}\right], \tag{4.63}$$

where $\mathbf{\Lambda u}_i$ is in practice obtained by computing $\mathcal{F}'_u(\mathbf{U}, T)\mathbf{u}_i$ and $T$ is hence the Arnoldi's period.
From this vector sequence, $m$ eigenvectors and corresponding eigenvalues of the largest magnitude are computed as follows:

(i) At the Arnoldi iteration $j \leq m-1$, the Krylov subspace $\mathbf{K}_j$ is updated, orthonormalization is performed by a modified Gram–Schmidt procedure, the eigenvectors of $\mathbf{H}_k$ (*i.e.* the upper Hessenberg matrix representing the orthogonal projection of $\mathbf{\Lambda}$ onto $\mathbf{K}_{j-1}$) are computed, and the associated residual norms $\epsilon_i,\ i \in [\![0, j]\!]$ are calculated.

(ii) If the required number of residual norms is not sufficiently small (*i.e.* if $\exists \epsilon_i > tol,\ i \in [\![0, m-1]\!]$, where *tol* is a specified convergence tolerance), then another Krylov vector is added to $\mathbf{K}_j$.

(iii) If the Krylov subspace dimension reaches a specified maximum before convergence, the oldest vector is discarded, thus keeping the Krylov subspace size constant. This is equivalent to restarting the method with the second oldest vector in the sequence.

(iv) Once the required eigenvalues have converged (*i.e.* if $\forall j \in [\![0, m-1]\!],\ \epsilon_j < tol$), the Ritz approximations of the correspondent eigenvectors of $\mathbf{\Lambda}$ are computed.

### 4.3.3 Implementation details

The Spectral/hp element method framework available through the library *Nektar++* (Cantwell et al., 2015) have been used in the present work. At the time of the study, the numerical framework already had the tools necessary to solve and compute, among others: the non-linear fluid structure interaction problem by coordinate transformation (Serson et al., 2016); the fluid-only direct (3.25) and adjoint (3.53) problems; the Arnoldi's iteration §4.3.3 for the linearised (both direct and adjoint) incompressible Navier-Stokes equations; the SFD method §4.3.1 for base flows generation.

To take into account the different coupling between the fluid and structural problems presented in chapter §3, the following modifications have been implemented to the numerical framework *Nektar++*:

1. The direct solver for two-dimensional, fluid/rigid structure interaction problems §3.2.4 have been modified to employ a blowing suction boundary condition (3.40) at the interface

of the direct fluid solver (3.25) using solutions of the structural problem (3.29) forced by the linearised aerodynamic forces and moment (identical in that case to the non-linear problem) (3.42) and (3.43).
Compactly presented in expression (3.46).

2. The adjoint solver for two-dimensional, fluid/rigid structure interaction problems §3.3.2 have been modified to employ a blowing suction boundary condition (3.60b) at the interface of the adjoint fluid solver (3.53) using solutions of the adjoint structural problem (3.52) forced by the adjoint aerodynamic forces and moment (3.57).
Compactly presented in expression (3.60).

3. The Arnoldi's iteration §4.3.3 was modified to take into account both the fluid and structural variables $\mathbf{s} = [\boldsymbol{\xi}\ \mathbf{q}]^T$ (instead of only $\mathbf{u}_i$ in expression (4.63)), such as the eigenvalue computation of the coupled fluid structure interaction system follow the same approach *i.e.*, the Krylov subspace is constructed by the temporal snapshots of the coupled fluid structure interaction linearised and adjoint systems.

4. A fictitious mass strategy (4.42) for the non-linear (3.13), direct and adjoint (3.60c) structural equations, that allows the numerical framework to deal with lower added mass ratios.

# Chapter 5

# Numerical scheme convergence and formulation validation

This chapter presents the results obtained varying the numerical parameters influencing the quality of the study, as the mesh refinement and spatial discretisation (*i.e.* the $h$-refinement presented in section §5.1), the order of the expansion basis, along with an appropriate time discretisation (*i.e.* the $p$-refinement presented in section §5.2) and the physical domain size required for both linear and non-linear analysis, presented in section §5.3.
The results presenting the non-linear (corresponding to the full order fluid operator $\mathcal{F}$) fluid convergence *i.e.* the sections §5.1, §5.2 and §5.3.1, are undertaken considering the flow configuration of a stationary circular cylinder of diameter $D$ without splitter plate immersed in a constant flow rate governed by the Navier-Stokes equations in incompressible regime presented in expression (4.20) at a fixed Reynolds number $Re = 100$, along with appropriate boundaries conditions, and a "no-slip" type at the cylinder interface, corresponding in full to the system (3.18) considering the solid at rest (*i.e.* $\dot{\gamma} = 0$ in the system (3.18)).

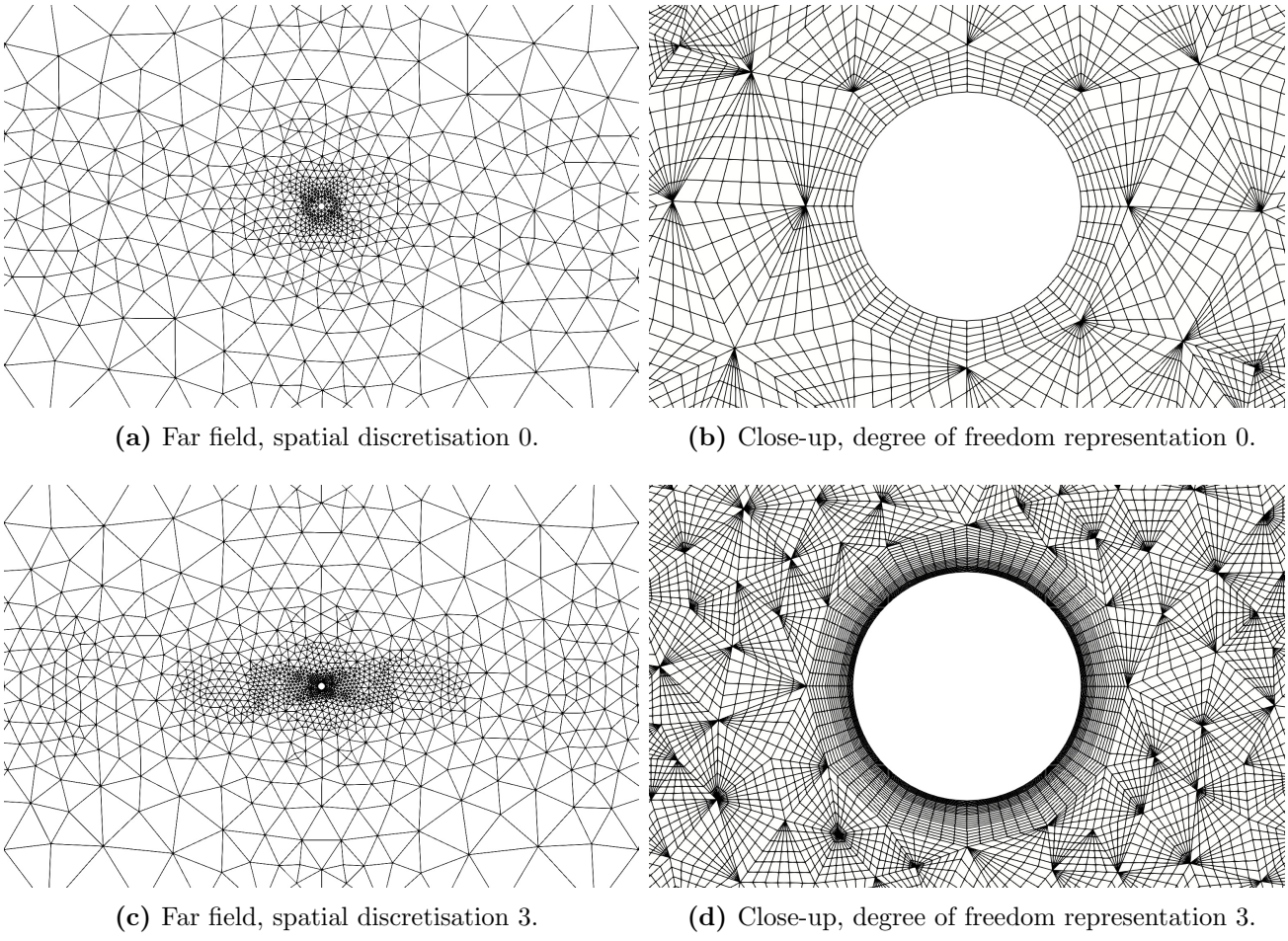
For the sections §5.1 and §5.2 the numerical accuracy *i.e.* the mesh refinement or the expansion basis order, have been gradually increased until 5 significant figures (corresponding to up to $\pm 10^{-3}\%$ of absolute relative change visible) precision where obtained for the data considered: $C_l'$, the root mean square of the lift coefficient $C_l$; $\bar{C}_d$, the temporal mean of the drag coefficient $C_d$; and $St$ the Strouhal frequency.
The quantities $C_l'$, $\bar{C}_d$ and $St$ are obtained and computed from the numerical time $t_f$ at which the simulations reaches a fully established regime.

Finally, for all the simulations presented, the domain is spatially symmetrically discretised in the in-line and cross-flow directions, and the cylinder is placed at the geometric centre of the computational domain, leading to about twice as much as elements than a "classically" discretised domain - as in this case the downstream direction is as long as the upstream direction. This choice of centred cylinder has been made to allow the adjoint system to benefit from the

same physical space than the direct system, as the adjoint perturbations tend to propagate in the upstream direction to the cylinder, whereas the direct perturbations are located downstream to the cylinder.

## 5.1 $h$-refinement

For this part of the convergence tests, the computational domain size is fixed to the dimensions: $-30 \leq y \leq 30$ and $-50 \leq x \leq 50$, where the circular cylinder is placed at $(x, y) = (0, 0)$ as stated above. The order of the expansion basis is set to $P = 7$, along with a non-dimensional time step $\Delta t = 1 \cdot 10^{-3}$.
For all the tests undertaken in this section (*i.e* thee meshes 0 to 4 in table 5.1), this choice of parameters has kept the Courant-Friedrichs-Lewy (CFL) in the range of $0 \lesssim CFL \lesssim 0.1$.



**(a)** Far field, spatial discretisation 0.

**(b)** Close-up, degree of freedom representation 0.

**(c)** Far field, spatial discretisation 3.

**(d)** Close-up, degree of freedom representation 3.

**Figure 5.1:** Example of size distribution of elements (a) used for the discretisations 0 and 3. The close-up in (b) shows the quadrature points for $P = 7$ in both cases (0 and 3).

Two representative examples of mesh are shown in figure 5.1, corresponding to the boundary layer thickness and numbers of layers used for the discretisations 0 and 3 in table 5.1. To test

the $h$-convergence, the domain computational $\Omega$ is spatially discretised and locally refined using $Nekmesh$, the built-in mesh generator of $Nektar++$ (Cantwell et al., 2015), which generates curvilinear boundary conforming meshes, where fourth order elements curvature is used for all the tests presented. Quadrilateral elements are adopted in the boundary layer's region close to the structure's interface organised in structured layers, and triangular elements are used in the other regions of the domain, resulting in an unstructured mesh.

Five meshes are tested following this spatial discretisation approach, represented by the meshes numerations from 0 to 4 in table 5.1. The "complexity" of the discretisation and the global refinement is increased gradually from mesh 0 (coarser) to mesh 5 (finer). The complexity parameters of the meshes considered in these tests are chosen to be the normalised boundary layer thickness (normalised by the cylinder diameter $D$) denoted by $BL_{th}$ in table 5.1, and the number of layers of quadrilateral elements inside the boundary layer, denoted by $BL_{el}$ in table 5.1. The global refinement of each mesh is also presented in table 5.1 denoted by $Nb_{el}$, corresponding to the total number of elements for the corresponding meshes.
Finally, for every mesh the corresponding physical quantities of interest $C_l'$, $\bar{C}_d$, and $St$ are also presented in table 5.1.

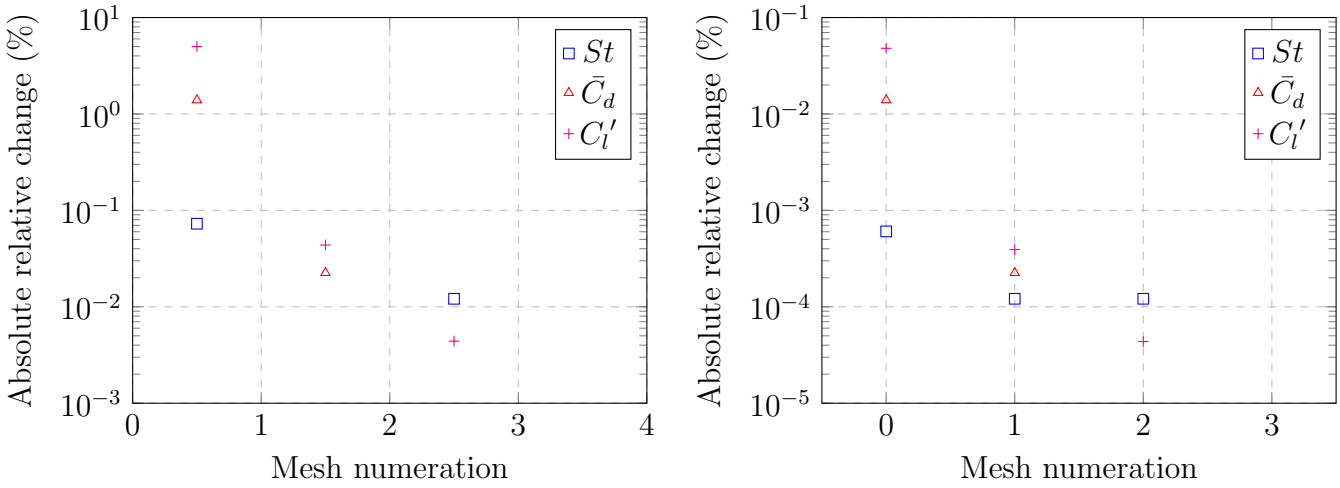
| Name | $Nb_{el}$ | $BL_{th}$ | $BL_{el}$ | $St \cdot 10^{-1}$ | $\bar{C}_d$ | $C_l' \cdot 10^{-1}$ |
|---|---|---|---|---|---|---|
| Mesh 0 | 892 | 0.3 | 1 | 1.6507 | 1.3150 | 2.1814 |
| Mesh 1 | 1342 | 0.2 | 1 | 1.6519 | 1.3333 | 2.2904 |
| Mesh 2 | 1810 | 0.2 | 2 | 1.6519 | 1.3336 | 2.2914 |
| Mesh 3 | 1892 | 0.2 | 3 | 1.6517 | 1.3336 | 2.2913 |
| Mesh 4 | 2282 | 0.2 | 4 | 1.6517 | 1.3336 | 2.2913 |

**Table 5.1:** $h$-refinement summary.

No changes in the physical quantities are noted between the discretisation 3 and 4, as presented in table 5.1. Thus the spatial discretisation of the mesh 3 is adopted to conduct the $p$-refinements tests presented in the following section.

In figure 5.2a is presented a visualisation of the relative change of the physical quantities $C_l'$, $\bar{C}_d$, and $St$, between two consecutive mesh numerations (*i.e.* spatial refinements) presented in table 5.1. This figure stresses the fact that changes inferior to $10^{-3}$ of relative change are presents comparing the refinements 3 and 4.

In figure 5.2b is presented the absolute value of the relative error taken by reference with regard to the most refined mesh: Mesh 4. The outcome is similar for this choice of error representation.




**(a)** Absolute value of the relative error taken in between two consecutive meshes.

**(b)** Absolute value of the relative error taken with regard to mesh 4.

**Figure 5.2:** $h$-convergency diagrams.

## 5.2 $p$-refinement

For this second part of convergence tests, the spatial discretisation 3 (see table 5.1) is adopted, and only the order of the expansion basis is varied between $3 < P < 11$. The non-dimensional time step $\Delta t$ is adjusted, such as the Courant-Friedrichs-Lewy is kept in the range $0.1 \leq CFL \leq 0.3$.

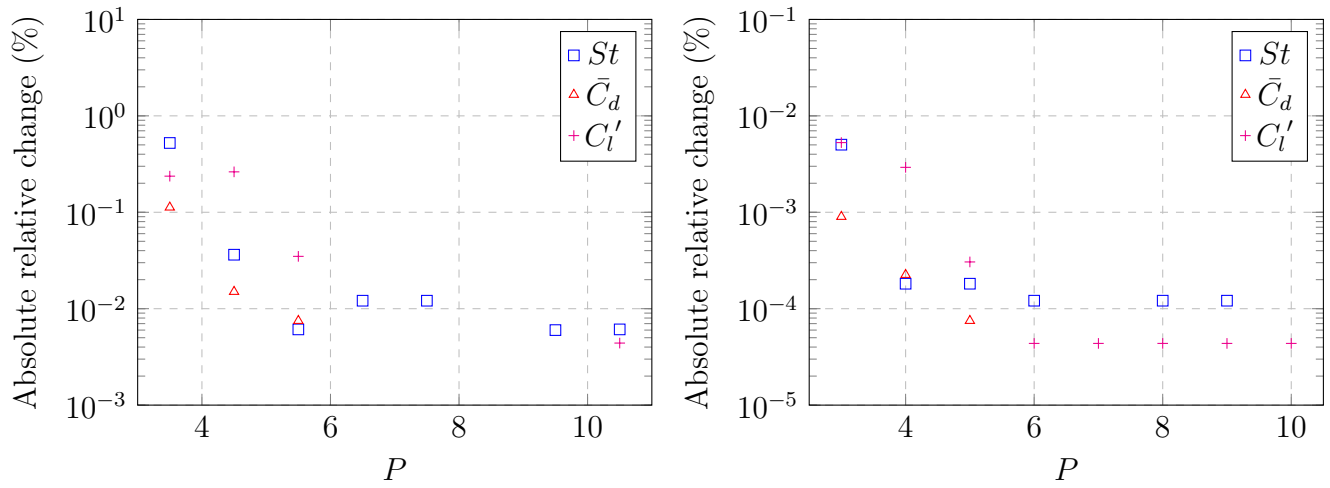
Table 5.2 summarises the values obtained for the physical quantities $C_l'$, $\bar{C}_d$, and $St$, varying the order of the expansion basis.

| P | $\Delta t$ | $St \cdot 10^{-1}$ | $\bar{C}_d$ | $C_l' \cdot 10^{-1}$ |
|---|---|---|---|---|
| 3 | $1 \cdot 10^{-2}$ | 1.6436 | 1.3348 | 2.2791 |
| 4 | $4 \cdot 10^{-3}$ | 1.6522 | 1.3333 | 2.2845 |
| 5 | $2 \cdot 10^{-3}$ | 1.6516 | 1.3335 | 2.2905 |
| 6 | $1 \cdot 10^{-3}$ | 1.6517 | 1.3336 | 2.2913 |
| 7 | $1 \cdot 10^{-3}$ | 1.6519 | 1.3336 | 2.2913 |
| 8 | $1 \cdot 10^{-3}$ | 1.6517 | 1.3336 | 2.2913 |
| 9 | $1 \cdot 10^{-3}$ | 1.6517 | 1.3336 | 2.2913 |
| 10 | $8 \cdot 10^{-4}$ | 1.6518 | 1.3336 | 2.2913 |
| 11 | $5 \cdot 10^{-4}$ | 1.6519 | 1.3336 | 2.2912 |

**Table 5.2:** $p$-refinement summary.

As also clearly visually represented in figure 5.3a, no considerable ($< 10^{-3}$) changes of time average drag and rms lift are noted from $P = 7$, hence the order of the expansion basis $P = 7$ is chosen for the rest of the study.

On the other hand, the value of the shedding frequency appears to stop converging from $P = 6$ on this particular test. This observation is associated with the fact that the vortex shedding frequency is sensitive to both the quality of the numerical discretisation (combination of $h$ and $p$-refinements) and the physical space in which the vortex street is able to evolve and converge through its fully established state. In numerical studies, the latter is associated to the physical size of the domain $\Omega$ and is kept constant ($i.e$ $-30 \leq y \leq 30$ and $-50 \leq x \leq 50$) in this section. The sensitivity to changes in the domain size of the physical quantities $C_l'$, $\bar{C}_d$, and $St$ discussed in these two sections §5.1 and §5.2 is presented in the following section §5.3.




**(a)** Absolute value of the relative error taken in between two consecutive orders $P$.

**(b)** Absolute value of the relative error taken with regard to $P$=11.

**Figure 5.3:** $p$-convergency diagrams.

On figure 5.3b, is also presented the absolute value of the relative error taken with regard to the highest polynomial order expansion tested in this study: $P = 11$. The outcome is similar for this choice of error representation than for figure 5.3a.

## 5.3 Domain size refinement

The effect of the computational domain size on the quality of the solutions is discussed in this section for both full order ($i.e.$ non-linear problem) and linear ($i.e.$ both direct and adjoint problems) simulations.

In the case of the non-linear simulations, the sensitivity of the physical quantities $C_l'$, $\bar{C}_d$, and $St$

with regard to the changes in the computational domain dimensions in the case of the circular cylinder at $Re = 100$ is discussed in the sub-section §5.3.1.
In the case of linear simulations, the quantity considered to evaluate the quality of the computational domain size is the difference between the eigenvalues of the vortex shedding mode for both direct and adjoint simulations. This analysis is presented in sub-section §5.3.2.

### 5.3.1 Domain size for non-linear analysis

The influence of the domain size on the quality of the simulation is first reviewed in this sub-section, taking the same test case presented in the sections §5.1 and §5.2 described above.

The strategy is to gradually increase the domain size in both the streamwise and cross-flow directions, starting from $-30 \leq x \leq 30$ and $-10 \leq y \leq 10$ until obtaining an acceptable absolute relative change of the physical quantities $C_l'$, $\bar{C}_d$, and $St$ between two consecutive steps.

| $\lvert y\rvert$ \ $\lvert x\rvert$ | 30 | 40 | 50 | 60 | 70 | 80 | 90 | 100 |
|---|---|---|---|---|---|---|---|---|
| 10 | 1.6884 | 1.6884 | 1.6884 | 1.6883 | 1.6883 | 1.6883 | 1.6883 | 1.6884 |
| 20 | 1.6603 | 1.6598 | 1.6597 | 1.6597 | 1.6595 | 1.6595 | 1.6595 | 1.6597 |
| 30 | 1.6535 | 1.6523 | 1.6519 | 1.6516 | 1.6515 | 1.6516 | 1.6515 | 1.6515 |
| 40 | 1.6509 | 1.6493 | 1.6484 | 1.6480 | 1.6479 | 1.6477 | 1.6477 | 1.6476 |
| 50 | 1.6497 | 1.6479 | 1.6469 | 1.6462 | 1.6459 | 1.6456 | 1.6456 | 1.6454 |
| 60 | 1.6493 | 1.6469 | 1.6459 | 1.6452 | 1.6446 | 1.6445 | 1.6442 | 1.6442 |
| 70 | 1.6489 | 1.6466 | 1.6452 | 1.6445 | 1.6437 | 1.6436 | 1.6433 | 1.6432 |
| 80 | 1.6487 | 1.6462 | 1.6449 | 1.6440 | 1.6433 | 1.6430 | 1.6427 | 1.6425 |

| $\lvert y\rvert$ \ $\lvert x\rvert$ | 110 | 120 | 130 |
|---|---|---|---|
| 90 | 1.6419 | 1.6418 | 1.6416 |
| 100 | 1.6415 | 1.6413 | 1.6412 |
| 110 | 1.6412 | 1.6410 | 1.6410 |

**Table 5.3:** $St \cdot 10^{-1}$ variations. Mesh 3, $P = 7$.

| $\lvert y\rvert$ \ $\lvert x\rvert$ | 30 | 40 | 50 | 60 | 70 | 80 | 90 | 100 |
|---|---|---|---|---|---|---|---|---|
| 10 | 1.3725 | 1.3725 | 1.3725 | 1.3725 | 1.3725 | 1.3725 | 1.3725 | 1.3725 |
| 20 | 1.3429 | 1.3422 | 1.3421 | 1.3420 | 1.3420 | 1.3420 | 1.3420 | 1.3420 |
| 30 | 1.3358 | 1.3342 | 1.3336 | 1.3333 | 1.3332 | 1.3332 | 1.3332 | 1.3332 |
| 40 | 1.3332 | 1.3309 | 1.3299 | 1.3293 | 1.3291 | 1.3290 | 1.3289 | 1.3289 |
| 50 | 1.3320 | 1.3294 | 1.3280 | 1.3272 | 1.3269 | 1.3266 | 1.3265 | 1.3264 |
| 60 | 1.3313 | 1.3285 | 1.3270 | 1.3260 | 1.3255 | 1.3252 | 1.3250 | 1.3248 |
| 70 | 1.3310 | 1.3280 | 1.3263 | 1.3253 | 1.3246 | 1.3242 | 1.3239 | 1.3238 |
| 80 | 1.3308 | 1.3277 | 1.3259 | 1.3248 | 1.3241 | 1.3236 | 1.3233 | 1.3230 |

| $\lvert y\rvert$ \ $\lvert x\rvert$ | 110 | 120 | 130 |
|---|---|---|---|
| 90 | 1.3223 | 1.3222 | 1.3221 |
| 100 | 1.3219 | 1.3217 | 1.3216 |
| 110 | 1.3216 | 1.3214 | 1.3213 |

**Table 5.4:** $\bar{C_d}$ variations. Mesh 3, $P = 7$.

| $\lvert y\rvert$ \ $\lvert x\rvert$ | 30 | 40 | 50 | 60 | 70 | 80 | 90 | 100 |
|---|---|---|---|---|---|---|---|---|
| 10 | 2.3767 | 2.3768 | 2.3769 | 2.3770 | 2.3770 | 2.3770 | 2.3769 | 2.3768 |
| 20 | 2.3123 | 2.3110 | 2.3110 | 2.3104 | 2.3106 | 2.3106 | 2.3105 | 2.3106 |
| 30 | 2.2972 | 2.2928 | 2.2913 | 2.2898 | 2.2899 | 2.2897 | 2.2897 | 2.2896 |
| 40 | 2.2918 | 2.2854 | 2.2825 | 2.2801 | 2.2797 | 2.2795 | 2.2791 | 2.2792 |
| 50 | 2.2895 | 2.2818 | 2.2779 | 2.2749 | 2.2740 | 2.2734 | 2.2728 | 2.2729 |
| 60 | 2.2881 | 2.2799 | 2.2755 | 2.2720 | 2.2707 | 2.2697 | 2.2690 | 2.2687 |
| 70 | 2.2874 | 2.2789 | 2.2739 | 2.2701 | 2.2686 | 2.2672 | 2.2663 | 2.2659 |
| 80 | 2.2872 | 2.2782 | 2.2729 | 2.2688 | 2.2673 | 2.2656 | 2.2645 | 2.2640 |

| $\lvert y\rvert$ \ $\lvert x\rvert$ | 110 | 120 | 130 |
|---|---|---|---|
| 90 | 2.2620 | 2.2616 | 2.2614 |
| 100 | 2.2609 | 2.2604 | 2.2602 |
| 110 | 2.2601 | 2.2596 | 2.2591 |

**Table 5.5:** $C_l' \cdot 10^{-1}$ variations. Mesh 3, $P = 7$.

As presented in tables 5.3, 5.4 and 5.5, the convergence criterion used for the $h$ and $p$ conver-

gence tests at $\leq 1 \cdot 10^{-3}\%$ between two consecutive steps would lead to a gigantic domain ($> 500$ diameters) in both directions $x$ and $y$. Thus for the domain size, the convergence criterion is set arbitrarily to $\leq 5 \cdot 10^{-1}\%$ of change between two consecutive steps, which leads to an overall size of $(\bar{x}, \bar{y}) = (80, 60) \Leftrightarrow |x| = 40$, and $|y| = 30$ with a centred cylinder.
Taking the example of the most sensible parameter to the domain size variation, the root mean square of the lift coefficient $C_l{}'$ here in the cross flow direction, from $|y| = 30$ to 40, the relative change is $\simeq 0.3227\%$ at $|x| = 40$. And in the streamwise direction from $|x| = 40$ to 50 the relative change is $\simeq 0.0006\%$ at $|y| = 30$.

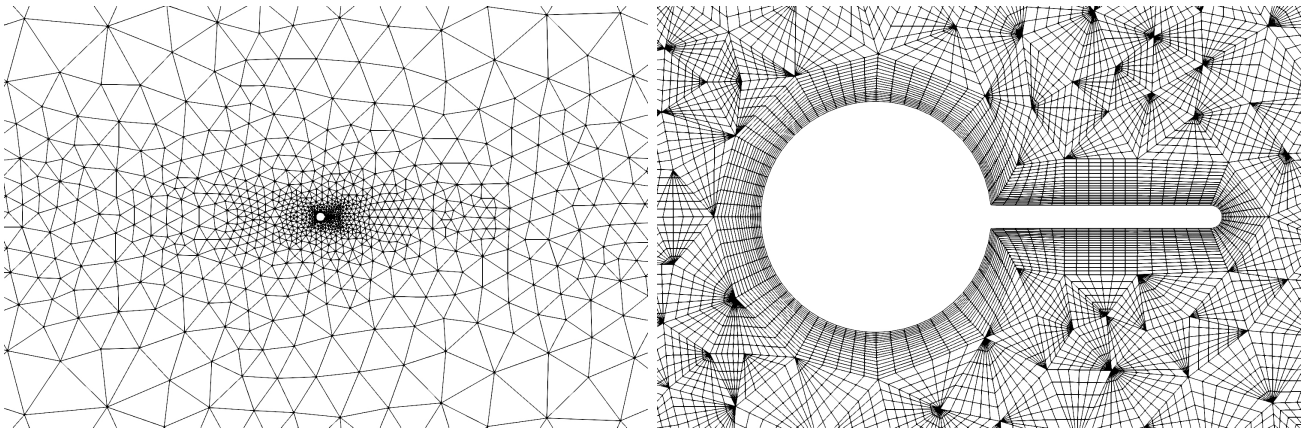
As a benchmark, the domain size used for non-linear simulation in the present study is compared to different domain sizes used in the literature as presented and summarised in table 5.6.
For every reference listed in table 5.6, the relevant domain size dimensions $\bar{x}$ and $\bar{y}$: the overall domain dimension in the streamwise and crossflow directions respectively, and $x^+$ and $x^-$: the distance from the cylinder centre to downstream and upstream far-fields respectively are presented, as well as $Re^{max}$: the maximum Reynolds number investigated in the corresponding study, are listed.

| Reference | $Re^{max}$ | $\bar{x}$ | $\bar{y}$ | $x^-$ | $x^+$ |
|---|---|---|---|---|---|
| Zhang et al. (2015) | 200 | 60 | 40 | 20 | 40 |
| Giannetti and Luchini (2007) | 120 | 75 | 40 | 25 | 50 |
| Carmo et al. (2011) | 300 | 81 | 100 | 36 | 45 |
| Sun et al. (2020) | 100 | 37.5 | 25 | 12.5 | 25 |
| Kwon and Choi (1996*a*) | 160 | 70 | 100 | 50 | 20 |
| Soumya and Prakash (2017) | 200 | 36 | 21 | 10.5 | 25.5 |
| Meliga and Chomaz (2011) | 50 | 250 | 50 | 100 | 150 |
| Cossu and Morino (2000) | 50 | 100 | 100 | 50 | 50 |

**Table 5.6:** Summary of dimensionless domain sizes ($/D$) used in literature for a circular cylinder, with or without splitter plate.

It is noted that the chosen domain size for the present study is of the order of magnitude of the one used in the listed literature for the same order of magnitude of Reynolds number, by looking at the values of $x^+$ and $\bar{y}$ (note that all the references are using a $y$-centred cylinder) presented in table 5.6, at the exception of a few reference (*e.g.* Cossu and Morino (2000); Giannetti and Luchini (2007); Meliga and Chomaz (2011)) which uses larger domain.
In particular, these references are conducting linear global stability analysis, and for this particular investigation, the simulations are more sensitive to the computational domain size, as presented in the following sub-section.

### 5.3.2 Domain size for linear analysis



**(a)** Far field spatial discretisation. **(b)** Close-up, degree of freedom representation.

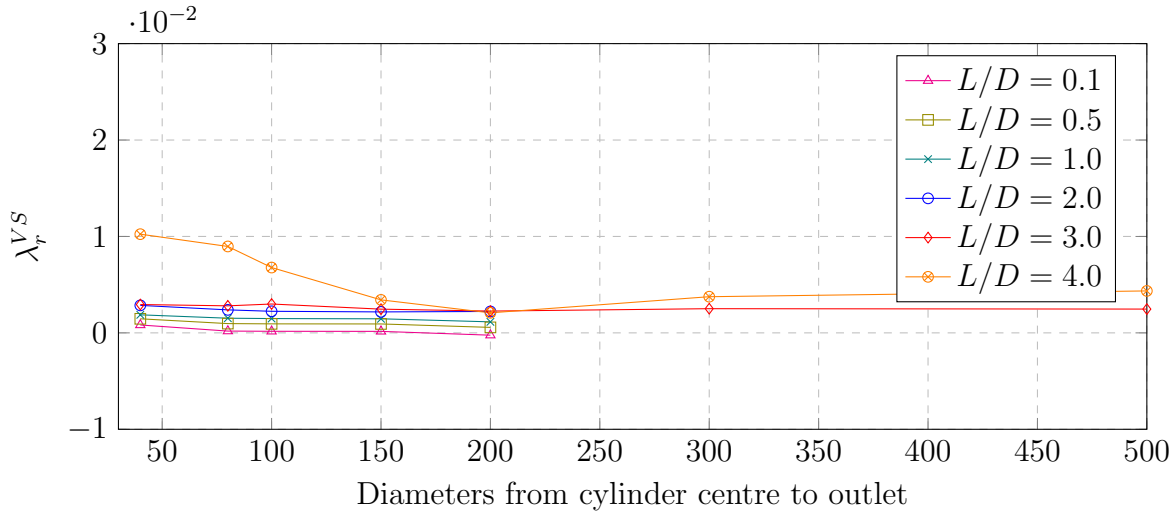
**Figure 5.4:** Example of size distribution of elements (a) used in the mesh for the splitter plate of length $L/D = 1$. The close-up in (b) shows the quadrature points for $P = 7$

Although not being the primary subject of this study, the vortex shedding mode developing in the wake of the fixed cylinder plus splitter plate is taken as the validation test case for the minimum domain size required ensuring the accuracy of the results for the different splitter plates lengths.

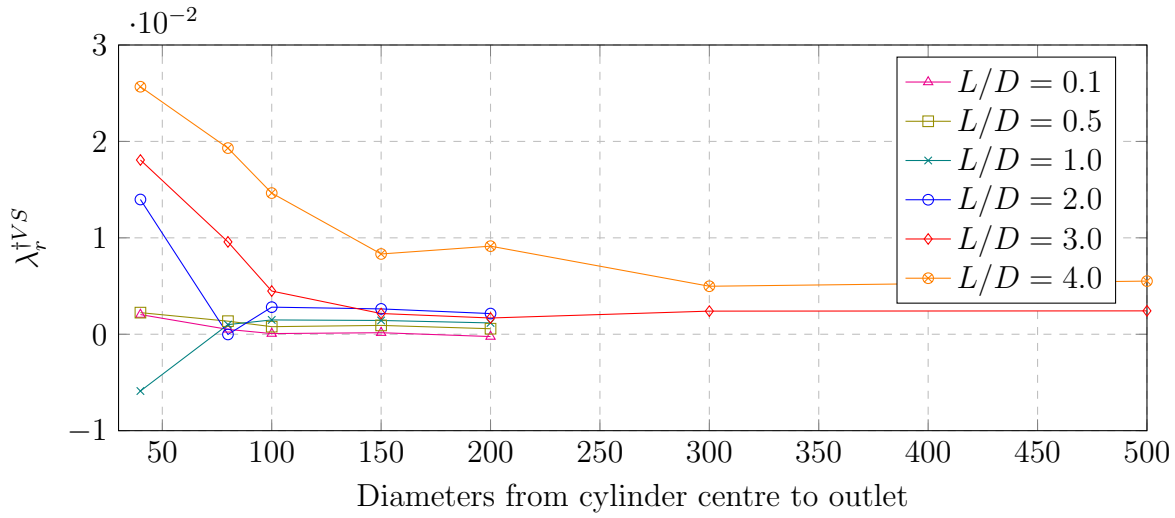
A representative mesh is shown in figure 5.4 corresponding to the boundary layer thickness and numbers of layers used for the mesh discretisation 3 in table 5.1, constituted of 1754 elements and 28104 degrees of freedom.

Figures 5.5 presents the computed numerical values of the real part of the direct and adjoint of the vortex shedding mode eigenvalues as a function of the domain size on the same vertical axis scale. Here, simulations are performed at a Reynolds number close to neutral stability for every plate length, leading to different Reynolds numbers for the different plate lengths.
It is noted that the minimum domain dimension required to obtain acceptable agreement between direct and adjoint simulations varies with the splitter plate length, which is presumably a consequence of the effect of the splitter plate length on the structure of the vortex shedding mode. In practice, as the splitter plate length increases, the peak magnitude of the vortex shedding mode is pushed farther downstream, and hence a larger domain is required to capture the instability.

For numerical efficiency, it is carefully chosen different domain sizes for each splitter plate length to ensure sufficiently small error between the eigenvalues of direct and adjoint modes: $200D$ in the downstream direction for $L/D \leq 2$, $300D$ for $L/D = 3$ and $500D$ for $L/D = 4$ respectively.



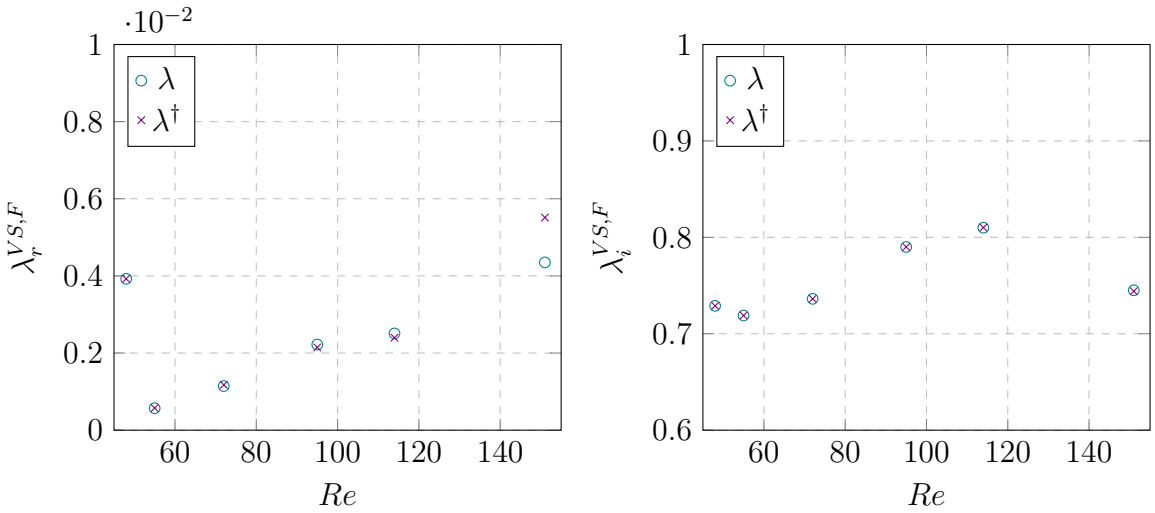

**(a)** Direct simulations.




**(b)** Adjoint simulations.

**Figure 5.5:** Comparison of real part of the computed (a) direct and (b) adjoint eigenvalues for every splitter plate length close to the onset of the instability. Here, $L/D = 0.1$ for $Re = 47$, $L/D = 0.5$ for $Re = 55$, $L/D = 1.0$ for $Re = 72$, $L/D = 2.0$ for $Re = 95$, $L = 3.0$ for $Re = 114$, and $L = 4.0$ for $Re = 151$.

Figure 5.6 presents a direct comparison of the values obtained computing the real and imaginary parts of the direct and adjoint simulation undertaken on the chosen domain sizes presented above for the different splitter plate lengths. By visualising the data on the same scale, an excellent qualitative agreement is observed between direct and adjoint both growth rates and frequencies, and a more significant gap is noted for the real part at the most extreme splitter plate length $L/D = 4$. For this particular case, the values presented in figures 5.5(a) and (b) show that the growth rate is little sensitive to the domain size from $300D$. Hence $500D$ is chosen as it does not affect the precision of the results anymore.




**(a)** Real part of $\lambda$ and $\lambda^\dagger$.

**(b)** Imaginary part of $\lambda$ and $\lambda^\dagger$.

**Figure 5.6:** Real and imaginary part eigenvalues comparison for linear and adjoint simulations for every splitter plate length close to the critical threshold. From lower to higher $Re$, it is presented [$L/D = 0.1$, at $x^+ = 200$], [$L/D = 0.5$, at $x^+ = 200$], [$L/D = 1.0$, at $x^+ = 200$], [$L/D = 2.0$, at $x^+ = 200$], [$L/D = 3.0$, at $x^+ = 300$], and [$L/D = 4.0$, at $x^+ = 500$].

## 5.4 Analytic formulation numerical validation

In this section is presented a comparison of direct and adjoint simulations to non-linear and literature results. Direct and adjoint resulting growth rates and frequencies are generated with the same Arnoldi method used throughout this work.

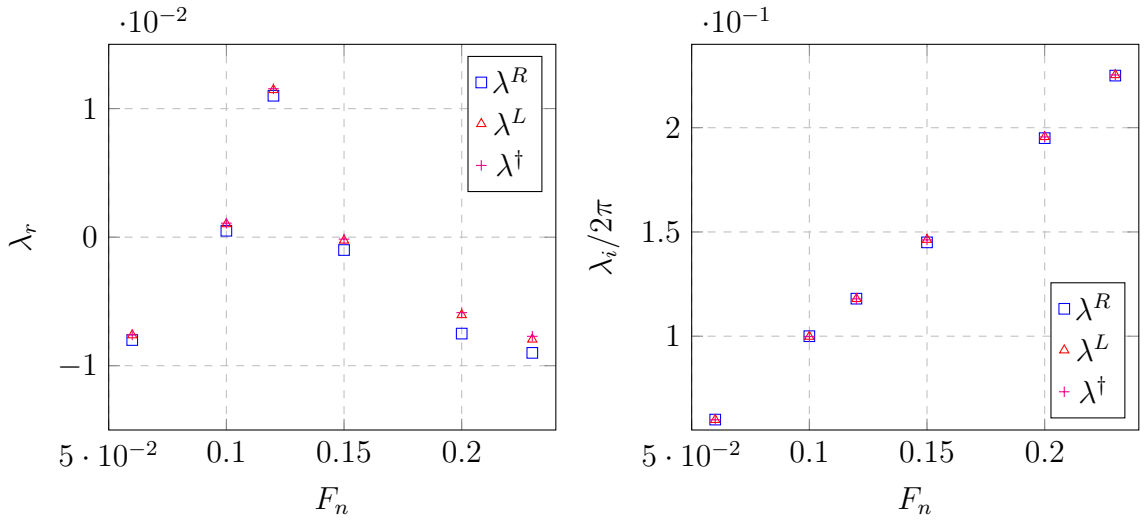
Hence this section focuses on the numerical validation of the equations presented in expressions (3.46) (for the direct problem) and (3.61) (for the adjoint problem), using the Spectral/hp element method previously presented.

### 5.4.1 Cross-flow VIV of a circular cylinder

The analytic formulation is first numerically validated in the cross flow direction, considering a circular cylinder of diameter $D$ undergoing vortex induced vibrations (VIV) at sub-critical Reynolds number $Re = 33$. The present results are validated against the reference Zhang et al. (2015) using the same structural parameters (*i.e.* dimensionless mass $m^* = 50$ and damping ratio $\zeta = 0$ in the following equation (5.1)) and domain size (*i.e.* $|y| = 20$ and $|x| = 40$), while using the numerical scheme of the present study.
The following dimensionless structural equation (Zhang et al., 2015) is considered

$$\ddot{y} + 4\pi F_n \zeta \dot{y} + (2\pi F_n)^2 y = \frac{2C_L}{\pi m^*}, \tag{5.1}$$

where the dimensionless mass $m^* = \dfrac{4m}{\pi\rho D^2}$ and $m$ is the physical mass per unit length and $\rho$ is density of the fluid. $\zeta = \dfrac{c}{2\sqrt{km}}$ is structural damping ratio, and $c$ and $k$ are the structural damping and stiffness respectively. Finally $F_n = \dfrac{f_n D}{U_\infty}$ is the reduced natural frequency where $f_n$ is the natural frequency of the cylinder.




**(a)** Real part of $\lambda^L$ and $\lambda^R$.

**(b)** Imaginary part of $\lambda^L$ and $\lambda^R$.

**Figure 5.7:** Mesh3, $P = 7$, domain size matching Zhang et al. (2015). Real and imaginary part of the leading eigenvalue $\lambda$ in function of the reduced frequency $F_n$. Comparison of linear and adjoints present simulations $\lambda^L$ and $\lambda^\dagger$ to the linear simulations from reference Zhang et al. (2015) $\lambda^R$.

In figure 5.7 is presented the comparison between the present direct $\lambda^L$ and adjoint $\lambda^\dagger$ simulations against the reference value $\lambda^R$ from Zhang et al. (2015). Both real and imaginary parts of the converged eigenvalues are presented, and good agreement is observed in the reduced natural frequency range investigated: $0.06 \leq F_n \leq 0.23$.

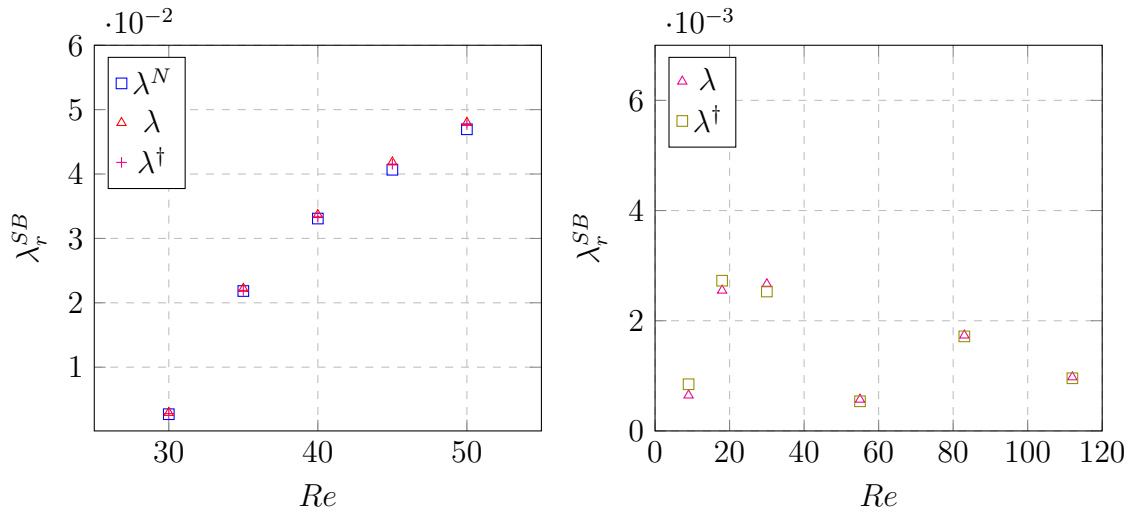
### 5.4.2 Symmetry breaking

Figure 5.8 presents the real part of the eigenvalue of the symmetry breaking mode from direct/adjoint analysis, and full non-linear simulation Serson et al. (2016), denoted by $\lambda$, $\lambda^\dagger$ and $\lambda^N$ respectively while varying the Reynolds number. It is noted that the growth rate from the non-linear simulation is obtained by fitting the early-stage evolution of a small perturbation to an exponential curve. Good agreement is obtained in the range of the Reynolds numbers investigated approximately up to the order of $10^{-3}$.

It is noted that a much smaller domain is required to obtain such a good agreement in the case of the symmetry breaking mode: for the results presented in figure 5.8, the computational domain is given by $|y| \leq 20$ and $|x| \leq 40$. This is probably due to the fact that in the current formulation and numerical implementation, the nature of the instability starts from the solid itself (*i.e.* its boundary). Indeed, the peak magnitude in the perturbed velocity field is located directly on the boundary (see section §6.3). Hence a smaller domain is enough to capture the mechanism accurately as long as the near-wake base flow is well established. This observation remains steadfast in the case of the torsional flapping mode, as is presented in the sub-section below.

Having verified the result with the domain of $|y| \leq 20$ and $|x| \leq 40$, a larger computational domain ($|y| \leq 30$ and $|x| \leq 40$) is used for the result in the present study.

For this study, the validation is undertaken varying the Reynolds number between $30 \leq Re \leq 50$ on Mesh 3, $P = 7$ and splitter plate length $L/D = 1$ thickness $l/D = 0.1$, as presented and used in Chapter §6.



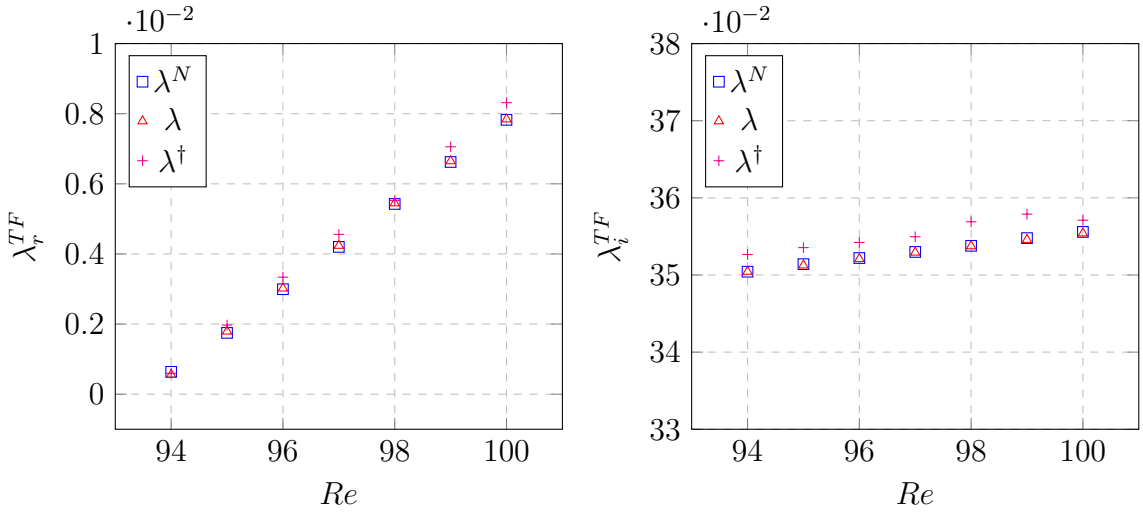

**(a)** Varying $Re$ only. **(b)** Varying $Re$ and $L/D$.

**Figure 5.8:** Comparison of the real part of eigenvalue of the symmetry breaking mode from the direct/adjoint mode computations and from full non-linear simulation: (a) $L/D = 1.0$ for $30 \leq Re \leq 50$; (b) $L/D = 0.1, 0.5, 1.0, 2.0, 3.0, 4.0$ at the Reynolds number near the onset of instability (note that growth rate is order of $10^{-3}$). Here, $\lambda^N$ indicates the eigenvalue obtained from full non-linear simulations, and the domain size is given by $|y| \leq 20$ and $|x| \leq 40$.

### 5.4.3 Torsional flapping

Analogously to the section 5.4.2, we present the numerical validation for the torsional flapping mode $\lambda^{TF}$ by comparing the results from direct/adjoint analysis with those from a full non-linear simulation. Figure 5.9 presents the real and imaginary part of the eigenvalues obtained

for $L/D = 4$ while varying the Reynolds number in the range $94 \leq Re \leq 100$. Good agreement between all cases is obtained for the parameters investigated.




**(a)** Growth rate. **(b)** Frequency.

**Figure 5.9:** Comparison of (a) real and (b) imaginary parts of the eigenvalue of the torsional flapping mode from direct/adjoint mode calculations and full non-linear simulations. Here, $\lambda^N$ indicates the eigenvalue obtained from full non-linear simulations, and the domain size is given by $|y| \leq 30$ and $|x| \leq 40$.

### 5.4.4 Fictitious parameters

The numerical validation of the fictitious mass equation (4.42) have been undertaken varying $I_\theta^{Fict}$, considering the unique structural degree of freedom $\theta$. For this study, a unique geometry have been considered corresponding to the geometrical setup presented in figure 6.1 with a splitter plate length $L/D = 1$ along with an inertia $I_\theta = 50$, damping coefficient $c_\theta = 0$ and spring constant $k_\theta = 1 \times 10^{-4}$. For all the variations of $I_\theta^{Fict}$, two flow conditions have been tested, $Re = 50$ and 60 when carrying the adjoint or direct simulations respectively.
Table 5.7 presents the converged growth rate of the symmetry breaking mode $\lambda_r^{SB}$ and $\lambda_r^{\dagger SB}$ for both direct and adjoint simulations, respectively, where the case $I_\theta^{Fict} = 0$ correspond to simulations carried without the fictitious mass consideration and is seen as the benchmark for the validation study.

Excellent agreement is noted between the simulations using the fictitious inertia parameter and the reference $I_\theta^{Fict} = 0$. It is noted that the adjoint equations appear slightly more sensitive to the variation of the fictitious inertia, which is suspected to be due to the more complex form of its aerodynamic forcing compared to the direct problem.

| $I_\theta^{Fict}$ | $\lambda_r^{SB}$ | $\lambda_r^{\dagger SB}$ |
|---|---|---|
| 0 | $6.1042 \times 10^{-2}$ | $4.7955 \times 10^{-2}$ |
| 100 | $6.1042 \times 10^{-2}$ | $4.7949 \times 10^{-2}$ |
| 200 | $6.1043 \times 10^{-2}$ | $4.7943 \times 10^{-2}$ |
| 300 | $6.1043 \times 10^{-2}$ | $4.7938 \times 10^{-2}$ |
| 400 | $6.1043 \times 10^{-2}$ | $4.7932 \times 10^{-2}$ |
| 500 | $6.1043 \times 10^{-2}$ | $4.7926 \times 10^{-2}$ |
| 600 | $6.1043 \times 10^{-2}$ | $4.7921 \times 10^{-2}$ |
| 700 | $6.1043 \times 10^{-2}$ | $4.7915 \times 10^{-2}$ |
| 800 | $6.1043 \times 10^{-2}$ | $4.7909 \times 10^{-2}$ |
| 900 | $6.1043 \times 10^{-2}$ | $4.7904 \times 10^{-2}$ |
| 1000 | $6.1043 \times 10^{-2}$ | $4.7898 \times 10^{-2}$ |

**Table 5.7:** Values of $\lambda_r^{SB}$ at $Re = 60$, and $\lambda_r^{\dagger SB}$ at $Re = 50$, in function of the fictitious inertia $I_\theta^{Fict}$ for $I_\theta = 50$, $c_\theta = 0$ and $k_\theta = 1 \times 10^{-4}$.

# Chapter 6

# Freely rotating cylinder fitted to a splitter plate

This section reviews the physical impacts of making the assumptions of either a mass ratio approaching infinity, *i.e* a static configuration presented in section §6.2, or a large reduced velocity, *i.e* small structural stiffness presented in the section §6.3, on the fluid and/or structural behaviours.
The strategy is first to question the first instability in the body wake in a static configuration applied to the present geometry of study (*i.e* a cylinder fitted to a splitter plate of length $L/D$ and thickness $l/D$, not currently clearly available in the literature to the knowledge of the author), and exploit the results as a benchmark for the second part of the study when considering actual fluid-structure interactions (*i.e.* a rotating motion).
The analysis presented in this chapter is organised around the particular case of a freely rotating cylinder fitted to a rigid splitter plate, making the rotational motion of the structure the only structural degree of freedom considered in this chapter. The complete configuration is first detailed and presented in the section §6.1, to complement the more general setup previously presented in chapter §3.

## 6.1 Problem description

A two-dimensional flow over a circular cylinder with a rigid splitter plate, sketched in figure 6.1 is considered, in an equivalent configuration to the one presented in Chapter §3. The free-stream velocity in the streamwise direction is given by $\mathbf{u}_\infty(=(U_\infty,0))$, and the density and the kinematic viscosity of the fluid are by $\rho$ and $\nu$, respectively. The cylinder diameter is set to be $D$, and the length of the splitter plate from the base is given by $L$ with the thickness $l$, note that $l$ is chosen constant through this study as $l=0.1D$. The downstream edge of the splitter plate is also set to be rounded with the radius of $l/2$. The cylinder is allowed to rotate about its

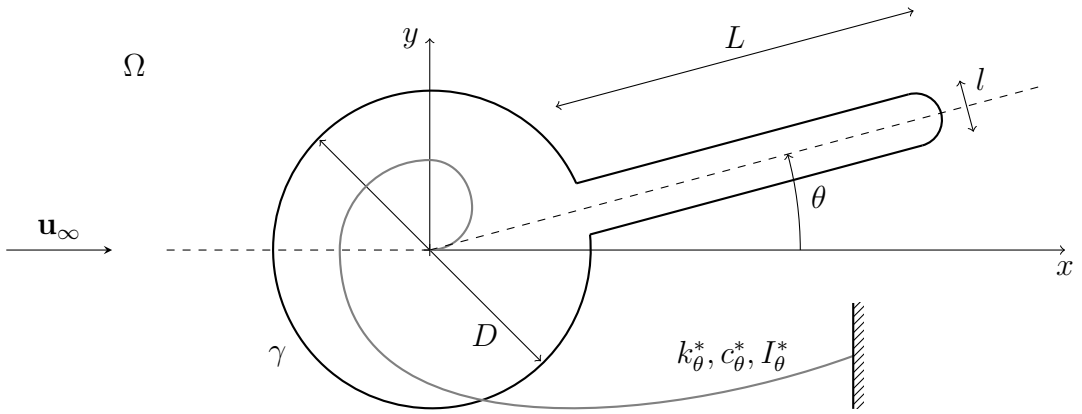



**Figure 6.1:** A schematic diagram of flow and structure configuration. Here, $\mathbf{u}_\infty(=(U_\infty, 0))$ is the freestream velocity, $\theta$ the counter-clockwise rotation angle of the cylinder, $k_\theta$ rotational stiffness, and $c_\theta$ rotational damping coefficient.

centre, and the rotational motion is coupled through a torsional spring-mass-damper system. The rotational stiffness, the damping coefficient and the moment of inertia are given by $k_\theta^*$, $c_\theta^*$ and $I_\theta^*$, respectively. The equations of motion and all the related variables (including $k_\theta^*$, $c_\theta^*$ and $I_\theta^*$) are made dimensionless with $U_\infty$ and $D$. The dimensionless spatial location is denoted by $\mathbf{x} = (x, y)$, where $x$ and $y$ are the streamwise and transverse coordinates, and the velocity is by $\mathbf{u} = (u, v)$ with its streamwise and transverse components $u$ and $v$. The fluid domain is denoted by $\Omega$, and the inner boundary of which is given by the cylinder surface. The cylinder centre is set to be located at $(x, y) = (0, 0)$.

In a matter of consistency, the state equations and quantities governing the coupled fluid structure problem are recalled, however their treatment to obtain the associated direct and adjoint operator is identical to the approach presented in the sections §3.2 and §3.3, considering however a unique structural degree of freedom $\theta$ instead of the full position vector $\boldsymbol{\eta} = [\chi\ \psi\ \theta]^T$. The equations for fluid motion are identical to the one presented previously and are given by the following momentum and mass conservation laws, *i.e.* the Navier-Stokes equations in incompressible regime:

$$\frac{\partial \mathbf{u}}{\partial t} + (\mathbf{u} \cdot \nabla)\,\mathbf{u} = -\nabla p + \frac{1}{Re}\nabla^2 \mathbf{u}, \tag{6.1a}$$

$$\nabla \cdot \mathbf{u} = 0, \tag{6.1b}$$

where $p$ is the dimensionless pressure and $Re = U_\infty D/\nu$ is the Reynolds number.

For the rotational motion of the cylinder, the following equation based on a linear spring-mass-damper system is considered:

$$\ddot{\theta} + \frac{4\pi\zeta_\theta}{U_R}\dot{\theta} + \left(\frac{2\pi}{U_R}\right)^2 \theta = \frac{4\mathfrak{m}_z(\mathbf{u}, p)}{\pi I_{\theta,r}}, \tag{6.2a}$$

where $\dot{(\cdot)}$ indicates $\mathrm{d}/\mathrm{d}t$, and $I_{\theta,r}$, $\zeta_\theta$ and $U_R$ are the dimensionless reduced moment of inertia, damping ratio and reduced velocity, *i.e.*

$$I_{\theta,r} = \frac{4I_\theta}{\pi}, \quad \zeta_\theta = \frac{c_\theta}{2\sqrt{k_\theta I_\theta}} \quad \text{and} \quad U_R = \frac{2\pi}{\omega_n}, \tag{6.2b}$$

with the dimensionless natural frequency $\omega_n (\equiv \sqrt{k_\theta / I_\theta})$, and the dimensionless moment of inertia, damping coefficient and rotational stiffness (or spring constant), $I_\theta$, $c_\theta$ and $k_\theta$, respectively.

The coupling of the equations (6.1) and (6.2a) is performed by employing the *kinematic* boundary condition at the cylinder surface (see expression (3.12)), and the *dynamic* (see expression (3.13)) is implemented considering $m_z$, the moment applied to the cylinder by fluid force per unit span:

$$\mathfrak{m}_z(\mathbf{u}, p)\mathbf{k} = \oint_\gamma \{\mathbf{r} \times (\sigma \cdot \mathbf{n})\} \, \mathrm{d}l, \tag{6.2c}$$

where $\mathbf{k}$ is the unit vector along the $z$ direction orthogonal to the $x$-$y$ plane, $\mathbf{n}$ is the outward unit normal vector on $\gamma$, and

$$\sigma = -p\mathbf{I} + Re^{-1}\left[\nabla\mathbf{u} + (\nabla\mathbf{u})^T\right]. \tag{6.2d}$$

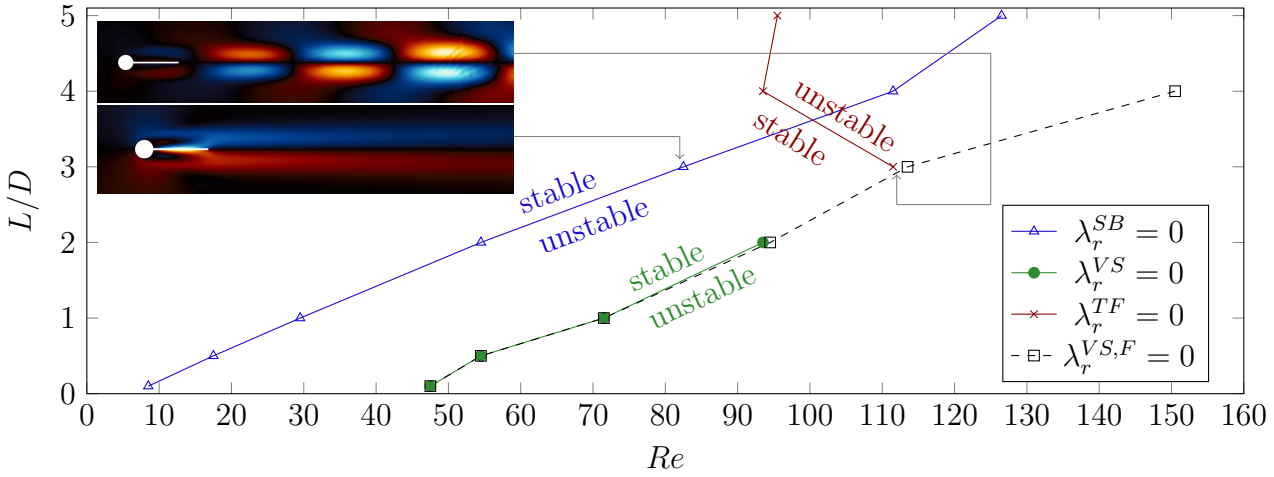
It is primarily considered a fixed reduced velocity $U_R = 3937$ (corresponding to $I_\theta = 50$, $c_\theta = 0$ and $k_\theta = 10^{-4}$). The value of such a reduced velocity is chosen as it displays the three instabilities of interest well (*i.e.* the vortex shedding, the symmetry breaking and the torsional flapping) with reasonable variations of the other parameters. In the following sections, the focus is put on three questions related to two-dimensional flow past a cylinder with a splitter plate of different lengths, namely:

i How does the rotational motion of the cylinder modify the instability of fluid motion (i.e. vortex shedding)?;

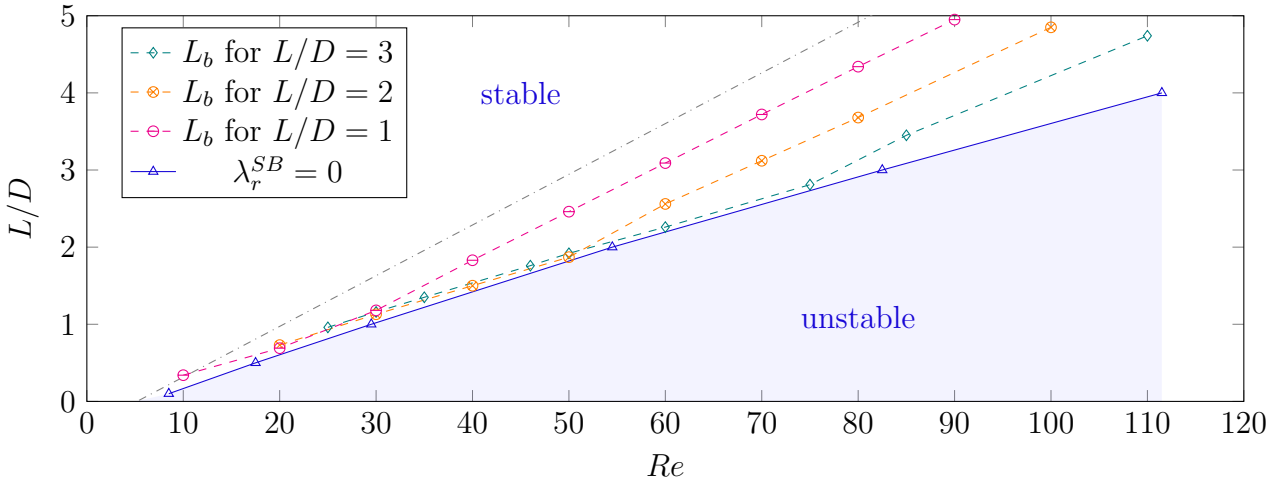
ii What are the instabilities caused by fluid-structure interaction and how do they compare to that arising in the flow past the fixed body case as the length of the splitter plate varies?;

iii How does the structure of the sensitivity field of these instability modes change with the length of the splitter plate?

To address questions (i) and (ii) above, we first consider the neutral stability curves of the various instability modes. Three types of instability modes were found in the presence of FSI, and their eigenvalues are denoted by $\lambda^{SB}$ (symmetry breaking mode), $\lambda^{TF}$ (torsional flapping) and $\lambda^{VS}$ (vortex shedding mode), respectively.




**(a)** The stability diagram of the instabilities obtained from symmetry breaking ($\lambda^{SB}$), vortex shedding ($\lambda^{VS}$) and torsional flapping ($\lambda^{TF}$) modes in the free-to-rotate cylinder wake, as a function of $Re$ and $L/D$ at $U_R = 3937$ (corresponding to $I_\theta = 50$, $c_\theta = 0$ and $k_\theta = 10^{-4}$). For comparison, the neutral stability curve of the vortex shedding mode is plotted for a fixed cylinder with a splitter plate ($\lambda^{VS,F}$).




**(b)** The empirical formula for the length of recirculation bubble in equation (2.4) (dotted-dashed grey line) is given and compared to its counterpart $L_b$ for three different plate lengths.

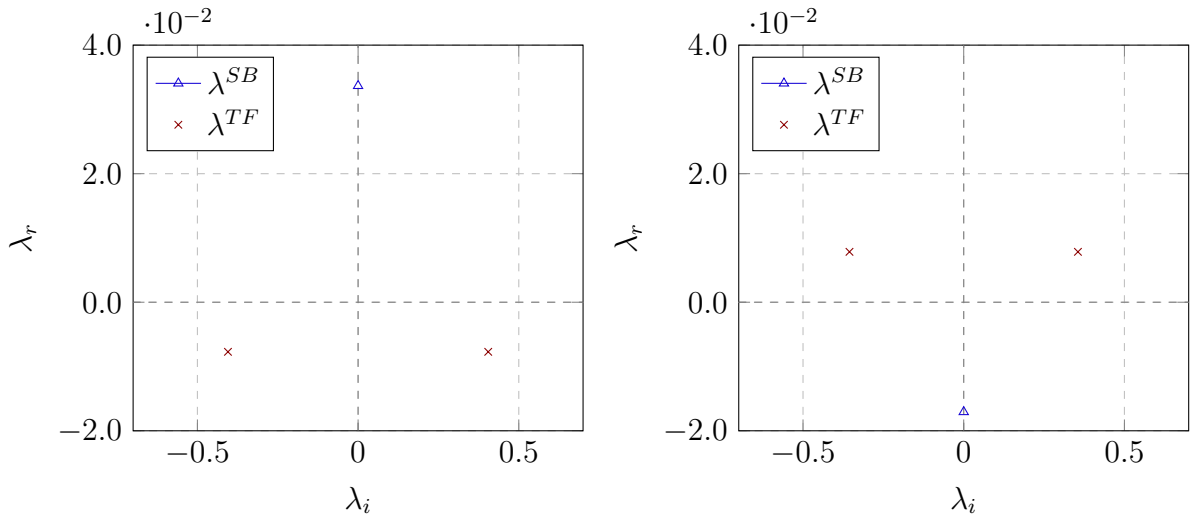
**Figure 6.2:** Neutral stability diagram (a), and recirculation length comparison for different splitter plate lengths as a function of the Reynolds number (b). The two figures in inset of (a) are the $u$ velocity fields of the symmetry breaking mode ($L/D = 3$, $Re = 83$) and the torsional flapping modes ($L/D = 3$, $Re = 112$), respectively.

Figure 6.2a summarises the critical Reynolds numbers for the onset of two leading FSI instability modes in the flow past the rotating cylinder as a function of the splitter plate length. As a reference, the onset of the vortex shedding mode in the absence of any fluid structural interaction is also plotted, and its eigenvalue is denoted by $\lambda^{VS,F}$ (the black dotted line with open square symbols). As the Reynolds number increases, the first instability mode arises for $L/D < 3.5$, and it is found to be stationary (*i.e.*, non-oscillatory) with $\lambda_i = 0$ ($\lambda^{SB}$; the blue line in figure 6.2). This mode corresponds to the symmetry-breaking structural mode previously observed

(Assi et al., 2010; Assi, Bearman and Tognarelli, 2014; Bagheri et al., 2012*b*; Cimbala and Garg, 1991; Lacis et al., 2014*b*; Pfister and Marquet, 2020). This instability arises notably earlier than the instability of the vortex shedding ($\lambda^{VS}$; the green line in figure 6.2)). For longer splitter plate ($L/D > 3$), a new type of 'dynamic' (or 'oscillatory') instability mode ($\lambda_i \neq 0$) appears ($\lambda^{TF}$; the red line in figure 6.2). In the following, this mode is referred to as 'torsional flapping', as described in more detail in section §6.4. Finally, it is worth mentioning that the vortex shedding mode in the absence of FSI ($\lambda^{VS,F}$) is found to coincide with that in the presence of FSI ($\lambda^{VS}$), at least in this case. Also, as is well known, the vortex shedding mode is stabilised on increasing the length of the splitter plate $L$ (Anderson and Szewczyk, 1997; Choi et al., 2008; Kwon and Choi, 1996*b*; Ozono, 1999; Roshko, 1954).

The critical Reynolds number data were obtained following the evaluation strategy presented in figure 6.4a where a series of linear eigenanalysis simulations is performed for every splitter plate length over a range of Reynolds number. For every simulation, the simulation is stopped when two leading eigenvalues with the largest real part have converged. Finally, the sign of the real part of the eigenvalues denotes the "stable" and "unstable" regions depicted in figure 6.2. In figure 6.2b, a linear empirical fit from Giannetti and Luchini (2007) (dotted-dashed grey line), which depicts the length of the recirculation zone measured from the rear stagnation point on a fixed circular cylinder without a splitter plate, is plotted as a function of the Reynolds number (see expression (2.4)).
The length of the recirculation zone with the splitter plate for $L/D = 1, 2, 3$ is also plotted. The length of the recirculation zone closely follows the neutral stability curve of the symmetry breaking mode (i.e. $\lambda_r^{SB} = 0$) when it is smaller than $L/D$, indicating that the emergence of this mode is closely linked to the flow structure related to the zone (Lacis et al., 2014*b*). When the size of the zone becomes greater than given $L/D$, it deviates from $\lambda_r^{SB} = 0$ considerably, and the slope of its growth with respect to $Re$ becomes similar to that of (2.4) given for the case without the splitter plate.

For clarity, the eigenvalues spectrum of the first two eigenvalues of highest magnitude, corresponding to the symmetry breaking ($\lambda^{SB}$) and torsional flapping ($\lambda^{TF}$) modes in the presented cases, for two different splitter plate lengths; $L/D = 3$ and 4, at $Re = 100$ are also presented in figure 6.3. Figure 6.3a represents a scenario where the symmetry breaking mode is unstable (*i.e.* $\lambda_r^{SB} > 0$) when the torsional flapping mode is stable (*i.e.* $\lambda_r^{TF} < 0$), and figure 6.3b represents a scenario where the symmetry breaking mode is stable (*i.e.* $\lambda_r^{SB} < 0$) when the torsional flapping mode is unstable (*i.e.* $\lambda_r^{TF} < 0$). From these figures, it is clear that the symmetry breaking mode have no frequency (*i.e.* no imaginary part *i.e.* $\lambda_i^{SB} = 0$), whereas the torsional flapping is a periodic instability (*i.e.* non-zero imaginary part *i.e.* $\lambda_i^{TF} \neq 0$).




**(a)** $L/D = 3$. **(b)** $L/D = 4$.

**Figure 6.3:** Comparison of the eigenvalues spectrum (first two eigenvalues of highest magnitude, corresponding in that case to the symmetry breaking ($\lambda^{SB}$) and torsional flapping ($\lambda^{TF}$) modes) for two different splitter plate lengths; $L/D = 3$ and 4, at $Re = 100$.

## 6.2 Stationary body

In this preliminary part of the study, the dimensionless moment of inertia $I_\theta$ is made approaching infinity and a "fluid only" (*i.e.* $\ddot{\theta} = 0$) problem is investigated.
The results of this investigation will be used as a benchmark in the rest of the study when comparing the influence of structural motion on the fluid modes. In particular, neutral stability curves, frequency and shapes of the vortex shedding mode will be compared whether the body is considered stationary or free to oscillate.

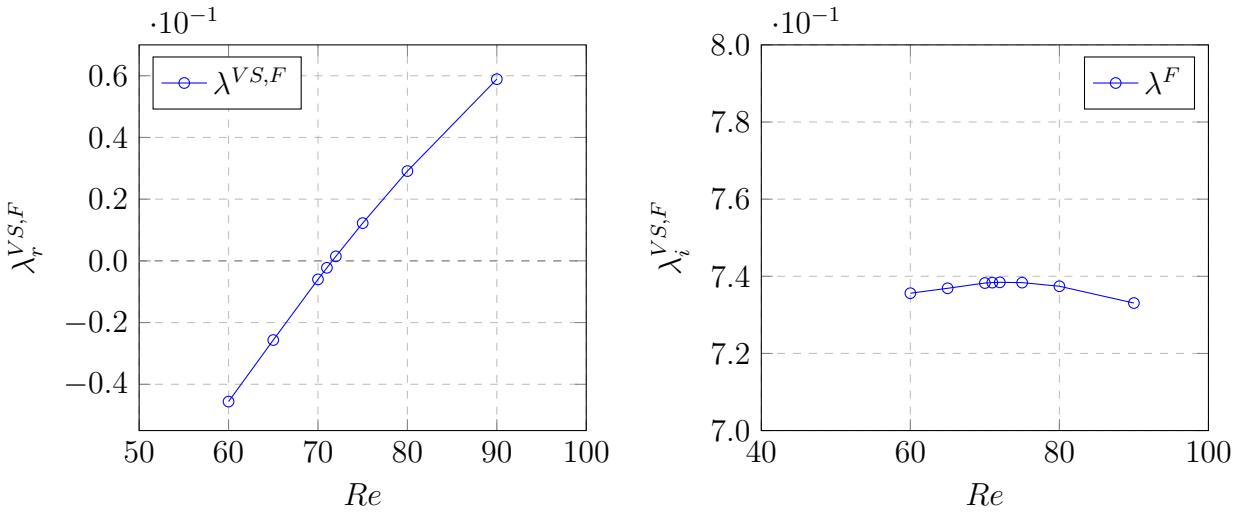
### 6.2.1 Linear stability

In figure 6.4 is plotted the real and imaginary part of the leading eigenvalue $\lambda^{VS,F}$ of the linear stability analysis around the fixed cylinder with a splitter plate of length $L/D = 1$, which physically corresponds to the vortex shedding mode. By increasing the Reynolds number, the eigenvalue associated with $\lambda^{VS,F}$ becomes positive, and for the $L/D = 1$ splitter plate, the flow becomes unstable through a Hopf bifurcation at $Re \simeq 72$, in a similar manner than the case of a fixed circular cylinder without splitter plate at $Re \simeq 48$.

Conducting and repeating this approach for the different splitter plate lengths studied in this work, a map of the neutral stability curve of this primary instability as a function of the splitter plate length is provided in figure 6.2. As the splitter plate length tends to zero, it is observed

that the configuration also approaches the classical critical Reynolds number instability for a circular cylinder. Indeed, at $L/D = 0.1$ it is observed that $Re_{crit} \simeq 48$ where the leading instability is the vortex shedding mode.

At this stage, no particular relationship is noted between the neutral stability curve of the vortex shedding mode for different splitter plate lengths and the empirical linear relationship of the recirculation bubble length in the wake of a cylinder without a splitter plate.




**(a)** Real part of $\lambda^F$.

**(b)** Imaginary part of $\lambda^{VS,F}$.

**Figure 6.4:** The linear growth rate and frequency of the vortex shedding mode ($\lambda^{VS,F}$) in the case of a stationary cylinder as a function of the Reynolds number ($L/D = 1$).

In figure 6.5 is shown the shape of the normalised $u$-component of the real part of the vortex shedding mode $\lambda^{VS,F}$ along the neutral stability curve for different plate lengths: $L/D = 0.1$, 1, 2 and 4. In every case, the upper figure represents a close-up of the mode shape in the near wake region, whereas the bottom figures represent a far-field visualisation of the mode shape. In both cases, the data is normalised for clarity, such as it is represented from its minimum to maximum value in the chosen frame (*i.e.* $u/||u||_\infty$).

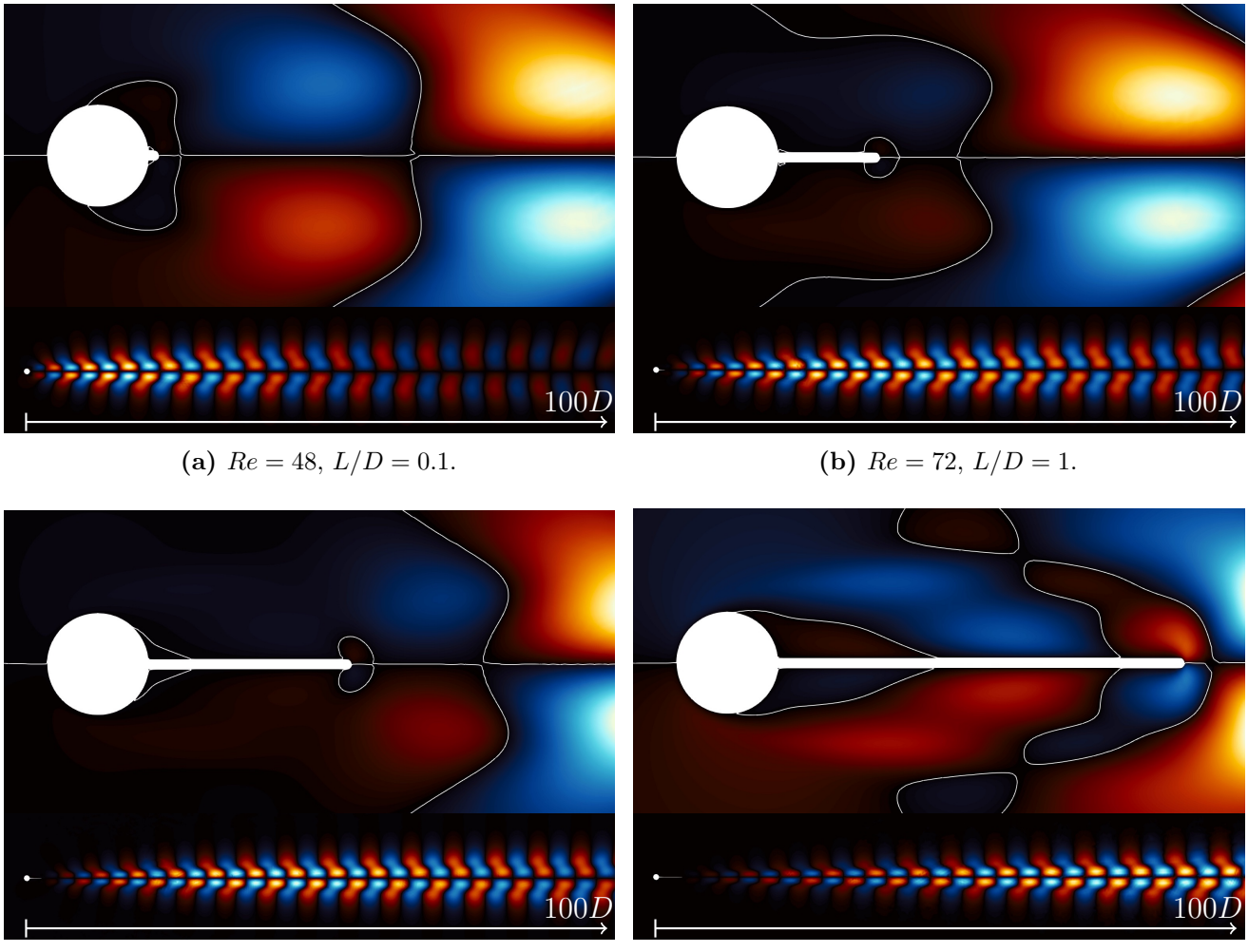
In the near wake region, the mode shape is noted to have a fairly similar shape for short splitter plates (*i.e.* $L/D = 0.1$ and 1 in that case), constituted of distributed equidistant pockets of alternative signs, represented in blue and orange on these figures. However, it is noted that from $L/D = 1$, an opposite pocket sign "bubble" is attached to the tip of the splitter plate, which might indicate that these pockets dynamically emerge from the tip of the splitter plate rather than from its root. This observation is maintained for longer plates (*i.e.* $L/D = 2$ and 4 in that case) where the opposite sign bubble is still present at the tip in addition to the presence of pockets at the root of the splitter plate. This possibly denotes physically the formation of vortices taking place from both the root and the tip of the splitter plate. This observation is also in agreement with the near conservation of the vortex shedding mode frequency along the

neutral stability curve for the different plate lengths, as presented in table 6.1.

| | $L/D = 0.1$ | $L/D = 0.5$ | $L/D = 1.0$ | $L/D = 2.0$ | $L/D = 3.0$ | $L/D = 4.0$ |
|---|---|---|---|---|---|---|
| $\lambda_i^{VS,F}$ | 0.7290 | 0.7189 | 0.7362 | 0.7900 | 0.8100 | 0.7451 |

**Table 6.1:** Values of the vortex shedding mode frequency $\lambda_i^{VS,F}$ along the neutral stability curve in function of the splitter plate length.

Indeed, also visualised on the bottom sub-figures in figure 6.5, the physical distance between two consecutive same sign pockets is relatively conserved (interpreted as the wavelength of the direct mode in that case), even though not following a monotonic behaviour, and as the splitter plate length increases and becomes longer than the mode wavelength, new pockets emerges from its root.




**(a)** $Re = 48$, $L/D = 0.1$.

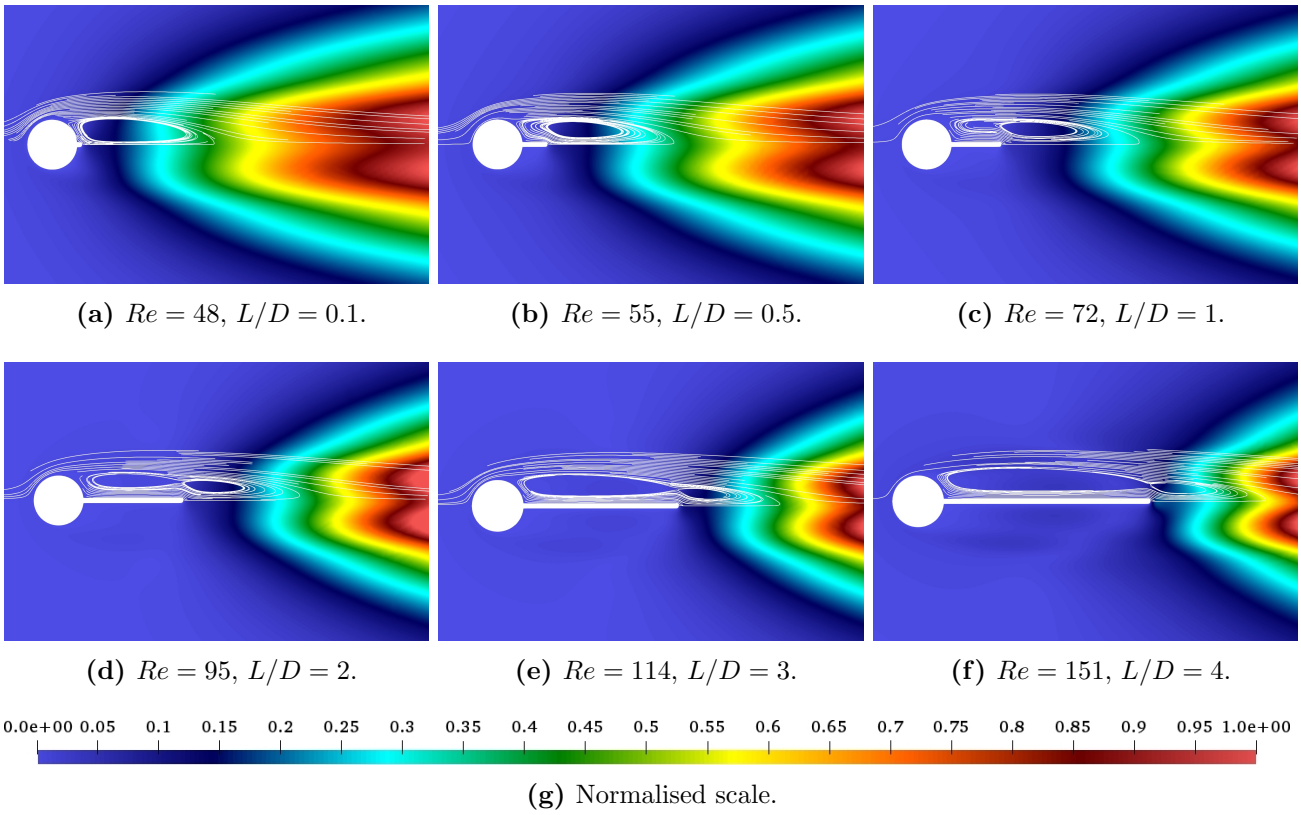
**(b)** $Re = 72$, $L/D = 1$.

**(c)** $Re = 95$, $L/D = 2$.

**(d)** $Re = 151$, $L/D = 4$.

**Figure 6.5:** Real part $u$-component of the vortex shedding direct mode shape evolution along the threshold of stability for different plate length. The red and blue colours denote positive and negative values respectively, and their brightness indicates the magnitude. The continuous lines are associated 0-isocontours of the perturbed fields.

In the far-field visualisations of figure 6.5, it is noted a strong positive correlation between the splitter plate length and the peak velocity magnitude location. Indeed, as the splitter plate length increases, the peak velocity magnitude tends to translate in the streamwise direction, apart from the cylinder.




**(a)** $Re = 48$, $L/D = 0.1$. **(b)** $Re = 55$, $L/D = 0.5$. **(c)** $Re = 72$, $L/D = 1$.

**(d)** $Re = 95$, $L/D = 2$. **(e)** $Re = 114$, $L/D = 3$. **(f)** $Re = 151$, $L/D = 4$.

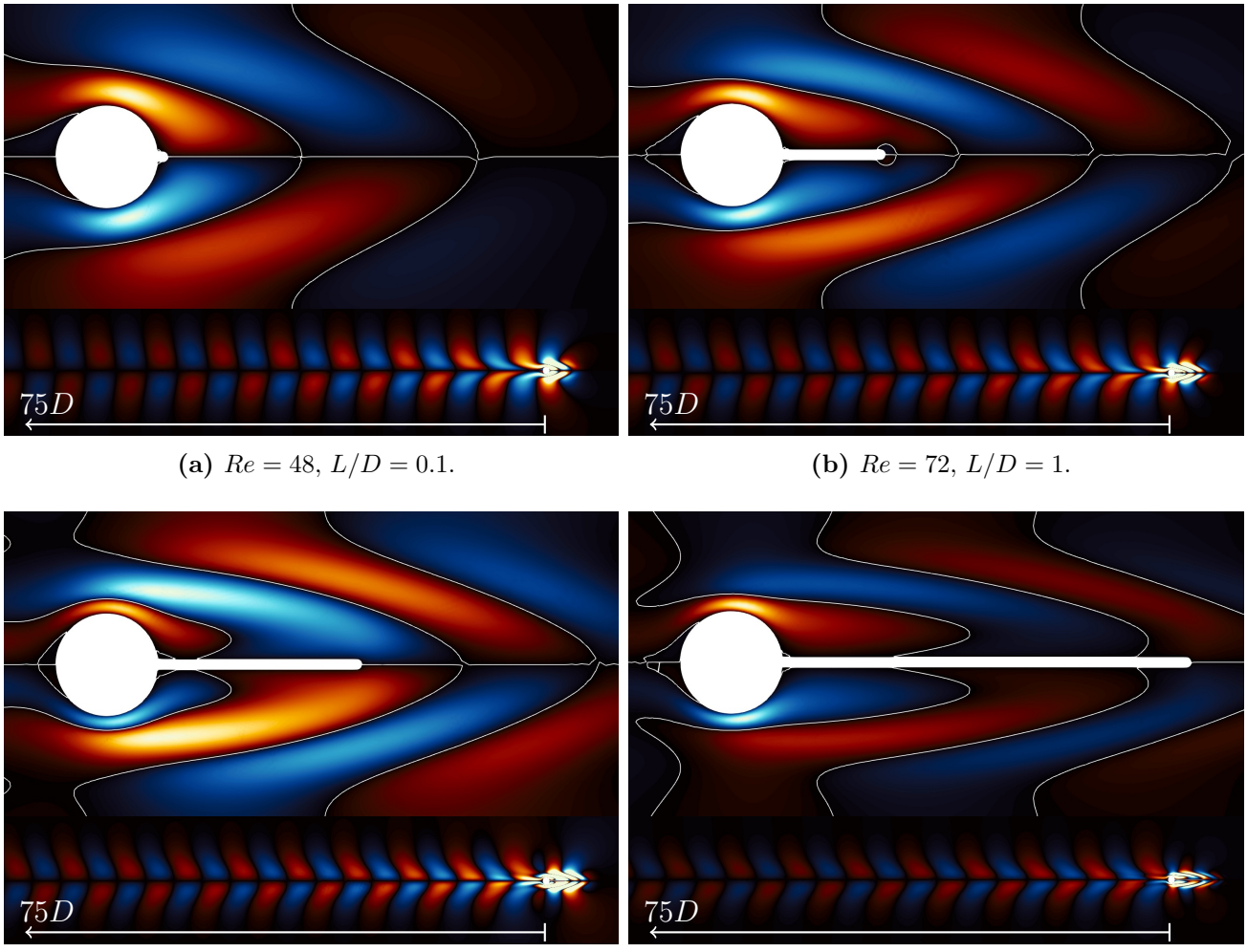
**(g)** Normalised scale.

**Figure 6.6:** Magnitude $\|\hat{\mathbf{u}}\|$ of the velocity components of the vortex shedding instability ($\lambda^{VS,F}$). The continuous lines are associated to the base flow streamlines for the corresponding Reynolds numbers.

Figure 6.6 shows the amplitude of the normalised perturbation velocity field $\|\hat{\mathbf{u}}(x,y)\|_2$ ($\equiv \sqrt{\hat{\mathbf{u}}^H\hat{\mathbf{u}}}$) of the vortex shedding mode close to the near wake region. It is noted that in contrast to figure 6.21 when visualising the direct mode of the symmetry breaking mode, the amplitude's shape of the normalised perturbation velocity field tends to be similarly distributed for all splitter plate lengths studied. The amplitude of the normalised perturbation velocity appears to be distributed symmetrically in the cross-flow in a similar disposition to the known shape of a circular cylinder without a splitter plate. Note that for clarity, these figures present $\|\hat{\mathbf{u}}\|$ on a scale from 0 to the maximum value in the selected close-up region.
On the same figures, the streamlines of the base flow are represented in white, and it is noted that no particular correlation is observable, in agreement with Figure 6.2

### 6.2.2 Adjoint-based sensitivity

For comparison with the direct mode shape distribution, the real part of the $u$-component of the adjoint vortex shedding mode along the neutral stability curve for different plate lengths: $L/D = 0.1$, 1, 2 and 4 are presented in figure 6.7. Similarly to figure 6.5, the upper figure represents a close-up on the mode shape in the near wake region (along with a min to max representation scale), whereas, for clarity, the bottom figures represent a far-field visualisation of the mode shape up to 10% of the maximum range as the peak magnitude is strongly located close to the cylinder in that case.




**(a)** $Re = 48$, $L/D = 0.1$.

**(b)** $Re = 72$, $L/D = 1$.

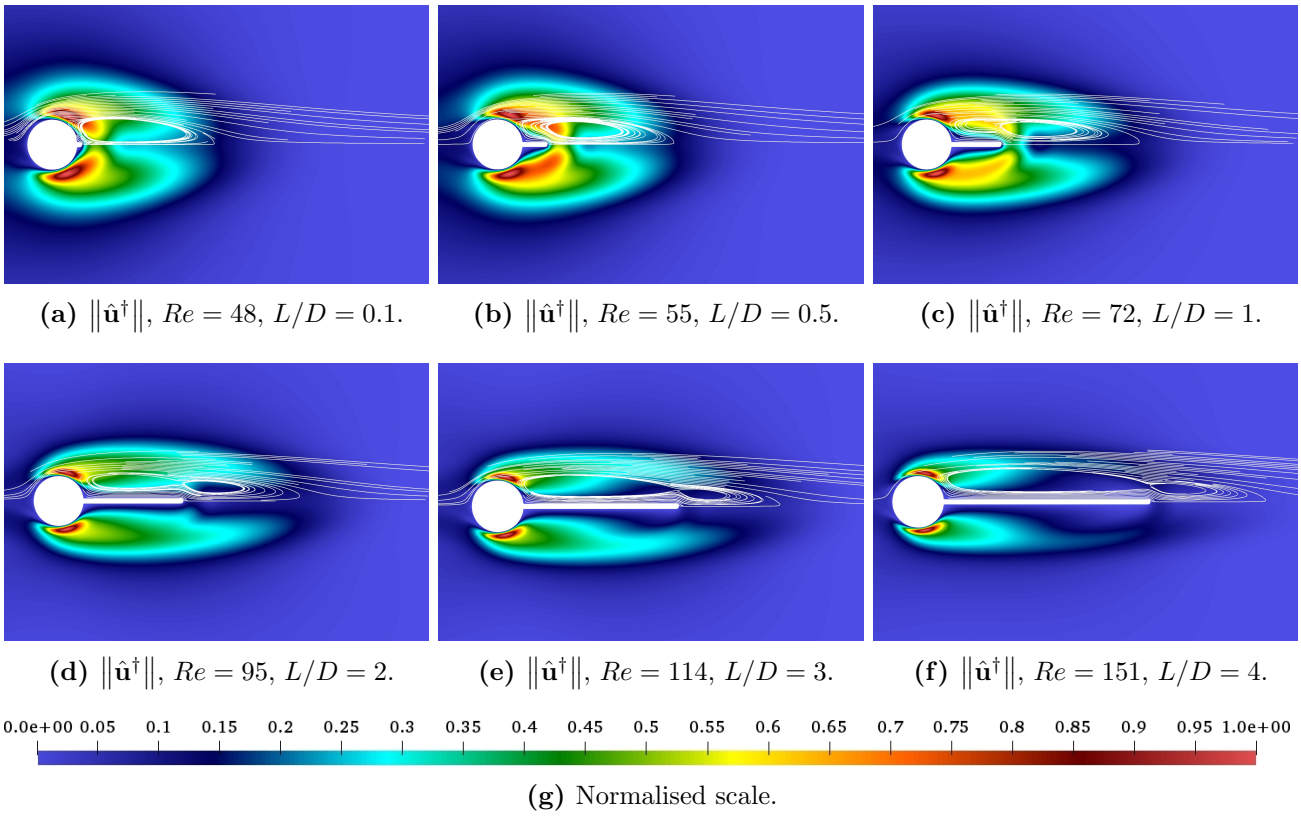
**(c)** $Re = 95$, $L/D = 2$.

**(d)** $Re = 151$, $L/D = 4$.

**Figure 6.7:** Real part $u$-component of the vortex shedding adjoint mode shape evolution along the threshold of stability for different plate length. The red and blue colours denote positive and negative values respectively, and their brightness indicates the magnitude. The continuous lines are associated 0-isocontours of the perturbed fields. The far field visualisations (lower figures) represents the data up to 10% of maximum range.

Even though the adjoint mode shape complexity appears to increase gradually as the splitter plate length increases, the very same key features are conserved in the near wake regions. First,

the velocity pockets of alternative signs are located anti-symmetrically across the $(x, 0)$ axis as for the direct mode shape. Second, the peak velocities appear to be located above and below the cylinder interface. Increasing the splitter plate length tends to elongate in the streamwise direction the shape obtained for short splitter plates.
In the far-field region, the adjoint mode propagates upfront the cylinder surface in the streamwise direction, and little difference is noted between the visualisations comparing the different splitter plate lengths.




**(a)** $\|\hat{\mathbf{u}}^\dagger\|$, $Re = 48$, $L/D = 0.1$. **(b)** $\|\hat{\mathbf{u}}^\dagger\|$, $Re = 55$, $L/D = 0.5$. **(c)** $\|\hat{\mathbf{u}}^\dagger\|$, $Re = 72$, $L/D = 1$.

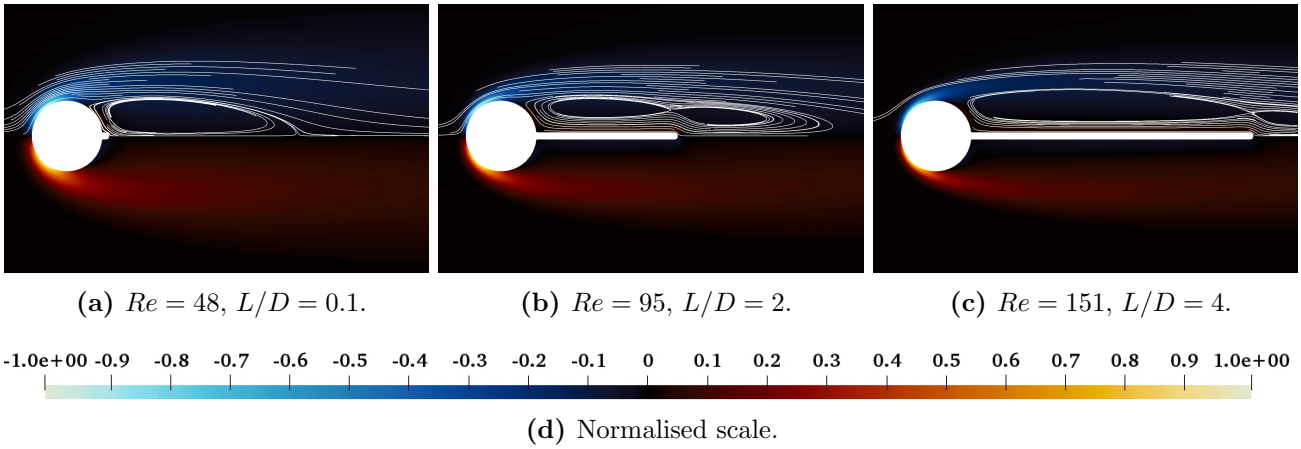
**(d)** $\|\hat{\mathbf{u}}^\dagger\|$, $Re = 95$, $L/D = 2$. **(e)** $\|\hat{\mathbf{u}}^\dagger\|$, $Re = 114$, $L/D = 3$. **(f)** $\|\hat{\mathbf{u}}^\dagger\|$, $Re = 151$, $L/D = 4$.

**(g)** Normalised scale.

**Figure 6.8:** Magnitude $\|\hat{\mathbf{u}}^\dagger\|$ of the velocity components of the vortex shedding instability ($\lambda^{VS,F}$). The continuous lines are associated to the base flow streamlines for the corresponding Reynolds numbers.

In figure 6.8, similarly to figure 6.6, is shown the the amplitude of the normalised adjoint velocity field $\left\|\hat{\mathbf{u}}^\dagger(x, y)\right\|_2$ of the adjoint vortex shedding mode close to the near wake region. It is first noted that as for the direct mode magnitude, even though the peak distribution appears close to the cylinder interface, it is completely detached, and the velocity at the interface is 0 due to the fixed wall and no-slip boundary condition in that case.
The shape of the amplitude of the normalised adjoint velocity field varies little by increasing the splitter plate length, conserving the same features for the geometries investigated: symmetrically distributed in the streamwise directions where the peak magnitude are located above and below the cylinder interface.
Interestingly, the location of the adjoint magnitude peaks and global shapes appear to be

strongly correlated to the streamlines of the base flows for the corresponding Reynolds numbers, represented by the white lines on the same figure 6.8. The location of the adjoint magnitude peaks and global shapes also coincide reasonably well with the base flow vorticity fields at the corresponding Reynolds numbers presented in figure 6.9.



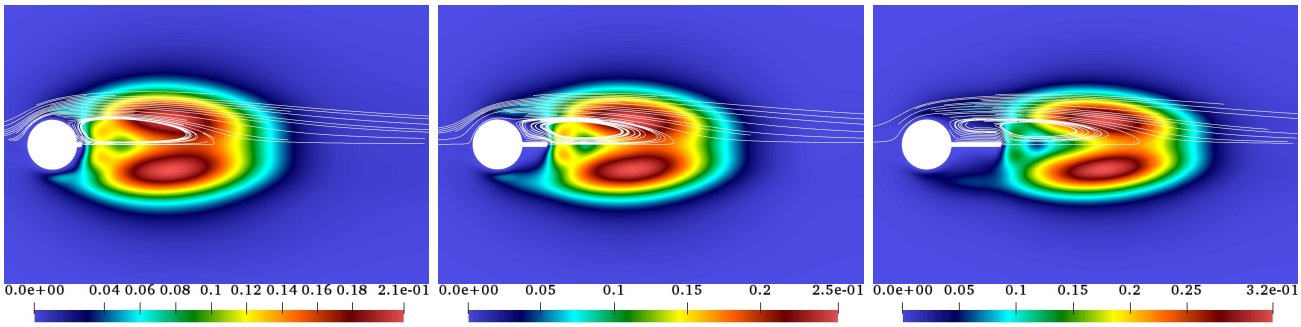

**(a)** $Re = 48$, $L/D = 0.1$. **(b)** $Re = 95$, $L/D = 2$. **(c)** $Re = 151$, $L/D = 4$.

**(d)** Normalised scale.

**Figure 6.9:** Normalised magnitude of the base flow vorticity. The continuous lines are associated to the base flow streamlines for the corresponding Reynolds numbers.

Indeed, the peak magnitude locations appear to be located right before the separations points of the base flow, previously denoted $S_1$ and $S_2$ in the schematic figure 2.3. This observation is in agreement with the fact that the adjoint solution itself can be physically interpreted as the "receptivity to momentum forcing and initial conditions" (Giannetti and Luchini, 2007) or "the sensitivity of the result to an instantaneous perturbation of the dependent variable" (Hall and Cacuci, 01 Oct. 1983). Hence, the adjoint solution corresponds and should be seen as the sensitivity of the direct mode to external disturbances (Hill, 1992). The rest of the adjoint magnitude fields also appears to be fairly distributed following the base flow shear layers of the recirculation bubble symmetrically above and below the splitter plate, in agreement with the previous comment.

Finally, figure 6.10 presents the map of the sensitivity to localised feedbacks (Giannetti and Luchini, 2007) represented by the value $\Theta_F(x, y)$ in the present study. The structure depicted by $\Theta_F(x, y)$ is noted to be similar to the one presented in the literature (Giannetti and Luchini, 2007; Negi et al., 2020) for the shortest splitter plate length $L/D = 0.1$, and this same structure also appears to be conserved yet gradually translated in the streamwise direction away from the cylinder as the splitter plate length increases up to $L/D = 3$. At $L/D = 4$, the vortex shedding shows significant sensible regions symmetrically distributed above and below the splitter plate located in the base flow shear layers. Interestingly at $L/D = 4$, the mode sensitivity to external disturbance $\left\|\hat{\mathbf{u}}^\dagger\right\|$ also appears significantly in the sensitivity map $\Theta_F(x, y)$, a feature which is not present for shorter lengths and to the knowledge of the author, not presented in the literature yet.




**(a)** $\Theta_F$, $Re = 48$, $L/D = 0.1$. **(b)** $\Theta_F$, $Re = 55$, $L/D = 0.5$. **(c)** $\Theta_F$, $Re = 72$, $L/D = 1$.

**(d)** $\Theta_F$, $Re = 95$, $L/D = 2$. **(e)** $\Theta_F$, $Re = 114$, $L/D = 3$. **(f)** $\Theta_F$, $Re = 151$, $L/D = 4$.

**Figure 6.10:** The sensitivity to spatially localised feedback $\Theta_F$ of the vortex shedding $\lambda^{VS,F}$ mode near the onset of the instability. The continuous lines are associated to the base flow streamlines for the corresponding Reynolds numbers.

Physically, the high magnitude regions of the structural sensitivity map $\Theta_F(x, y)$ presented in figure 6.10 depicted by the two symmetric bubbles close to the splitter plate tip, represent the flow regions in which small perturbations will affect the most the eigenvalue of the mode in question, here the vortex shedding formation. Finally, it is noted that neither the direct or the adjoint mode magnitudes shapes (at the exception of the splitter plate length $L/D = 4$) are noticeably visible in the structural sensitivity map $\Theta_F(x, y)$. This observation means that none of these fields considered independently is likely to give any relevant information on the structural sensitivity map $\Theta_F(x, y)$. Indeed, the structural sensitivity map $\Theta_F(x, y)$ proportionally results from the dot product of both the direct and adjoint magnitude fields (see expression (3.71)).

The values of $\|\Theta_F\|_\infty$ ($\equiv \max_{\mathbf{x}} \Theta_F$) along the threshold of stability in function of the splitter plate length for the fixed cylinder case corresponding to the cases presented in figure 6.10 are presented in table 6.2. This table shows that as the splitter plate length increases, the vortex shedding mode becomes more sensitive to structural perturbations, as the actual value of $\|\Theta_F\|_\infty$ is positively correlated to the length of the splitter plate. This observation physically implies that the vortex shedding mode can be more easily triggered for longer plates.

| $L/D$ | $Re$ | $\|\Theta_F\|_\infty$ |
|---|---|---|
| 0.1 | 48 | 0.209 |
| 0.5 | 55 | 0.253 |
| 1.0 | 72 | 0.325 |
| 2.0 | 95 | 0.324 |
| 3.0 | 114 | 0.357 |
| 4.0 | 151 | 0.593 |

**Table 6.2:** Values of $\|\Theta_F\|_\infty (\equiv \max_{\mathbf{x}} \Theta_F)$ along the threshold of stability in function of the splitter plate length for the fixed cylinder case (matching figure 6.10).

It should be noted that the critical Reynolds number for which the vortex shedding instability starts is also positively correlated to the splitter plate length. In other words, the longer the plate, the greater the critical Reynolds number from which the vortex shedding instability initiates. Hence the higher $\|\Theta_F\|_\infty$, presented in table 6.2, might also be physically associated with the increase in Reynolds number and the smaller "apparent viscosity" of the flow, which naturally tend to make most flows configurations more unstable.

## 6.3 Symmetry breaking

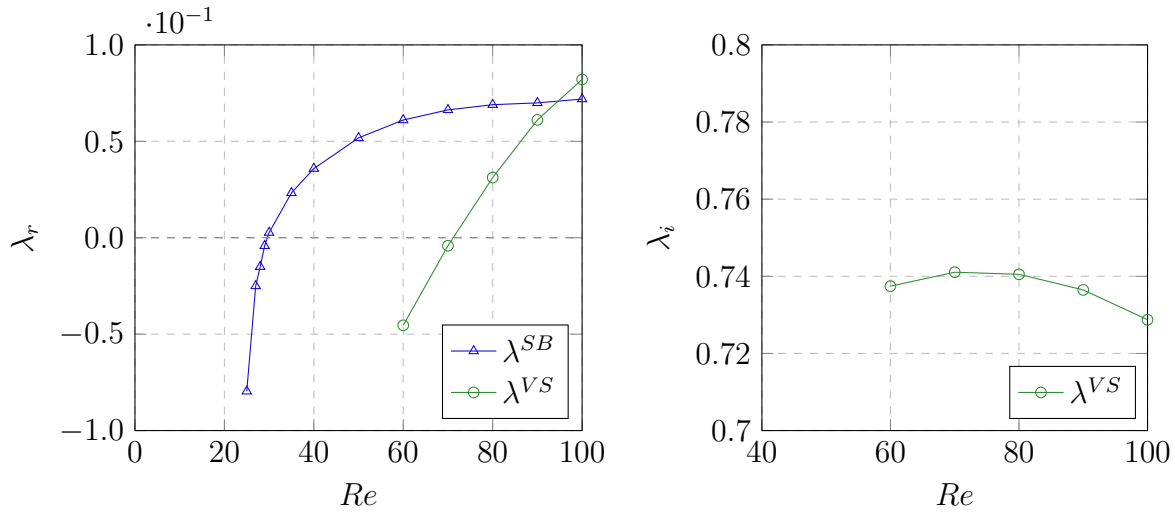
In this second part of the study is considered the case where the cylinder is released and free to rotate around the $z$ Cartesian axis as presented in figure 6.1, and governed by the equation (6.2). The reduced velocity is now decreased to the fixed value $U_R = 3937$ (corresponding to $I_\theta = 50$, $c_\theta = 0$ and $k_\theta = 10^{-4}$).

First, the stability and the sensitivity of the symmetry breaking mode are discussed. The results of the present study show that, apart from the strong correlation of the emergence of this mode with the length of the recirculation zone (or Reynolds number in other references) - also observed in the works of Bagheri et al. (2012*b*); Cimbala and Garg (1991); Lacis et al. (2014*b*) - it has consistently been found that this mode is most unstable for $L/D \simeq 1$ (see figure 6.12). Therefore, in this section, the focus is put on the case of $L/D = 1$, while discussing the other $L/D$ if necessary.

### 6.3.1 Linear stability

In this section, we only focus on the locations of the stability/instability regions in the $Re$ - $L/D$ plane. It is known that once unstable, the plate tends to dynamically migrate to a stable position (where the tip of the splitter plate is fairly located near the shear layer region of the

base flow recirculation bubble), which is seen as the saturated state of the instability (Lacis et al., 2014*b*). The saturated plate angle is not sought in the present study.




**(a)** Growth rate. **(b)** Frequency.

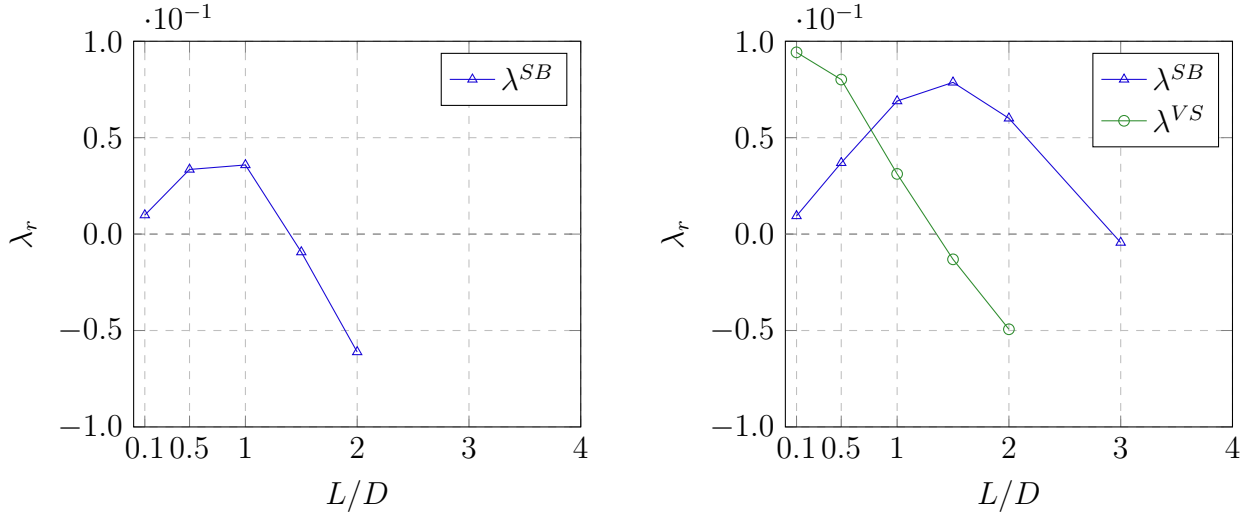
**Figure 6.11:** The linear growth rate and frequency of symmetry breaking mode ($\lambda^{SB}$) and vortex shedding mode ($\lambda^{VS}$) as a function of the Reynolds number ($L/D = 1$, $I_\theta = 50$, $U_R = 3937$). Note that the frequency of the symmetry breaking mode is not drawn in (b), since $\lambda_i^{SB} = 0$.

Figure 6.11 presents the variation of the two leading eigenvalues (symmetry breaking mode and vortex shedding mode) in a range of Reynolds number from $Re = 20$ to $Re = 100$ for a fixed splitter length of $L/D = 1$. In figure 6.11(a), it is observed that the symmetry breaking mode is the first instability, as was also highlighted in Figure 6.2. It is noted that for $Re > 70$, the vortex shedding mode is also unstable if the cylinder is held fixed. However, if it is not initially fixed, the symmetry breaking mode would have been initiated. Therefore, in this case, a competition between the two modes will emerge in a transition to a non-linear state, depending on how the two modes are non-linearly coupled and initiated.

Figure 6.12 shows the variation of the growth rate of the symmetry breaking mode as a function of the splitter plate length $L/D$ at two different Reynolds numbers. In figures 6.12(a) and 6.12(b), it is noted that for $L/D < 1$, the symmetry breaking mode is stabilised as the splitter plate length $L/D$ decreases. This would physically be anticipated since the body shape becomes a circular cylinder as $L/D \to 0$.

In figure 6.12(b), it is observed that the vortex shedding mode grows faster than the symmetry breaking mode for $L/D < 0.75$. This implies that the flow is most likely to transition through the fluid instability mode before the structural mode if the angle of the cylinder is initially placed to be $\theta = 0$ at the given Reynolds number, $Re = 80$. This is not immediately clear from the neutral stability curve in figure 6.2. However, one must recall that if the flow at a Reynolds number of $Re = 80$ is realised by increasing the flow speed, the flow regime will

change along a horizontal line in figure 6.2 for a fixed $L/D$. Hence, in that case, the flow would first experience the symmetry breaking mode at a lower Reynolds number. This implies two possibly different routes of the transition to the final fully non-linear state at $Re = 80$. It is noted that understanding the detailed transition dynamics needs a further non-linear analysis beyond the scope of the present study. Lastly, figure 6.12 also indicates a specific splitter plate length, at which the growth rate of the symmetry breaking mode becomes maximum. This length appears to be around $L/D \simeq 1$ for the two Reynolds numbers $Re = 40$ and $Re = 80$.



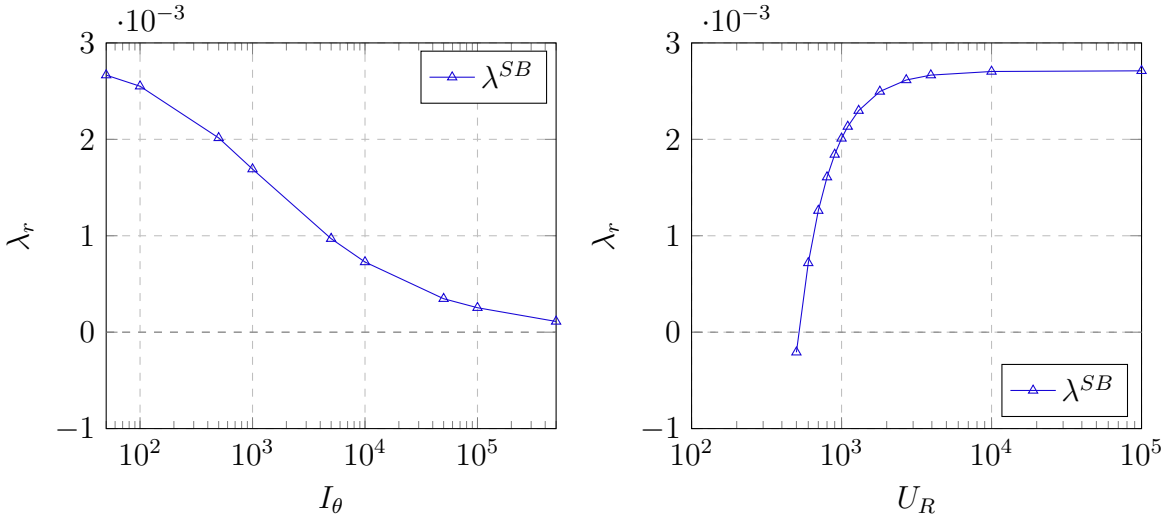

**(a)** $Re = 40$. **(b)** $Re = 80$.

**Figure 6.12:** The linear growth rate of symmetry breaking mode ($\lambda^{SB}$) and vortex shedding mode ($\lambda^{VS}$) as a function of the plate length $L/D$ ($I_\theta = 50$).

In figure 6.13, the behaviour of the symmetry breaking mode with the changes in the structural parameters $I_\theta$ and $U_R$ (or equivalently the torsional spring stiffness) for a fixed splitter plate length of $L/D = 1$ at $Re = 30$ is considered. Figure 6.13(a) shows that the linear growth rate of the symmetry breaking mode always remains positive for all $I_\theta$ considered, while it tends to decrease on increasing $I_\theta$. This observation is consistent with the expression (6.2a), where $I_\theta$ appears to effectively control the strength of the coupling between fluid and structural motions: the higher $I_\theta$ is, the weaker the coupling is. This observation also suggests that the symmetry breaking mode is indeed a consequence of FSI.

Figure 6.13(b) shows that the growth of the symmetry breaking mode changes very little above a reduced velocity $U_R \simeq 4000$. As $U_R$ is reduced from this value, the growth rate quickly decreases and eventually becomes stable (negative) at $U_R \simeq 520$. This is a simple physical consequence of the fact that the body's rotational motion is prevented by a very stiff torsional spring – note that the rigid case is given in the limit of $U_R \to 0$. The lower reduced velocity ($U_R \simeq 520$) for which the symmetry breaking mode becomes stable can be physically interpreted as a bound to the structural stiffness at which the symmetry breaking begins to appear, as intuitively for

a structurally "very stiff" body, we would not observe any rotation of the splitter plate due to the motion of the surrounding flow.




**(a)** Varying the inertia for $U_R = 3937$.

**(b)** Varying the reduced velocity for $I_\theta = 50$.

**Figure 6.13:** The linear growth rate of symmetry breaking mode ($\lambda^{SB}$) at $Re = 30$ and $L/D = 1$, as a function of (a) inertia and (b) reduced velocity.

### 6.3.2 Physical mechanism of instability

To understand how the symmetry breaking mode is initiated, the structural part of equation (3.64) is now rearranged to examine what physical quantities drive the instability. In particular, as presented in more details in Appendix B, the eigenvalue $\lambda$ is decomposed into the structural and fluid components, $\lambda^S$ and $\lambda^F$ respectively, such that

$$\begin{aligned} \mathbf{I}\dot{\hat{\boldsymbol{\xi}}} + \hat{\mathcal{S}}\hat{\boldsymbol{\xi}} &= \mathcal{A}\hat{\mathbf{q}} \\ \Leftrightarrow \lambda &= \underbrace{-\frac{\hat{\boldsymbol{\xi}}^H \mathbf{W}_S \hat{\mathcal{S}} \hat{\boldsymbol{\xi}}}{\hat{\boldsymbol{\xi}}^H \mathbf{W}_S \hat{\boldsymbol{\xi}}}}_{\lambda^S} + \underbrace{\frac{\hat{\boldsymbol{\xi}}^H \mathbf{W}_S \mathcal{A}\hat{\mathbf{q}}}{\hat{\boldsymbol{\xi}}^H \mathbf{W}_S \hat{\boldsymbol{\xi}}}}_{\lambda^F}, \end{aligned} \tag{6.3}$$

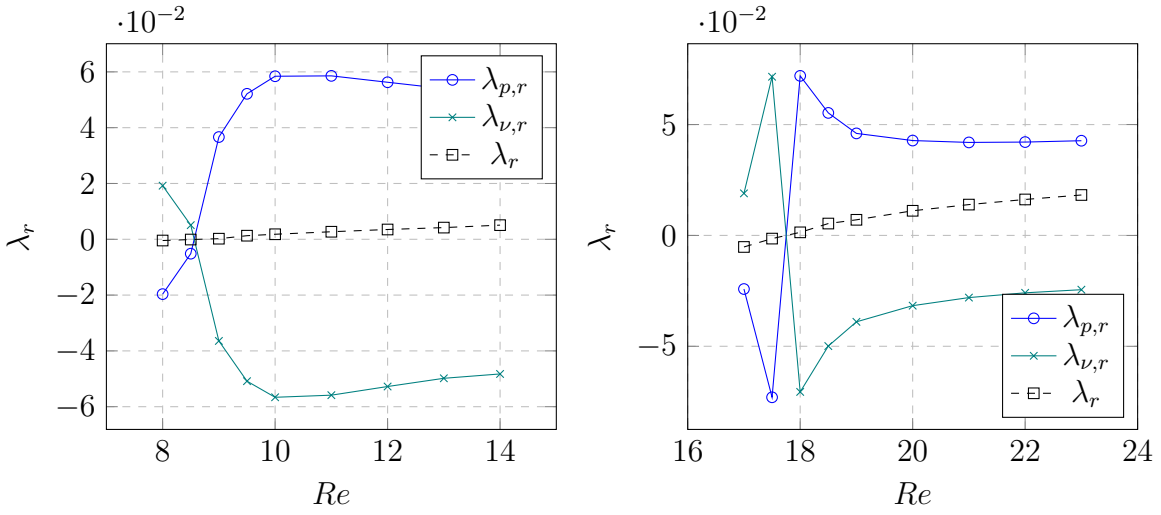
where in that case $\hat{\boldsymbol{\xi}} = [\hat{\theta}\ \dot{\hat{\theta}}]^T = [\hat{\theta}\ \hat{\phi}]^T$ is the vector containing the structural variables and $\hat{\phi}$ represents the angular velocity, $\hat{\mathcal{S}}$ is the structural part of the operator $\hat{\mathcal{H}}$ defined in (3.64) considering the unique structural degree of freedom $\theta$, $\mathcal{A}\mathbf{q} = [\mathbf{0}\ \frac{\mathfrak{m}_z}{I_\theta}]^T$ is the moment matrix defined in (3.64) as part of the global operator $\hat{\mathcal{H}}$ and $\mathbf{W}_S$ is the weight matrix defined in (3.48b).

Without the presence of a structural damping parameter ($\zeta_\theta = 0$), the growth rate structural

contributions $\lambda^S$ are identically 0, and it holds

$$\lambda = \lambda^F = \lambda_p + \lambda_v. \tag{6.4}$$

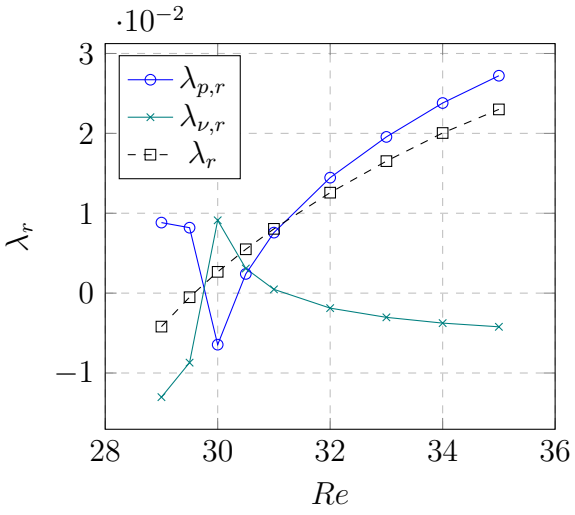
In figure 6.14 is presented the growth rate contributions $\lambda_p$ pressure and $\lambda_v$ viscous, as well as the total contribution $\lambda_{tot}$.



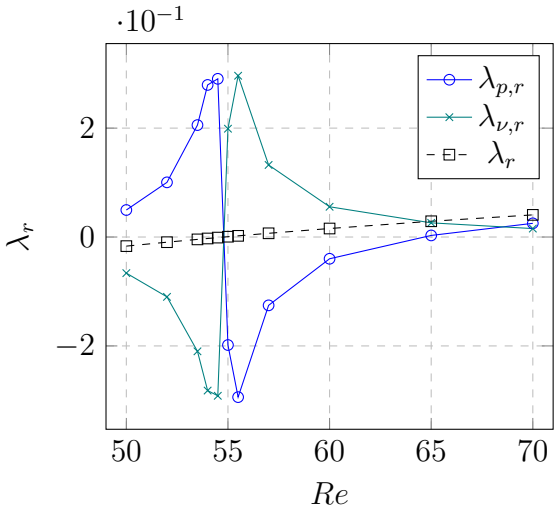

**(a)** $L/D = 0.1$.




**(b)** $L/D = 0.5$.




**(c)** $L/D = 1$.




**(d)** $L/D = 2$.

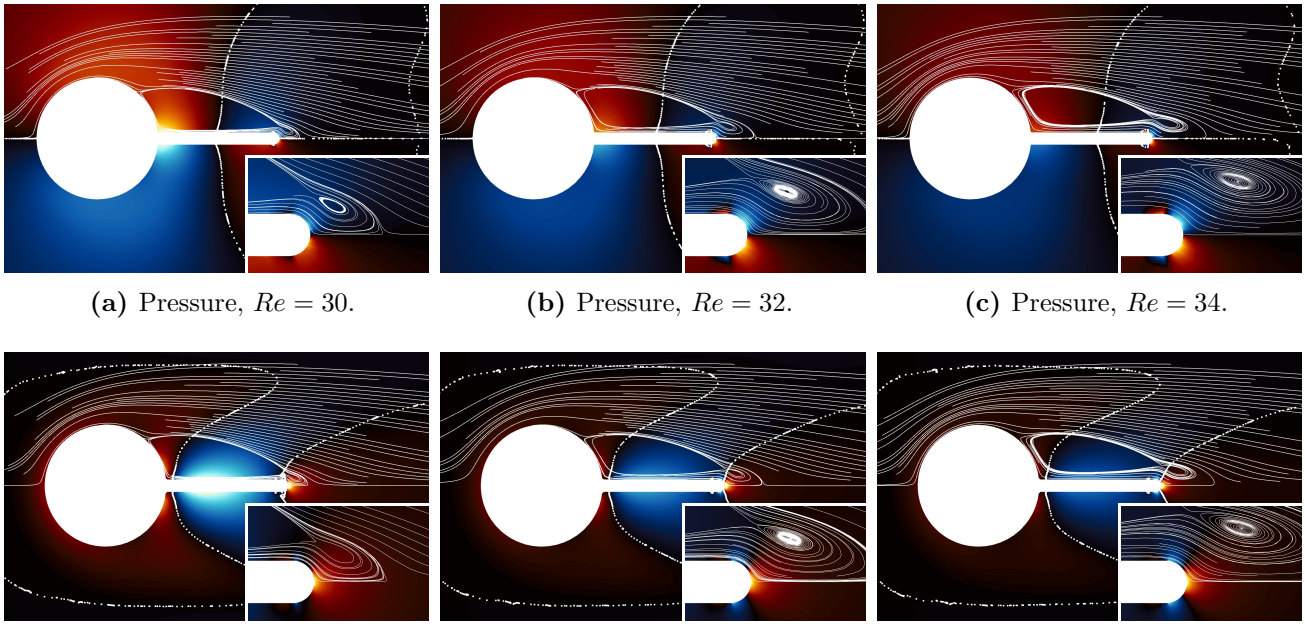
**Figure 6.14:** Componentwise contributions to the instability growth rate (see ((6.4))): $\lambda_{p,r}$, pressure; $\lambda_{\nu,r}$ viscous stress; $\lambda_r$ the growth rate as a function of the Reynolds number.

In figure 6.14 is reported how the torque from pressure and viscous stress contributes to the symmetry breaking mode as $Re$ changes: i.e. the contributions of $\lambda_{p,r}$ and $\lambda_{\nu,r}$ to $\lambda_r$. It is first considered relatively short plates ($L/D = 0.1, 0.5$ in figures 6.14(a,b)).

When $Re$ is lower than that for the onset of the symmetry-breaking instability, the pressure

stabilises the flow while the viscous stress plays a destabilising role at low Reynolds numbers. As $Re$ is increased, this balance reverses near the onset of the instability. In this case, the pressure drives the instability, and the viscous stress plays a stabilising role, which remains the dominant behaviour forming the symmetry-breaking instability with a further increase of $Re$. The predominance in the destabilising role of pressure is also seen for longer plates ($L/D = 1, 2$; figure 6.14(c,d)), when $Re$ is sufficiently large than that for the onset of the instability. However, in this case, there is also a range of $Re$, in which the pressure stabilises the mode, while the viscous stress destabilises it: for example, $Re \simeq 30$ for $L/D = 1$ (figure 6.14(c)) and $55 \lesssim Re \lesssim 65$ for $L/D = 2$ (figure 6.14(d)).

The observations made here suggest that the balance between the pressure and viscous stress plays a crucial role in the symmetry breaking mode. It is noted that the change of the pressure and stress balance with $Re$ is likely to be associated with the recirculation zone in the near-wake region, given that the length of the recirculation zone is approximately linearly proportional to the Reynolds number $Re$ (see expression (6.3)).



**(a)** Pressure, $Re = 30$. **(b)** Pressure, $Re = 32$. **(c)** Pressure, $Re = 34$.

**(d)** Vorticity, $Re = 30$. **(e)** Vorticity, $Re = 32$. **(f)** Vorticity, $Re = 34$.

**Figure 6.15:** Pressure and spanwise vorticity of the eigenmode of symmetry breaking instability for $L/D = 1$ for different Reynolds numbers. Here, the red and blue colours denote positive and negative values respectively, and their brightness indicates the magnitude. The continuous lines are associated to the base flow streamlines for the corresponding Reynolds numbers and the dotted contours represents the 0-isocontour of the perturbed fields.

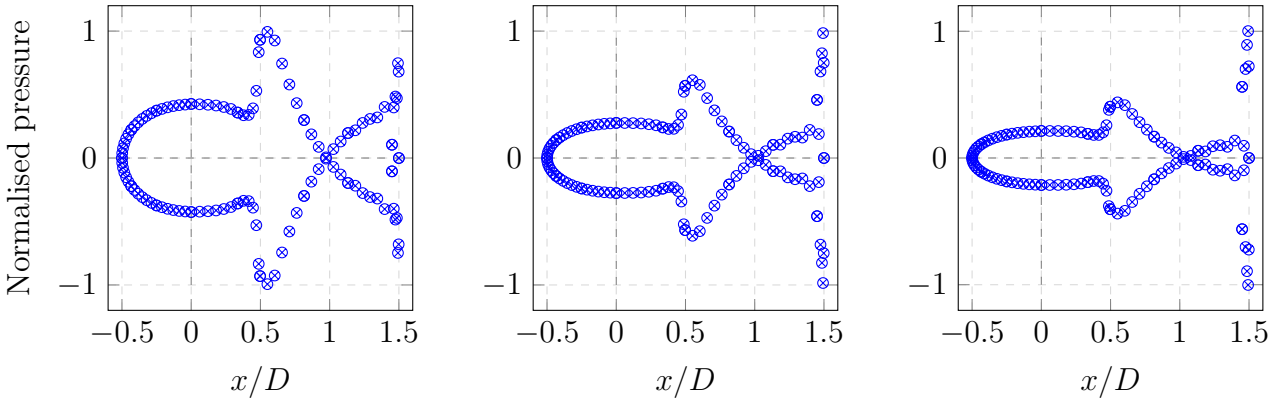
To understand how the symmetry breaking mode is associated with the recirculation zone, figure 6.15 further examine the symmetry breaking mode in relation to the flow structure of the recirculation zone for $L/D = 1$.

Figure 6.15 shows the pressure $p$ and vorticity $\omega_z$ distributions of the eigenmode presented

for an instability with a counter-clockwise rotation of the cylinder at Re=30, 32 and 34. From figure 6.14(c), it is observed that this is just after the onset of the symmetry-breaking instability and covers the range where the roles of pressure and viscous stress are interchanged. In these plots, the streamlines of the base flow are also indicated to visualise the recirculation bubble. It is observed that the flow feature is relatively similar for all $Re$ considered, although slightly changing in magnitude. The data is normalised so that the maximum value of the pressure and velocity magnitude is set to one.

First, considering the pressure distribution where it is noted that the moment is generated by normal forces acting on the splitter plate since the centre of rotation is at the centre of the cylinder so that no contribution is provided to the moment from the cylinder surface. There is a stabilising clockwise moment being generated by the pressure force on the inner part of the splitter plate from the root of the plate to approximately its midpoint. Analogously, there is a destabilising counter-clockwise pressure force acting from approximately the middle of the plate to the tip. As shown in figure 6.14, at $Re = 30$ the contribution to the clockwise moment is larger but this swaps over to a counter-clockwise pressure contribution at $Re = 32$ and 34. This change in sign is rather subtle and is not associated with any significant change in the structure of the pressure distribution but rather a change in the magnitude of each contribution (figures 6.15(a-c)).

Indeed, as presented in figures 6.16, the maximum pressure location increasingly shifts from the root of the splitter plate ($x/D = 0.5$) from $Re = 30$ to the tip of the splitter plate ($x/D = 1.5$) as the Reynolds number increases, as presented at $Re = 32$ and 34.




**(a)** $Re = 30$. **(b)** $Re = 32$. **(c)** $Re = 34$.

**Figure 6.16:** Normalised pressure distribution: $p/\max(p)$ at the solid interface of the cylinder with a splitter plate length $L/D = 1$ for three different Reynolds numbers: $Re = 30$, 32, and 34.

A similar observation can be made from the vorticity plots and the contribution towards the viscous moment component (figures 6.15(d-f)). The vorticity $\omega$ is chosen to be presented since

the vorticity is the negative of the strain tensor $E$ at the surface of the body (*i.e.* $E = -\omega$), and so the tangential direction of the viscous shear stress force can be inferred as the negative of the dynamics viscosity multiplied by the vorticity:

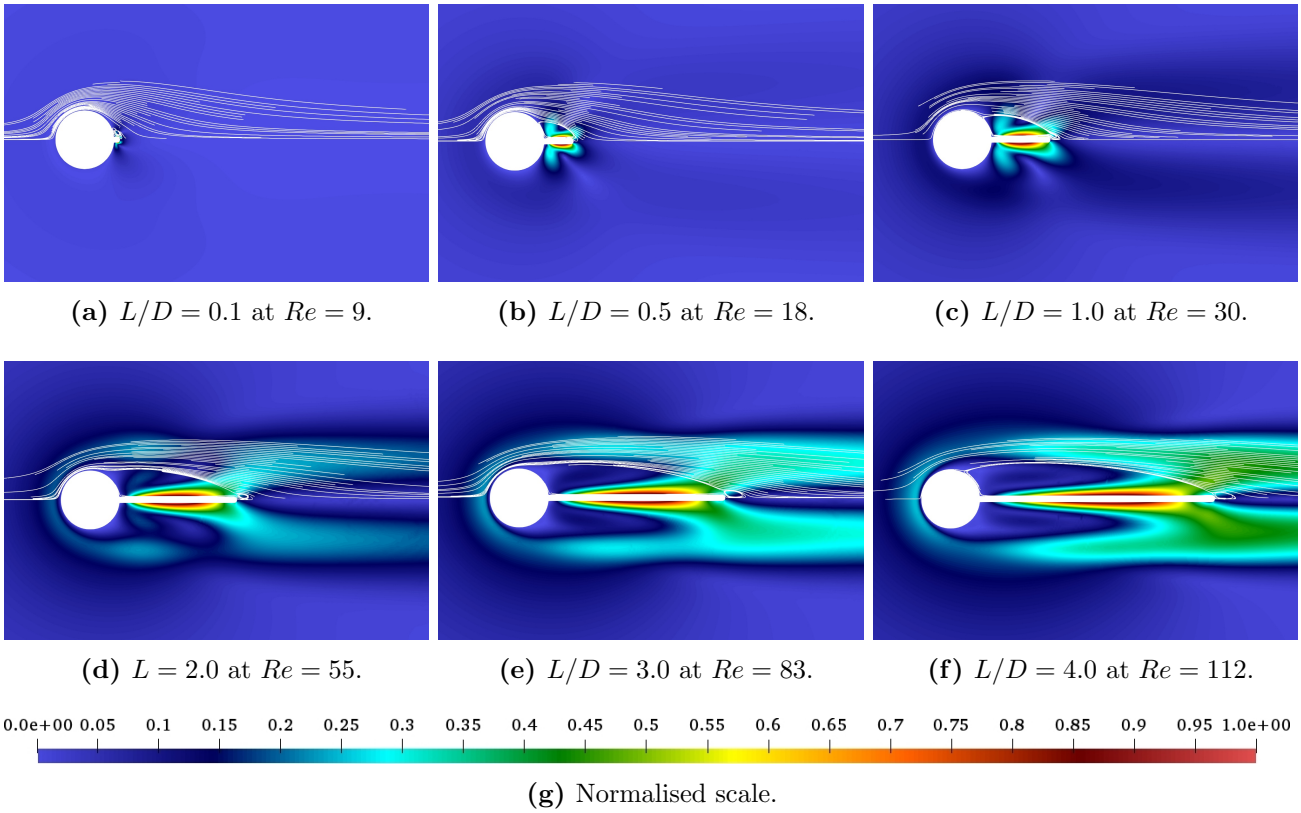
$$\varepsilon = -\nu\omega, \tag{6.5}$$

with $\varepsilon = \nu E$ in a Newtonian, isotropic medium.
On the upper surface of the splitter plate where is observed negative vorticity, therefore, the viscous shear stress is acting in the positive x-direction, and analogously the negative vorticity on the lower surface of the splitter plate (where the surface normal is now negated) is associated with shear stress in the negative x-direction. These shear components act over a large portion of the splitter plate surface and together generate a clockwise moment on the body. However, the magnitude of this moment is associated with a moment arm that is only half the thickness of the splitter plate.
Correspondingly, the positive vorticity on the cylinder surface and at the tip of the splitter plate is associated with a surface shear stress that generates a counter-clockwise contribution to the moment where the moment arm around the cylinder is equal to the radius and the moment arm at the tip is obviously equal to the splitter plate length plus the radius. Once again, there is a subtle balance between these two contributions where at $Re = 30$, the counter-clockwise contribution from the cylinder and tip dominate, but at $Re = 32, 34$, the clockwise contribution from the plate is more significant but relatively balanced. As with the pressure distribution, there is no significant change in structure with the change in Reynolds number.

Interestingly, as the symmetry breaking mode becomes unstable with increasing $Re$, the original recirculation bubble appears to develop a more substantial secondary daughter bubble near the tip with its increased size (see the inset of figures 6.15(a-c)) of which the size might also be associated with the splitter plate thickness.
This further suggests the importance of the structure of the base flow at the tip of the plate, as is also expected to see in the sensitivity analysis. This observation is also in agreement with the early experimental study of Toebes and Eagleson (1961), where vortex-induced vibrations of thin flat plates have been studied as a function of the trailing edge geometry and the motion's responses were reported to be largely sensitive to this parameter.

Finally, figure 6.17 presents the amplitude of the normalised perturbation velocity field $\|\hat{\mathbf{u}}(x,y)\|_2$ ($\equiv \sqrt{\hat{\mathbf{u}}^H\hat{\mathbf{u}}}$) of the symmetry breaking mode. In this figure is considered different splitter-plate lengths at Reynolds numbers close to the point of instability as presented in figure 6.2, where in every case a slightly unstable configuration is chosen.
The peak value of $\|\hat{\mathbf{u}}(x,y)\|_2$ on the boundary is located along the length of the splitter plate. Also, visualisation of the base flow's streamlines indicates that the peak perturbation along the splitter plate boundary is also centred at the approximate mid-point of the recirculation zone,

which is qualitatively about the length of the plate in every case. This figure also stresses the fact that the velocity magnitude field results principally from the stream-wise velocity $u$.




**(a)** $L/D = 0.1$ at $Re = 9$. **(b)** $L/D = 0.5$ at $Re = 18$. **(c)** $L/D = 1.0$ at $Re = 30$.

**(d)** $L = 2.0$ at $Re = 55$. **(e)** $L/D = 3.0$ at $Re = 83$. **(f)** $L/D = 4.0$ at $Re = 112$.

**(g)** Normalised scale.

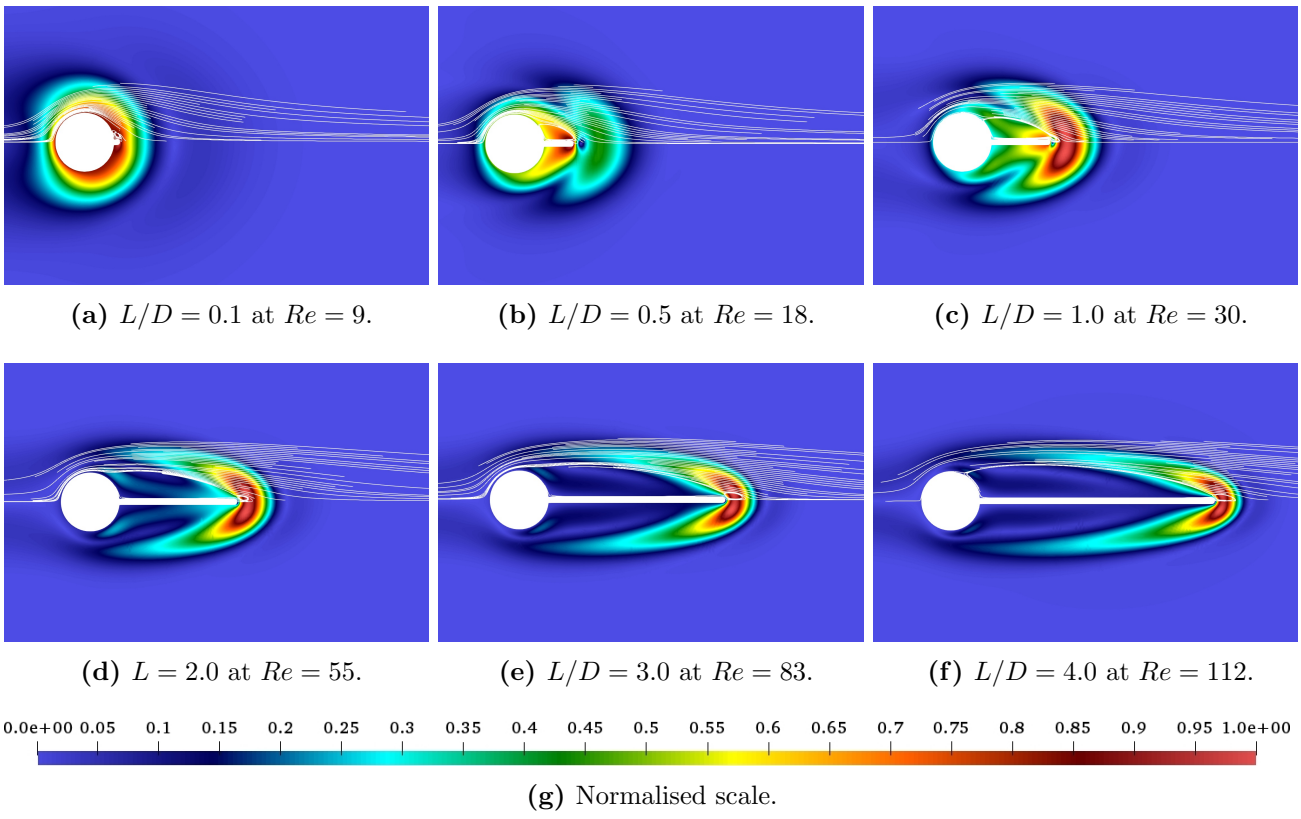
**Figure 6.17:** Visualisation of the normalised perturbed velocity field modulus $\|\hat{\mathbf{u}}\|$ of the symmetry breaking mode $\lambda^{SB}$. The white lines indicate the base flow streamlines.

### 6.3.3 Adjoint-based sensitivity

Next, the sensitivity of the symmetry breaking mode is considered. As for the stationary cylinder case, the adjoint perturbation velocity field $\hat{\mathbf{u}}^\dagger(x, y)$ represents the sensitivity to an open-loop body forcing in a weakly non-linear regime, whereas $\Theta_F(x, y)$ indicates the sensitivity to a small forcing in the form of localised feedback (Chomaz, 2005; Giannetti and Luchini, 2007). In particular, the sensitive region characterised by $\Theta_F(x, y)$ has often been referred to as the 'wavemaker' region for the vortex shedding mode.

Figure 6.18 shows the amplitude of the adjoint mode $\left\|\hat{\mathbf{u}}^\dagger(x, y)\right\|_2$. The shape of the adjoint mode changes notably as a function of the plate length. For shorter splitter plate lengths ($L/D < 1.5$), the peak of the adjoint mode amplitude is most energetic around the cylinder and splitter plate boundary, whereas for longer plates ($L/D > 1.5$) it becomes detached and appears slightly downstream of the tip of the splitter plate. It should be mentioned that the localisation of the adjoint mode amplitude near the tip of the splitter plate in figure 6.18 cannot be a consequence of increasing the Reynolds number. Indeed, while the role of the advection

increases with $Re$, it should be noted that the adjoint operator has advection towards upstream. Therefore, the consistent localisation of the adjoint mode around the tip is presumably a consequence of the increasing length of the splitter plate because exerting a force at the tip would lead to the largest torque to the cylinder.




**(a)** $L/D = 0.1$ at $Re = 9$. **(b)** $L/D = 0.5$ at $Re = 18$. **(c)** $L/D = 1.0$ at $Re = 30$.

**(d)** $L = 2.0$ at $Re = 55$. **(e)** $L/D = 3.0$ at $Re = 83$. **(f)** $L/D = 4.0$ at $Re = 112$.

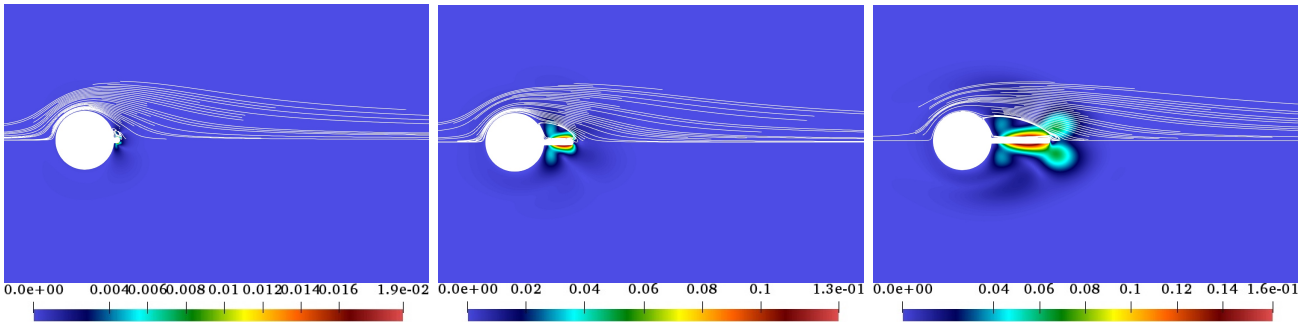
**(g)** Normalised scale.

**Figure 6.18:** Isocontours of the amplitude of the adjoint eigenmode of the symmetry breaking mode near the point of instability. Here, the contour levels are noramlised by the peak adjoint mode amplitude.

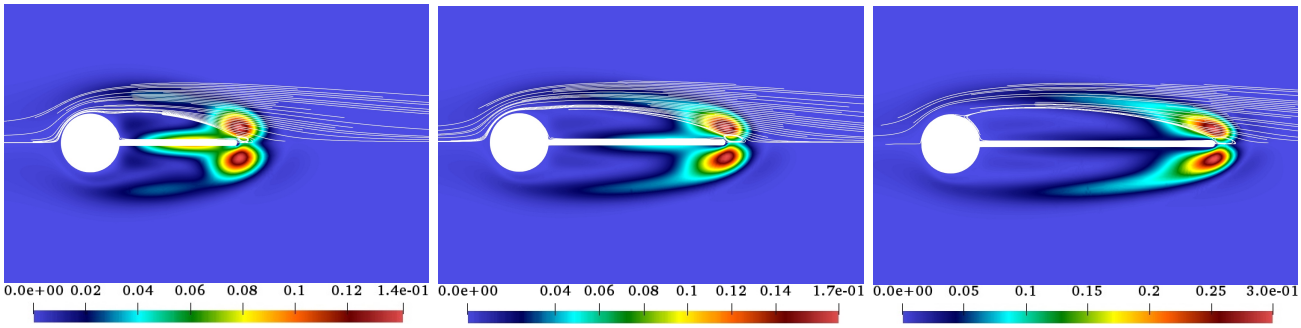
Also presented in these figures, the base flow streamlines do not appear to be strongly correlated to the adjoint eigenmode spatial distribution for very short splitter plate length. However, the adjoint eigenmode tip distribution appears to follow the curves of the recirculation zones for every splitter plate length and corresponding Reynolds numbers, and is most sensitive either inside (for short plates) or outside (for longer plates) of the recirculation bubble.

Analogous to figure 6.18 in figure 6.19, is represented the isocontours of the sensitivity to a spatially localised feedback $\Theta_F$ along the instability threshold for different splitter plate lengths. In this figure, as the splitter plate length $L/D$ increases, the spatial location of the most sensitive region is also shifted downstream due to the adjoint mode distribution shown in figure 6.18. For shorter splitter plate lengths $L/D < 1$, the sensitive region is located mainly across the splitter plate, whereas for longer splitter plate lengths $L/D > 1$, the highest sensitivity region is found to emerge at the end of the splitter plate. For $L/D = 1$, we observe that both of the

regions are equally energetic.




**(a)** $L/D = 0.1$ at $Re = 9$. **(b)** $L/D = 0.5$ at $Re = 18$. **(c)** $L/D = 1.0$ at $Re = 30$.



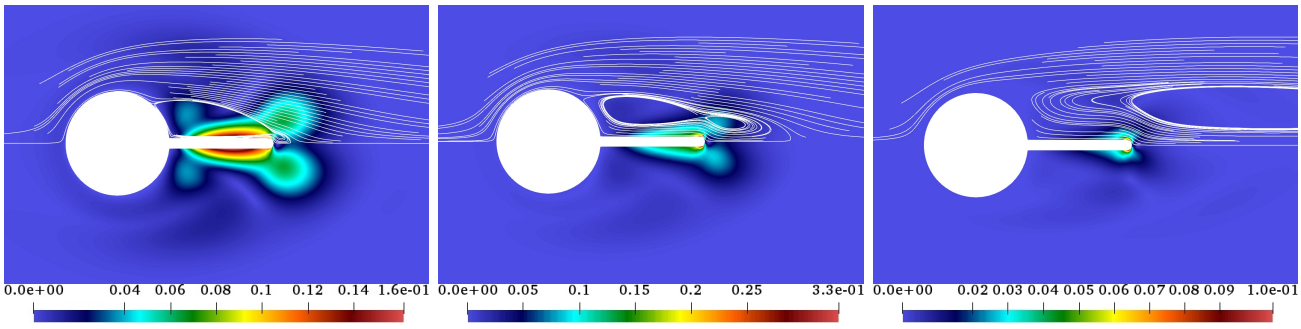

**(d)** $L/D = 2.0$ at $Re = 55$. **(e)** $L/D = 3.0$ at $Re = 83$. **(f)** $L/D = 4.0$ at $Re = 112$.

**Figure 6.19:** The sensitivity to spatially localised feedback $\Theta_F$ of the symmetry breaking mode near the onset of the instability.

Table 6.3 presents the numerical values of $\|\Theta_F\|_\infty$ ($\equiv \max_{\mathbf{x}} \Theta_F$) and $\Theta_S$ along the threshold of stability as a function of the splitter plate length and corresponding Reynolds number. It is noted that several order of magnitudes differentiates $\|\Theta_F\|_\infty$ ($\equiv \max_{\mathbf{x}} \Theta_F$) from $\Theta_S$ for every case, and no particular trend is noted between $\Theta_S$ and the increase in splitter plate length or Reynolds number for these particular tests. Hence, table 6.3 suggests that the instability appears to be strongly dominated by the structural quantities.

| $L/D$ | $Re$ | $\|\Theta_F\|_\infty$ | $\Theta_S$ |
|---|---|---|---|
| 0.1 | 9 | 0.019 | $4.636 \times 10^3$ |
| 0.5 | 18 | 0.127 | $7.109 \times 10^3$ |
| 1.0 | 30 | 0.163 | $9.508 \times 10^3$ |
| 2.0 | 55 | 0.142 | $9.508 \times 10^3$ |
| 3.0 | 83 | 0.168 | $8.564 \times 10^3$ |
| 4.0 | 112 | 0.303 | $6.727 \times 10^3$ |

**Table 6.3:** Values of $\|\Theta_F\|_\infty$ ($\equiv \max_{\mathbf{x}} \Theta_F$) and $\Theta_S$ along the threshold of stability as a function of the splitter plate length. The cases here correspond to those in figure 6.19.




**(a)** $Re = 30$. **(b)** $Re = 40$. **(c)** $Re = 100$.

**Figure 6.20:** Visualisation of the receptivity to spatially localised feedbacks, $\Theta_F$ of the symmetry breaking mode, for $L/D = 1.0$, varying the Reynolds number.

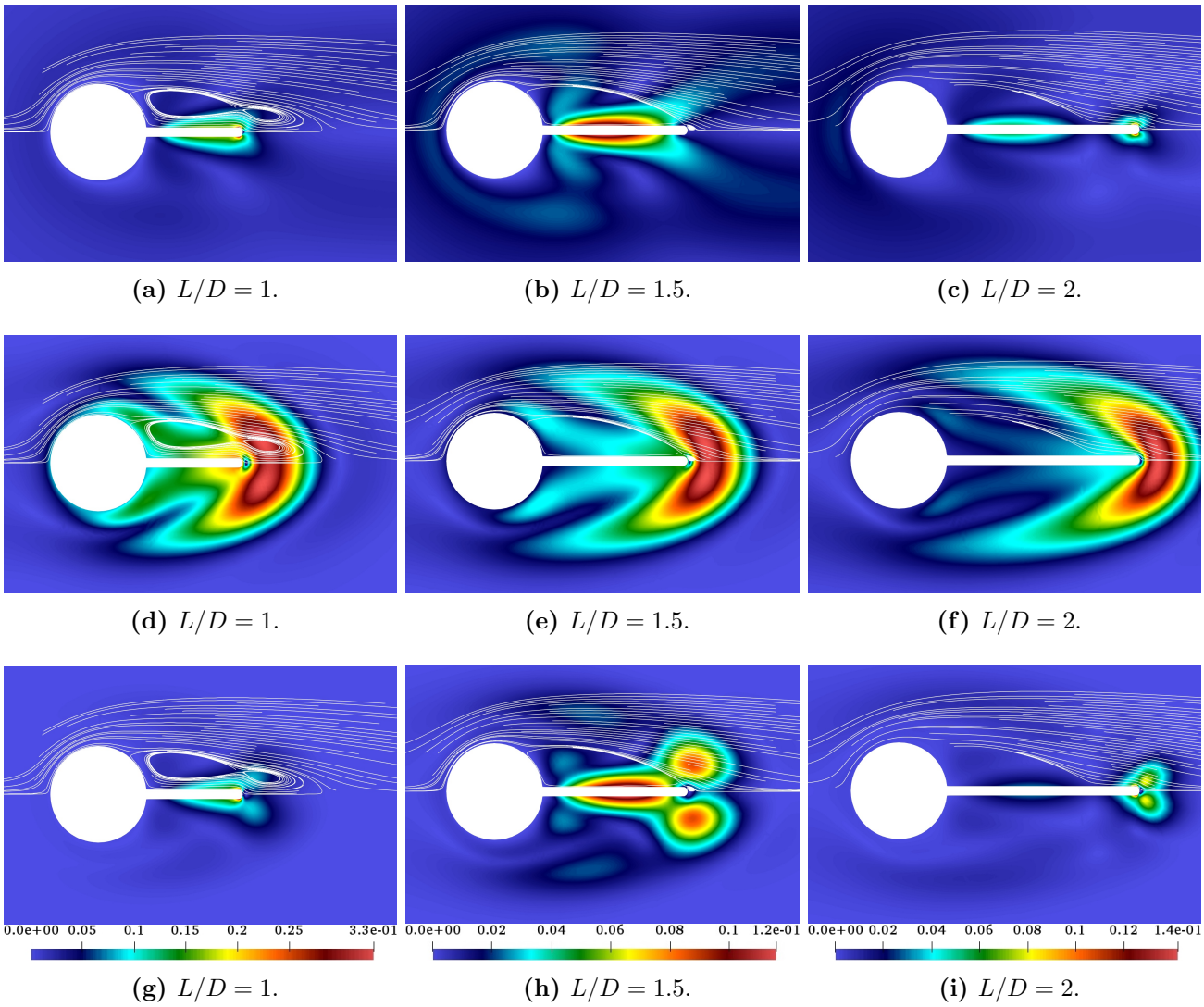
Next is considered in figure 6.20 the receptivity to spatially localised feedbacks $\left\|\hat{\mathbf{u}}^\dagger\right\| \cdot \|\hat{\mathbf{u}}\|$ as a function of the Reynolds number, for a fixed splitter plate length $L/D = 1.0$.
When $Re = 30$ there is a single unstable mode which correspond symmetry breaking instability, and this is also the case when $Re = 40$. The configuration at $Re = 30$ however correspond to a slightly unstable case as the Reynolds number is close to its critical value, as shown in figure 6.11(a). The case $Re = 100$, (shown in 6.20(c)) corresponds to a "bi-unstable" configuration when $\lambda^{SB}$ and $\lambda^{VS}$ are both unstable with $\lambda_r^{SB} < \lambda_r^{VS}$.
On these figures, it is noted that as the Reynolds number increases, the sensitivity region becomes more concentrated around the tip of the splitter plate, and the peak region becomes increasingly small. This might be in part be explained by the direction of the base flow in these configurations as depicted by the white streamlines. Indeed, as the Reynolds number increases, the base flow's re-circulation zone becomes more elongated, as presented in figure 6.2, and the ratio of the splitter plate length to the re-circulation length bubble $L/L_f$ becomes smaller. As a consequence, the splitter plate only "sees" a small fraction of the region that drive the instability (*i.e.* the recirculation zone), resulting in a smaller "control" region for these Reynolds numbers (*i.e.* for $Re = 40$ and 100). However, the value of the sensitivity at the peak location can be interpreted as an indicator on the difficulty to control the instability in these configurations.

| $L/D$ | $Re$ | $\|\Theta_F\|_\infty$ | $\Theta_S$ |
|---|---|---|---|
| 1.0 | 30 | 0.163 | 9508 |
| 1.0 | 40 | 0.332 | 6985 |
| 1.0 | 100 | 0.105 | 241.1 |

**Table 6.4:** Values of $\|\Theta_F\|_\infty$ and $\Theta_S$ in function of the Reynolds number for $L/D = 1$ (matching figure 6.20).

In table 6.4 are presented the values of $\|\Theta_F\|_\infty$ and $\Theta_S$ in function of the Reynolds number

for the splitter plate length $L/D = 1$, as discussed above. It is noted that the structural sensitivity is strongly correlated to the Reynolds number in this case, as about two orders of magnitude separate $\Theta_S$ at $Re = 30$ from $\Theta_S$ at $Re = 100$. These values, as well as the sensitivities visualisations $\Theta_F$ presented in figure 6.20, are indicators of the possibles controls of this instability.




**(a)** $L/D = 1$. **(b)** $L/D = 1.5$. **(c)** $L/D = 2$.

**(d)** $L/D = 1$. **(e)** $L/D = 1.5$. **(f)** $L/D = 2$.

**(g)** $L/D = 1$. **(h)** $L/D = 1.5$. **(i)** $L/D = 2$.

**Figure 6.21:** Comparison of the magnitude of (a-c) the direct mode $\|\hat{\mathbf{u}}\|$, (e-f) the magnitude of the adjoint mode $\left\|\hat{\mathbf{u}}^\dagger\right\|$ and (g-i) the sensitivity to localised forcing $\Theta_F$ for different plate length at $Re = 40$.

Finally, the direct mode, adjoint mode and sensitivity to localised feedback $\Theta_F$ for three different splitter plate length $L/D = 1, 1.5, 2$ at $Re = 40$ are compared, and this is shown in figure 6.21. The three plate lengths correspond to an unstable ($L/D = 1.0$), marginally stable ($L/D = 1.5$) and stable ($L/D = 2.0$) conditions, respectively.
The first row of plots (*i.e.* figures 6.21 (a-c)) shows the perturbed velocity field amplitude $\|\mathbf{u}\|_2$, the second row of plots (*i.e.* figures 6.21 (d-f)) presents the adjoint velocity field amplitude

$\left\|\mathbf{u}^\dagger\right\|_2$, and the last row of plots (*i.e.* figures 6.21 (g-i)) show the corresponding sensitivity to localised feedback $\Theta_F(x,y)$. In all the cases, the region of large $\|\mathbf{u}\|$ is located mostly around the splitter plate. For the longest plate $L/D = 2$, it also shows large intensity localised around the tip. The adjoint velocity field $\left\|\mathbf{u}^\dagger\right\|$ consistently exhibits the peak near the tip in all the cases (figure 6.18(d-f)). As the splitter plate length $L/D$ is increased, the peak region of the adjoint velocity field $\left\|\mathbf{u}^\dagger\right\|$ also consistently shifts downstream along with the tip location.
The sensitivity field $\Theta_F(x,y)$, which is a combination of the last two fields, has peak amplitude around the plate midpoint at $L/D = 1$. As the splitter plate length $L/D$ is increased, $\Theta_F(x,y)$ around the tip gradually becomes large. When $L/D = 2$, it exhibits its peak sensitivity only around the splitter plate tip. It is interesting to note that when $\Theta_F(x,y)$ appears to be distributed around the entire splitter plate for $L/D = 1$ and $L/D = 1.5$, at which the symmetry breaking mode is highly unstable ($L/D \simeq 1.0$; see also figure 6.12).
In any case, the importance of the flow around the tip is clearly well visible in the sensitivity analysis in this section, and this is consistent with the discussion in §6.3.2. Finally, the sensitivity to the structural parameters $\Theta_S$ is compared with the maximum value of $\theta_F$ in table 6.5. In all the cases investigated, the symmetry breaking mode has been found to be much more sensitive to the structural parameters, indicating that the symmetry breaking mode can easily be controlled by structural damping and stiffness.

| $L/D$ | $Re$ | $\|\Theta_F\|_\infty$ | $\Theta_S$ |
|---|---|---|---|
| 1.0 | 40 | 0.332 | 6985 |
| 1.5 | 40 | 0.111 | 9390 |
| 2.0 | 40 | 0.142 | 5100 |

**Table 6.5:** Values of $\|\Theta_F\|_\infty$ and $\Theta_S$ in function of the plate length at $Re = 40$ (matching figure 6.21).

## 6.4 Torsional flapping

For longer splitter plate lengths ($L/D > 3$), the leading instability is no longer the symmetry breaking mode, as shown in figure 6.2. Unlike the stationary symmetry breaking mode, which has a purely real eigenvalue, the eigenvalue of this mode has a non-zero imaginary part, indicating that it is an oscillatory/dynamic instability. Furthermore, the neutral stability curve of this mode in figure 6.2 does not seem to be correlated with the length of the recirculation zone, indicating that their origin is not necessarily related to the separation of the flow. As will be discussed later, this mode appears to share many similarities to the flapping instability of flag (Shelley and Zhang, 2011). One shall therefore refer to this mode as *torsional flapping*.

### 6.4.1 Linear stability

The linear stability characteristics of the torsional flapping mode are first explored. Figure 6.22 plots the linear frequency of the instability mode as a function of Reynolds number for different splitter plate lengths and compares it to that of the vortex shedding mode with or without FSI. Here, the frequencies are obtained when the modes are close to neutrally stability (i.e. $\lambda_r \simeq 0$). Regardless of the coupling with structural motion, the frequency of the vortex shedding mode always stays around $\lambda_i^{VS} \simeq 0.7 - 0.8$ for all the values of $L/D$ considered. As mentioned previously, the torsional flapping mode only appears for sufficiently long plates ($L/D \geq 3$ in this study). The frequency of the flapping mode ($\lambda_i^{TF} \simeq 0.3 - 0.4$) is found to be lower than that of the vortex shedding mode ($\lambda_i^{VS} \simeq 0.7 - 0.8$), although they both are in the same order of magnitude.

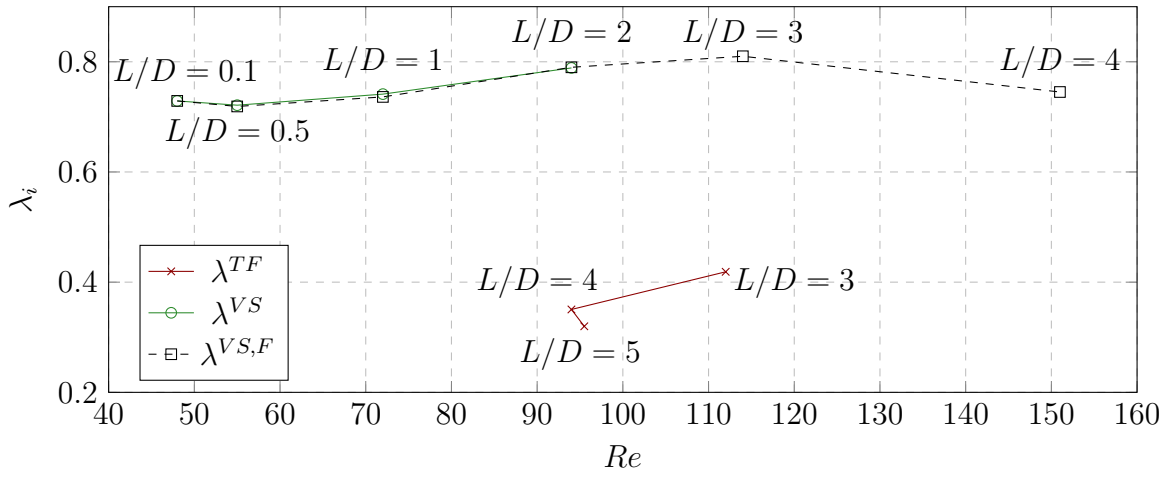
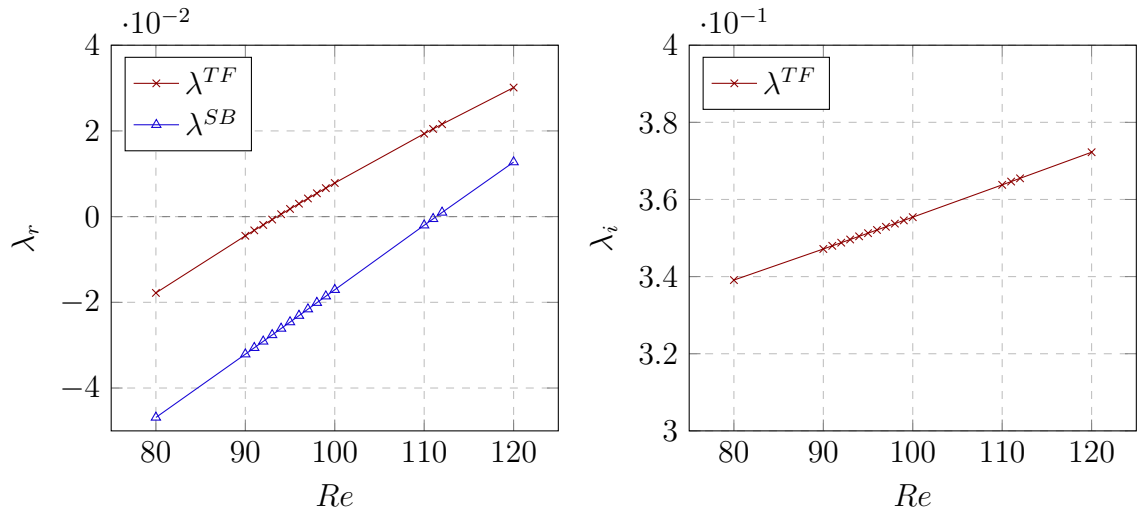



**Figure 6.22:** The linear frequency of torsional flapping mode and vortex shedding mode as a function of the Reynolds number ($I_\theta = 50$, $L/D = 0.1$ to 4, $U_R = 3937$). Here, $\lambda_r \simeq 0$.

Finally, the frequency of the flapping mode is found to change little with the variation of the Reynolds number (equivalently the length of recirculation zone), as is shown in figure 6.23.

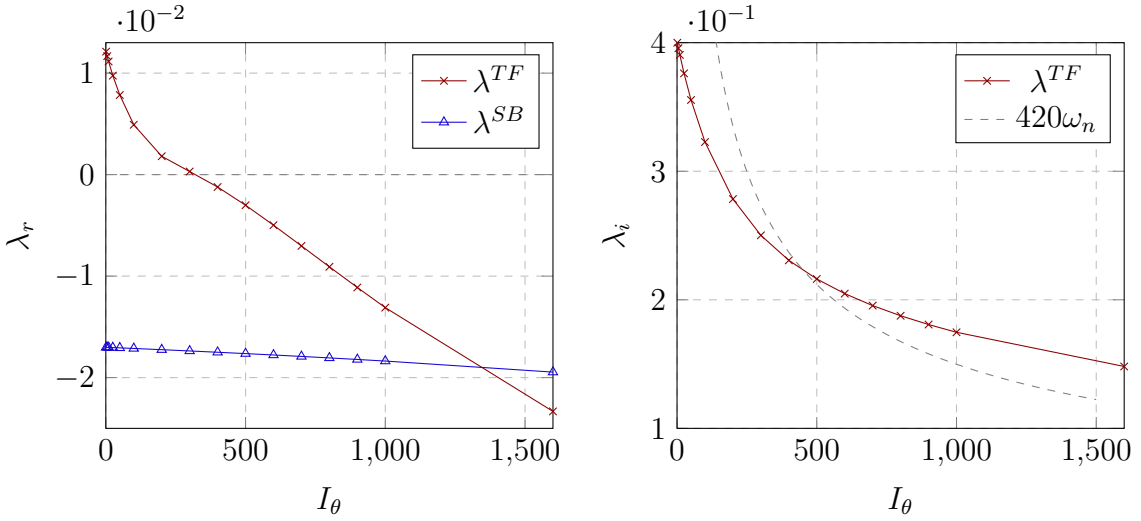
The change of the eigenvalue of the torsional flapping mode with the inertia $I_\theta$ is also reported with that of the symmetry breaking mode in figure 6.24. It is observed that the growth rate of the torsional flapping mode is reduced on increasing $I_\theta$ from a very low value ($I_\theta = 1$) and that the mode is completely stabilised at $I_\theta \simeq 300$ (figure 6.24(a)). It is noted that the stabilisation of the flapping mode with increasing $I_\theta$ is more rapid than that of the symmetry breaking mode. Therefore, it remains more stable than the symmetry breaking mode when $I_\theta$ is sufficiently great ($I_\theta \gtrsim 1300$ in this case). Finally, it is also observed that the frequency of the flapping mode decreases as $I_\theta$ is increased.




**(a)** Growth rate. **(b)** Frequency.

**Figure 6.23:** Linear growth rate and frequency of the torsional flapping ($\lambda^{TF}$) and symmetry breaking ($\lambda^{SB}$) mode as a function of the Reynolds number ($I_\theta = 50$, $L/D = 4$, $U_R = 3937$).

As a comparison, an harmonic of the natural angular frequency $\omega_n$ is also plotted on the same graph and interestingly, both curves appears to share similar shapes features.

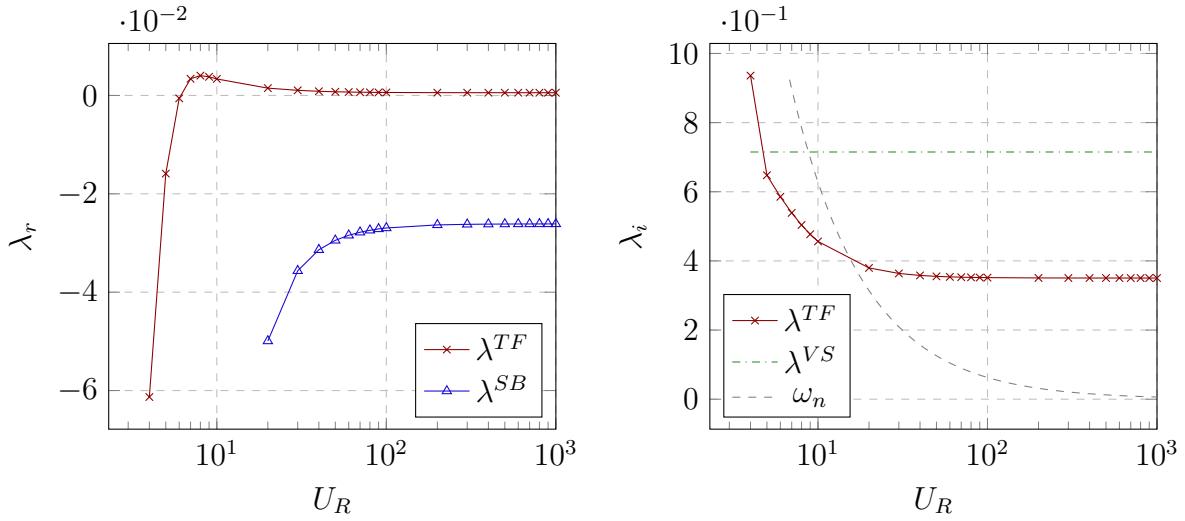



**(a)** Growth rate. **(b)** Frequency.

**Figure 6.24:** Variation of linear growth rate and frequency of the torsional flapping ($\lambda^{TF}$) and the symmetry breaking mode ($\lambda^{SB}$) with the dimensionless inertia $I_\theta$ ($L/D = 4$, $U_R = 3937$, $Re = 100$).

In figures 6.25 is shown the variation of the linear growth rate and frequency of the torsional flapping mode, $\lambda^{TF}$, at $Re = 94$ (the critical Reynolds number is $Re \simeq 93.5$ in this case) for a splitter plate length $L/D = 4$, with regards to the change in reduced velocity $U_R$. In the

same figure 6.25(a), it is also presented the growth rate of the symmetry breaking mode for comparison. Both of the instabilities appear to be insensitive, both in terms of growth rates and frequency, to the change in reduced velocity around the reference value studied in this work (i.e. $U_R = 3937$). For low values of $U_R$, the growth rate of the torsional flapping mode displays a small increase up to a local maximum value around $U_R \simeq 8$ before sharply decreasing as $U_R \to 0$ (*i.e.* to a rigid body configuration). This behaviour differs from that of the symmetry breaking mode, which is monotonically stabilised as $U_R \to 0$.




**(a)** Growth rate. **(b)** Frequency.

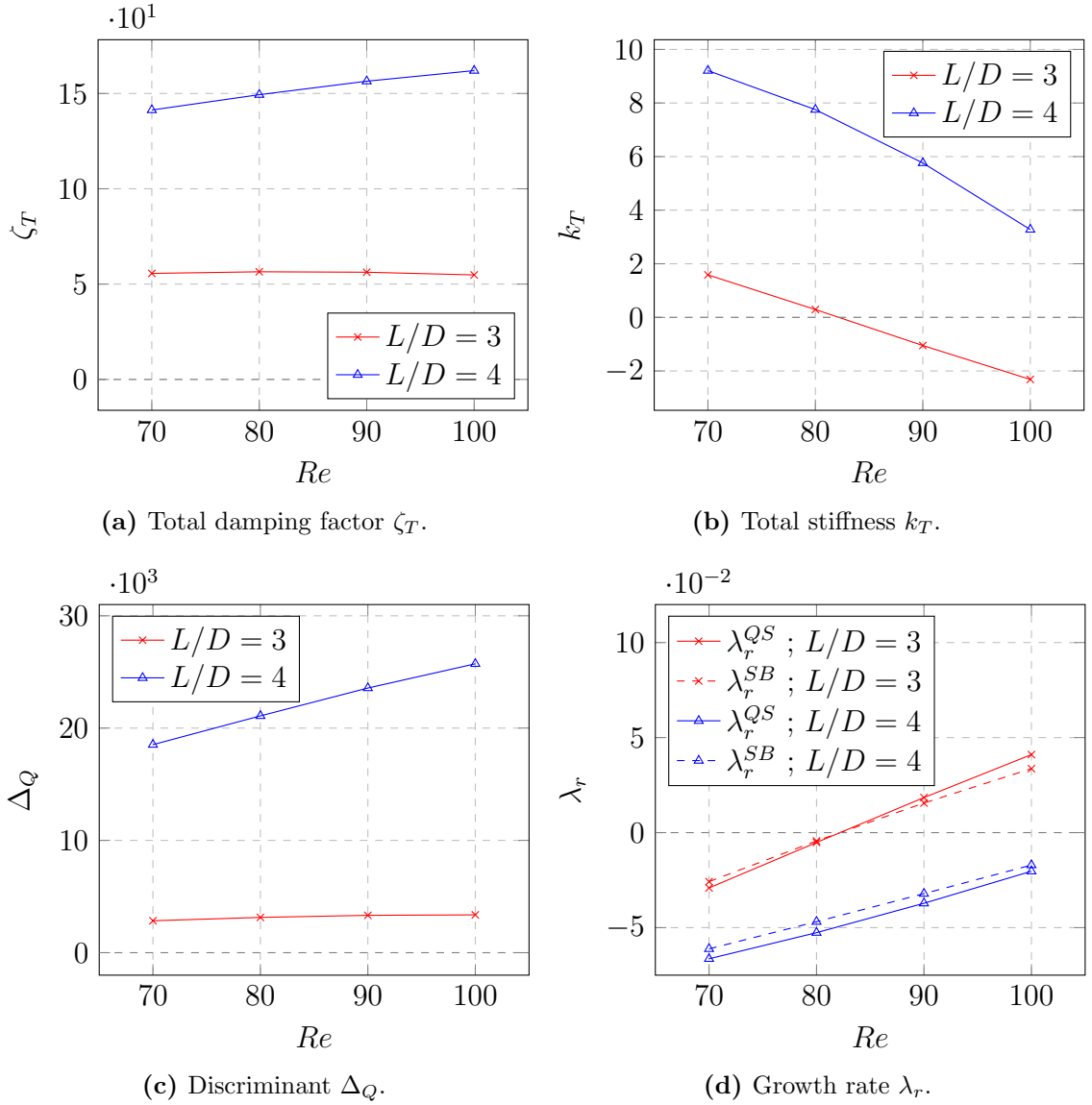
**Figure 6.25:** Variation of linear growth rate and frequency of the torsional flapping ($\lambda^{TF}$) and the symmetry breaking mode ($\lambda^{SB}$) with the reduced velocity $U_R$ ($L/D = 4$, $I_\theta = 50$, $Re = 94$).

Figure 6.25(b) shows the frequency of the torsional flapping mode as a function of the reduced velocity $U_R$. For larger reduced velocity $U_R \to +\infty$, the frequency remains mostly non-sensitive to the changes in reduced velocity, whereas it is noted that in that particular case, a sharp increase in frequency for reduced velocities gradually lower than $U_R \simeq 50$. For lower reduced velocities, the overall shape of the frequency curve is similar to the "natural frequency" of an object mounted on an elastic basis. Hence a strong dependency on the structural parameters is expected for low reduced velocities. As a comparison, the natural angular frequency $\omega_n$ is also plotted on the same graph, as well as the vortex shidding frequency at this particular Reynolds number, $Re = 94$.

However, the choice of the reduced velocity in the present study ($U_R = 3937$) appears to be far from this "transient" regime observed at low reduced velocity for the growth rate and frequency, and the present mode responses can be considered non-sensitive to this parameter.

### 6.4.2 Quasi-steady analysis

An interesting question might be whether the quasi-steady analysis can capture the torsional flapping instability. In this section, the question is investigated following the methodology previously presented in section §2.3.2 applied to torsional galloping.
To do so, the two splitter plate lengths that are undergoing the torsional flapping, given the choice of fluid and structural parameters in the present study, are tested, $L/D = 3$ and 4 over the range of Reynolds number $70 \leq Re \leq 100$ containing the threshold of instability of the torsional flapping mode for both splitter plate lengths.




**(a)** Total damping factor $\zeta_T$.

**(b)** Total stiffness $k_T$.

**(c)** Discriminant $\Delta_Q$.

**(d)** Growth rate $\lambda_r$.

**Figure 6.26:** Coefficients of the quasi steady homogeneous differential equation of motion, resulting solution regime, and growth rate in the range of Reynolds number $70 \leq Re \leq 100$.

In figure 6.26(a)(b) is shown the total damping $\zeta_T$ and the total stiffness $k_T$, resulting from the assumptions inspired from the quasi steady theory considering the moment as a function

of the angle $\theta$ and the angular velocity $\dot{\theta} = \phi$. Such considerations leads to the expression of the moment of the aerodynamic force around the $z$ Cartesian direction as $\mathfrak{m}_z = \mathfrak{m}_z^\theta + \mathfrak{m}_z^\phi$, and equation (6.2) can be rewritten as

$$\ddot{\theta} + \frac{4\pi\zeta_\theta}{U_R}\dot{\theta} + \left(\frac{2\pi}{U_R}\right)^2 \theta = \frac{4(\mathfrak{m}_z^\theta + \mathfrak{m}_z^\phi)}{\pi I_{\theta,r}}, \tag{6.6}$$

and linearised around the equilibrium point $(\theta, \phi) = (0, 0)$. Injecting the first order quantities $\partial_\theta \mathfrak{m}_z^\theta = \dfrac{\partial \mathfrak{m}_z^\theta}{\partial \theta}$ and $\partial_\phi \mathfrak{m}_z^\phi = \dfrac{\partial \mathfrak{m}_z^\phi}{\partial \phi}$ into the equation (6.6) leads to a homogeneous differential equation common to the quasi-steady literature (see Blevins (2001); Païdoussis et al. (2010)) corresponding to the linearised equation of motion under the assumption of a "frozen" displacement (*i.e.* $\theta$ and $\phi$ are considered constants in time over the fluid characteristic time scale), defined as

$$I_{\theta,r}\ddot{\theta} + \zeta_T\dot{\theta} + k_T\theta = 0, \tag{6.7}$$

where the total damping and stiffness respectively read

$$\zeta_T = I_{\theta,r}\frac{4\pi\zeta_\theta}{U_R} - \frac{4\partial_\phi \mathfrak{m}_z^\phi}{\pi} \quad \text{and} \quad k_T = I_{\theta,r}\left(\frac{2\pi}{U_R}\right)^2 - \frac{4\partial_\theta \mathfrak{m}_z^\theta}{\pi}. \tag{6.8}$$

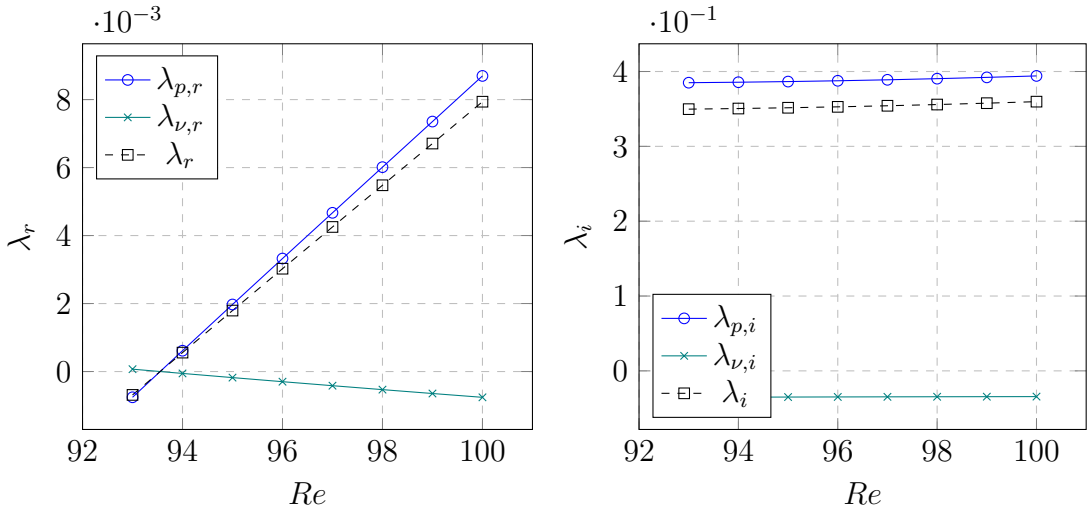
Finally, it is possible to evaluate the solutions of the equation (6.7) once the moment derivatives $\partial_\theta \mathfrak{m}_z^\theta$ and $\partial_\phi \mathfrak{m}_z^\phi$ are obtained numerically for a particular Reynolds number, by measuring the moment around the structure with a slight angle of attack and by modifying the boundary condition to emulate a rotating motion respectively (see section §2.3.2).
Figure 6.26 also presents the value of the discriminant $\Delta_Q$ in (c) of the characteristic equation associated to the equation (6.7) which associate the solution regime to aperiodic (*i.e.* $\Delta_Q > 0$), critical (*i.e.* $\Delta_Q = 0$), and pseudo-periodic (*i.e.* $\Delta_Q < 0$) depending on its sign. The real part of dominant root $\lambda_r$ of the characteristic equation associated to the equation (6.7), corresponding to the growth rate of the instability is finally presented in figure 6.26(d) (note that on this subfigure, $\lambda^{QS}$ stands for the dominant root obtained from quasi steady analysis and $\lambda^{SB}$ stands for the eigenvalues obtained from linear stability analysis).

This study shows that the structural rotational behaviour resulting from assuming steady moments derivatives belongs to the aperiodic regime in the range investigated ($70 < Re < 100$ for the splitter plate lengths $L/D = 3$ and 4), and does not capture the periodic mechanism observed when $L/D = 4$ from $Re = 94$ (*i.e.* $\Delta_Q > 0$ in figure 6.26(c)). Instead, it demonstrates the existence of the symmetry breaking mode with a good qualitative agreement to the mode growth rate $\lambda_r^{SB}$ obtained from the linear stability analysis presented in section §6.3 in figure 6.26(d), matching the results obtained in the previous section.
Figures 6.26(a) and (b) also show that the symmetry breaking mode results from a negative

total stiffness $k_T < 0$ rather than negative damping and hence belongs to the "static" instabilities family as *divergence* or *buckling* according to the quasi-steady assumptions, also in agreement with the results shown in the section above. Note that the divergence instability is usually practically observed when the hinge point is positioned behind the centre of pressure in the inline flow direction, which is not the case here (the centre of pressure is located between the hinge point and the splitter plate tip).
The galloping instability, on the other hand, is defined as resulting from and negative damping ($\zeta_T < 0$) in the pseudo periodic regime (*i.e.* $\Delta_Q < 0$) as first originating from the quasi-steady theory (Hartog, 1956).

### 6.4.3 Physical mechanism of instability

Now is explored the underlying physical mechanism of this oscillatory instability. Similarly to the symmetry breaking mode analysis in section §6.3.2, it is considered the pressure and viscous-stress contributions to the torsional flapping mode $\lambda^{TF}$ and this is shown in figure 6.27 for $L/D = 4$. It is evident that the flapping mode is predominantly driven by pressure, while the viscous stress plays a stabilising role in this oscillatory instability.

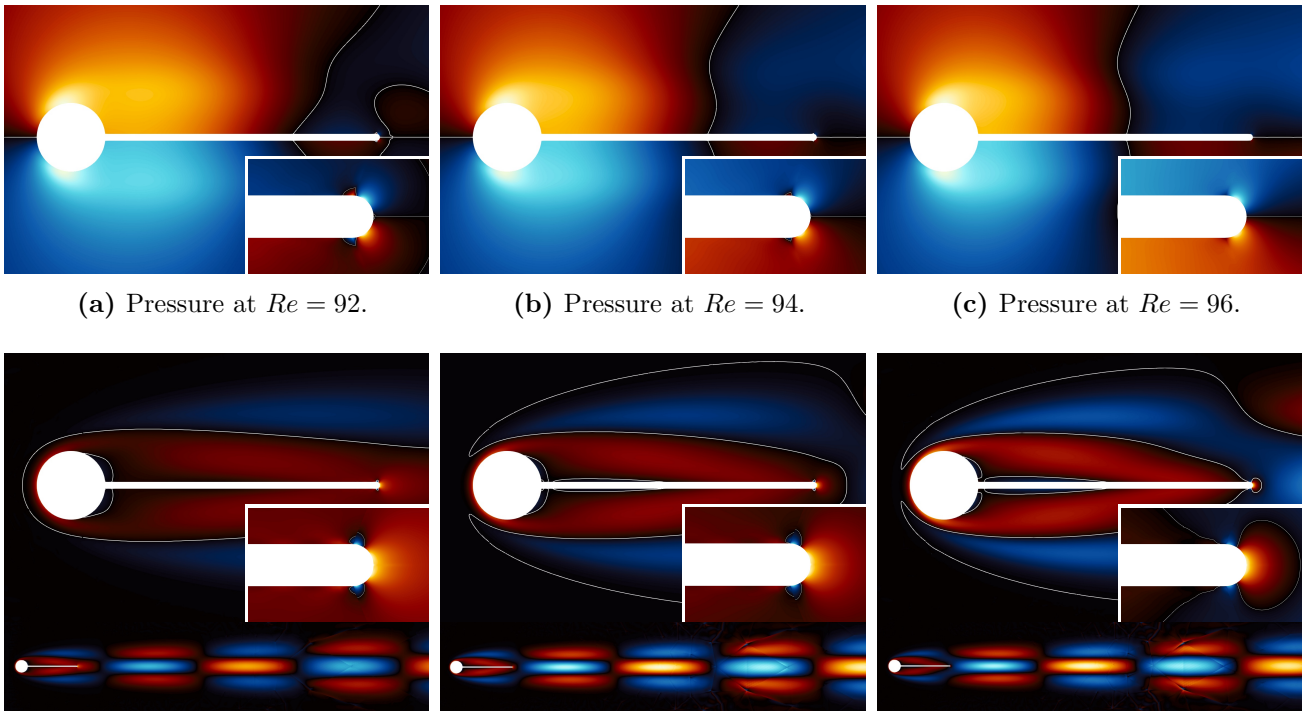



**(a)** Growth rate contributions. **(b)** Frequency contributions.

**Figure 6.27:** Componentwise contributions to the instability growth rate and frequency as a function of the Reynolds number for $L/D = 4$ (see (6.4)): $\lambda_{p,r}$, $\lambda_{p,i}$ pressure; $\lambda_{\nu,r}$, $\lambda_{\nu,i}$ viscous stress; $\lambda_r$, $\lambda_i$ the growth rate and frequency. Here, the critical Reynolds number for the onset of the instability is $Re_c \simeq 93.5$.

Pressure and spanwise vorticity fields of the torsional flapping mode are visualised at three different Reynolds numbers ($Re = 92, 94, 96$; note the critical Reynolds number for the onset of the instability is $Re_c \simeq 93.5$) in figure 6.28, where the phase of the eigenmode is set for a

time instance of counter-clockwise rotation of the cylinder.



**(a)** Pressure at $Re = 92$. **(b)** Pressure at $Re = 94$. **(c)** Pressure at $Re = 96$.

**(d)** Vorticity at $Re = 92$. **(e)** Vorticity at $Re = 94$. **(f)** Vorticity at $Re = 96$.

**Figure 6.28:** Pressure and spanwise vorticity of the eigenmode of symmetry breaking instability for $L/D = 4$ at $Re = 92$, 94 and 95. Here, the red and blue colours denote positive and negative values respectively, and their brightness indicates the magnitude. The white contour lines indicate $\hat{p} = 0$ and $\hat{\omega}_z = 0$.

First, given that the pressure generates the moment acting in the normal direction to the surface, only the pressure distribution around the plate can cause the rotation of the cylinder (see also the discussion in section §6.3.2 for the symmetry breaking mode). In all three cases, it is seen that the pressure distribution from the root of the plate to approximately the midpoint creates a moment in the clockwise direction, indicating its stabilising role in the rotation of the cylinder caused by the instability (figures 6.28(a-c)).

In contrast, the tip pressure distribution generates a moment in the counter-clockwise direction, thereby being the key mechanism of the instability. Indeed, as $Re$ is increased, the region with the destabilising pressure distribution in the near tip becomes wider with more elevated intensity. Second, the eigenmode of flapping mode shows a symmetric distribution of the spanwise vorticity about $y = 0$ (figures 6.28(d-f)). This indicates that the moments generated by most of the viscous shear stress in the upper and the lower part of the plate would cancel each other out. Therefore, the main contribution of the viscous shear stress to the moment would arise from the front stagnation point of the cylinder and from the tip of the plate.

The visualisation of the eigenmode reveals that the vorticity at the front stagnation point is much smaller than that at the tip. Also, the tip has a much longer moment arm than the

front stagnation point, indicating the importance of the tip vorticity distribution. For the cylinder rotating in the counter-clockwise direction due to the flapping mode instability, the positive spanwise vorticity near the tip indicates the stabilising role of the viscous shear stress, consistent with figure 6.27. Furthermore, the downstream vorticity right next to the region of the positive vorticity near the tip is negative (i.e. clockwise direction), indicating the emergence of a vortical structure rotating in the counter-clockwise direction in accordance with Kelvin's circulation theorem.

Let us now summarise the key features of the oscillatory instability discussed so far. First, the instability appears when the length of the splitter plate is sufficiently long. Importantly, the neutral stability does not show any correlation with the length of the recirculation zone (figure 6.2), indicating that the origin of this instability is not necessarily related to the recirculation zone in the near wake. Second, the mode is destabilised with increased frequency, as the mass of the splitter plate is gradually reduced from a significant value (figure 6.24). Third, the mode is stabilised by increasing the stiffness (figure 6.25). Finally, the mode is destabilised primarily due to pressure acting on the tip of the plate, while the viscous stress merely stabilises the mode (figure 6.27).
These features can be compared with those observed in a simple model for the flapping (or flutter instability) for flag and elastic plate immersed in an inviscid uniform flow (see the analysis on page 455 in Shelley and Zhang, 2011). The dispersion relation of their model is given by

$$(\omega + k)^2 = \frac{1}{2}(-R_1|k|^2\omega^2 + R_2|k|^5), \tag{6.9}$$

where $k$ is the spatial streamwise wavenumber of the flag (or plate) and $\omega$ the complex frequency for the instability frequency and growth rate, $R_1$ the dimensionless inertia of the flag (or plate) and $R_2$ its dimensionless stiffness (or rigidity). When (6.9) exhibits an instability, its real frequency (denoted by $\omega_r$) is given by

$$\omega_r = -\frac{2k}{2 + R_1|k|} \tag{6.10a}$$

and the growth rate for instability is proportional to

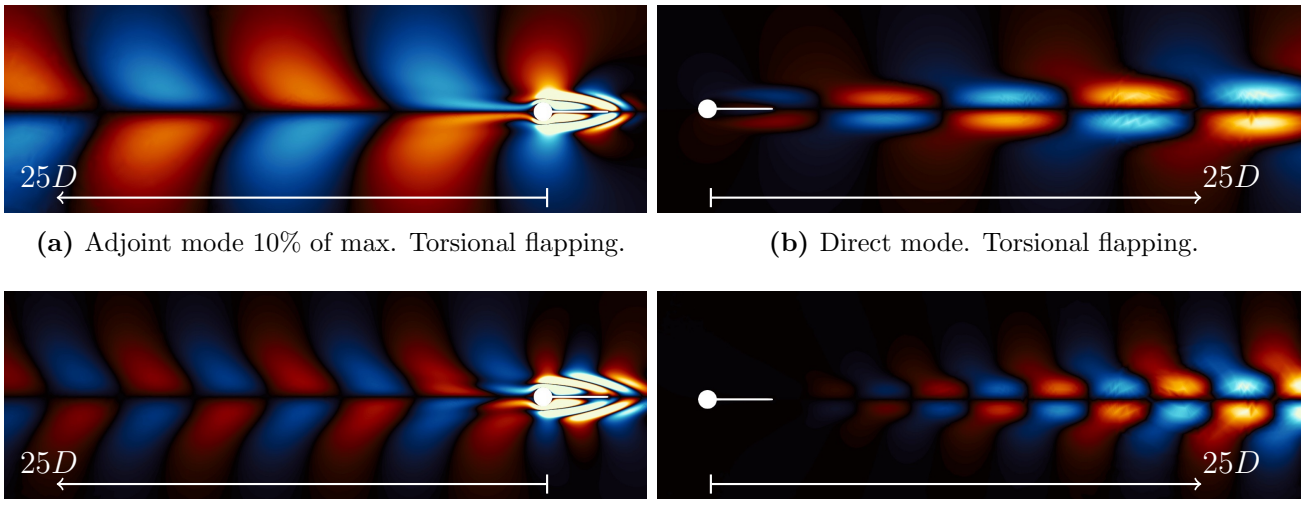
$$d_k = -R_1(R_2|k|^3 - 2) - 2R_2|k|^2. \tag{6.10b}$$

For a comparison of this instability with the torsional flapping mode, the wavenumber $k$ here may be set to be a fixed value (say $k \sim O(1/(L + D/2))$) because the cylinder with the splitter plate considered in the present study only admits rotation around the centre. From (6.10b), the instability given by (6.9) arises when $L$ is sufficiently large (i.e. when $k$ is sufficiently small). The instability frequency in (6.10a) increases on decreasing dimensionless inertia $R_1$. The growth rate in (6.10b) also becomes smaller as the dimensionless stiffness $R_2$ increases.

Lastly, given that the model is based on the inviscid fluid assumption, the fluid force considered in (6.9) is only from pressure (see also Shelley and Zhang, 2011). It is evident that all these features from this simple model are consistent with those of the torsional flapping instability in the present study (see the paragraph above). It appears that a similar low-frequency instability was also observed in the recent work by Pfister and Marquet (2020), where a flow over a fixed circular cylinder with a flexible plate is studied. However, a direct comparison of this instability mode with that of the model in Shelley and Zhang (2011) is made here for the first time, and it clarifies the origin of this type of instability.
Finally, the torsional flapping instability is shown not to be captured by the quasi-steady analysis, stressing its potential distinction to the galloping or flutter instabilities.

### 6.4.4 Adjoint-based sensitivity

In figure 6.29, the overall shape of the $u$-component of the real part of the adjoint mode of torsional flapping (a) is presented and compared to the $u$-component of the real part of the adjoint vortex shedding mode (c) for the same splitter plate length $L/D = 3$, and at the same Reynolds number $Re = 112$. On the same figure, the $u$-component of the real part of the direct modes (b)-(d) of these two instabilities are also shown to help in the comparison. On these figures, the adjoint fields are shown on a reduced scale which corresponds to 10% of its maximum value, for far-field visualisations concerns.




**(a)** Adjoint mode 10% of max. Torsional flapping.

**(b)** Direct mode. Torsional flapping.

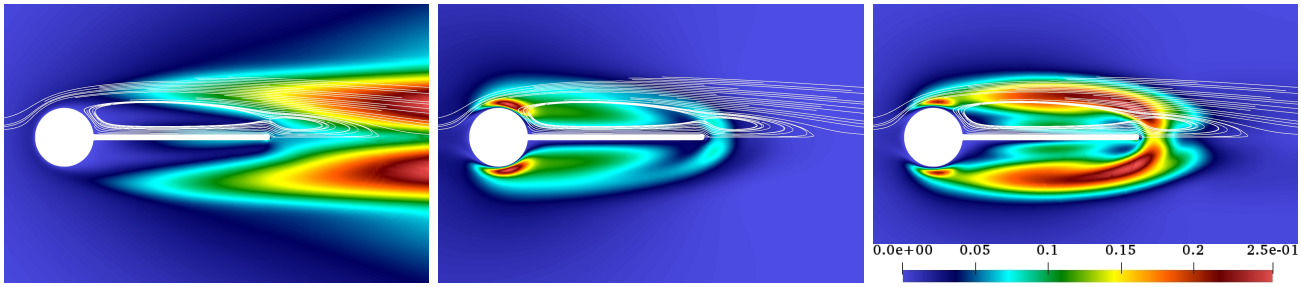
**(c)** Adjoint mode 10% of max. Vortex shedding.

**(d)** Direct mode. Vortex shedding.

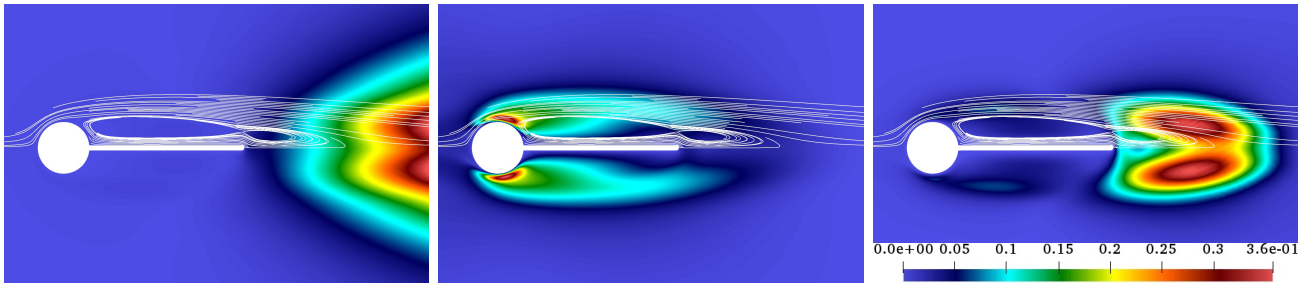
**Figure 6.29:** Far field visualisation of the $u$-component of the real part of the vortex shedding (bottom) and torsional flapping (top) mode ($\lambda^{TF}$) for $L/D = 3$ at $Re = 112$.

It is noted that both adjoint and direct modes of the torsional flapping and vortex shedding instabilities share common key representation aspects, such as the concentration of the perturbations close to the cylinder for the adjoint mode and the gradual increase of the perturbations

in the streamwise direction further to the cylinder in the case of the direct mode.
The far-field visualisations of these modes also depict the interesting feature of lower frequency of the torsional flapping mode initially shown in figure 6.22. Indeed, the distance separating every couple of alternative sign velocity pockets can be related to the wavelength of the corresponding modes, and it is noted that the torsional flapping clearly has a lower frequency than the vortex shedding mode by having a larger wavelength.
Finally, on this figure, in opposition to the symmetry breaking mode, the torsional flapping mode seems to be presumably initially physically triggered by far-field perturbations in the same manner as the vortex shedding mode, as the peak velocity magnitude is located further downstream the cylinder.




**(a)** Torsional flapping direct mode. **(b)** Torsional flapping adjoint mode. **(c)** Torsional flapping sensitivity.



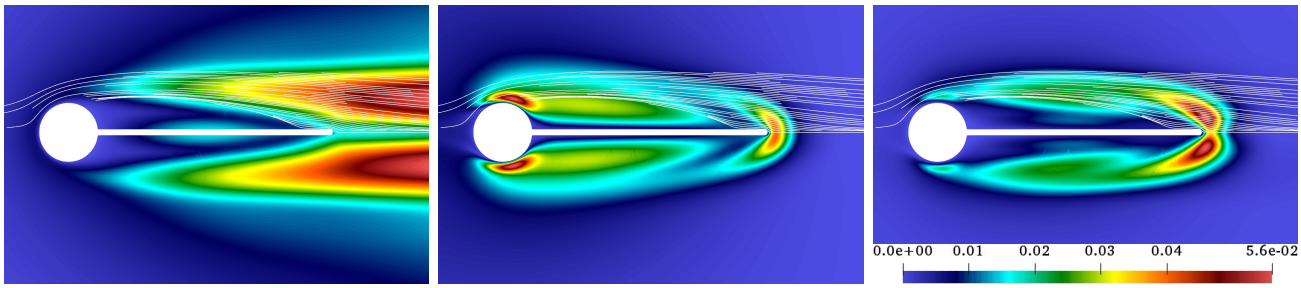

**(d)** Vortex shedding direct mode. **(e)** Vortex shedding adjoint mode. **(f)** Vortex shedding sensitivity.

**Figure 6.30:** Direct mode $\|\hat{\mathbf{u}}\|$, adjoint mode $\left\|\hat{\mathbf{u}}^{\dagger}\right\|$, and sensitivity to localised forcing $\Theta_F$ for $L/D = 3$: (a-c) the torsional flapping instability at $Re = 112$ (d-f) the vortex shedding instability at $Re = 114$. Here, white solid lines indicate streamlines of the corresponding base flow.

Finally, It is considered the adjoint sensitivity of the flapping instability mode. Here, it is shown the results for $L/D = 3$ and 4 in two different figures for clarity.
Figure 6.30 and 6.31 show the magnitude of the direct $\|\hat{\mathbf{u}}\|$ and adjoint $\left\|\hat{\mathbf{u}}^{\dagger}\right\|$ modes and the sensitivity to localised forcing $\Theta_F$ for $L/D = 3$ and 4 respectively. Here, in each case, the Reynolds number is chosen so as for the corresponding mode to be slightly unstable, corresponding to $Re = 112$ and $Re = 114$ for a splitter plate length of $L/D = 3$ for the torsional flapping and vortex shedding respectively (figure 6.30), and to $Re = 94$ and $Re = 151$ for a splitter plate length of $L/D = 4$ for the torsional flapping and vortex shedding respectively (figure 6.31).

Figures 6.30(a) and 6.31(a) show that the velocity perturbation magnitude of the torsional flapping mode is distributed symmetrically about $y = 0$. The mode exhibits a non-negligible large perturbation velocity throughout the separating shear layer, and it develops the peak value downstream of the plate. This is in contrast to the vortex shedding mode in figures 6.30(d) and 6.31(d), which exhibits its perturbation velocity only downstream of the plate.
It is presumable that the large perturbation velocity developed from the separation point is due to the fact that the flapping mode directly involves the motion of the plate, whereas the vortex shedding mode does not require the motion of the plate at least near the onset.

An interesting feature of the flapping instability is that the adjoint mode exhibits large values both in the separating shear layer around the plate and near the tip of the plate, as shown in figures 6.30(b) and 6.31(b). This feature is distinguished from the adjoint mode of the vortex shedding instability shown in figures 6.30(e) and 6.31(e) and the symmetry-breaking instability shown in figure 6.18(f), which have large values only either in the separating shear layer (figure 6.30(e) and 6.31(e)) or near the tip of the plate (figure 6.18(f)).
While the tip behaviour of the adjoint mode of the flapping instability is consistent with the discussion in §6.4.3, its behaviour in the separating shear layers somewhat resembles that of the vortex shedding mode. This further suggests that the structure of the adjoint flapping mode in the separating shear layers might be due to the oscillating nature of the instability like the vortex shedding mode.




**(a)** Torsional flapping direct mode **(b)** Torsional flapping adjoint mode. **(c)** Torsional flapping sensitivity.

**(d)** [Vortex shedding direct mode. **(e)** Vortex shedding adjoint mode. **(f)** Vortex shedding sensitivity.

**Figure 6.31:** Direct mode $\|\hat{\mathbf{u}}\|$, adjoint mode $\left\|\hat{\mathbf{u}}^{\dagger}\right\|$, and sensitivity to localised forcing $\Theta_F$ for $L/D = 4$: (a-c) the torsional flapping instability at $Re = 94$ (d-f) the vortex shedding instability at $Re = 151$. Here, white solid lines indicate streamlines of the corresponding base flow.

The sensitivity to localised feedback forcing $\Theta_F(\equiv \|\hat{\mathbf{u}}\| \left\|\hat{\mathbf{u}}^\dagger\right\|)$ of the flapping mode are shown in figures 6.30(c) and 6.31(c). In these cases, $\Theta_F$ are large both in the separating shear layer and near the tip, although the tip region now has the maximum magnitude due to the spatial structure of the direct mode $\|\hat{\mathbf{u}}\|$ (figures 6.30(a) and 6.31(a)).
The overall spatial structure of $\Theta_F$ of the flapping mode is similar to that of the vortex shedding mode, although the tip sensitivity region of the vortex shedding mode is developed further downstream compared to that of the flapping mode. Finally, similarly to the symmetry breaking mode, the flapping mode also shows significant sensitivity to the change in the structural parameters, as is shown in table 6.6.

| $L/D$ | $Re$ | $\Theta_{F,\max}$ | $\Theta_S$ |
|---|---|---|---|
| 3.0 | 112 | $2.541 \times 10^{-1}$ | $4.636 \times 10^{3}$ |
| 4.0 | 94 | $5.584 \times 10^{-2}$ | $1.174 \times 10^{2}$ |

**Table 6.6:** Values of $\Theta_{F,\max}(\equiv \max_{\mathbf{x}} |\Theta_F|)$ and $\Theta_S$ along the threshold of stability as a function of the splitter plate length. Here, $\lambda_r^{TF} \simeq 0$.

# Chapter 7

# Conclusion

## 7.1 Achievements

A theoretical linear stability and sensitivity methodology is derived for a non-rotationally symmetric problem which is observed to be more intricate than the rigid body stability methodology due to the boundary condition coupling of the base flow in the linearised problem at the fluid-structure interface, which emulates the position and velocity of the structure in a static geometrical configuration. The theoretical models are derived for a complete plane motion *i.e.*, three degrees of freedom: streamwise, cross flow and rotation of the structural geometry, immersed in a steady free stream flow velocity.

Instabilities and their sensitivity in a flow over a rotationally flexible circular cylinder with a rigid splitter plate have been studied. The cylinder is coupled with a spring-mass-damper system at its centre, such that it can rotate in response to the torque applied by the surrounding fluid flow.

Three types of instabilities have been found: the vortex shedding mode, the symmetry breaking mode and the torsional flapping mode. A particular focus of this study has been given to the understanding of the symmetry breaking and torsional flapping modes which originate from FSI. It was found that the emergence of the symmetry-breaking instability mode is strongly correlated with the length of the recirculation zone and the related flow structure near the tip region of the plate. The distribution of the pressure and viscous stress balance of the mode near the root and tip regions of the splitter plate was also found to play a crucial role in the symmetry breaking mode. In particular, as the Reynolds number is increased, the distribution near the tip gradually becomes more important, resulting in destabilisation of the symmetry breaking mode. The importance of the tip region was further identified by the subsequent adjoint sensitivity analysis. An oscillatory instability, which is referred to as 'torsional flapping' in the present study, was also found in this flow. This type of instability has not been widely reported, with the only other case the author is aware of being in the recent work of Pfister and Marquet

(2020) who considered a flexible splitter plate. This instability emerges when the length of the splitter plate is sufficiently large enough ($L/D \geq 3$ in this study). Unlike the symmetry breaking mode, this instability mode does not appear to be correlated to the length of the recirculation zone. However, the pressure and viscous stress balance distribution revealed that flow near the tip region of the plate is also crucial for this mode, and the sensitivity analysis also confirmed this. Lastly, all the observed physical features of the oscillatory instability mode were very similar to those of the flapping (or flutter) instability observed in a flag or a flexible plate, indicating that these two instabilities of the same type.

Perhaps, the most important finding of this work would be the identification of the importance of the flow in the near-tip region of the plate for both the symmetry breaking and flapping instabilities. The strong sensitivity, presumably also related to the long moment arm of the region, suggests that the two instabilities originating from FSI can effectively be controlled by carefully modifying the flow in the tip region. This is also consistent with the early experimental study of Toebes and Eagleson (1961) which showed how different shapes of the trailing edge of a thin plate could drastically modify the behaviour of the vortex-induced vibration.

## 7.2 Future work

Studying the same physical configuration of the rotating cylinder and splitter plate immersed in a steady flow, an interesting question would be to study the saturated state of the symmetry breaking mode. Indeed, the current work has questioned the stability of the splitter plate angular position for different flow regimes initially aligned with the free stream velocity direction. It is known that once unstable, the plate tends to dynamically migrate to a stable position (where the tip of the splitter plate is fairly located near the shear layer region of the base flow recirculation bubble), seen as the saturated state of the instability.
By using directly the analytical and numerical tools proposed in this work, one could obtain physical insights on the fluid-structure interaction mechanism behind the angular stabilisation of the splitter plate rather than the destabilisation mechanism.

Using the present analysis, it is also possible to question the stability of the cylinder for the different structural degrees of freedom. In particular, the same present configuration (*i.e* choice of structural and flow parameters) could be studied for a cylinder fitted to a splitter plate free to translate in the cross-flow direction, and for high reduced velocities as studied in the present document, the analysis could lead to further physical understanding on the galloping phenomenon. It would also be interesting to compare the present neutral stability curve, and sensitivity maps of the same cylinder fitted to a splitter plate free to rotate to the one of a cylinder fitted to a splitter plate free to translate in the cross-flow direction, as one can recognise that the flow disposition of the saturated angular state of the symmetry breaking mode, coincide

to the arrangement of a cylinder continuously translating in the cross-flow direction immersed in a flow with constant free stream velocity.
Further to this question, one could also challenge the physical interpretation of stability and sensitivity for a problem of multiple structural degrees of freedom, *e.g*, the flutter instability.

The same questions raised above can also be studied, taking into account an oscillating base flow rather than a steady-state configuration, by further conducting a Floquet analysis and modifying the analytical expression and hence the numerical tools. With such addition, one could study the fluid-structure interaction systems in the case of fully established periodic flow regimes and extend the analysis to a higher Reynolds number and implicitly to a wider range of phenomena found in nature.

A direct continuation to this work could also be to further formulate a sensitivity analysis in a similar manner than to one used in this study or with a more specific form of objective functionals (e.g. lift and drag), to optimise the shape of the trailing edge, that would be physically seen an optimal passive control device.
Finally, as the adjoint fields are now available from this study, they can be used to formulate a weakly non-linear analysis in a similar manner to Meliga and Chomaz (2014). Such an analysis would also be helpful to identify the competition dynamics between the different instability modes as well as to interpret the results of full non-linear simulations incorporating the motion of the structure.

These are the directions one can pursue and remain as future work.

# Bibliography


Achenbach, E. and Heinecke, E. (1981), 'On vortex shedding from smooth and rough cylinders in the range of reynolds numbers $6 \times 10^3$ to $5 \times 10^6$', *Journal of Fluid Mechanics* **106**, 239–251.

Akervik, E., Brandt, L., Henningson, D. S., Hoepffner, J., Marxen, O. and Schlatter, P. (2006*a*), 'Steady solutions of the navier-stokes equations by selective frequency damping', *Physics of Fluids* **18**(6), 068–102.
**URL:** *https://aip.scitation.org/doi/abs/10.1063/1.2211705*

Akervik, E., Brandt, L., Henningson, D. S., Hoepffner, J., Marxen, O. and Schlatter, P. (2006*b*), 'Steady solutions of the navier-stokes equations by selective frequency damping', *Physics of Fluids* **18**(6), 068102.
**URL:** *https://aip.scitation.org/doi/abs/10.1063/1.2211705*

Anderson, E. A. and Szewczyk, A. A. (1997), 'Effects of a splitter plate on the near wake of a circular cylinder in 2 and 3-dimensional flow configurations', *Experiments in Fluids* **23**(2), 161–174.

Assi, G., Bearman, P. and Kitney, N. (2009), 'Low drag solutions for suppressing vortex-induced vibration of circular cylinders', *Journal of Fluids and Structures* **25**(4), 666 – 675. Bluff Body Wakes and Vortex-Induced Vibrations (BBVIV-5).

Assi, G., Bearman, P., Kitney, N. and Tognarelli, M. (2010), 'Suppression of wake-induced vibration of tandem cylinders with free-to-rotate control plates', *Journal of Fluids and Structures* **26**, 1045–1057.

Assi, G., Bearman, P. and Tognarelli, M. (2014), 'On the stability of a free-to-rotate short-tail fairing and a splitter plate as suppressors of vortex-induced vibration', *Ocean Engineering* pp. 234 – 244.

Assi, G., Franco, G. and Vestri, M. (2014), 'Investigation on the stability of parallel and oblique plates as suppressors of vortex-induced vibration of a circular cylinder', *Journal of Offshore Mechanics and Arctic Engineering* **136**(3), 031802–031802.

Baek, H. and Karniadakis, G. (2012), 'A convergence study of a new partitioned fluid-structure interaction algorithm based on fictitious mass and damping', *J. Comput. Physics* **231**, 629–652.

Bagheri, S., Mazzino, A. and Bottaro, A. (2012*a*), 'Spontaneous symmetry breaking of a hinged flapping filament generates lift', *Physical Review Letters* **109**.

Bagheri, S., Mazzino, A. and Bottaro, A. (2012*b*), 'Spontaneous symmetry breaking of a hinged flapping filament generates lift'.

Barkley, D., Blackburn, H. M. and Sherwin, S. J. (2008*a*), 'Direct optimal growth analysis for timesteppers', *Int. J. Numer. Meth. Fluids* **57**, 1435–1458.

Barkley, D., Blackburn, H. M. and Sherwin, S. J. (2008*b*), 'Direct optimal growth analysis for timesteppers', *International Journal for Numerical Methods in Fluids* **57**(9), 1435–1458.
**URL:** *https://onlinelibrary.wiley.com/doi/abs/10.1002/fld.1824*

Bearman, P. W., Gartshore, I. S., Maull, D. J. and Parkinson, G. V. (1987), 'Experiments on flow-induced vibration of a square-section cylinder', *Journal of Fluids and Structures* **1**, 19–34.

Bechert, D., Hage, W. and Meyer, R. (2006), 'Self-actuating flaps on bird and aircraft wings', *WIT Transactions on State of the Art in Science and Engineering* **4**.

Bisplinghoff, R. L., Ashley, H. and Halfman, R. L. (1966), *Aeroelasticity*, Courier Corporation.

Blevins, R. D. (2001), *Flow-Induced Vibration*, second edn, Krieger publishing company, Krieger drive, Malabar, Florida 32950.

Cantwell, C. D., Moxey, D., Comerford, A., Bolis, A., Rocco, G., Mengaldo, G., Grazia, D. D., Yakovlev, S., Lombard, J.-E., Ekelschot, D., Jordi, B., Xu, H., Mohamied, Y., Eskilsson, C., Nelson, B., Vos, P., Biotto, C., Kirby, R. M. and Sherwin, S. J. (2015), 'Nektar++: An open-source spectral/hp element framework', *Computer physics communications* **192**, 205–219.

Carmo, B. S., Sherwin, S. J., Bearman, P. W. and Willden, R. (2011), 'Flow-induced vibration of a circular cylinder subjected to wake interference at low reynolds number', *Journal of Fluids and Structures* **27**, 503–522.

Carmo, B. S., Sherwin, S. J., Bearman, P. W. and Willden, R. H. J. (2008), 'Wake transition in the flow around two circular cylinders in staggered arrangements', *Journal of Fluid Mechanics* **597**, 1–29.

Choi, H., Jeon, W.-P. and Kim, J. (2008), 'Control of flow over a bluff body', *Annual Review of Fluid Mechanics* **40**(1), 113–139.

Chomaz, J.-M. (2005), 'Global instabilities in spatially developing flows: Non-normality and nonlinearity', *Annual Review of Fluid Mechanics* **37**(1), 357–392.

Cimbala and Garg, S. (1991), 'Flow in the wake of a freely rotatable cylinder with splitter plate', *AIAA Journal* **29**(6), 1001–1003.

Cossu, C. and Morino, L. (2000), 'On the instability of a spring-mounted circular cylinder in a viscous flow at low reynolds numbers', *Journal of Fluids and Structures* **14**, 183–196.

Den-Hartog, J. P. (1956), *Mechanical Vibrations*, fourth edn, McGraw-Hill Book Company, New York, McGraw-Hill.

Dolci, D. and Carmo, B. (2018), 'Sensitivity analysis applied for a flow around spring-mounted cylinder', *9th International Symposium on Fluid-Structure Interactions, Flow-Sound Interactions, Flow-Induced Vibration  Noise* .

Dolci, D. I. and Carmo, B. S. (2019), 'Bifurcation analysis of the primary instability in the flow around a flexibly mounted circular cylinder', *Journal of Fluid Mechanics* **880**, R5.

Fernandez, M. A. and Tallec, P. L. (2002*a*), 'Linear stability analysis in fluid-structure interaction with transpiration. part i: formulation and mathematical analysis.', *Research Report INRIA* .

Fernandez, M. A. and Tallec, P. L. (2002*b*), 'Linear stability analysis in fluid-structure interaction with transpiration. part ii: numerical analysis and applications.', *Research Report INRIA* .

Gerbeau, J. F., Nobile, F. and Causin, P. (2005), 'Added-mass effect in the design of partitioned algorithms for fluid-structure problems', *Computer Methods In Applied Mechanics And Engineering* **194**(42-44), 4506–4527.
**URL:** *http://infoscience.epfl.ch/record/176343*

Giannetti, F. and Luchini, P. (2007), 'Structural sensitivity of the first instability of the cylinder wake', *Journal of Fluid Mechanics* **581**, 167–197.

Gordon, W. and Hall, C. (1973), 'Transfinite element methods: blending-function interpolation over arbitrary curved element domains', *Numerische Mathematik* **21**(2), 109–129.

Guermond, J. L. and Shen, J. (2003), 'Velocity-correction projection methods for incompressible flows', *SIAM Journal on Numerical Analysis* **41**, 112–134.

Hall, M. C. G. and Cacuci, D. G. (01 Oct. 1983), 'Physical interpretation of the adjoint functions for sensitivity analysis of atmospheric models', *Journal of Atmospheric Sciences* **40**(10), 2537 – 2546.

Hartog, J. P. D. (1956), *Mechanical Vibrations*, McGraw-Hill, New York.

Hill, D. C. (1992), 'A theoretical approach for analyzing the restabilization of wakes', NASA STI/Recon Technical Report N.

Huerre, P. and Monkewitz, P. A. (1990), 'Local and global instabilities in spatially developing flows', *Annual Review of Fluid Mechanics* **22**(1), 473–537.

Jordi, B. E., Cotter, C. J. and Sherwin, S. J. (2014), 'Encapsulated formulation of the selective frequency damping method', *Physics of Fluids* **26**.

Karniadakis, G. E., Israeli, M. and Orszag, S. A. (1991), 'High-order splitting methods for the incompressible navier-stokes equations', *Journal of Computational Physics* **97**(2), 414 – 443.

Karniadakis, G. E. and Sherwin, S. J. (2005), *Spectral/hp Element Methods for Computational Fluid Dynamics*, second edn, Oxford University Press.

Kim, J. and Bewley, T. R. (2007), 'A linear systems approach to flow control', *Annual Review of Fluid Mechanics* **39**(1), 383–417.
**URL:** *https://doi.org/10.1146/annurev.fluid.39.050905.110153*

Knacke, M. S. T., Thiele, F., Meyer, R., Hage, W. and Bechert, D. W. (2004), 'Separation control by self-activated movable flaps', *42nd AIAA Aerospace Sciences Meeting and Exhibit* .

Kwon, K. and Choi, H. (1996*a*), 'Control of laminar vortex shedding behind a circular cylinder using splitter plates', *Phys. Fluids* **8**, 479.

Kwon, K. and Choi, H. (1996*b*), 'Control of laminar vortex shedding behind a circular cylinder using splitter plates', *Physics of Fluids* **8**(2), 479–486.

Lacis, U., Brosse, N., Ingremeau, F., Mazzino, A., Lundell, F., Kellay, H. and Bagheri, S. (2014*a*), 'Passive appendages generate drift through symmetry breaking', *Nature Communications* **5**.

Lacis, U., Brosse, N., Ingremeau, F., Mazzino, A., Lundell, F., Kellay, H. and Bagheri, S. (2014*b*), 'Passive appendages generate drift through symmetry breaking', *Nature Communications* **5:5310**.

Lienhard, J. H. (1966), *Synopsis of Lift, Drag, and Vortex Frequency Data for Rigid Circular Cylinders*, Technical Extension Service, Washington State University.

Luchini, P. and Bottaro, A. (2014), 'Adjoint equations in stability analysis', *Annual Review of Fluid Mechanics* **46**(1), 493–517.
**URL:** *https://doi.org/10.1146/annurev-fluid-010313-141253*

Luo, H. and Bewley, T. (2004), 'On the contravariant form of the navier-stokes equations in time-dependent curvilinear coordinate system', *Journal of Computational Physics* **199**, 355–375.

Marquet, O., Sipp, D. and Jacquin, L. (2008), 'Sensitivity analysis and passive control of cylinder flow', *Journal of Fluid Mechanics* **615**, 221 – 252.

Meliga, P. and Chomaz, J.-M. (2011), 'An asymptotic expansion for the vortex-induced vibrations of a circular cylinder', *Journal of Fluid Mechanics* **671**, 137 – 167.

Meliga, P. and Chomaz, J. M. (2014), 'An asymptotic expansion for the vortex-induced vibrations of a circular cylinder', *HAL archives-ouvertes* **hal-00994505**.

Nakamura, Y. (1990), 'Recent research into bluff-body flutter', *Journal of Wind Engineering and Industrial Aerodynamics* **33**(1), 1–10.
**URL:** *https://www.sciencedirect.com/science/article/pii/0167610590900155*

Nakamura, Y. and Mizota, T. (1975), 'Torsional flutter of rectangular prisms', *Journal of Engineering Mechanics* **101**. Title from ASCE journal home page, viewed Jan. 12, 2000.

Nakamura, Y. and Yoshimura, T. (1982), 'Flutter and vortex excitation of rectangular prisms in pure torsion in smooth and turbulent flows.', *Journal of Sound and Vibration* **84**, 305–317.

Negi, P. S., Hanifi, A. and Henningson, D. S. (2020), 'On the linear global stability analysis of rigid-body motion fluid–structure-interaction problems', *Journal of Fluid Mechanics* **903**, A35.

Noack, B. R. and Eckelmann, H. (1994), 'A global stability analysis of the steady and periodic cylinder wake', *Journal of Fluid Mechanics* **270**, 297–330.

Ozono, S. (1999), 'Flow control of vortex shedding by a short splitter plate asymmetrically arranged downstream of a cylinder', *Physics of Fluids* **11**(10), 2928–2934.

Païdoussis, M., J. Price, S. and de Langre, E. (2010), *Fluid-structure Interactions: Cross-flow-induced Instabilities*, Cambridge University press.

Park, H., Bae, K., Lee, B., Jeon, W. P. and Choi, H. (2010), 'Aerodynamic performance of a gliding swallowtail butterfly wing model', *Experimental Mechanics* **50**(9), 1313–1321.

Pfister, J.-L. (2019), Instabilities and optimization of elastic structures interacting with laminar flows, PhD thesis, Thèse de doctorat de l'Université Paris-Saclay préparée à l'École polytechnique et à l'Office National d'Études et de Recherches Aérospatiales.

Pfister, J.-L. and Marquet, O. (2020), 'Fluid structure stability analyses and nonlinear dynamics of flexible splitter plates interacting with a circular cylinder flow', *Journal of Fluid Mechanics* **896**.

Pruett, C. D., Gatski, T. B., Grosch, C. E. and Thacker, W. D. (2003), 'The temporally filtered navier-stokes equations: Properties of the residual stress', *Physics of Fluids* **15**(8), 2127–2140.
**URL:** *https://doi.org/10.1063/1.1582858*

Pruett, C. D., Thomas, B. C., Grosch, C. E. and Gatski, T. B. (2006), 'A temporal approximate deconvolution model for large-eddy simulation', *Physics of Fluids* **18**(2), 028104.
**URL:** *https://doi.org/10.1063/1.2173288*

Roshko, A. (1954), 'On the drag and shedding frequency of two-dimensional bluff bodies', *NACA Technical Note 3169. National Advisory Committee for Aeronautics* .

Saad, Y. (1992), *Numerical Methods for Large Eigenvalue Problems*, Wiley: New York.

Serson, D., Meneghini, J. R. and Sherwin, S. J. (2016), 'Velocity-correction schemes for the incompressible navier-stokes equations in general coordinate systems', *Journal of Computational Physics* **316**, 243–254.

Shelley, M. J. and Zhang, J. (2011), 'Flapping and bending bodies interacting with fluid flows', *Annual Review of Fluid Mechanics* **43**(1), 449–465.
**URL:** *https://doi.org/10.1146/annurev-fluid-121108-145456*

Slater, J. E. (1969), Aeroelastic instability of a structural angle section, PhD thesis, University of British Columbia.

Soumya, S. and Prakash, K. A. (2017), 'Effect of splitter plate on passive control and drag reduction for fluid flow past an elliptic cylinder', *Ocean Engineering* **141**, 351 – 374.

Strykowski, P. and Sreenivasan, K. (1990), 'On the formation and suppression of vortex at low reynolds numbers', *Journal of Fluid Mechanics* **218**.

Sun, X., Suh, C. S., Ye, Z.-H. and Yu, B. (2020), 'Dynamics of a circular cylinder with an attached splitter plate in laminar flow: A transition from vortex-induced vibration to galloping', *Phys. Fluids* **32**.

Theofilis, V. (2011), 'Global linear instability', *Annual Review of Fluid Mechanics* **43**(1), 319–352.

Toebes, G. H. and Eagleson, P. S. (1961), 'Hydroelastic vibrations of flat plates related to trailing edge geometry.', *ASME. J. Basic Eng.* **83**, 671 – 678.

Tuckerman, L. S. and Barkley, D. (2000), Bifurcation analysis for timesteppers, *in* E. Doedel and L. S. Tuckerman, eds, 'Numerical Methods for Bifurcation Problems and Large-Scale Dynamical Systems', Springer New York, New York, NY, pp. 453–466.

van Dyke, M. (1982), *An album of fluid motion*, 1st edn, Parabolic Press.

Vos, P. E., Eskilsson, C., Bolis, A., Chun, S., Kirby, R. M. and Sherwin, S. J. (2011), 'A generic framework for time-stepping partial differential equations (pdes): general linear methods, object-oriented implementation and application to fluid problems', *International Journal of Computational Fluid Dynamics* **25**(3), 107–125.

Vu, H. C., Ahn, J. and Hwang, J. H. (2016), 'Numerical investigation of flow around circular cylinder with splitter plate', *KSCE Journal of Civil Engineering* **20(6)**, 2559–2568.

Washizu, K., Ohya, A., Otsuki, Y. and Fujii, K. (1978), 'Aeroelastic instability of rectangular cylinders in a heaving mode', *Journal of Sound and Vibration* **59**, 195–210.

Williamson, C. H. K. (1996), 'Vortex dynamics in the cylinder wake', *Annual Review of Fluid Mechanics* **28**(1), 477–539.
**URL:** *https://doi.org/10.1146/annurev.fl.28.010196.002401*

Zdravkovich, M. (1997), *Flow Around Circular Cylinders: Volume I: Fundamentals*, OUP Oxford.

Zebib, A. (1987), 'Stability of viscous flow past a circular cylinder', *Journal of Engineering Mathematics* **21**(2), 155–165.

Zhang, W., Li, X., Ye, Z. and Jiang, Y. (2015), 'Mechanism of frequency lock-in in vortex-induced vibrations at low reynolds numbers', *Journal of Fluid Mechanics* **783**, 72–102.

Zienkiewicz, O. C. and Taylor, R. L. (2000), *The Finite Element Method. Volume 1: the basis*, Butterworth-Heinemann Stoneham.

# Appendix A

# Adjoint equations

The adjoint operators of the linearised fluid and structural operators are directly obtained from applying the inner product on the linearised global operator $\mathcal{H}'$ as

$$\left\langle \mathcal{H}'\mathbf{s}', \mathbf{s}^\dagger \right\rangle = \left\langle \mathbf{s}', \mathcal{H}^\dagger\mathbf{s}^\dagger \right\rangle + \mathcal{B}\left(\mathbf{s}', \mathbf{s}^\dagger\right). \tag{A.1}$$

Indeed, the linearised global operator $\mathcal{H}'$ can be decomposed in block matrix form, and its diagonal terms (*i.e.* the linearised fluid and structural operator) can be treated separately for simplicity, which results in the following expression

$$\left\langle \mathcal{H}'\mathbf{s}', \mathbf{s}^\dagger \right\rangle \;=\; \left\langle \mathcal{F}'\mathbf{q}', \mathbf{q}^\dagger \right\rangle_F + \left\langle \mathcal{A}\mathbf{q}', \boldsymbol{\xi}^\dagger \right\rangle_S + \left\langle \mathcal{S}\boldsymbol{\xi}', \boldsymbol{\xi}^\dagger \right\rangle_S .$$

This appendix focuses on the derivation of the fluid and structural adjoint operators $\mathcal{F}^\dagger$ and $\mathcal{S}^\dagger$, respectively.

## A.1 Structural adjoint operator

By definition, applying the structural inner product to the linearised structural operator,

$$\begin{aligned}
\left\langle \mathcal{S}\boldsymbol{\xi}', \boldsymbol{\xi}^\dagger \right\rangle_S &= \int_0^\tau \left(\mathcal{S}\boldsymbol{\xi}'\right)^H \mathbf{W}_S \boldsymbol{\xi}^\dagger \,\mathrm{d}t \\
&= \int_0^\tau \left( \begin{bmatrix} -\mathbf{I}\partial_t & \mathbf{I} \\ -\mathbf{M}^{-1}\mathbf{K} & -\mathbf{M}^{-1}\mathbf{C} - \mathbf{I}\partial_t \end{bmatrix} \begin{bmatrix} \boldsymbol{\eta}' \\ \boldsymbol{\zeta}' \end{bmatrix} \right)^H \begin{bmatrix} \mathbf{K} & 0 \\ 0 & \mathbf{M} \end{bmatrix} \begin{bmatrix} \boldsymbol{\eta}^\dagger \\ \boldsymbol{\zeta}^\dagger \end{bmatrix} \,\mathrm{d}t \\
&= \int_0^\tau \begin{bmatrix} \boldsymbol{\eta}' \\ \boldsymbol{\zeta}' \end{bmatrix}^H \begin{bmatrix} \mathbf{K} & 0 \\ 0 & \mathbf{M} \end{bmatrix} \begin{bmatrix} \mathbf{I}\partial_t & -\mathbf{I} \\ \mathbf{M}^{-1}\mathbf{K} & -\mathbf{M}^{-1}\mathbf{C} + \mathbf{I}\partial_t \end{bmatrix} \begin{bmatrix} \boldsymbol{\eta}^\dagger \\ \boldsymbol{\zeta}^\dagger \end{bmatrix} \,\mathrm{d}t \\
&= \left\langle \boldsymbol{\xi}', \mathcal{S}^\dagger\boldsymbol{\xi}^\dagger \right\rangle_S .
\end{aligned} \tag{A.2}$$

Hence no spatial boundary terms result from the derivation of the adjoint structural operator, which simply reads

$$\mathcal{S}^\dagger = \left[\begin{array}{c|c} \mathbf{I}\partial_t & -\mathbf{I} \\ \hline \mathbf{M}^{-1}\mathbf{K} & -\mathbf{M}^{-1}\mathbf{C} + \mathbf{I}\partial_t \end{array}\right], \tag{A.3}$$

and it is noted a substantial similarity with the linearised operator $\mathcal{S}'$ at the exception that the time integration has changed the sign of the time-dependent components of the linearised operator.

## A.2 Fluid adjoint operator

Following the same process as described for the equations (A.2), *i.e* starting with the expression

$$\left\langle \mathcal{F}'\mathbf{q}', \mathbf{q}^\dagger \right\rangle_F = \int_0^\tau \int_\Omega \left( \left(\mathcal{F}'\mathbf{q}'\right)^H \mathbf{W}_F \mathbf{q}^\dagger \right) \mathrm{d}\mathbf{x}\mathrm{d}t, \tag{A.4}$$

one can obtain the fluid adjoint operator using integration by parts, the divergence theorem, and vector identities. By doing so, the resulting fluid adjoint operator $\mathcal{F}^\dagger$ finally reads:

$$\mathcal{F}^\dagger = \left[\begin{array}{c|c} \partial_t - \mathbf{A}^\dagger + Re^{-1}\nabla^2 & -\nabla \\ \hline \nabla\cdot & 0 \end{array}\right] + \mathcal{B}_F, \tag{A.5}$$

where the fluid bilinear concomitant $\mathcal{B}_F$ have the same dimension of $\mathcal{F}^\dagger$ and contains the boundary terms resulting from the calculations, and $\mathbf{A}^\dagger$ is the adjoint of the linearised advection terms is defined as:

$$\mathbf{A}^\dagger\mathbf{u}^\dagger = -(\mathbf{u}_0 \cdot \nabla)\mathbf{u}^\dagger + (\mathbf{u}_0\nabla)^T \cdot \mathbf{u}^\dagger. \tag{A.6}$$

The fluid bilinear concomitant $\mathcal{B}_F$ is obtained from the computation process, which is detailed below term by term for each component of the fluid linearised operator $\mathcal{F}'$, in items 1 to 6. The fluid inner product can be applied component wise on $\mathcal{F}'$ and the derivation of the six components of the fluid adjoint operator $\mathcal{F}^\dagger$ reads, expressing $\partial\Omega = \partial\Omega_{ext}^{in} \cup \partial\Omega_{ext}^{out} \cup \partial\Omega_{in}$:

1. The pressure gradient $-\nabla p'$:

$$\int_0^\tau \int_\Omega (-\nabla p') \cdot \mathbf{u}^\dagger \mathrm{d}\mathbf{x}\mathrm{d}t \;=\; \int_0^\tau \left[ \int_\Omega p' \left(\nabla \cdot \mathbf{u}^\dagger\right) \mathrm{d}\mathbf{x} + \int_{\partial\Omega} - \left(p'\mathbf{u}^\dagger\right) \cdot \mathbf{n} \; \mathrm{d}l \right] \mathrm{d}t,$$

the pressure gradient being an off-diagonal term in the fluid linearised operator $\mathcal{F}'$, its adjoint counterpart is symmetrically block positioned in the fluid adjoint operator $\mathcal{F}^\dagger$. However, its adjoint gives the divergence operator. Hence no change is directly visible looking directly at the fluid adjoint operator $\mathcal{F}^\dagger$.

2. The divergence $\nabla \cdot \mathbf{u}'$:

$$\int_0^\tau \int_\Omega (\nabla \cdot \mathbf{u}')\, p^\dagger \mathrm{d}\mathbf{x}\mathrm{d}t \;=\; \int_0^\tau \left[ \int_\Omega (-\nabla p') \cdot \mathbf{u}^\dagger \mathrm{d}\mathbf{x} + \int_{\partial\Omega} \left(p^\dagger \mathbf{u}'\right) \cdot \mathbf{n} \mathrm{d}\mathbf{x} \right] \mathrm{d}t,$$

the divergence operator also being an off-diagonal term in the fluid linearised operator $\mathcal{F}'$, its adjoint counterpart is symmetrically block positioned in the fluid adjoint operator $\mathcal{F}^\dagger$ identically to the pressure gradient operator. The adjoint of the divergence operator results in a pressure gradient, as shown by the first integral on the right-hand side of the previous equation. Hence the off diagonals terms of $\mathcal{F}'$ are permuted in the adjoint calculation.

3. The temporal variation $\partial_t \mathbf{u}'$:

$$\int_0^\tau \int_\Omega (-\partial_t \mathbf{u}') \cdot \mathbf{u}^\dagger \, \mathrm{d}\mathbf{x}\mathrm{d}t \;=\; \int_0^\tau \int_\Omega \mathbf{u}' \cdot \left(\partial_t \mathbf{u}^\dagger\right) \, \mathrm{d}\mathbf{x}\mathrm{d}t + \int_\Omega \left[-\mathbf{u}' \cdot \mathbf{u}^\dagger\right]_0^\tau \, \mathrm{d}\mathbf{x},$$

the adjoint temporal variation $\partial_t \mathbf{u}^\dagger$ is obtained by employing the integration by parts on $\partial_t \mathbf{u}'$ and this operation results in a simple change of sign, as shown in the first integral on the right-hand side of the previous equation.

4. The first term of the linearised advection $(\mathbf{u}_0 \cdot \nabla)\mathbf{u}'$:

$$\int_0^\tau \int_\Omega \left(\left(\mathbf{u}_0 \cdot \nabla\right) \mathbf{u}'\right) \cdot \mathbf{u}^\dagger \mathrm{d}\mathbf{x}\mathrm{d}t \;=\; \int_0^\tau \left[ \int_\Omega \mathbf{u}' \cdot \left( - \left(\mathbf{u}_0 \cdot \nabla\right) \mathbf{u}^\dagger \right) \mathrm{d}\mathbf{x} + \int_{\partial\Omega} \left( \left(\mathbf{u}' \cdot \mathbf{u}^\dagger\right) \mathbf{u}_0 \right) \cdot \mathbf{n} \, \mathrm{d}l \right] \mathrm{d}t,$$

vector identities are applied to the left-hand side of the equation, followed by the divergence theorem on the second term of the right-hand side, which results in a surface integral, and leads to the first part of the adjoint advection operator.

5. The second term of the linearised advection $(\mathbf{u}_0 \nabla) \cdot \mathbf{u}'$:

$$\int_0^\tau \int_\Omega \left(\left(\mathbf{u}_0 \nabla\right) \cdot \mathbf{u}'\right) \cdot \mathbf{u}^\dagger \mathrm{d}\mathbf{x}\mathrm{d}t \;=\; \int_0^\tau \int_\Omega \mathbf{u}' \cdot \left( \left(\mathbf{u}_0 \nabla\right)^T \cdot \mathbf{u}^\dagger \right) \mathrm{d}\mathbf{x}\mathrm{d}t,$$

no boundary terms result from applying vector identities in that case, and the second part of the adjoint advection operator is obtained.

6. The Laplacian operator $\nabla^2 \mathbf{u}'$:

$$\begin{aligned} \int_0^\tau \int_\Omega \left(\nabla^2 \mathbf{u}'\right) \cdot \mathbf{u}^\dagger \, \mathrm{d}\mathbf{x}\mathrm{d}t \;=\; & \int_0^\tau \int_\Omega \mathbf{u}' \cdot \left(\nabla^2 \mathbf{u}^\dagger\right) \, \mathrm{d}\mathbf{x}\mathrm{d}t \\ & + \int_0^\tau \int_{\partial\Omega} \left( \mathbf{u}^\dagger \cdot \left(\nabla_{\mathbf{n}} \mathbf{u}'\right) - \mathbf{u}' \cdot \left(\nabla_{\mathbf{n}} \mathbf{u}^\dagger\right) \right) \mathrm{d}l\mathrm{d}t, \end{aligned}$$

with the notation $\nabla_{\mathbf{n}} = \left(\frac{\partial}{\partial n}, \frac{\partial}{\partial n}\right)$. The same process than for the first term of the linearised

advection is used to obtain the adjoint Laplacian operator.

In items 1 to 6, combining the volume integral leads to the adjoint fluid operator $\mathcal{F}^\dagger$ given in expression (A.5), whereas the surface integral leads to the fluid bilinear concomitant $\mathcal{B}_F$. Indeed, by combining all the previous surface integrals from items 1 to 6, one finally obtains the expression of the fluid bilinear concomitant $\mathcal{B}_F$ as

$$\int_\Omega \left[-\mathbf{u}'\cdot\mathbf{u}^\dagger\right]_0^\tau \,\mathrm{d}\mathbf{x} \;+ \tag{A.7a}$$

$$\int_0^\tau\int_{\partial\Omega} \left(\left(\mathbf{u}'\cdot\mathbf{u}^\dagger\right)\mathbf{u}_0\right)\cdot\mathbf{n}\,\mathrm{d}l\mathrm{d}t \;+ \tag{A.7b}$$

$$\int_0^\tau\int_{\partial\Omega} \left(\mathbf{u}^\dagger\cdot\left(\nabla_\mathbf{n}\mathbf{u}'\right) - \mathbf{u}'\cdot\left(\nabla_\mathbf{n}\mathbf{u}^\dagger\right)\right)\,\mathrm{d}l\mathrm{d}t \;+ \tag{A.7c}$$

$$\int_0^\tau\int_{\partial\Omega} -\left(p'\mathbf{u}^\dagger\right)\cdot\mathbf{n}\,\mathrm{d}l\mathrm{d}t \;+ \tag{A.7d}$$

$$\int_0^\tau\int_{\partial\Omega} \left(p^\dagger\mathbf{u}'\right)\cdot\mathbf{n}\,\mathrm{d}l\mathrm{d}t \;=\; \mathcal{B}_F\left(\mathbf{q}',\mathbf{q}^\dagger\right). \tag{A.7e}$$

The fluid bilinear concomitant $\mathcal{B}_F$ results from the spatial boundary terms (*i.e.* the expressions (A.7b), (A.7c), (A.7d), (A.7e)), and the resulting term of the linearised advection (A.7b) is first shown to be identically 0. Indeed, decomposing the frontier integration on $\partial\Omega$ into the sum of the integration on the external and internal (structural interface) boundaries, the integral expression (A.7b) reads

$$\int_0^\tau\int_{\partial\Omega} \left(\left(\mathbf{u}'\cdot\mathbf{u}^\dagger\right)\mathbf{u}_0\right)\cdot\mathbf{n}\,\mathrm{d}l\mathrm{d}t \;=$$

$$\int_0^\tau\left[\oint_{\partial\Omega_{ext}}\left(\left(\underbrace{\mathbf{u}'\cdot\mathbf{u}^\dagger}_{=0}\right)\mathbf{u}_0\right)\cdot\mathbf{n}\,\mathrm{d}l + \oint_{\partial\Omega_{in}}\left(\left(\mathbf{u}'\cdot\mathbf{u}^\dagger\right)\underbrace{\mathbf{u}_0}_{=0}\right)\cdot\mathbf{n}\,\mathrm{d}l\right]\mathrm{d}t \;=\; 0.$$

With no-slip at the interface in the basic state (*i.e* $\mathbf{u}_0 = 0$ on $\Gamma = \partial\Omega_{in}$), and homogeneous boundary conditions of the forward system on the external boundaries (*i.e* $\mathbf{u}' = 0$ on $\partial\Omega_{ext}$). Hence the fluid bilinear concomitant $\mathcal{B}_F\left(\mathbf{q}',\mathbf{q}^\dagger\right)$ results from the integrals (A.7c), (A.7d) and (A.7e), and can be rearranged into the following expression (omitting the time integral):

$$\mathcal{B}_\mathcal{F}\left(\mathbf{q},\mathbf{q}^\dagger\right) \;=\; \oint_{\partial\Omega_{in}}\left[\mathbf{u}^\dagger\cdot\left(\left(Re^{-1}\nabla\mathbf{u}' - p'\mathbf{I}\right)\cdot\mathbf{n}\right) - \mathbf{u}'\cdot\left(\left(Re^{-1}\nabla\mathbf{u}^\dagger - p^\dagger\mathbf{I}\right)\cdot\mathbf{n}\right)\right]\mathrm{d}l$$

$$\Leftrightarrow\quad \mathcal{B}_\mathcal{F}\left(\mathbf{q},\mathbf{q}^\dagger\right) \;=\; \oint_{\partial\Omega_{in}}\left[\underbrace{\mathbf{u}^\dagger\cdot\left(\mathbf{f}\mathbf{q}\cdot\mathbf{n}\right)}_{\text{gives B.C.}} - \underbrace{\mathbf{u}\cdot\left(\mathbf{f}\mathbf{q}^\dagger\cdot\mathbf{n}\right)}_{\text{gives }\mathcal{A}^\dagger}\right]\mathrm{d}l. \tag{A.8}$$

This final expression is decomposed and used to obtain the adjoint boundary condition, given by the left-hand side of the integrand, and the adjoint aerodynamic operator, given by the right-hand side of the integrand.

# Appendix B

# Eigenvalue decomposition

Once the eigenvalue $\lambda$ and the corresponding eigenvectors are computed, they exactly satisfy the governing linearised equations (3.64). Using this feature, the eigenvalue $\lambda$ may be decomposed into the contributions from a structural and fluid components, $\lambda^S$ and $\lambda^F$, respectively. The structural part of (3.64) is given by

$$\lambda \mathbf{I}\hat{\boldsymbol{\xi}} + \hat{\mathcal{S}}\hat{\boldsymbol{\xi}} - \mathcal{A}\hat{\mathbf{q}} = \mathbf{0}, \tag{B.1}$$

where

$$\hat{\mathcal{S}} = \begin{bmatrix} 0 & 1 \\ -(2\pi/U_R)^2 & -4\pi\zeta_\theta/U_R \end{bmatrix}, \tag{B.2}$$

$\hat{\boldsymbol{\xi}} = [\hat{\theta}\ \dot{\hat{\theta}}]^T = [\hat{\theta}\ \hat{\phi}]^T$ is the vector containing the structure variables, $\mathcal{A} = [\mathbf{0}\ \frac{\hat{\mathfrak{m}}_z}{I_\theta}]^T$ with $\hat{\mathfrak{m}}_z = [\hat{m}_{z,p}\ \hat{m}_{z,\nu}]^T$ the moment matrix defined in (3.64) as part of the global operator $\hat{\mathcal{H}}$, and $\mathbf{W}_S$ the weight matrix defined in (3.48a). After a left multiplication of (B.1) by $\hat{\boldsymbol{\xi}}^H\mathbf{W}_S$, the eigenvalue $\lambda$ is written as

$$\lambda = \underbrace{-\frac{\hat{\boldsymbol{\xi}}^H\mathbf{W}_S\hat{\mathcal{S}}\hat{\boldsymbol{\xi}}}{\hat{\boldsymbol{\xi}}^H\mathbf{W}_S\hat{\boldsymbol{\xi}}}}_{\lambda^S} + \underbrace{\frac{\hat{\boldsymbol{\xi}}^H\mathbf{W}_S\mathcal{A}\hat{\mathbf{q}}}{\hat{\boldsymbol{\xi}}^H\mathbf{W}_S\hat{\boldsymbol{\xi}}}}_{\lambda^F}. \tag{B.3}$$

Without the presence of the structural damping parameter (i.e. $\zeta_\theta = 0$), the growth rate structural contribution $\lambda^S$ is identically 0, as $\lambda^S$ reads

$$\lambda^S = -\frac{\hat{\boldsymbol{\xi}}^H\mathbf{W}_S\hat{\mathcal{S}}\hat{\boldsymbol{\xi}}}{\hat{\boldsymbol{\xi}}^H\mathbf{W}_S\hat{\boldsymbol{\xi}}} = -\frac{-k_\theta\hat{\theta}\hat{\phi} + \hat{\phi}I_\theta\left(k_\theta\hat{\theta}I_\theta^{-1} + \zeta_\theta\hat{\phi}\right)}{k_\theta\hat{\theta}^2 + \hat{\phi}^2 I_\theta}. \tag{B.4}$$

Furthermore, the moment matrix $\mathcal{A}\hat{\mathbf{q}}$ in (B.3) may be decomposed into the contributions from

pressure and from viscous stress, such that

$$\mathcal{A}\hat{\mathbf{q}} = \underbrace{\begin{bmatrix} 0 & 0 \\ \hat{m}_{z,p} & 0 \end{bmatrix}}_{\mathcal{A}\hat{\mathbf{q}}_p} + \underbrace{\begin{bmatrix} 0 & 0 \\ 0 & \hat{m}_{z,\nu} \end{bmatrix}}_{\mathcal{A}\hat{\mathbf{q}}_\nu}. \tag{B.5}$$

This then leads to a further decomposition of $\lambda^F$ into

$$\lambda^F = \underbrace{\frac{\hat{\boldsymbol{\xi}}^H \mathbf{W}_S \mathcal{A}\hat{\mathbf{q}}_p}{\hat{\boldsymbol{\xi}}^H \mathbf{W}_S \hat{\boldsymbol{\xi}}}}_{\lambda_p} + \underbrace{\frac{\hat{\boldsymbol{\xi}}^H \mathbf{W}_S \mathcal{A}\hat{\mathbf{q}}_\nu}{\hat{\boldsymbol{\xi}}^H \mathbf{W}_S \hat{\boldsymbol{\xi}}}}_{\lambda_\nu}, \tag{B.6}$$

where $\lambda_p$ and $\lambda_\nu$ indicate the contributions from pressure and viscous stress respectively.